Redox-Active Ligand Mediated Single Electron Transfer Towards Homogeneous Catalysis

Vikramjeet Singh

A thesis submitted for the partial fulfillment of
the degree of Doctor of Philosophy

Department of Chemical Sciences
Indian Institute of Science Education and Research (IISER) Mohali
Knowledge city, Sector 81, SAS Nagar, Manauli PO, Mohali 140306, Punjab, India.

May 2024

Dedicated to

My Beloved Family

&

Supervisor

Dr. Debashis Adhikari

Declaration

I do hereby declare that the work presented in this thesis titled "***Redox-Active Ligand Mediated Single Electron Transfer Towards Homogeneous Catalysis***" has been carried out by me under the supervision of Dr. Debashis Adhikari in the Department of Chemical Sciences, Indian Institute of Science Education and Research (IISER) Mohali, India.

This work has not been submitted in part or full for a degree, diploma, or fellowship to any other university or institute. Whenever contributions of others are involved, every effort is made to indicate this clearly with due acknowledgments of collaborative work and discussions. This thesis is a bona fide record of original work done by me, and all sources listed within have been detailed in the bibliography.

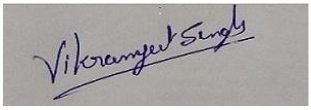

Vikramjeet Singh

Date: 30/05/2024

Place: Indian Institute of Science Education and Research (IISER) Mohali, India

In my capacity as the supervisor of the candidate's thesis work, I certify that the above statements by the candidate are true to the best of my knowledge.

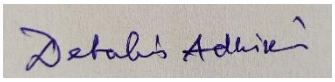

Dr. Debashis Adhikari

Associate Professor

Department of Chemical Sciences

Indian Institute of Science Education and Research Mohali

Date: 30/05/2024

Place: IISER Mohali

Acknowledgments

I express gratitude to God for his kindness and mercy, enabling me to navigate challenges and accomplish my responsibilities with strength, wisdom, and determination.

I wish to convey my sincere appreciation to my supervisor, Dr. Debashis Adhikari, for his unwavering guidance and support throughout the completion of this thesis. Your commitment to dedicating extensive time and patience to teach me essential techniques has been truly invaluable. I want to express gratitude for your consistent support as we delve into the marvels of science across diverse sectors. Additionally, I extend thanks for your uplifting pep talks and motivational stories during the challenging phases of my Ph.D. As your graduate student, I look forward to a future marked by great success, guided by divine providence.

I'd also like to express my gratitude to the members of my doctoral committee, Dr. Angshuman Roy Choudhury and Dr. Ujjal K. Gautam, for their valuable suggestions and helpful recommendations throughout my Ph.D. journey.

I extend my gratitude to the present director of IISER Mohali, Prof. Jayaraman Gowrishankar, and the former director, Prof. D. P. Sarkar, for providing state-of-the-art research facilities. Special thanks are also due to the current head of the department, Dr. S. S. V. Ramasastry, the former head, Dr. Sanjay Singh, and Dr. S. A. Babu for endorsing the use of various departmental instruments and offering their valuable recommendations. The outstanding capabilities of IISER Mohali's NMR, X-ray, and HRMS facilities are duly recognized. I appreciate Dr. A. R. Choudhury for his assistance in conducting X-ray analyses and resolving issues related to my samples. My thanks also go to Dr. Raj Kumar Roy, Dr. S. S. V. Ramasastry and Prof. Kavita Dorai, the current and former conveners of the NMR facility and NMR operator Mr. Balvir, for their collaboration. Furthermore, I express my heartfelt thanks to the committee members of the HRMS facility, particularly Dr. S. A. Babu and HRMS operator Mr. Triveni. I'd like to thank teaching lab members, Mr. Bahadur, Mr. Mangat. Next, I would like to acknowledge CSIR for the research fellowship.

I'd like to thank Dr. Kirti Singh and Manu Adhikari for their help with crystal data collecting and their intellectual insights and suggestions and again my senior Dr. Kirti Singh and Dr. Amreen Kaur Bains for their help with air-sensitive procedures.

I take immense pleasure in expressing my gratitude to all my past and present colleagues in the laboratory: Dr. Dhanajay Dey, Dr. Kirti Singh, Dr. Amreen Kaur Bains, Abhishek Kundu, Ayanangshu Biswas, Baisanal Mandal, Supriya Haldar, Monojit Roy, Rahul Singh, Shyamli Maji, Sourav Mandal, Dr. Bikramaditya Mandal, Himanshi Mittal, Vidhyalakshi Sridharan, Md Misbahur Rahman, Sudha Yadav, and Harshit Jain, who feel like an extended family to me. I extend my thanks to Abhishek Kundu for his unwavering support and assistance with theoretical calculations. I am truly grateful for the camaraderie of my juniors, Harshit Jain and Rahul Singh, who have fostered a positive environment and contributed significantly to my work. Special appreciation goes to Shyamli Maji for her assistance with my desk work. Last but not least, I appreciate the efforts of our lab intern, Nidhi Sinha, who provided valuable assistance with my desk work, and from whom I gained valuable insights during her training period.

I extend my appreciation to my collaborators and co-authors, namely Prof. Biprajit Sarkar (University of Stuttgart), his Postdoc fellow Dr. Arijit Singha Hazari for conducting EPR analysis on my samples, and Prof. Christian Limberg (Humboldt University of Berlin) and his student Mr. Kilian Weißer for their contribution to Mössbauer measurements. It seems like you're expressing gratitude towards Dr. Bhaskar Mandal for assistance with broken symmetry calculations. It's wonderful to acknowledge and appreciate the contributions of colleagues and mentors in scientific endeavors. Collaboration and support within the scientific community play a crucial role in advancing research and knowledge. I extend my appreciation to the members of the RKR and SSG labs for the enjoyable moments we experienced together.

I want to express my heartfelt thanks to my friends, Ankita Kumari, Ketan Kumar, Dr. Bara Singh, Manu Adhikari, Shakshi Chawla and Shaheen for their steadfast support throughout my Ph.D. journey. Additionally, I appreciate the valuable suggestions and troubleshooting assistance from my batchmates. I am also thankful to my IISER friends, Ishfaq and Vishnu for their support and motivation. Special thanks to my childhood best friends Harinder Singh, Inspector Dr. Harpal Singh and Abhinav Kumar for consistently being there for me.

This journey would not have commenced without the unwavering love and support of my parents. My father, Mr. Babu Ram, and my mother, Mrs. Geeta Rani, have toiled tirelessly in the face of adversity to establish a strong foundation for my life and future. Beyond that, I'm profoundly grateful for the presence of my exceptional grandparents, the late Mr. Krishan Chand and Mrs. Phoolwati. I owe my existence to both of them, and I am thankful for their

care during the formative first seven years of my childhood. They imparted crucial life lessons about perseverance, principles, and honesty that have guided me in my career, relationships, and life. I aspire to excel and make them proud.

My sisters, Amandeep Kaur, and my brother, Vijay Kumar, are my wellsprings of motivation and encouragement. I'm thankful for the joy brought by my little stars, Ranbir Singh, and my little angel, Annaya. A special thanks to my dear brother-in-law, Mr. Balbir Singh, for reminding me that life encompasses more than just work and for always finding time for shared laughter and moments of living together.

Finally, but certainly not least, I express my heartfelt gratitude to my best friend forever, Dr. Pooja Rani. Without her unwavering support, I believe completing my Ph.D. would have been a formidable challenge. I am profoundly thankful for her constant presence during both difficult and joyous times, particularly in the initial stages of my Ph.D. Her motivational talks remain etched in my memory, serving as a beacon of positivity akin to the sun. I commend her for her consistent support, both emotionally and intellectually, throughout the research journey. I consider myself extremely fortunate to have her in my life, and I anticipate that our friendship will continue to flourish in the future.

Vikramjeet Singh

About the author

Vikramjeet Singh, the author, originates from Patran in District Patiala, Punjab, India, where he was born and brought up. His educational journey began at Tagore Public Sen. Sec. School, and he earned a B.Sc. degree from Post Graduate Govt. College, Sector-11, Chandigarh, Panjab University in 2015. His educational pursuits continued at the same institution, culminating in a Master's degree in Chemistry in 2017. Demonstrating excellence, Vikramjeet achieved notable rankings in the CSIR-JRF national level exams in December 2017 and June 2018, securing AIR-21 and AIR-3, respectively. Additionally, he achieved an AIR-139 in the GATE-2018 exam.

In August 2018, Vikramjeet embarked on his Ph.D. journey, joining the research group led by Dr. Debashis Adhikari in the Department of Chemical Science at the Indian Institute of Science Education and Research (IISER) Mohali. He actively contributed as a graduate teaching assistant at IISER Mohali from 2019 to 2020. Currently, he holds the position of Senior Research Fellow in the Department of Chemical Sciences at IISER Mohali.

List of Publications:

1. **Vikramjeet Singh**, Harshit Jain, Shounak Nath, Debashis Adhikari*. Multielectron Redox Afforded by a Pincer Ligand Promoting Kumada Cross-Coupling Reactions. *Chem. Eur. J.*, **2023**, e202303189.
DOI: https://doi.org/10.1002/chem.202303189

2. **Vikramjeet Singh**, Rahul Singh, Arijit Singha Hazari, Debashis Adhikari*. Unexplored Facet of Pincer Ligands: Super-Reductant Behavior Applied to Transition-Metal-Free Catalysis. *JACS Au* **2023**, *3,* 1213–1220.
DOI: https://doi.org/10.1021/jacsau.3c00077

3. **Vikramjeet Singh**, Abhishek Kundu, Kirti Singh, Debashis Adhikari*. Redox Noninnocence of the Formazanate Ligand Applied to Catalytic Formation of α-Ketoamides. *Chem. Commun.*, **2022**, *58*, 6630–6633.
DOI: https://doi.org/10.1039/D2CC02089K

4. Dhananjay Dey, Abhishek Kundu, Monojit Roy, **Vikramjeet Singh**, Shyamali Maji, Debashis Adhikari*. Single Electron Transfer Catalysis by Diphenylthiourea Under Visible Light Photoredox Conditions. *Org. Chem. Front.*, **2023**, *10*, 5248–5253.
DOI : https://doi.org/10.1039/D2CC02089K

5. Amreen K. Bains, **Vikramjeet Singh**, Debashis Adhikari*. Homogeneous Nickel-Catalyzed Sustainable Synthesis of Quinoline and Quinoxaline under Aerobic Conditions. *J. Org. Chem.* **2020**, *85*, 14971−14979.
DOI: https://doi.org/10.1021/acs.joc.0c01819

6. **Vikramjeet Singh**, Abhishek Kundu, Kilian Weisser, Arijit Singha Hazari, Debashis Adhikari*. Exclusively Ligand Redox-Promoted C-H Tertiary Alkylation of Heteroarenes. (Communicated)

7. **Vikramjeet Singh**, Nidhi Sinha, Debashis Adhikari*. Trianionic NNN Pincer: A Photo-Redox catalyst for Transition-Metal-Free Reductive Cyclisation of Organic Halides to Access Indolines and Oxindoles. (Under preparation)

List of Conferences:

Oral presentation	"*Ligand Redox–Mediated Alcohol Dehydrogenation Towards Efficient Synthesis of Heterocycles*" in International Conference on Intellection, Innovation and Implication in Chemistry (IIIC-2021) organized by DAV University, Jalandhar, India in virtual mode.
Poster presentation	"*Redox noninnocence of the formazanate ligand applied to catalytic formation of a-ketoamides*" in International Conference on Modern Trends in Inorganic Chemistry –XIV (MTIC-2022) organized by Department of Chemistry, Institute of Science, Banaras Hindu University, Varanasi, India.
Poster presentation	"*Ligand Redox–Mediated Alcohol Dehydrogenation Towards Efficient Synthesis of Heterocycles*" in International Conference on Recent Advances in Chemical Sciences (ICRACS-2021) held in virtual mode organized by J. C. Bose University of Science and Technology, YMCA, Faridabad, India. (**Awarded for best poster presentation**)
Volunteer Poster presentation	"*Redox noninnocence of the formazanate ligand applied to catalytic formation of a-ketoamides*" in 29th CRSI National Symposium in Chemistry (CRSI-NSC-29) & CRSI - ACS Symposium Series in Chemistry organized by Department of Chemical Sciences, IISER Mohali, Mohali, Punjab, India.
Participated	1ST CRIKC Chemistry Symposium (CCS 2019) held in IISER Mohali organized by Department of Chemical Sciences, IISER Mohali in association with Panjab University, IIT Ropar, INST Mohali.
Participated	Recent Advances in Organic and Bioorganic Chemistry (RAOBC) organized by Department of Chemical Sciences, IISER Mohali.

Participated	Instrumental Techniques for Chemical & Material Analysis organized by PEC University, Chandigarh, India

Abbreviations

Units

A	Ampere
V	Volt
W	Watt
atm	Atmospheric (unit of pressure)
a.u	Arbitrary units
°C	Degree Celsius (0 °C= 273.15 K)
h	Hour/s
Hz	Hertz
MHz	Megahertz
K	Kelvin
mg	milli gram(s)
min	minute(s)
mL	milliliter(s)
mmol	milli mole(s)
mol%	Molar percent
ppm	parts per million
Å	Ångström (1 Å = 10^{-10} m)
nm	Nanometer (1 nm = 10^{-9} m)
μ	Micro (prefix: 10^{-6})

Chemical Notations

Ar	Argon Gas
MeCN	Acetonitrile
MeOH	Methanol
DMSO	Dimethylsulfoxide
THF	Tetrahydrofuran
EtOAc	Ethyl Acetate
TMS	Tetramethylsilane
BHT	3,5-Di-tert-4-butylhydroxytoluene
TEMPO	2,2,6,6-Tetramethyl-1-piperidinyloxy
$CDCl_3$	Deuterated Chloroform
DMSO-d_6	Deuterated Dimethylsulfoxide

C_6D_6	Deuterated Benzene
MeCN-d_3	Deuterated Acetonitrile
Me	Methyl
Et	Ethyl
^{t}Bu	Tert-butyl

Other Notations

TLC	Thin layer chromatography
equiv	Equivalent
DFT	Density functional theory
HRMS	high resolution mass spectrometry
m/z	Mass-to-charge ratio
NMR	Nuclear magnetic resonance
δ	Chemical shift in NMR
J	Coupling constant in NMR
d	Doublet in NMR Spectrum
dd	Doublet of doublet in NMR Spectrum
s	singlet in NMR Spectrum
t	triplet in NMR Spectrum
LMCT	Ligand to metal charge transfer
MLCT	Metal to ligand charge transfer
HOMO	Highest occupied molecular orbital
LUMO	Lowest unoccupied molecular orbital
PC	Photocatalyst
IC	Internal conversion
ISC	Intersystem crossing
MC	Metal centered
MLCT	Metal to ligand charge transfer
UV-VIS	Ultraviolet-visible spectroscopy
λ	wavelength
λ_{ex}	Maxima of the excitation wavelength
λ_{max}	Maxima of the emission maximum
a, b, c	Lattice parameters (X-ray)
α, β, γ	interaxial angles (X-ray)

Synopsis

Redox-Active Ligand Mediated Single Electron Transfer Towards Homogeneous Catalysis

A thesis submitted for the degree of Doctor of Philosophy

Vikramjeet Singh, Ph.D. in Chemical Sciences (PH18029); February-2024

This thesis delves into a detailed exploration of the ligand-assisted electron transfer processes in conjunction with 3d metals, aiming to replicate the redox chemistry observed in precious metals. Our focus is on elucidating how redox events can facilitate reversible electron transfers, that is dependent on accessible stable redox states of the catalyst molecule. The ease of electron transfer from the ligand backbone can be integrated with bond activation processes so that such events can be translated to efficient catalytic reactions. The thesis presents five chapters.

The first chapter introduces the concept of redox non-innocent ligands and provides a literature review on recent advancements in redox-active ligands exhibiting transition metal activity, particularly in the realm of homogeneous catalysis. The subsequent four chapters describe our efforts to develop single electron transfer-mediated transformations using redox-active ligands, both in the presence and absence of metals, under thermal or photochemical conditions. These chapters present a range of spectroscopic data aided by theoretical calculations that contribute to a deeper understanding of reaction mechanisms for the discussed chemical transformations.

Chapter 1. Literature Survey on Redox Active Ligands and Scope of Redox Active Ligands with First-Row Transition Metal Towards Base Metal-based Catalysis

In this chapter, we have conducted a thorough examination of the existing literature on redox-active ligands and delved into the potential applications of these ligands in catalytic processes involving first-row transition metals. Our primary focus has been on exploring opportunities for 3d transition metal-based catalysis. The chapter is structured into two major sections. The first section entails a discussion on the background information of redox-active ligands and a review of previous work concerning catalytic applications of 3d transition metal complexes utilizing these ligands. We delve into how 3d transition metals can replicate the redox chemistry of heavy metals by leveraging redox-active ligands, to make the synthesis process cost-effective and sustainable. The second section of the chapter examines the photo-physics of some transition metal complexes and their application in photocatalysis, aiming to transform simple molecules or ligands into highly effective super-reductants.

Chapter 2. Multielectron Redox Afforded by Pincer Ligand Promoting Kumada Cross-coupling Reactions

In this chapter, the redox-active nature of a pincer has been exploited to conduct C-C cross-coupling reactions under mild conditions. A nickel complex comprising NNN-pincer is dimeric in solid state, and the structure displays a Ni_2N_2 diamond core. In the dimeric structure both ligand backbones house an electron, in the iminosemiquinonate form, to keep the metal's oxidation state at +2. In the presence of aryl Grignard reagent, only 3 mol% loading the nickel complex generates Kumada cross-coupled product in good yield from a wide variety of aryl-X (X = I, Br, Cl) substrates. The ligand-based radical remains responsible to promote such coupling reaction following a radical pathway that is suggested by TEMPO quenching. Furthermore, a radical-clock experiment tracing linear vs cyclic product distribution unambiguously supports the radical's involvement through the catalytic cycle. A series of thorough mechanistic probation including computational DFT analysis disclose the cooperative action of both redox-active pincer ligand and the metal centre to drive the reaction.

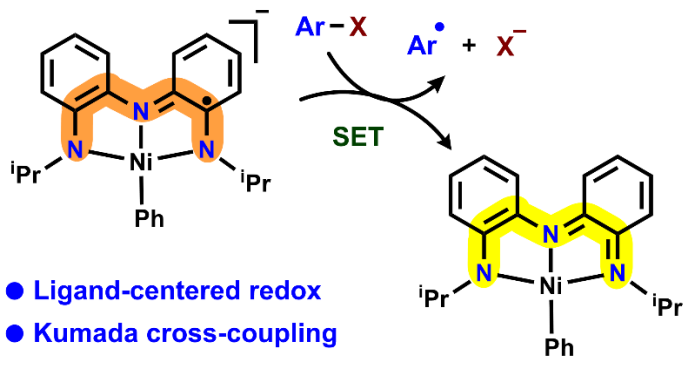

Scheme 1. Activation of aryl halides via single electron transfer from ligand backbone.

Chapter 3. Unexplored Facet of Pincer Ligands: Super-Reductant Behavior Applied to Transition-Metal-Free Catalysis

In this chapter, we harnessed the highly reducing capabilities exhibited by a pincer ligand. Pincer ligands are well-established supporting ancillaries to afford robust coordination to metals across the periodic table. Despite their widespread use in developing homogeneous catalysts, the redox non-innocence of the ligand backbone is less utilized in steering catalytic transformations. Here we showcased a trianionic, symmetric NNN pincer to drive C−C cross-coupling reactions and heterocycle formation *via* C−H functionalization, without any coordination to transition metals. The starting substrates are aryl chlorides that can tease the

limit of a catalyst's ability to promote a reductive cleavage at a much demanding potential of −2.90 V vs SCE. The reducing power of the simple trianionic ligand backbone has been

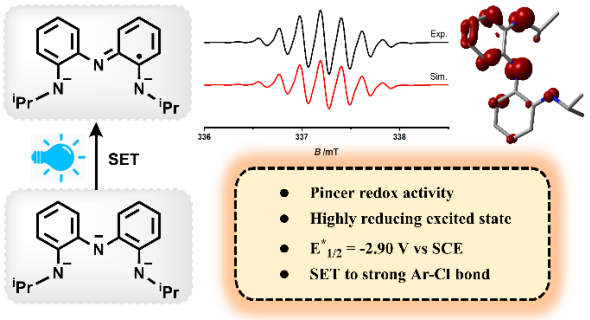

Scheme 2. Redox properties of trianionic NNN pincer under photochemical conditions.

tremendously amplified by shining visible light on it. The catalyst's success relies on its easy access to the one-electron oxidized iminosemiquinonate form that has been thoroughly characterized by X-band electron paramagnetic resonance spectroscopy through spectroelectrochemical experiments. The moderately long-lived excited-state lifetime (10.2 ns) and such a super-reductive ability dependent on the one-electron redox shuttle between the *bis*amido and iminosemiquinonato forms make this catalysis effective.

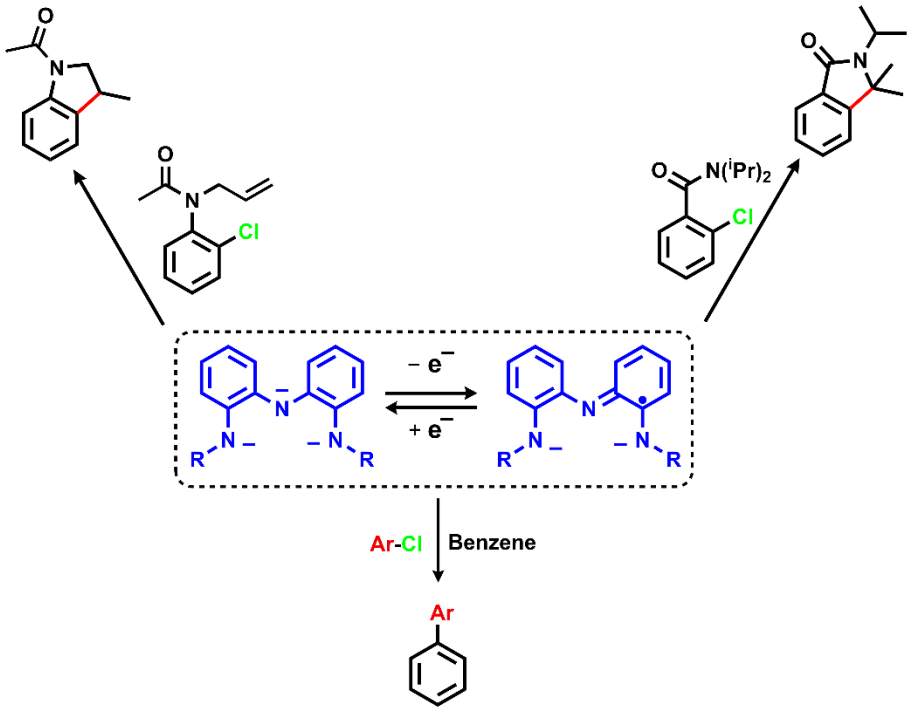

Scheme 3. Various organic transformations via trianionic pincer ligand.

The chapter is partitioned into two segments. The initial part outlines the photophysical property, C−C cross-coupling reactions, and the formation of heterocycles through C−H functionalization. The second part extends the catalytic application of the pincer ligand, focusing on the preparation of indolines and oxindoles, with potassium tert-butoxide playing a pivotal and multifaceted role. It serves as a base for deprotecting the pincer ligand to generate the active ligand catalyst, acts as a reductant to reduce the oxidized ligand, and serves as a hydrogen atom transfer reagent.

Chapter 4. Redox Non-Innocence of Formazanate Ligand Applied to Catalytic Formation of *α*-Ketoamides

In this chapter, we have developed the redox noninnocence of formazan ligand in iron(III) formazanate complex. The formazan ligands have been investigated as redox non-innocent backbones for a long time. Despite their well-established behaviour as redox reservoirs, the demonstration of catalytic efficiency governed by redox non-innocence remains elusive. We report an iron–formazanate molecule for efficiently preparing *α*-ketoamides, where a crucial reductive cleavage of the substrate molecule is tightly regulated by the electron donation from the formazanate, in a reversible manner. The ligand-based radical remains instrumental in facilitating the reaction through a radical pathway. Additionally, conducting a TEMPO quenching experiment and tracking the product distribution unequivocally substantiates the involvement of radicals throughout the catalytic cycle. A comprehensive exploration of the mechanistic intricacies, including computational DFT analysis, reveals the collaborative role of both the redox-active pincer ligand and the metal center in propelling the reaction.

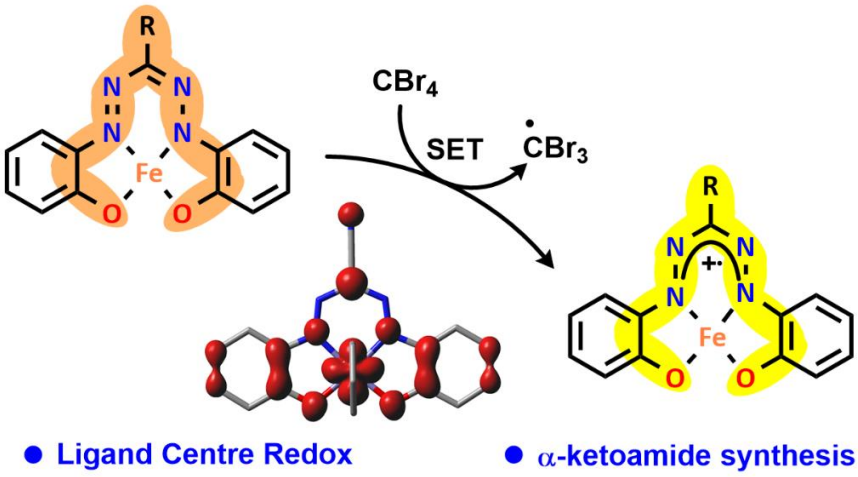

Scheme 4. Redox non-innocence of iron-formazanate complex to promote single electron transfer and reductive cleavage of tetrabromomethane.

Chapter 5. Exclusively Ligand Redox-Promoted C-H Tertiary Alkylation of Heteroarenes

In this chapter, we described a preponderant role of the redox active formazanate ligand backbone in steering 3d transition metal iron catalysis. The iron complex of the chosen formazanate ligand exhibits speciation comprising two species with high-spin, S = 5/2 Fe(III) that has been probed thoroughly by zero-field Mössbauer and X-band EPR spectroscopies at low temperature. The one-electron oxidation of the bulk sample proves completely ligand-based process, as examined by these spectroscopic techniques. The ligand-redox process has been exploited to develop an iron catalyst used for C-H tertiary alkylation for a host of heterocycles and styrenes. The efficiency of such ligand-promoted catalysis is further attested by only 1 mol% of catalyst loading that affords products in high yields. Plausibly the vacant site at Fe(III) helps in substrate binding, leading to reductive bond cleavage of a substrate C-Br bond, while the electron for this purpose is entirely provided by the formazanate backbone. Several key intermediate isolation speaks for the radical process and delineate the mechanism for C-H alkylative transformation proving the great utility of the ligand redox in executing such a process.

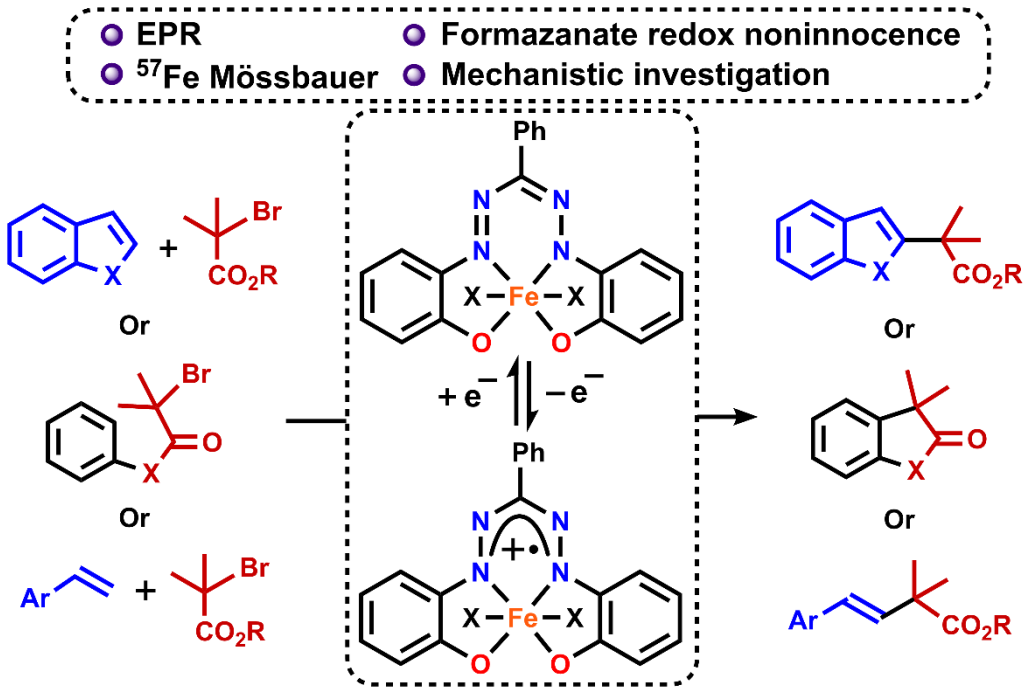

Scheme 5. Elucidation of Redox non-innocence of iron-formazanate complex by various spectroscopic technique to promote single electron transfer and mechanistic investigation.

Table of Contents

xxx

Chapter 1

Literature Survey on Redox Active Ligands and Scope of Redox Active Ligands with First-Row Transition Metal Towards Base Metal-Based Catalysis

1.1. Redox-Noninnocent Ligands

1.1.1. Introduction

The concept of oxidation state is widely used in the inorganic chemistry for the purpose of electron bookkeeping.[1] However, one can confidently assign the metal oxidation state without any ambiguity when an innocent ligand is coordinated to the metal center. Usually, one electron oxidation or reduction of spectator "redox-inactive" ligands require more energy in comparison to redox events occurring on the metal center. While this approach is often correct, such presumptions may provide answer that are deceiving. To dissect between cases where metal oxidation state determination is (un)ambiguous, the term innocent and noninnocent were introduced by Jørgensen in 1966.[2] He proposed a ligand can be described as either innocent or noninnocent is dependent on whether a ligand permits the oxidation state of the central metal to be well defined. The term noninnocent ligands implies as an uncertainty in oxidation state assignment for the metal center. In case of redox inactive ligands, the removal of an electron from a coordination complex results in change in the electronic structure of metal center and negligible or no change at coordinated ligands. For example, a classical Werner-type compounds such as *cis*-$[Co(NH_3)_4Cl_2]$ or organometallic species such as ferrocene, the oxidation-state assignment and subsequent determination of a d^n electron configuration can be easily predicted by formal charge distribution. These examples provide convenient and portable explanations for the substitutional lability of the cobalt(II) compound or the stability of the organometallic ferrous species.

On the other hand, redox active ligands possess more energetically accessible energy levels for oxidation and reduction.[3] So, either ligands can undergo the redox processes without any change in metal oxidation state or both the ligand and metal center can undergo oxidation/reduction in a synergistic fashion. This scenario creates ambiguity about the electronic state of both the metal and ligand.

Redox innocence of ligands has been recognized a long time back in coordination chemistry. Gray and co-workers showed two square-planar cobalt[4] and nickel[5] complexes with two dithiolene ligand and described these as metal(II) compounds with two ligand radical anions, rather than the metal in the +4 oxidation state with a dianionic ligand. One of the most common example in redox noninnocence is NO ligand, that may bind as a cation in linear geometry or an anion with a bent geometry.[3] In this scenario, if the same assumption of innocent ligand is followed, an erroneous oxidation state of the metal could be assigned,

depending upon the redox state of ligands.[6] As a simple example, dioxygen has been recognized as a non-innocent ligand and that exist in three redox states (O_2, $O_2^{\cdot-}$, O_2^{-2}). Although, the difference between the triplet neutral O_2, the doublet intermediate $O_2^{\cdot-}$, the diamagnetic O_2^{-2} has been well established, yet the proper description of oxymyoglobin and oxyhemoglobin is under debate.[7]

Nature has created various metalloenzymes wherein the active site of enzyme employs redox active ligands which acts in synergy with the metal ion.[8, 9] Metalloproteins have evolved to incorporate abundant metal ions such as iron and copper, which preferentially react via one-electron redox couples. A metal complex with radical on the supporting ligand is also present in multiple active sites of metalloproteins, responsible for enzymatic catalysis.[8] In these enzymatic catalytic pathways, the multi-electron process/reactions are broken into smaller steps, which helps the reactions to occur near thermodynamic potential and enable metal to expand upon a metal's ''common'' reactivity.[10-14] Many important biological transformations are multielectron processes, where redox active ligand in the active site of metalloenzyme not only afford two or four electron chemistry, but also inhibit potentially deleterious radical reactions. A widely known example of redox-active ligands containing metalloenzyme is galactose oxidase[15], known to oxidise the alcohol to aldehyde. This enzyme carries Cu(II) ion coordinated to a modified tyrosyl radical. This special bonding environment gives rise to the function of the enzyme.[16] Other than that, quinones (both ortho and para) has shown their versatile activity in many biologically relevant reactions like photosynthesis,[17-19] respiration[20] and enzymatic processes.[21] Bioactive cofactors/ enzymes with redox noninnocent ligands like tyrosyl/tyrosinate redox pair[22], porphyrins[23], pterins[24], flavins[25] are involved in various biological transformations with or without enrolment of metals.

During such activation, sometimes substrate often itself develops redox non-innocent character and prominent examples in this category are carbenes[26], nitrenes[26], oxygen[7], etc. In 2010, Kaim highlighted some of the well-established redox-active ligands[9] in bioinorganic chemistry that include organic ligands such as diimines[27], o-quinone[28], bipyridyl[29], pyridinediimine[30], amidophenolate[31], porphyrins[23], formazanate[32, 33], β-diketiminates[34]. Spectroscopic and theoretical investigation of the redox behavior of a few redox systems containing catechol, o-phenyldiamine, phenyldithiolene system were thoroughly investigated by Pierpont[35, 36], Lever[37, 38] and Wieghardt.[22, 39]

Various kinds of redox-active ligands have been designed and explored in recent decades, resulting in important applications in catalysis.[28] Redox noninnocent ligands have an individual potential to form radical species, which would be unstable in solution. Few examples of ligands which can undergo reversible one/two electron reduction keeping formal oxidation state of metal unchanged, are enlisted in Figure 1.1.

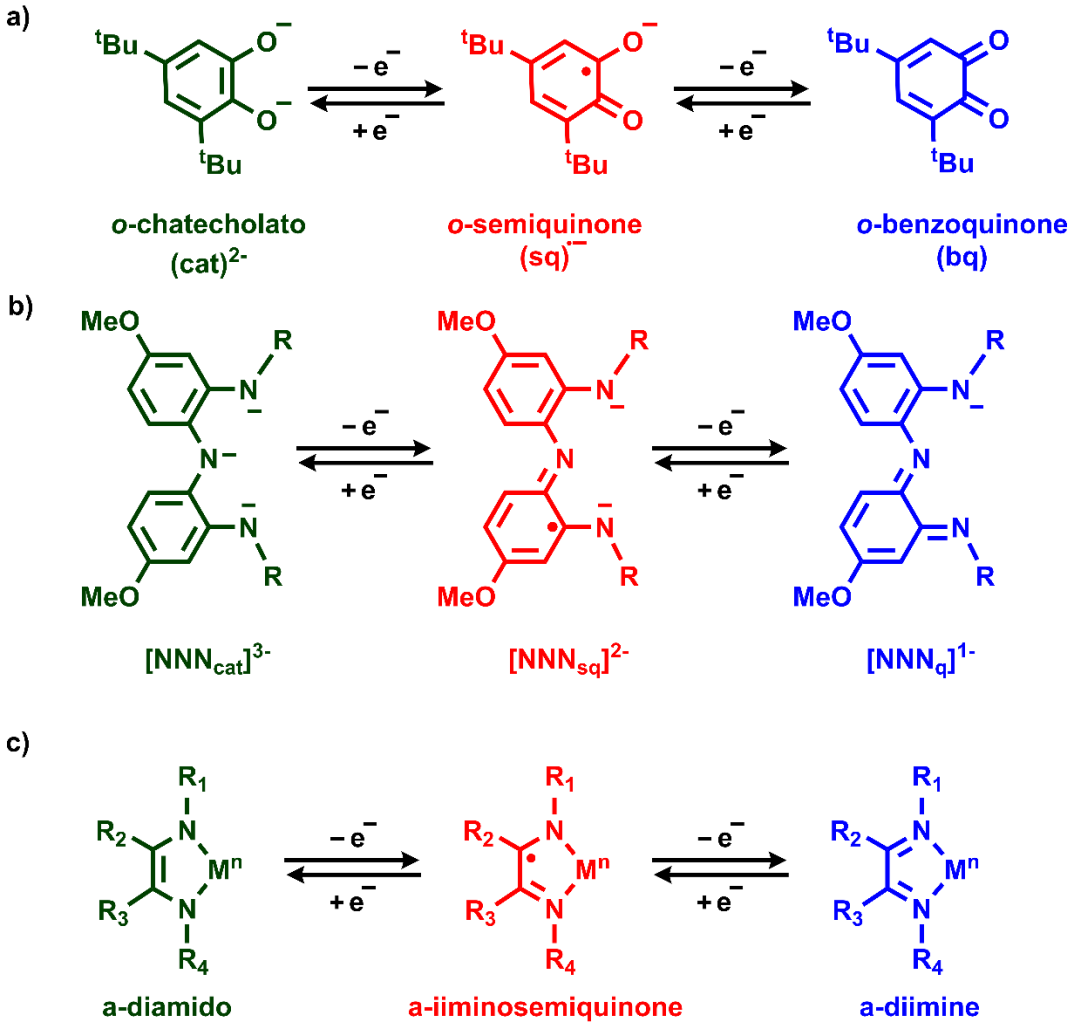

Figure 1.1. Oxidation levels of some redox active ligands.

A fully reduced catecholate as ligand can undergo one electron reversible oxidation giving semiquinone and a subsequent oxidation of the ligand will give fully oxidized o-benzoquinone (Figure 1.1a). Similar behavior can be seen in other derivatives of these ligands having similar architecture, like α-diamine, aminophenol's and animothiophenol. As depicted by Heyduk and coworkers, trianionic pincers like [ONO] and [NNN] can also exist in three oxidations states. In a similar way as shown in (Figure 1.1b), the redox activity of the ligand can be attained when coordinated to metal (Figure 1.1c).

1.1.2. Mode of Reactivity of Redox-Active Ligands

Although, the principles of redox active ligands have been established several decades ago, the true potential of these ligands has not been tested widely in synthetic chemistry. For a large part they were spectroscopic curiosities and evaluation of non-trivial electronic structure configurations. In the last decade, various classes of redox active ligands have been extensively investigated towards their applications in catalysis and material science. These ligands can expand the reactivity of metals in several ways and based on their mode of reactivity, the ligands are broadly classified into four categories (Figure 1.2)

a) Electron reservoirs and store electrons.

b) Beyond electron reservoirs.

c) Variation in the Lewis acidity or basicity of the metal center.

d) (i) Direct redox-active ligand-to-substrate single electron transfer and (ii) generation of reactive ligand-centered radicals.

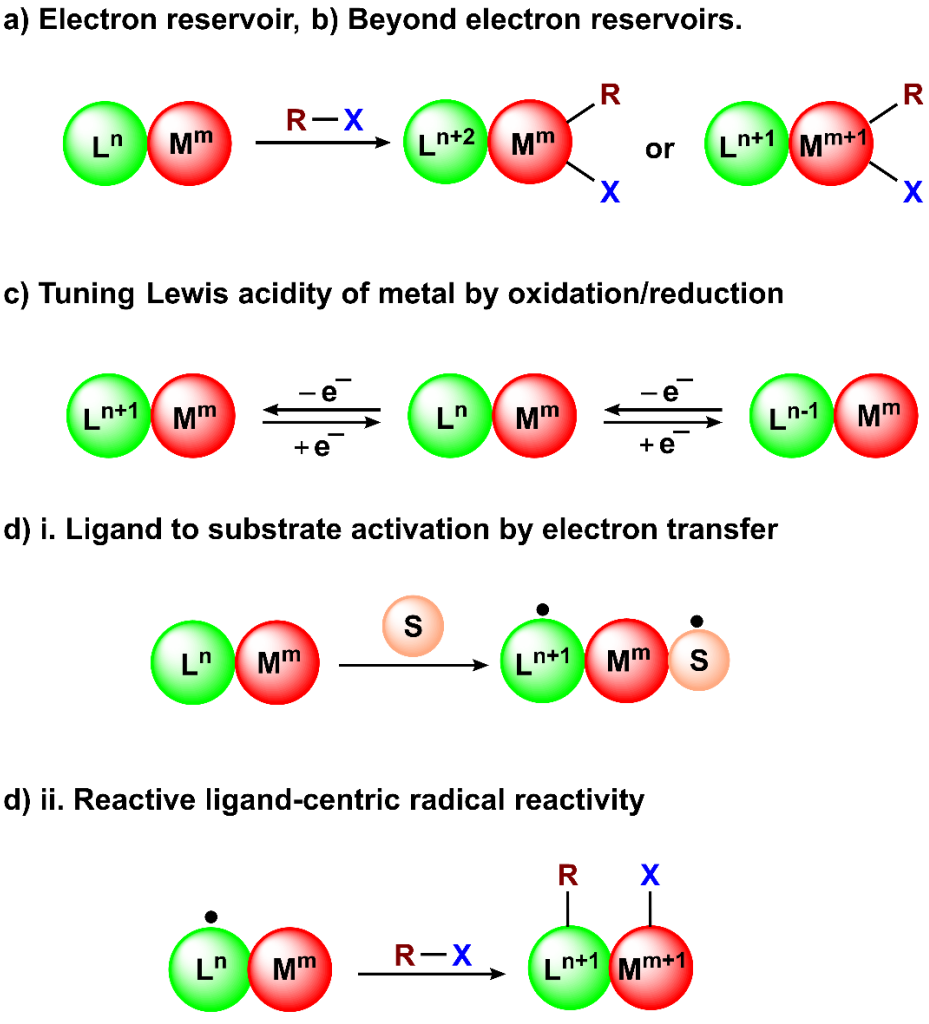

Figure 1.2. Mode of reactivity of redox active ligands.

a) Redox-Active Ligands as Electron Reservoir and Store Electrons

The redox active ligands act as electron reservoirs and store electrons, which it can give back during catalysis avoiding uncommon oxidation states of the metal. In case of early transition metal complexes, metal ions often exist in fully oxidised (high-valent) form with d^0 configuration. Due to this, traditional oxidative addition is considered to be impossible for d^0 metal ions. Redox active ligands are powerful tools to exhibit new reactivity on metal complexes, in a way that the redox properties can be tuned by steering the electron transfer to or from the ligand scaffold. Heyduk group in 2005, reported an important proof of redox activity of a trianionic tridentate NNN ligand bearing a redox active phenylenediamine with a flanking anilide donor arm[40] and substituents on this backbone allowed the tuneability for redox potential.[41] Using this ligand they described a reaction between a d^0 zirconium(IV) complex and molecular chlorine, which resulted in oxidative addition to yield the Zr(IV) dichloride derivative which was thought to be impossible with a metal complex having metal center in d^0 configuration. Upon interaction between Zr complex and chlorine molecule, both the redox active ligand in reduced form donate one electron to facilitate the homolytic activation of Cl-Cl bond. The catecholate ligand backbone during this oxidation event changes to semiquinone that has been proved by spectroscopic analysis. The same group also showed that aminophenol-based ligands are also capable of facilitating a formal reductive elimination of a C–C bond on a metal centre with a d^0 electron count[42] and a catalytic nitrene transfer of organoazides to isocyanides to afford carbodiimides is feasible using Zn(NNN) analogue.[43, 44] Mechanistic investigation led to the proposal that the NNN ligand is oxidized by two electron from reduced to quinone oxidation state and organoazide substrate is activated to form imido complex with release of N_2 gas. Similarly, redox active aminophenol (ON) and o-phenylenediamine (NN) based Zr(IV) and titanium complex are capable to undergo formal reductive elimination on metal center with a d^0 electron upon oxidation on ligand center.[45] ONO ligand also works similar to NNN ligand but apart from oxidative addition reactivity, Ta complex of ONO ligand is able to catalytically convert aniline[46] and phenyl azide[47] to the corresponding azobenzene. To convert aniline into azobenzene, four electron oxidations of aniline is facilitated by ONO ligand, being shuttled from catecholate to quinone oxidation state. Afterwards, Baik group produced a detailed computational mechanism which strongly supports the mechanism proposed by Heyduk, and revealed that electron transfer from ligand to substrate is more favorable as compared to direct metal to substrate electron transfer.[48] However, computed pathways revealed that there was no direct two electron transfer but it followed the two

consecutive, non-concerted ligand to substrate single electron transfer. Heyduck group recently investigated the effect of metal centre on the electronic structure of complex using a series of isostructural ONO pincer complexs (V, Nb, Ta).[49]

In 2018, Mandal and coworkers developed Ni(II)[50] and Co(II)[51] complexes with a redox active phenalenyl ligand (PLY) and utilized as an electron reservoir to develop a 3d transition metal-assisted catalyst. The mechanistic aspect of a ligand to substrate electron transfer though metal centre has been investigated using various spectroscopy and theoretical studies and this strategy has been successfully applied on hydrosilylation of a wide variety of olefin substrates under ambient conditions.

b) Beyond Electron Reservoirs

Although the major involvement of redox active ligands is to store one or two electrons for tuning reactivity at the metal center, there are many other delicate facets that assist a chemical transformation. The ability of these species to stabilize or generate substrate centered radicals in the coordination sphere of metal via ligand to substrate single electron transfer enable odd electron reactivity in a controlled manner. Bioinspired metal–ligand bifunctional activation of substrates and cooperative catalysis using 'reactive ligands' have attracted much attention in the last decade. A plethora of ligand motifs have been developed to facilitate a wide variety of bond activation processes.[52-54] Galactose oxidase enzyme is one of the most studied example of ligand-centred cooperative reactivity which effectively converts the primary alcohols into aldehyde using oxygen as oxidant and generate H_2O_2 as side product. Inspired by metalloenzymes, Wieghardt reported Cu(II) and Zn(II) complexes of ONNO redox active tetradentate ligand. These metal complexes actively catalyze oxidation of alcohols to aldehyde under aerobic conditions. In the similar direction, Storr investigated the aminophenol based Cu(II) metal complex. This complex performs alcohols oxidation converting it to aldehyde using oxygen as oxidant. However, no experimental evidence or proposal for the active role of the redox-active ligand in these transformations is provided.[55] Heyduk et al. explored the use of an (phenol)aminophenol ONO ligand as both electron- and proton-reservoir for the reduction of molecular oxygen with zirconium(IV).[56]

c) Changing the Lewis Acidity/Basicity

The change in the oxidation state of a ligand coordinated to metal center can have a significant alternation in Lewis acidity or basicity of metal center.[57-59] As a result, coordination behaviour of ligand associated with hemilabile donor opens a new window for redox switchable catalysis.

The ability to switch a catalyst by reduction or oxidation can be used to design a catalyst that behaves orthogonal towards different substrates, a new approach allowing for chemo selective conversions and potentially catalytic cascade reactions. Towards this goal, Rauchfuss and co-workers showed the redox switchable activations of alkene with a redox active amidophenolate based platinum(II) complex.[60]

d) Direct Redox-Active Ligand-to-Substrate Single Electron Transfer and Generation of Reactive Ligand-Centered Radicals

Redox active ligands generate reactive ligand-centered radicals[61] which further helps in activation of substrate and directly activate substrates via radical-type reactions.[62-64] The reactive intermediates are generated by electron transfer from ligand to substrate. Fine tuning of the orbital energy enables the metal complex to stabilize ligand centered radical by delocalization over the ligand backbone. This fine tuning in metal ligand cooperativity upon a suitable stimulus can empower intramolecular single electron transfer from ligand backbone to metal-bounded substrate and generate a substrate-centered radical in the proximity of the metal.

1.1.3. Determination of the Ligand Oxidation State of a Redox Non-Innocent Ligand

As mentioned above, these ligands can exist in various oxidation levels. The different oxidation state can be attained by sequential one electron reduction or oxidation via chemical or electrochemical pathways. The exact oxidation state of transition metal complexes coupled with redox noninnocent ligands is not always easy to determine due to delocalization of charge density of metal to ligand backbone. So, the exact formal oxidation state of metal center is questionable. This question can be addressed by determining the physical oxidation state rather a formal one.

As such prediction of the oxidation state of the ligand when it is coordinated to the metal center is difficult to predict by using standard formal charge methods due to accessible ligand oxidation state. There are several analytical tools for determining the oxidation state of both the redox-active ligand and the metal ion. For example, electronic spectroscopy, magnetic data, electron paramagnetic resonance (EPR) data, single crystal X-ray diffraction (SC-XRD), theoretical modelling, and patterns of reactivity are often required to assign the true electronic structure description of a transition metal complex.

Cyclic voltammetry (CV) is insignificant to find the locus of redox event in molecule but it provides insight into the potential window for different metals and ligand-based transitions. By comparing the redox potential of metal complex with respect to metal redox potential, it can be sometimes predicted whether the metal or ligand is undergoing

oxidation/reduction. EPR spectroscopy along with density functional theory (DFT) calculations can afford information about the location of the unpaired electron. In 2005, Wieghardt reported palladium complex of redox active 2-(2-trifluoromethyl)anilino-4,6-di-tert-butylphenol ligand and elaborated the spectroscopic analysis of parent complex and its oxidized form. The X-band EPR spectrum of the single electron oxidized complex was performed which disclosed a signal at $g_{iso} = 2.0007$ and S = 1/2 ground state, indicating that an organic radical was primarily located on a redox noninnocent ligand backbone. However, it may be difficult to detect two radical ligands, because they may be strongly coupled through a central metal and not produce a distinctive signature in spectroscopic studies.[65] In the case of a system possessing two unpaired electrons, there are two possibilities, a) the electrons are strongly antiferromagnetically (AF) coupled or b) weakly antiferromagnetically coupled. In the strongly AF-coupled scenario, metal complex can be EPR silent. To clear out this ambiguity, the magnetic moment analysis could be a crucial tool, while the magnetic moment analysis can determine the strength of coupling. A magnetic moment measurement (in solid or solution state) can provide the description of spin state of metal complex i.e., number of unpaired electrons present in the system. The temperature dependent spin-state changes can be investigated using SQUID magnetometer. In a redox active ligand, as the redox process predominately takes place on the ligand backbone.

In case of oxidation of ligand, electrons are taken from HOMO of ligand and in case of reduction electron are filled in the LUMO of ligand. Upon the redox process change in the bond length is often expected, if the appropriate frontier orbital is located on the specific part of the ligand. X-ray crystallographic analysis shows bond metrical parameters which helps to pinpoint the locus of oxidation. In some instances, porphyrin and β-diketiminate shows exceptional behavior, where ligand-based redox does not leave a significant change in in metrical parameters. This unusual behavior was termed as *hidden non-innocence* by Wieghardt Brown, he has developed a method that allows for the quantification of the oxidation state for amino phenolate and catecholate derived ligands.[66] He proposed on the basis of C-C, C-O and C-N bond length a metical oxidation state (MOS) can be assigned. Additionally, spectro-electrochemistry (either UV-vis or IR) in an optically transparent thin-layer electrolysis (OTTLE) cell is another informative technique to shed light on species generated transiently. On the other hand, cyclic voltammetry can provide information about the reversibility of redox events, whether a redox event is metal or ligand centered and about the potential required for

bulk electrolysis.[66] Sometimes, Mössbauer spectroscopy is also helpful in case of Mössbauer active metal center like iron.

Theoretical calculations are invaluable tools to understand ligand redox noninnocence. DFT calculations elicit the molecular orbital picture and electronic structure of metal complex and shows the locus of an electron on a metal and/or ligand.

1.1.4. Need of Redox-Active Ligands in Catalysis

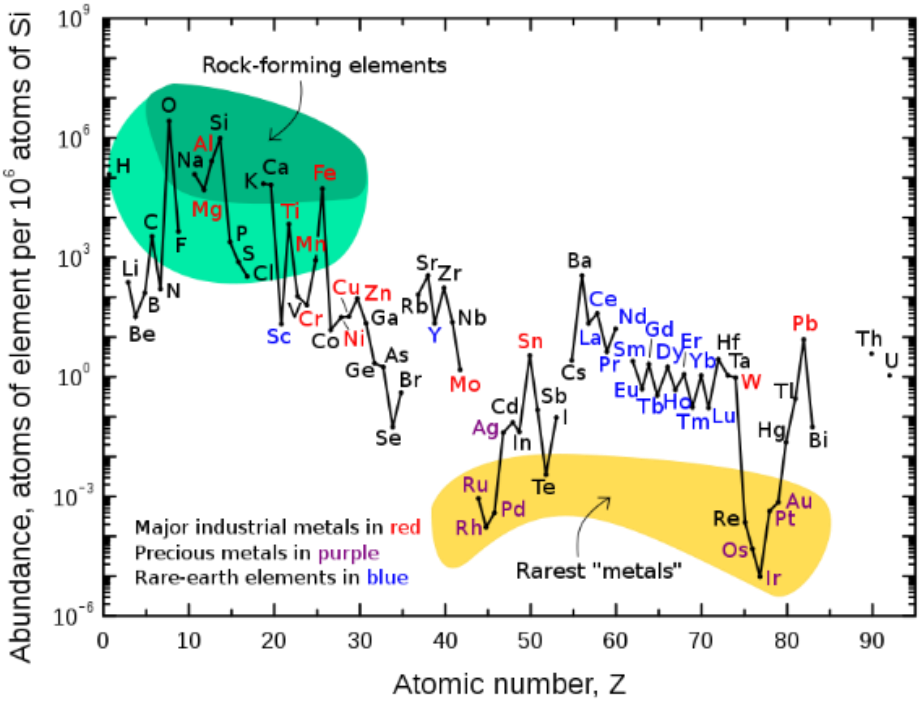

Figure 1.3. Abundance of metals in Earth's upper crust.[67]

Nowadays most of catalytic processes require metal-based redox to facilitate desirable chemical transformations. Late transition metals, especially the 2nd and 3rd-row elements, have reached to epic stage in well-established catalysis due to their easy affordability of a redox state separated by two electrons.[68] Many catalytic processes are predominantly oxidative addition or reductive elimination, which proceed via two-electron steps and require easily accessible M^{+n} and $M^{+(n+2)}$ oxidation states. Group 10 metals Ni, Pd are commonly applied for cross-coupling reactions because these metals can provide two electron transfer by virtue of M^{0}-M^{II} redox cycle. In coventional catalysis, usually the entire redox process is metal-centered where ligands playing a vital role of fine tuning the reactivity through steric and electronic interactions. Such ligands are called *spectator ligands* and their interaction with metal determines overall property of a catalyst; however, they are inactive in redox processes. Some

formally redox neutral involve two electron chemistry are connected to transition metals. On the other hand, the first-row transition (base) metals don't allow the same transformations and predominantly undergo single electron changes. Likely, these heavy metal photocatalyst has been tested in various organic transformations like C-C, C-N, C-O coupling reaction, and cyclization reactions. Despite the usefulness of such photocatalysts, their sustainability is a matter of concern due to their high cost, environmental non compatibility and dependency on precious metals. Furthermore, the use of heavy metals even in a catalytic amount, results metal contamination in most the synthesized pharmaceutical and biological active molecules which causes serious health issues.

However, significant demand for the absence of a heavy-metal impurity in pharmaceutical molecules motivated chemists to seek catalysts employing 3d-block metals. Toward this end, electron transfer catalysis has emerged as a viable alternative to the traditional heavy metal

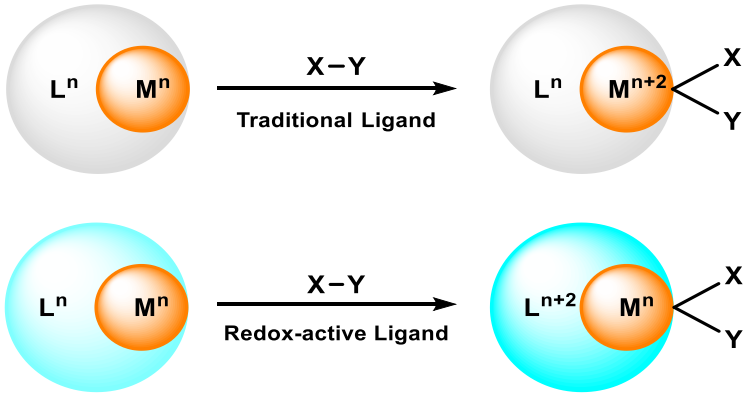

Figure 1.4. Course of action of redox in-active and redox active ligands.

mediated two-electron chemistry. The disadvantage of first-row transition metals is their operation via one-electron steps, limited catalytic effectiveness, and susceptibility to decomposition/oxidation/corrosion. They are not also very efficient in determining product selectivity. To circumvent the limitation, ligand design can play a significant role where ligands can execute a primary role rather being a spectator. Another class of ligands, referred to as *redox-active ligand* can participate in catalytic cycle. The direct involvement of ligand in bond activation processes and enables 3d transition metals complexes to undergo overall two-electron processes, thus preventing unfavorable oxidation state of metal center. With proper synergy with metal center, redox active ligands can also stabilize charge during a catalytic cycle. Redox-active ligands have tendency to do to multi-electron redox chemistry by working

in synergistic manner with 3d metals by expanding upon a metal's uncommon reactivity.[11, 14, 69, 70] Thus, a combined action of a 3d transition metal and redox active ligand may allow to mimic the chemistry exhibited by noble metal; two electron transfer chemistry without any need to access high energy redox states.

This work has been essential to our understanding on how these ligands can bind and react in different oxidation states to metals. Several catalysts based on redox active copper, nickel, zirconium, tungsten, cobalt, chromium and iron-based metal complexes have shown amazing response in mimicking reactions that were once limited to noble metals.

In this direction, Heyduk developed a library of 3d metal complexes with pincer redox active ligands and show the various reactivity pattern of these metal complexes, like reduction elimination of disulfides from an iron(III) complex without changing iron oxidation state by using redox active ONO ligand.[71] Heyduk and coworkers fabricated the vast theoretical and spectroscopic information of the redox behavior of a trianionic pincer redox systems. A redox

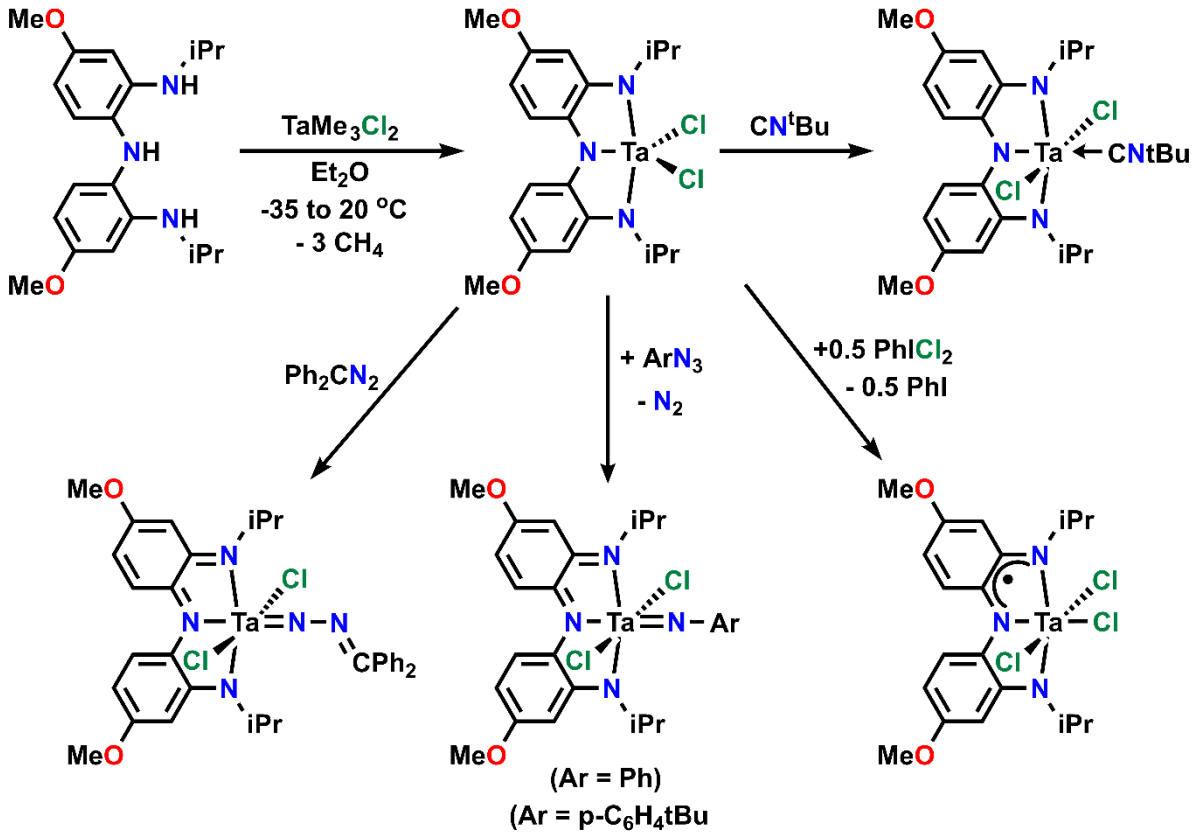

Figure 1.5. Activation of small molecule by electron transfer from redox active NNN pincer ligand-based metal complex.

active [NON] and [NNN]-based pincer ligands has been explored in the activation of early transition metal imido complexes.[41] Generally, activation of early-transition-metal nitrogen bonds of imides and amides is challenging; however, the inception of noninnocent ligands has fabricated rare examples of nitrene transfer from tantalum imido complexes (Figure 1.4).

Another contribution from Soper group describe the single electron type reaction by redox active amido phenolate ligands-based ruthenium oxo compounds.[72] In a cobalt complex, comprising of two of aminophenols, both ligands can undergo one electron oxidation to activate the substrate and subsequently acts as electron sink to facilitate reductive elimination without any change in oxidation state of the metal center. These creative idea opens up the possibility of ligand based one electron reservoir that enable the radical generation step for multielectron chemistry.[73]

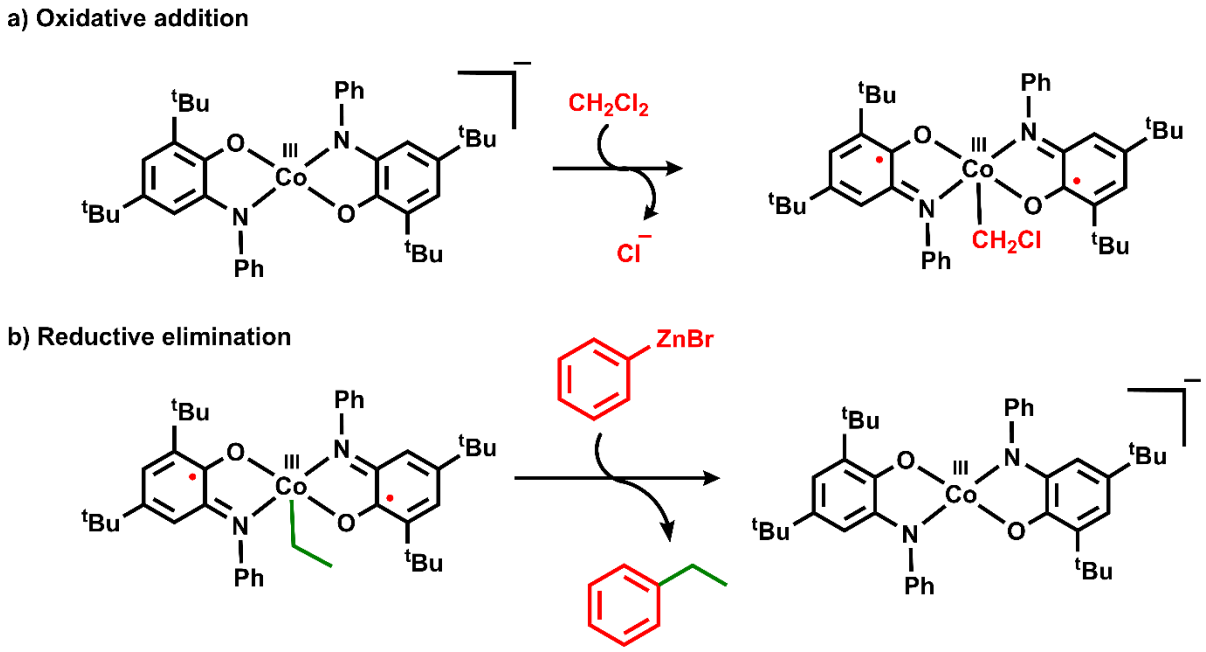

Figure 1.6. a) Oxidative addition by aminophenolate ligand b) Reductive elimination by iminosemiquinonate form of aminophenolate ligand.

Cobalt is smoothly associated with single electron transfer radical reactions. However, the electron required to undergo oxidative addition are provided by the two NO ligands which are oxidised to sq oxidation state (Figure 1.5a). Another work from the same group reported a Negishi like cross coupling of alkyl halide with organozinc reagent using a square planer amidophenolato cobalt(III) complex (Figure 1.5b).[73] Similarly, Sarkar group also reported a o-

phenylenediamide ligands based cobalt complex. The four coordinate cobalt species is capable of electrocatalytic C–C bond formation.[74]

The *beta*-diketiminate backbone (also known as NacNac) is a highly versatile ligand due to its characteristics and applications in organometallic chemistry.[75, 76] Their easy synthesis, extensive delocalization of π electron cloud and ability in tuning the electronic and steric by ligand substitution, is the main reason of their popularity. The redox property of this ligand has been extensively studied with various 3d metals.[77-79] In the same direction, our group has also studied the photo-redox activity of *beta*-diketiminate backbone with Zn based complex. In that work, we described single electron transfer and storage of electron in NacNac backbone using Zn(II)NacNac complex under photocatalytic conditions.[80, 81]

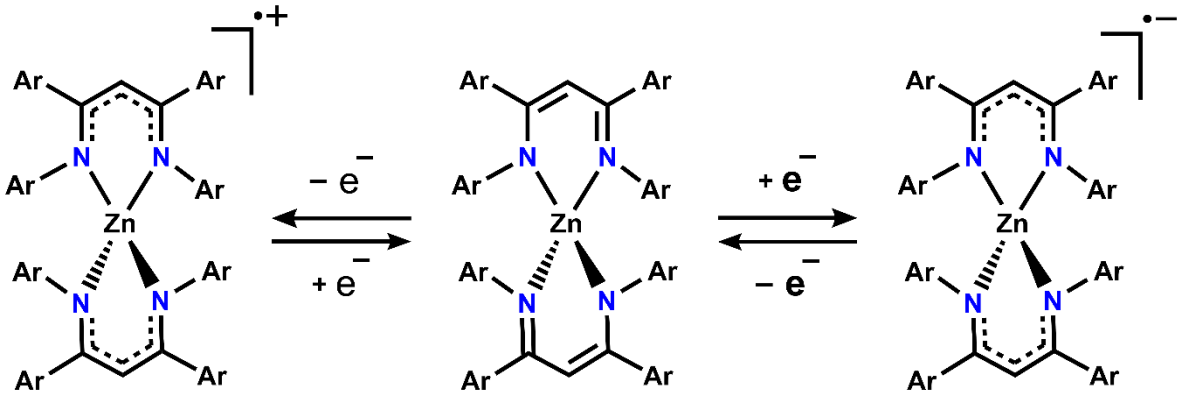

Figure 1.7. Redox activity of Zn-beta-diketiminate complex (Zn(II)NacNac).

From previous sections, we can see redox-non innocent ligands work on the principle of radical chemistry/ single electron transfer mechanisms which is again a crucial pathway for transition metal-based catalysis. In this direction, we tried to merge 3d transition metal and redox active ligand to elaborate their potential in catalysis. We relied on the ability of the ligand to operate as a source and sink of electrons in a catalytic cycle for electron transfer. Electron transfer catalysis has recently emerged as a very effective tool for constructing C–C and C–heteroatom bonds towards the formation of value-added products. In this regard, direct C–H functionalization of an arene or heteroarene ring is very desirable, so the process can be step-economic by easily obviating a bond prefunctionalization step. This approach is also lucrative from the environmental perspective since it can obviate the need for heavy metals to drive the cross-coupling reactions.

This chapter has discussed a large collection of redox active ligand-based metal complex's that has been reported till now, to the best of our knowledge. We hope that a comparative study of such metal complex will offer to develop 3d metal-based complex along with redox active backbone that will mimic noble metal chemistry and will help in better understanding of metal driven enzymatic chemistry. This collection shows that noninnocent ligands are not just oddities for oxidation-state assignment but rather an intriguing design element for the synthesis of both main-group and transition-metal compounds. Fully exploiting the potential of noninnocent ligands in catalysis, group-transfer chemistry, energy storage and conversion, and biological applications remains in its infancy.

This remarkable reactivity in a metal complex comprising of redox noninnocent ligands is attributed to the ligand's role as an electron reservoir which is analogous to most of the biological cofactors. This demonstrates that the redox potential and molecular energy levels of metal and ligand must be finely tuned for the development of catalyst with improved synthetic utility of reaction.

As a result, redox noninnocent ligands help affording multiple redox states of a complex, facilitating the catalyst to attain unusual physical oxidation states and activate small molecules. The extended π bond network in these ligands empowers them not only to stabilize the ligand centred radicals but also facilitate reversible reactions at metal centre that may involve radical formations. The important fact is the metal ligand covalency developed in such systems where ligand frontier molecular orbitals and metal d-orbitals are of compatible energy.

1.2. Photoredox Catalysis by Redox Active Ligands

1.2.1. Introduction

Solar light is an infinite source of clean, safe, inexpensive and renewable energy on Earth, by which demand of rising population can be fulfilled.[82] Over the decades of research, hundreds of photocatalyst have been developed that can be categorised into mainly two types – metal based and metal free. Metal-based photocatalysts have been extensively researched since 1972. Metal-free photocatalysts are made up of earth abundant inexpensive materials, lighter in weight and less corrosive than heavy metal based photocatalyst. While stable and scalable production is yet elusive with metal-based photocatalysts; metal-free photocatalysts (MFP), in this regard, hold true promise provided that they can overcome poor conversion efficiency.

A radical mediated methodology has witnessed an extraordinary advent of preparative visible light photoredox catalysis.[83] A mild reaction conditions and a wide collection of radical allow retrosynthetic planning and new synthetics routs of valuable products. Therefore, development of photocatalysis gained intense research interest by synthetic community within the last 10 years. The synthetic community is making continuous efforts to develop molecules and devices in order to make best use of solar energy, which can effectively serve the purpose of "green energy technology".

With an objective of sustainable catalysis, photocatalysis has captured unusual attention due its ability to covert the light energy into chemical potential.[84, 85] Different photocatalysts undergo excitation upon absorbing light at a particular wavelength in the visible or near-UV region. But high energy UV-light can lead to detrimental bond cleavage to give undesired side products and also may cause the health hazard for the user. Therefore, the photocatalysts which absorb light in visible region are much more reliable Most of the organic transformation involves radical species which are generally generated via single electron transfer. The excited photocatalyst takes part in bond activation and generates such radical which leads to the final product by further radical attack or radical rearrangement. Overall, photocatalysis solves the problem of high energy demanding transformation at a much milder condition, that is extremely difficult to achieve by thermal pathways.

1.2.2. Working Principle of a Photocatalyst

Photocatalysis is a process in which chemical transformation is taking place in the presence of light with the help of a photosensitizer. Basically, a photocatalyst is a motif which converts the photon energy into chemical potential.[86] A photocatalyst's oxidizing or reducing power can be significantly enhanced by shining light on the molecule. Upon absorption of light in the form of photon, molecule gets excited to its higher energy level, in the other words the light energy pumps the electrons from HOMO (singlet ground state, S_0) to LUMO or higher excited energy levels (Singlet excited state, S_n). The photocatalyst can remain in its excited state for a certain period of time which is known as excited state life time of the molecule. The life time of molecule can be determined by a time-related photon counting experiment (TCSPC) or other transient ultrafast techniques. The molecule in the excited state dissipates energy in several ways in order to come to ground state.

The molecule can directly come to ground state via a non-radiative pathway (internal conversion, k_{nr}) i.e., emitting energy in the form of heat energy or via emitting a photon in spin allowed radiative decay called fluorescence, k_f. Besides that, excited molecule moves to some triplet energy levels in the close proximity of excited singlet states (Figure 1.7). It can also undergo a non-radiative spin forbidden intersystem crossing to excited triplet state T_n which subsequentially leads to a delayed radiative decay called phosphorescence, k_p. The fluorescence lifetime is on the order of 10^{-9} to 10^{-7} seconds while phosphorescence lifetime is several times higher than fluorescence lifetime; in the order of 10^{-4} to 10^{-1} seconds.

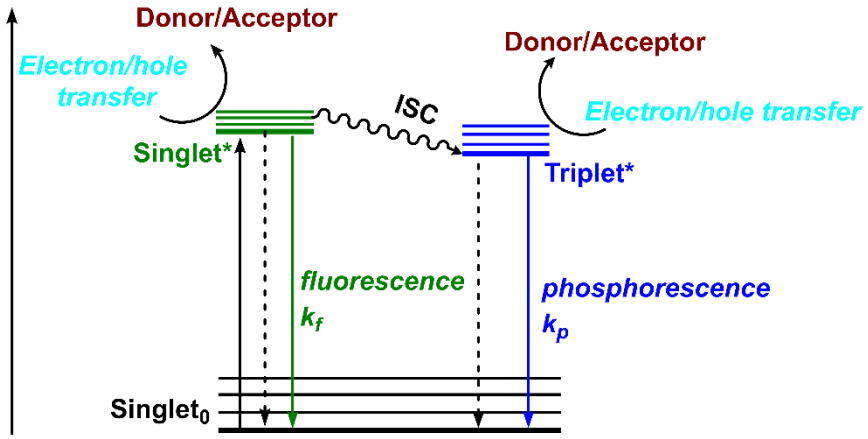

Figure 1.8. Simplified Jabolanski diagram for showing excited state phenomenon of photocatalyst.

The photocatalyst in its excited state can behave as strong reducing and/or oxidizing agent than the corresponding ground state. The excited state energy ($E_{0,0}$) which is defined as the gap between zeroth vibrational states of the electronic ground and excited states, plays a keys role in enhancing redox power of photocatalyst. $E_{0,0}$ modifies the value of redox potential of a molecule in its excited state from its ground state value. A larger $E_{0,0}$ value translates the ground state redox potentials to a large positive or negative reduction or oxidation potentials, which significantly modulates the molecule's redox power.

With the help of $E_{0,0}$ value, the excited state oxidation potential and excited state reduction potential can be estimated from Rehm-Weller equation[87], as shown below.

$$E^*_{ox} = E^0_{ox} - E_{0,0}$$

$$E^*_{red} = E^0_{red} + E_{0,0}$$

Where, $E_{0,0}$ = the energy gap between the zeroth vibrational states of ground and excited states.

For example, a iridium metal based photocatalyst $[Ir(ppy)_2(bpy)]^+$ has ground state redox potentials, E_{ox} = +1.27 V (vs SCE) and E_{red} = −1.38 V (vs SCE) in acetonitrile. when excited, the corresponding values are modified by excited state energy ($E_{0,0}$) value, it is found that the $[Ir(ppy)_2(bpy)]^+$ photocatalyst has an excited state oxidation potential E^*_{ox} = -0.96 V (vs SCE) which makes it a strong reducing agent. Similarly, $[Ir(ppy)_2(bpy)]^+$ has an excited state reduction potential E^*_{red} = +0.66 V (vs SCE) which makes it a strong oxidizing agent.

The photoredox catalysis apart from being good reductant/oxidant, is also atom economical and eliminates the hazards of wastes. In the reaction medium as both the oxidants and reductants are momentarily generated, so the reaction doesn't need stoichiometric amount of external oxidant and reductants. Sometimes, sacrificial reductant/oxidant are needed to complete the overall catalytic cycle to regenerate the catalyst or to generate the active photocatalyst from parent molecule, but these reductants/oxidants are much milder in comparison with external strong reductant/oxidant. Meanwhile, a photocatalyzed reaction generates the highly reactive radical intermediate by photoinduced electron transfer.

Furthermore, a photocatalytic reaction can follow an oxidative quenching or a reductive quenching pathway. Depending upon the excited state redox behavior and lifetime of excited state of photocatalyst, nature of reacting molecule in reaction medium or desired outcome of the reaction, a photocatalyst can be either photo-oxidized or photo-reduced.

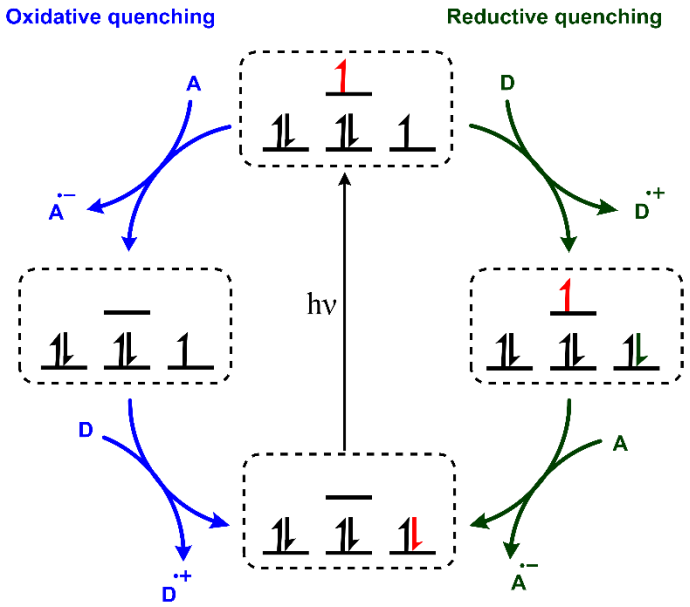

Figure 1.9. Reductive and oxidative quenching cycles of a photocatalyst (PC).

Upon excitation of photocatalyst (PC) with a photon of particular wavelength, an electron gets promoted from the HOMO to the LUMO of molecule which results into creating a hole on the HOMO and an unpaired electron on the LUMO. Depending upon the lifetime of the PC, as determined by ultrafast transient spectroscopic techniques, the electron can remain in the excited state as long as lifetime of PC is. The hole created in the HOMO of PC can be filled by an electron from a donor (reductive quenching) and the electron in the LUMO of PC can be abstracted by an acceptor (oxidative quenching). Recently, several metal and metal free catalysts have been found to follow both the modes of quenching thus expanding the net redox window for the photocatalyst.

1.2.3. Need of Metal Free Photocatalyst

A century ago, the visionary scientist Giacomo Ciamcian insisted the need to develop methodology that enable the conversion of light into chemicals and fuels.[88] The initiation of redox transformation by use of low energy light and generation of highly reactive intermediates through photoinduced electron transfer (PET) opened up the new era of photocatalysis. This has enabled the synthetic community to develop a wide range of reaction, including the synthesis of complex molecules.[89-91] In this context, Iridium and ruthenium based photocatalyst are incredibly valuable motif for many of those photo redox transformations due to their adaptable redox potentials and the comparatively prolonged lives of their excited states.[83, 92, 93] Due to ready modification in ligand structure in polypyridine ligand, a majority of photocatalyst rely on polypyridyl ligand based heavy metal complex's such as ruthenium, iridium and platinum etc.[94, 95] With the help of proper substitution on ligand, either by electron donating or electron withdrawing group redox and photophysical properties of photocatalyst can be readily tuned for specific purpose. The combination of photocatalysis with transition metal catalysis generates metallaphotocatalysis[96, 97], that enables valuable selective preparative transformations under milder conditions. So, heavy metal complexes such as $[Ir(ppy)_2(dtbpy)]PF_6$ (Ir-II) and *fac*-$Ir(ppy)_3$, $Ru(bpy)_3Cl_2$ have been tested for majority of transformations.

Multiple precious 4d and 5d metals with multidentate ligands such as porphyrin, corrole, and phthalocyanins produced several successful photosensitizers.[98-100] The most commonly employed (visible light photocatalysts or VLPs) like $Ir(bpy)^{2+}$ and $Ru(bpy)^{2+}$ are commercially available. The efficiency of these VLPs has been recognized and extensively investigated for applications in water splitting, C-H activation, cross coupling reactions.[101]

Despite their efficiency to catalyze a plethora of organic transformations, application of noble metal VLPs is obstructed due to their high toxicity and carcinogenic effects even when present in tiny amount. They also come with the disadvantage of being rare, difficult to mine and extract, which makes them very expensive. The search for greener and more sustainable catalysts has accelerated finding organic catalyst, main group metals, and base metal catalysts among the top priorities.

For instance, organo-photocatalyst can be seen as a great alternative for heavy metal - based photocatalyst. Even, commercially available organic dyes like Flavins[102] and eosin Y[103] show interesting photochemical properties as catalyst but variation in their structure scaffolds sometimes inhibits their use in many photocatalysis. It encouraged the synthetic community to develop some practically simple organic molecules which can be easily tuned to access new and effective organo-photocatalysts.[104, 105] Fukuzumi[106, 107] introduced the organic motif "acridinium" which was further modified by Nicewicz[84] are now established as valuable catalytic motifs for various organic synthesis. These organophotoredox catalysts have been successfully tested for various reaction like oxidative annulation[108], Oxidative Alkylation[109], Oxidative C−H Functionalization[110], Dehydrogenative Couplings[111], Reductive Cyclization's[112], Povarov reaction[113], Trifluoromethylation[114].

1.2.4. Strong Reductive Behaviour of Small Molecule Under Light

In comparison to the neutral species, the organic anionic species absorb light in red regions of visible light spectrum. An anionic molecule is usually a superior electron donor than its neutral parent compound as both the electron-electron repulsion and the shielding from the nucleus are increased. As a consequence, the excess negative charge facilitates the removal of an electron. Single electron transfer (SET) based reductive cleavage conceived that the generated radical can pursue the process catalysis which offer novel and unique routes to expand synthetic toolbox in organic chemistry. These redox properties can be fine-tuned by attaching electron-donating or -withdrawing substituents.[115-118]

In single electron transfer (SET) catalysis, a plethora of small molecule that are efficient electron donor have been discovered. Usually, such simple molecules in the combination with the KO^{t}Bu forms an electron donor species that activates a wide range of C–X bonds like halides, diazonium, phosphates esters etc. to generate the radicals.[168-172] The resultant radicals can be engaged in various synthetically useful transformations to furnish arylboronate,

arylstannane, biaryl products, cyclization, dehalohydrogenation and heterocycles synthesis. Therefore, a reductive bond cleavage by small molecules either under thermal or photochemical conditions became a centre of interest in synthetic community. Along this goal, photochemical reductive cleavage of a strong bond becomes immensely popular as cheap abundant and atom economical pathways. There are continuous efforts from researcher to elaborate the molecules that can itself or by some chemical transformations during reaction, get converted into super reducing species upon photoexcitation. Murphy[119-123], Jiao[124, 125], Lei[126], Studer and Curran[127, 128] have extensively contributed in discovering specific molecules or their combinations that engage in efficient SET. König reported many molecules that can behave as good photoreductants when in situ generated anions are irradiated under light. Often such anions directly cleave the bond in reductive fashion. On the other hand, in case of $Ru(bpy)_3^{2+}$ photocatalyst, there is a need of sacrificial reductant such as tertiary amine to reduce the photocatalyst.

Carbon−Carbon bond-forming reaction has been widely tested as a ground for easy generation of aryl radical from C-X bonds as shown in Figure 1.10.

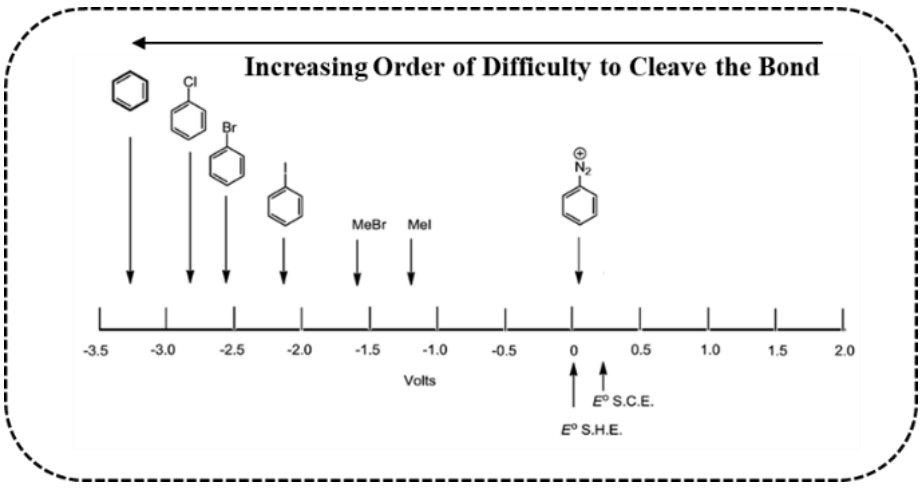

Figure 1.10. Increasing order of reduction potential value aryl/alkyl halides.

Aryldiazonium salts are highly susceptible to single-electron reduction as indicated by their reduction potentials is closer to zero vs SCE. The reduction potential of alkyl/aryl halides tend to hold negative value as moving from right to left in the Figure 1.8. Aryl chloride and benzene cannot be easily reduced. Very recently, Song Lin has reported a consecutive dual photoredox to access extremely reducing intermediates via tandem cathodic potential and photoexcitation with merging electricity and light to achieve extreme reduction potentials.[129] In this reductive

electrophotocatalysis approach, cathodic reduction of dicyanoanthracene (DCA; $E_{1/2} = -0.82$ V) results in the corresponding radical anion $DCA^{\bullet-}$, which absorbs visible light and exhibits an exceptionally high reducing potential of −3.2 V (vs SCE). In 2020, Chengfeng Xia group reported the redox potential of the excited phenolate anion of 2,6-di-tert-butyl-4-phenylphenol (-3.16 V vs. SCE) which indicated that the reduction of iodobenzene (-2.24 V vs. SCE), bromobenzene (-2.44 V vs. SCE), and even chlorobenzene (-2.78 V vs. SCE) by this excited phenolate anion is thermodynamically feasible.[130] 2-naphtholate anion[131], benzimidazolium naphtholate BINA[132] (E_{ox}^{*} = -2.08 vs. SCE), tetramethoxyanthrolate TMA- (E_{ox}^{*} = -2.92 V vs SCE)[133] has been tested for dehalogenation of aryl bromides and chlorides.

Photoredox catalysis promotes SET trough conversion of energy from visible into chemical redox potential that enable the generation of radical which undergoes various pathways to give C-C and C-heteroatom bond forming reactions. As mentioned earlier, while considering a substrate that suitable for photoredox reduction, two basic parameters need to be considered: (1) $E_{1/2}(PC^{\bullet+}/PC^{*})$ and (2) $E_{1/2}(PC/PC^{\bullet-})$. These redox potential values are bounded by energy of photons in the visible region.

It is therefore very timely to assess the current progress and determine the outstanding challenges with various metal free photocatalyst to make it super reducing species having significant efficiency.

1.3. References:

1. Cotton, F. A.; Wilkinson, G.; Murillo, C. A.; Bochmann, M., *Advanced Inorganic Chemistry*. John Wiley & Sons: 1999.

2. Jørgensen, C. K., Differences Between the Four Halide Ligands, and Discussion Remarks on Trigonal-Bipyramidal Complexes, on Oxidation States, and on Diagonal Elements of One-Electron Energy. *Coord. Chem. Rev.* **1966,** *1* (1), 164-178.

3. Chirik, P. J.; Wieghardt, K., Radical Ligands Confer Nobility on Base-Metal Catalysts. *Science* **2010,** *327* (5967), 794-795.

4. Gray, H. B.; Williams, R.; Bernal, I.; Billig, E., A Spin-Free Square Planar Cobaltous Complex. *J. Am. Chem. Soc.* **1962,** *84* (18), 3596-3597.

5. Billig, E.; Williams, R.; Bernal, I.; Waters, J. H.; Gray, H. B., The Electronic Structures of Square-Planar Metal Complexes. II. The Complexes of Maleonitriledithiolate with Copper (II), Nickel (II), Palladium (II), and Platinum (II). *Inorg. Chem.* **1964,** *3* (5), 663-666.

6. Chirik, P. J., Preface: Forum on Redox-Active Ligands. *Inorg. Chem.* **2011,** *50* (20), 9737-9740.

7. Cramer, C. J.; Tolman, W. B., Mononuclear Cu–O_2 Complexes: Geometries, Spectroscopic Properties, Electronic Structures, and Reactivity. *Acc. Chem. Res.* **2007,** *40* (7), 601-608.

8. Stubbe, J.; van Der Donk, W. A., Protein Radicals in Enzyme Catalysis. *Chem. Rev.* **1998,** *98* (7), 2661-2662.

9. Kaim, W.; Schwederski, B., Non-Innocent Ligands in Bioinorganic Chemistry—An Overview. *Coord. Chem. Rev.* **2010,** *254* (13-14), 1580-1588.

10. Dzik, W. I.; van der Vlugt, J. I.; Reek, J. N. H.; de Bruin, B., Ligands that Store and Release Electrons during Catalysis. *Angew. Chem., Int. Ed.* **2011,** *50* (15), 3356-3358.

11. Luca, O. R.; Crabtree, R. H., Redox-Active Ligands in Catalysis. *Chem. Soc. Rev.* **2013,** *42* (4), 1440-1459.

12. Praneeth, V. K.; Ringenberg, M. R.; Ward, T. R., Redox-Active Ligands in Catalysis. *Angew. Chem., Int. Ed.* **2012,** *51* (41), 10228-10234.

13. Lyaskovskyy, V.; de Bruin, B., ACS Catal., 2012, 2, 270;(b) VKK Praneeth, MR Ringenberg and TR Ward. *Angew. Chem., Int. Ed.* **2012,** *51*, 10228.

14. van der Vlugt, J. I., Cooperative Catalysis with First-Row Late Transition Metals. *Euro. J. Inorg. Chem.* **2012,** *2012* (3), 363-375.

15. Borman, C. D.; Saysell, C. G.; Sokolowski, A.; Twitchett, M. B.; Wright, C.; Sykes, A. G., Reactivity of Galactose Oxidase. *Coord. Chem. Rev.* **1999,** *190*, 771-779.

16. Whittaker, J. W., Free Radical Catalysis by Galactose Oxidase. *Chem. Rev.* **2003,** *103* (6), 2347-2364.

17. Ishikita, H.; Morra, G.; Knapp, E.-W., Redox Potential of Quinones in Photosynthetic Reaction Centers from Rhodobacter Sphaeroides: Dependence on Protonation of Glu-L212 and Asp-L213. *Biochemistry* **2003,** *42* (13), 3882-3892.

18. Breton, J.; Boullais, C.; Berger, G.; Mioskowski, C.; Nabedryk, E., Binding Sites of Quinones in Photosynthetic Bacterial Reaction Centers Investigated by Light-Induced FTIR Difference Spectroscopy: Symmetry of the Carbonyl Interactions and Close Equivalence of the QB Vibrations in Rhodopseudomonas Sphaeroides and Rhodobacter Viridis Probed by Isotope Labeling. *Biochemistry* **1995,** *34* (36), 11606-11616.

19. Wraight, C. A., Proton and Electron Transfer in the Acceptor Quinone Complex of Photosynthetic Reaction Centers from Rhodobacter Sphaeroides. *Front. Biosci.* **2004,** *9* (1), 309-337.

20. Redfearn, E. R.; Burgos, J., Ubiquinone (Coenzyme Q) and the Respiratory Chain. *Nature* **1966,** *209* (5024), 711-713.

21. Izumi, Y.; Sawada, H.; Sakka, N.; Yamamoto, N.; Kume, T.; Katsuki, H.; Shimohama, S.; Akaike, A., p-Quinone Mediates 6-Hydroxydopamine-Induced Dopaminergic Neuronal Death and Ferrous Iron Accelerates the Conversion of p-Quinone into Melanin Extracellularly. *J. Neurosci. Res.* **2005,** *79* (6), 849-860.

22. Chun, H.; Weyhermüller, T.; Bill, E.; Wieghardt, K., Tuning the Electronic Structure of Halidobis (o-imino-benzosemiquinonato) Iron (iii) Complexes. *Angew. Chem., Int. Ed.* **2001,** *40* (13), 2489-2492.

23. Shimizu, D.; Osuka, A., Porphyrinoids as a Platform of Stable Radicals. *Chem. Sci.* **2018,** *9* (6), 1408-1423.

24. Lorente, C.; Thomas, A. H., Photophysics and Photochemistry of Pterins in Aqueous Solution. *Acc. Chem. Res.* **2006,** *39* (6), 395-402.

25. Walsh, C., Flavin Coenzymes: at the Crossroads of Biological Redox Chemistry. *Acc. Chem. Res.* **1980,** *13* (5), 148-155.

26. van Leest, N. P.; Tepaske, M. A.; Oudsen, J.-P. H.; Venderbosch, B.; Rietdijk, N. R.; Siegler, M. A.; Tromp, M.; van der Vlugt, J. I.; de Bruin, B., Ligand Redox Noninnocence in [CoIII (TAML)]$^{0/-}$ Complexes Affects Nitrene Formation. *J. Am. Chem. Soc.* **2019,** *142* (1), 552-563.

27. Bernauer, J.; Pölker, J.; Jacobi von Wangelin, A., Redox-Active BIAN-Based Diimine Ligands in Metal-Catalyzed Small Molecule Syntheses. *ChemCatChem* **2022,** *14* (1), e202101182.

28. Broere, D. L.; Plessius, R.; van der Vlugt, J. I., New Avenues for Ligand-Mediated Processes–Expanding Metal Reactivity by the Use of Redox-Active Catechol, o-Aminophenol and o-Phenylenediamine Ligands. *Chem. Soc. Rev.* **2015,** *44* (19), 6886-6915.

29. Li, B.; Geoghegan, B. L.; Wölper, C.; Cutsail III, G. E.; Schulz, S., Redox Activity of Noninnocent 2, 2′-Bipyridine in Zinc Complexes: An Experimental and Theoretical Study. *ACS Omega* **2021,** *6* (28), 18325-18332.

30. Chirik, P. J., Iron-and Cobalt-Catalyzed Alkene Hydrogenation: Catalysis with both Redox-Active and Strong Field Ligands. *Acc. Chem. Res.* **2015,** *48* (6), 1687-1695.

31. Jacquet, J.; Chaumont, P.; Gontard, G.; Orio, M.; Vezin, H.; Blanchard, S.; Desage-El Murr, M.; Fensterbank, L., C− N Bond Formation from a Masked High-Valent Copper Complex Stabilized by Redox Non-Innocent Ligands. *Angew. Chem., Int. Ed.* **2016,** *128* (36), 10870-10874.

32. Chang, M.-C.; Roewen, P.; Travieso-Puente, R.; Lutz, M.; Otten, E., Formazanate Ligands as Structurally Versatile, Redox-Active Analogues of β-Diketiminates in Zinc Chemistry. *Inorg. Chem.* **2015,** *54* (1), 379-388.

33. Chang, M. C.; Dann, T.; Day, D. P.; Lutz, M.; Wildgoose, G. G.; Otten, E., The Formazanate Ligand as an Electron Reservoir: bis (Formazanate) Zinc Complexes Isolated in Three Redox States. *Angew. Chem., Int. Ed.* **2014,** *126* (16), 4202-4206.

34. Camp, C.; Arnold, J., On the Non-Innocence of "Nacnacs": Ligand-Based Reactivity in β-Diketiminate Supported Coordination Compounds. *Dalton Trans.* **2016,** *45* (37), 14462-14498.

35. Pierpont, C. G., Redox Isomerism for Quinone Complexes of Chromium and Chromium Oxidation State Assignment from X-ray Absorption Spectroscopy. *Inorg. Chem.* **2001,** *40* (22), 5727-5728.

36. Suenaga, Y.; Pierpont, C. G., Binuclear complexes of Co (III) Containing Extended Conjugated bis (Catecholate) Ligands. *Inorg. Chem.* **2005,** *44* (18), 6183-6191.

37. Metcalfe, R. A.; Lever, A., Tetraammineruthenium (II) and-Ruthenium (III) Complexes of o-Benzoquinone Diimine and Their Redox Series. *Inorg. Chem.* **1997,** *36* (21), 4762-4771.

38. Metcalfe, R. A.; Dodsworth, E. S.; Fielder, S. S.; Stufkens, D. J.; Lever, A.; Pietro, W. J., Influence of Remote Ligand Lone Pairs on the Electronic Structure and Spectrum of Bis (bipyridine) ruthenium (II) 3, 4-Diamino-3 ', 4 '-diimino-3 ', 4 '-dihydrobiphenyl. Tuning by External Donors and Acceptors. *Inorg. Chem.* **1996,** *35* (26), 7741-7750.

39. Chaudhuri, P.; Verani, C. N.; Bill, E.; Bothe, E.; Weyhermüller, T.; Wieghardt, K., Electronic Structure of Bis (o-iminobenzosemiquinonato) Metal Complexes (Cu, Ni, Pd). The Art of Establishing Physical Oxidation States in Transition-Metal Complexes Containing Radical Ligands. *J. Am. Chem. Soc.* **2001,** *123* (10), 2213-2223.

40. Blackmore, K. J.; Ziller, J. W.; Heyduk, A. F., "Oxidative Addition" to a Zirconium (IV) Redox-Active Ligand Complex. *Inorg. Chem.* **2005,** *44* (16), 5559-5561.

41. Munhá, R. F.; Zarkesh, R. A.; Heyduk, A. F., Tuning the Electronic and Steric Parameters of a Redox-Active Tris (amido) Ligand. *Inorg. Chem.* **2013,** *52* (19), 11244-11255.

42. Haneline, M. R.; Heyduk, A. F., C− C Bond-Forming Reductive Elimination from a Zirconium (IV) Redox-Active Ligand Complex. *J. Am. Chem. Soc.* **2006,** *128* (26), 8410-8411.

43. Munhá, R. F.; Zarkesh, R. A.; Heyduk, A. F., Group Transfer Reactions of d 0 Transition Metal Complexes: Redox-Active Ligands Provide a Mechanism for Expanded Reactivity. *Dalton Trans.* **2013,** *42* (11), 3751-3766.

44. Nguyen, A. I.; Zarkesh, R. A.; Lacy, D. C.; Thorson, M. K.; Heyduk, A. F., Catalytic Nitrene Transfer by a Zirconium (IV) Redox-Active Ligand Complex. *Chem. Sci.* **2011,** *2* (1), 166-169.

45. Szigethy, G.; Heyduk, A. F., Steric and Electronic Consequences of Flexibility in a Tetradentate Redox-Active Ligand: Ti (IV) and Zr (IV) Complexes. *Inorg. Chem.* **2011,** *50* (1), 125-135.

46. Zarkesh, R. A.; Ziller, J. W.; Heyduk, A. F., Four-Electron Oxidative Formation of Aryl Diazenes Using a Tantalum Redox-Active Ligand Complex. *Angew. Chem. Int. Ed.* **2008,** *47* (25), 4715-4718.

47. Nguyen, A. I.; Blackmore, K. J.; Carter, S. M.; Zarkesh, R. A.; Heyduk, A. F., One-and Two-electron Reactivity of a Tantalum (V) Complex with a Redox-Active Tris (amido) Ligand. *J. Am. Chem. Soc.* **2009,** *131* (9), 3307-3316.

48. Ghosh, S.; Baik, M. H., Mechanism of Redox-Active Ligand-Assisted Nitrene-Group Transfer in a ZrIV Complex: Direct Ligand-to-Ligand Charge Transfer Preferred. *Chem.–Euro. J.* **2015,** *21* (4), 1780-1789.

49. Hananouchi, S.; Krull, B. T.; Ziller, J. W.; Furche, F.; Heyduk, A. F., Metal Effects on Ligand Non-Innocence in Group 5 Complexes of the Redox-Active [ONO] Pincer Ligand. *Dalton Trans.* **2014,** *43* (48), 17991-18000.

50. Vijaykumar, G.; Pariyar, A.; Ahmed, J.; Shaw, B. K.; Adhikari, D.; Mandal, S. K., Tuning the Redox Non-Innocence of a Phenalenyl Ligand Toward Efficient Nickel-Assisted Catalytic Hydrosilylation. *Chem. Sci.* **2018,** *9* (10), 2817-2825.

51. Bhunia, M.; Sahoo, S. R.; Shaw, B. K.; Vaidya, S.; Pariyar, A.; Vijaykumar, G.; Adhikari, D.; Mandal, S. K., Storing Redox Equivalent in the Phenalenyl Backbone Towards Catalytic Multi-electron Reduction. *Chem. Sci.* **2019,** *10* (31), 7433-7441.

52. Morris, R. H., Exploiting Metal–Ligand Bifunctional Reactions in the Design of Iron Asymmetric Hydrogenation Catalysts. *Acc. Chem. Res.* **2015,** *48* (5), 1494-1502.

53. Gunanathan, C.; Milstein, D., Bond Activation and Catalysis by Ruthenium Pincer Complexes. *Chem. Rev.* **2014,** *114* (24), 12024-12087.

54. Younus, H. A.; Ahmad, N.; Su, W.; Verpoort, F., Ruthenium Pincer Complexes: Ligand Design and Complex Synthesis. *Coord. Chem. Rev.* **2014,** *276*, 112-152.

55. Balaghi, S. E.; Safaei, E.; Chiang, L.; Wong, E. W.; Savard, D.; Clarke, R. M.; Storr, T., Synthesis, Characterization and Catalytic Activity of Copper (II) Complexes Containing a Redox-Active Benzoxazole Iminosemiquinone Ligand. *Dalton Trans.* **2013,** *42* (19), 6829-6839.

56. Lu, F.; Zarkesh, R. A.; Heyduk, A. F., A Redox-Active Ligand as a Reservoir for Protons and Electrons: O_2 Reduction at Zirconium (IV). Wiley Online Library: 2012.

57. Paretzki, A.; Bubrin, M.; Fiedler, J.; Záliš, S.; Kaim, W., Correlated Coordination and Redox Activity of a Hemilabile Noninnocent Ligand in Nickel Complexes. *Chem.–Euro. J.* **2014,** *20* (18), 5414-5422.

58. Hübner, R.; Weber, S.; Strobel, S.; Sarkar, B.; Záliš, S.; Kaim, W., Reversible Intramolecular Single-Electron Oxidative Addition Involving a Hemilabile Noninnocent Ligand. *Organometallics* **2011,** *30* (6), 1414-1418.

59. Ringenberg, M. R.; Kokatam, S. L.; Heiden, Z. M.; Rauchfuss, T. B., Redox-Switched Oxidation of Dihydrogen using a Non-Innocent Ligand. *J. Am. Chem. Soc.* **2008,** *130* (3), 788-789.

60. Boyer, J. L.; Cundari, T. R.; DeYonker, N. J.; Rauchfuss, T. B.; Wilson, S. R., Redox Activation of Alkene Ligands in Platinum Complexes with Non-Innocent Ligands. *Inorg. Chem.* **2009,** *48* (2), 638-645.

61. Wang, K.; Stiefel, E. I., Toward Separation and Purification of Olefins using Dithiolene Complexes: an Electrochemical Approach. *Science* **2001,** *291* (5501), 106-109.

62. van der Vlugt, J. I., Radical-Type Reactivity and Catalysis by Single-Electron Transfer to or from Redox-Active Ligands. *Chem.– Euro. J.* **2019,** *25* (11), 2651-2662.

63. Lippert, C. A.; Hardcastle, K. I.; Soper, J. D., Harnessing Redox-Active Ligands for Low-Barrier Radical Addition at Oxorhenium Complexes. *Inorg. Chem.* **2011,** *50* (20), 9864-9878.

64. Kuijpers, P. F.; Tiekink, M. J.; Breukelaar, W. B.; Broere, D. L.; van Leest, N. P.; van der Vlugt, J. I.; Reek, J. N.; de Bruin, B., Cobalt-Porphyrin-Catalysed Intramolecular Ring-

Closing C− H Amination of Aliphatic Azides: A Nitrene-Radical Approach to Saturated Heterocycles. *Chem.–Euro. J.* **2017,** *23* (33), 7945-7952.

65. Herebian, D.; Wieghardt, K. E.; Neese, F., Analysis and Interpretation of Metal-Radical Coupling in a Series of Square Planar Nickel Complexes: Correlated ab initio and Density Functional Investigation of [Ni (LISQ) 2](LISQ= 3, 5-di-tert-butyl-o-diiminobenzosemiquinonate (1-)). *J. Am. Chem. Soc.* **2003,** *125* (36), 10997-11005.

66. Brown, S. N., Metrical Oxidation States of 2-Amidophenoxide and Catecholate Ligands: Structural Signatures of Metal–Ligand π Bonding in Potentially Noninnocent Ligands. *Inorg. Chem.* **2012,** *51* (3), 1251-1260.

67. Haxel, G., *Rare Earth Elements: Critical Resources for High Technology*. US Department of the Interior, US Geological Survey: 2002; Vol. 87.

68. Johansson Seechurn, C. C.; Kitching, M. O.; Colacot, T. J.; Snieckus, V., Palladium-Catalyzed Cross-Coupling: a Historical Contextual Perspective to the 2010 Nobel Prize. *Angew. Chem., Int. Ed.* **2012,** *51* (21), 5062-5085.

69. Dzik, W. I.; van der Vlugt, J. I.; Reek, J. N.; de Bruin, B., Ligands that Store and Release Electrons During Catalysis. *Angew. Chem. Int. Ed.* **2011,** *50* (15), 3356-3358.

70. Lyaskovskyy, V.; de Bruin, B., Redox Non-Innocent Ligands: Versatile New Tools to Control Catalytic Reactions. *ACS Catal.* **2012,** *2* (2), 270-279.

71. Wong, J. L.; Sánchez, R. H.; Logan, J. G.; Zarkesh, R. A.; Ziller, J. W.; Heyduk, A. F., Disulfide Reductive Elimination from an Iron (III) Complex. *Chem. Sci.* **2013,** *4* (4), 1906-1910.

72. Lippert, C. A.; Arnstein, S. A.; Sherrill, C. D.; Soper, J. D., Redox-Active Ligands Facilitate Bimetallic O_2 Homolysis at Five-coordinate Oxorhenium (V) Centers. *J. Am. Chem. Soc.* **2010,** *132* (11), 3879-3892.

73. Smith, A. L.; Hardcastle, K. I.; Soper, J. D., Redox-Active Ligand-Mediated Oxidative Addition and Reductive Elimination at Square Planar Cobalt (III): Multielectron Reactions for Cross-Coupling. *J. Am. Chem. Soc.* **2010,** *132* (41), 14358-14360.

74. van der Meer, M.; Rechkemmer, Y.; Peremykin, I.; Hohloch, S.; van Slageren, J.; Sarkar, B., (Electro) Catalytic C–C bond Formation Reaction with a Redox-Active Cobalt Complex. *Chem. Commun.* **2014,** *50* (76), 11104-11106.

75. Ibrahim, S. K.; Khvostov, A. V.; Lappert, M. F.; Maron, L.; Perrin, L.; Pickett, C. J.; Protchenko, A. V., An Electrochemical and DFT Study on Selected β-Diketiminato Metal Complexes. *Dalton Trans.* **2006,** (21), 2591-2596.

76. Khusniyarov, M. M.; Bill, E.; Weyhermüller, T.; Bothe, E.; Wieghardt, K., Hidden Noninnocence: Theoretical and Experimental Evidence for Redox Activity of a β-Diketiminate (1−) Ligand. *Angew., Chem. Int. Ed.* **2011,** *7* (50), 1652-1655.

77. Takaichi, J.; Morimoto, Y.; Ohkubo, K.; Shimokawa, C.; Hojo, T.; Mori, S.; Asahara, H.; Sugimoto, H.; Fujieda, N.; Nishiwaki, N., Redox Chemistry of Nickel (II) Complexes Supported by a Series of Noninnocent β-Diketiminate Ligands. *Inorg. Chem.* **2014,** *53* (12), 6159-6169.

78. Yoshii, R.; Hirose, A.; Tanaka, K.; Chujo, Y., Functionalization of Boron Diiminates with Unique Optical Properties: Multicolor Tuning of Crystallization-Induced Emission and Introduction into the Main Chain of Conjugated Polymers. *J. Am. Chem. Soc.* **2014,** *136* (52), 18131-18139.

79. Ito, S.; Tanaka, K.; Chujo, Y., Characterization and Photophysical Properties of a Luminescent Aluminum Hydride Complex Supported by a β-Diketiminate Ligand. *Inorg. Chem.* **2019,** *7* (8), 100.

80. Singh, K.; S, V.; Adhikari, D., Visible light photoredox by a (ph,ArNacNac)2Zn Photocatalyst: Photophysical Properties and Mechanistic Understanding. *Inorg. Chem. Front.* **2021,** *8* (8), 2078-2087.

81. Singh, K.; Singh, R.; Hazari, A. S.; Adhikari, D., Bimodal Photocatalytic Behaviour of a Zinc β-Diketiminate: Application to Trifluoromethylation Reactions. *Chem. Commun.* **2022,** *58* (27), 4384-4387.

82. Anastas, P.; Eghbali, N., Green Chemistry: Principles and Practice. *Chem. Soc. Rev.* **2010,** *39* (1), 301-312.

83. Prier, C. K.; Rankic, D. A.; MacMillan, D. W., Visible Light Photoredox Catalysis with Transition Metal Complexes: Applications in Organic Synthesis. *Chem. Rev.* **2013,** *113* (7), 5322-5363.

84. Romero, N. A.; Nicewicz, D. A., Organic Photoredox Catalysis. *Chem. Rev.* **2016,** *116* (17), 10075-10166.

85. Tucker, J. W.; Stephenson, C. R., Shining Light on Photoredox Catalysis: Theory and Synthetic Applications. *J. Org. Chem.* **2012,** *77* (4), 1617-1622.

86. Brown, D. G.; Sanguantrakun, N.; Schulze, B.; Schubert, U. S.; Berlinguette, C. P., Bis (tridentate) Ruthenium–Terpyridine Complexes Featuring Microsecond Excited-State Lifetimes. *J. Am. Chem. Soc.* **2012,** *134* (30), 12354-12357.

87. Rehm, D.; Weller, A., Kinetics of Fluorescence Quenching by Electron and H-Atom Transfer. *Isr. J. Chem.* **1970,** *8* (2), 259-271.

88. Ciamician, G., The Photochemistry of the Future. *Science* **1912,** *36* (926), 385-394.

89. Eberhard, J.; Peuntinger, K.; Fröhlich, R.; Guldi, D. M.; Mattay, J., Synthesis and Properties of Acridine and Acridinium Dye Functionalized Bis (terpyridine) Ruthenium (II) Complexes. *Euro. J. Org. Chem.* **2018,** *2018* (20-21), 2682-2700.

90. Gini, A.; Uygur, M.; Rigotti, T.; Alemán, J.; García Mancheño, O., Novel Oxidative Ugi Reaction for the Synthesis of Highly Active, Visible-Light, Imide-Acridinium Organophotocatalysts. *Chem.– Euro. J.* **2018,** *24* (48), 12509-12514.

91. Tlili, A.; Lakhdar, S., Acridinium Salts and Cyanoarenes as Powerful Photocatalysts: Opportunities in Organic Synthesis. *Angew. Chem., Int. Ed.* **2021,** *133* (36), 19678-19701.

92. Narayanam, J. M.; Stephenson, C. R., Visible Light Photoredox Catalysis: Applications in Organic Synthesis. *Chem. Soc. Rev.* **2011,** *40* (1), 102-113.

93. Yoon, T. P.; Ischay, M. A.; Du, J., Visible Light Photocatalysis as a Greener Approach to Photochemical Synthesis. *Nature Chem.* **2010,** *2* (7), 527-532.

94. Arias-Rotondo, D. M.; McCusker, J. K., The Photophysics of Photoredox Catalysis: a Roadmap for Catalyst Design. *Chem. Soc. Rev.* **2016,** *45* (21), 5803-5820.

95. Buzzetti, L.; Crisenza, G. E.; Melchiorre, P., Mechanistic Studies in Photocatalysis. *Angew. Chem., Int. Ed.* **2019,** *58* (12), 3730-3747.

96. Chan, A. Y.; Perry, I. B.; Bissonnette, N. B.; Buksh, B. F.; Edwards, G. A.; Frye, L. I.; Garry, O. L.; Lavagnino, M. N.; Li, B. X.; Liang, Y., Metallaphotoredox: the Merger of Photoredox and Transition Metal Catalysis. *Chem. Rev.* **2021,** *122* (2), 1485-1542.

97. Nguyen, V. T.; Nguyen, V. D.; Haug, G. C.; Dang, H. T.; Jin, S.; Li, Z.; Flores-Hansen, C.; Benavides, B. S.; Arman, H. D.; Larionov, O. V., Alkene Synthesis by Photocatalytic Chemoenzymatically Compatible Dehydrodecarboxylation of Carboxylic Acids and Biomass. *ACS Catal.* **2019,** *9* (10), 9485-9498.

98. Darwent, J. R.; Douglas, P.; Harriman, A.; Porter, G.; Richoux, M.-C., Metal Phthalocyanines and Porphyrins as Photosensitizers for Reduction of Water to Hydrogen. *Coord. Chem. Rev.* **1982,** *44* (1).

99. Fukuzumi, S.; Honda, T.; Kojima, T., Structures and Photoinduced Electron Transfer of Protonated Complexes of Porphyrins and Metallophthalocyanines. *Coord. Chem. Rev.* **2012,** *256* (21-22), 2488-2502.

100. Shanmugam, S.; Xu, J.; Boyer, C., Exploiting Metalloporphyrins for Selective Living Radical Polymerization Tunable Over Visible Wavelengths. *J. Am. Chem. Soc.* **2015,** *137* (28), 9174-9185.

101. Nicewicz, D. A.; MacMillan, D. W., Merging Photoredox Catalysis with Organocatalysis: the Direct Asymmetric Alkylation of Aldehydes. *Science* **2008,** *322* (5898), 77-80.

102. Metternich, J. B.; Gilmour, R., A bio-inspired, catalytic E→ Z Isomerization of Activated Olefins. *J. Am. Chem. Soc.* **2015,** *137* (35), 11254-11257.

103. Hari, D. P.; König, B., Synthetic Applications of Eosin Y in Photoredox Catalysis. *Chem. Commun.* **2014,** *50* (51), 6688-6699.

104. Tan, F.-F.; He, X.-Y.; Tian, W.-F.; Li, Y., Visible-Light Photoredox-Catalyzed C–O Bond Cleavage of Diaryl Ethers by Acridinium Photocatalysts at Room Temperature. *Nature Commun.* **2020,** *11* (1), 6126.

105. Cao, Y.-X.; Zhu, G.; Li, Y.; Le Breton, N.; Gourlaouen, C.; Choua, S.; Boixel, J.; Jacquot de Rouville, H.-P.; Soulé, J.-F., Photoinduced Arylation of Acridinium Salts: Tunable Photoredox Catalysts for C–O Bond Cleavage. *J. Am. Chem. Soc.* **2022,** *144* (13), 5902-5909.

106. Fukuzumi, S.; Ohkubo, K.; Suenobu, T.; Kato, K.; Fujitsuka, M.; Ito, O., Photoalkylation of 10-alkylacridinium Ion via a Aharge-Shift type of Photoinduced Electron Transfer Controlled by Solvent Polarity. *J. Am. Chem. Soc.* **2001,** *123* (35), 8459-8467.

107. Fukuzumi, S.; Kotani, H.; Ohkubo, K.; Ogo, S.; Tkachenko, N. V.; Lemmetyinen, H., Electron-Transfer State of 9-Mesityl-10-methylacridinium Ion with a Much Longer Lifetime and Higher Energy than that of the Natural Photosynthetic Reaction Center. *J. Am. Chem. Soc.* **2004,** *126* (6), 1600-1601.

108. Pandey, G.; Murugan, A.; Balakrishnan, M., A New Strategy Towards the Total Synthesis of Phenanthridone Alkaloids: Synthesis of (+)-2, 7-Dideoxypancratistatin as a Model Study. *Chem. Commun.* **2002,** (6), 624-625.

109. Pandey, G.; Sochanchingwung, R., Photoinduced electron Transfer (PET) Promoted Cross-Coupling of Organoselenium and Organosilicon Compounds: a New Carbon–Carbon Bond Formation Strategy. *Chem. Commun.* **1994,** (17), 1945-1946.

110. Pandey, G.; Laha, R., Visible-Light-Catalyzed Direct Benzylic C (sp3)–H Amination Reaction by Cross-Dehydrogenative Coupling. *Angew. Chem. Int. Ed.* **2015,** *54* (49), 14875-14879.

111. Liu, Q.; Li, Y. N.; Zhang, H. H.; Chen, B.; Tung, C. H.; Wu, L. Z., Reactivity and Mechanistic Insight into Visible-Light-Induced Aerobic Cross-Dehydrogenative Coupling Reaction by Organophotocatalysts. *Chem.–Euro. J.* **2012,** *18* (2), 620-627.

112. Neumann, M.; Zeitler, K., A Cooperative Hydrogen-Bond-Promoted Organophotoredox Catalysis Strategy for Highly Diastereoselective, Reductive Enone Cyclization. *Chem.–Euro. J.* **2013,** *19* (22), 6950-6955.

113. Liang, Z.; Xu, S.; Tian, W.; Zhang, R., Eosin Y-Catalyzed Visible-Light-Mediated Aerobic Oxidative Cyclization of N, N-dimethylanilines with Maleimides. *Beilstein J. Org. Chem.* **2015,** *11* (1), 425-430.

114. Cantillo, D.; de Frutos, O.; Rincon, J. A.; Mateos, C.; Kappe, C. O., Continuous Flow α-Trifluoromethylation of Ketones by Metal-Free Visible Light Photoredox Catalysis. *Org. lett.* **2014,** *16* (3), 896-899.

115. Joshi-Pangu, A.; Lévesque, F.; Roth, H. G.; Oliver, S. F.; Campeau, L.-C.; Nicewicz, D.; DiRocco, D. A., Acridinium-Based Photocatalysts: a Sustainable Option in Photoredox Catalysis. *J. Org. Chem.* **2016,** *81* (16), 7244-7249.

116. Speckmeier, E.; Fischer, T. G.; Zeitler, K., A Toolbox Approach to Construct Broadly Applicable Metal-Free Catalysts for Photoredox Chemistry: Deliberate Tuning of Redox Potentials and Importance of Halogens in Donor–Acceptor Cyanoarenes. *J. Am. Chem. Soc.* **2018,** *140* (45), 15353-15365.

117. Speck, F.; Rombach, D.; Wagenknecht, H.-A., N-Arylphenothiazines as Strong Donors for Photoredox Catalysis–Pushing the Frontiers of Nucleophilic Addition of Alcohols to Alkenes. *Beilstein J. Org. Chem.* **2019,** *15* (1), 52-59.

118. Vega-Peñaloza, A.; Mateos, J.; Companyó, X.; Escudero-Casao, M.; Dell'Amico, L., A Rational Approach to Organo-Photocatalysis: Novel Designs and Structure-Property Relationships. *Angew. Chem. Int. Ed.* **2021,** *60* (3), 1082-1097.

119. Murphy, J. A., Discovery and Development of Organic Super-Electron-Donors. *J. Org. Chem.* **2014,** *79* (9), 3731-3746.

120. Zhou, S.; Anderson, G. M.; Mondal, B.; Doni, E.; Ironmonger, V.; Kranz, M.; Tuttle, T.; Murphy, J. A., Organic Super-Electron-Donors: Initiators in Transition Metal-Free Haloarene–Arene Coupling. *Chem. Sci.* **2014,** *5* (2), 476-482.

121. Barham, J. P.; Coulthard, G.; Kane, R. G.; Delgado, N.; John, M. P.; Murphy, J. A., Double Deprotonation of Pyridinols Generates Potent Organic Electron-Donor Initiators for Haloarene–Arene Coupling. *Angew. Chem. Int. Ed.* **2016,** *55* (14), 4492-4496.

122. Zhou, S.; Doni, E.; Anderson, G. M.; Kane, R. G.; MacDougall, S. W.; Ironmonger, V. M.; Tuttle, T.; Murphy, J. A., Identifying the Roles of Amino acids, Alcohols and 1, 2-Diamines as Mediators in Coupling of Haloarenes to Arenes. *J. Am. Chem. Soc.* **2014,** *136* (51), 17818-17826.

123. Cumine, F.; Zhou, S.; Tuttle, T.; Murphy, J. A., A Study of Diketopiperazines as Electron-Donor Initiators in Transition Metal-Free Haloarene–Arene Coupling. *Org. Biomol. Chem.* **2017,** *15* (15), 3324-3336.

124. Yang, H.; Chu, D.-Z.; Jiao, L., Aromatization Modulates the Activity of Small Organic Molecules as Promoters for Carbon–Halogen Bond Activation. *Chem. Sci.* **2018,** *9* (6), 1534-1539.

125. Zhang, L.; Yang, H.; Jiao, L., Revisiting the Radical Initiation Mechanism of the Diamine-Promoted Transition-Metal-Free Cross-Coupling Reaction. *J. Am. Chem. Soc.* **2016,** *138* (22), 7151-7160.

126. Liu, W.; Cao, H.; Zhang, H.; Zhang, H.; Chung, K. H.; He, C.; Wang, H.; Kwong, F. Y.; Lei, A., Organocatalysis in Cross-Coupling: DMEDA-Catalyzed Direct C− H Arylation of Unactivated Benzene. *J. Am. Chem. Soc.* **2010,** *132* (47), 16737-16740.

127. Studer, A.; Curran, D. P., Organocatalysis and C-H Activation Meet Radical-and Electron-Transfer Reactions. *Angew. Chem. Int. Ed.* **2011,** *22* (50), 5018-5022.

128. Studer, A.; Curran, D. P., The Electron is a Catalyst. *Nature Chem.* **2014,** *6* (9), 765-773.

129. Kim, H.; Kim, H.; Lambert, T. H.; Lin, S., Reductive Electrophotocatalysis: Merging Electricity and Light to Achieve Extreme Reduction Potentials. *J. Am. Chem. Soc.* **2020,** *142* (5), 2087-2092.

130. Liang, K.; Liu, Q.; Shen, L.; Li, X.; Wei, D.; Zheng, L.; Xia, C., Intermolecular Oxyarylation of Olefins with Aryl Halides and TEMPOH Catalyzed by the Phenolate Anion Under Visible Light. *Chem. Sci.* **2020,** *11* (27), 6996-7002.

131. Soumillion, J.-P.; Vandereecken, P.; Van der Auweraer, M.; De Schryver, F.; Schanck, A., Photophysical Analysis of Ion Pairing of. Beta.-Naphtholate in Medium Polarity Solvents: Mixtures of Contact and Solvent-Separated Ion Pairs. *J. Am. Chem. Soc.* **1989,** *111* (6), 2217-2225.

132. Hasegawa, E.; Izumiya, N.; Miura, T.; Ikoma, T.; Iwamoto, H.; Takizawa, S.-y.; Murata, S., Benzimidazolium Naphthoxide Betaine is a Visible Light Promoted Organic Photoredox Catalyst. *J. Org. Chem.* **2018,** *83* (7), 3921-3927.

133. Schmalzbauer, M.; Svejstrup, T. D.; Fricke, F.; Brandt, P.; Johansson, M. J.; Bergonzini, G.; König, B., Redox-Neutral Photocatalytic C− H Carboxylation of Arenes and Styrenes with CO_2. *Chem* **2020,** *6* (10), 2658-2672.

Chapter 2

Multielectron Redox Afforded by Pincer Ligand Promoting Kumada Cross-coupling Reactions

A part of this work has been published in Chem. Eur. J., **2023**, *30,* e202303189

2.1. Introduction

There is a significant demand towards the design of base-metal catalysts, that can be true surrogates to their precious metal analogues.[1, 2] Although, chemical transformations which involve multielectron redox are greatly facilitated by the 4d or 5d metals, their scarcity, cost and toxicity strongly warrant their substitution.[3] Their efficiency of performing redox transformations stems from the ability to carry out two-electron chemistry very easily. On the contrary, 3d metals are much inclined to adopt one-electron redox processes. Along this direction, redox-active ligands offer a viable solution which can work in tandem with 3d transition metals so that altogether two-electron processes are accomplished.[4, 5] In the recent time, many examples demonstrated active participation of the ligand backbone in a particular redox transformation while they were seemingly believed to be innocent.[6] Beyond being a spectroscopic curiosity, redox active ligand's active utilization in catalysis is a spawning area.[7-9] A decade ago, Soper demonstrated that a simple catecholate ligand in co-operation with cobalt drives some cross-coupling chemistry.[10] Similarly, Chirik utilized an α-diimine nickel catalyst for alkene hydrosilylation, where the ligand backbone has important redox role to play.[11] Our strong interest in 3d transition metal catalysis where ligands play a preeminent role[12-14] prompted us to identify other ligand backbones that can afford multielectron redox transformations, without undergoing detrimental irreversible bond cleavage.

Along this direction, a pincer-based ligand has been explored which are extremely popular in catalysis for their multidentate nature, easy tunability and robust framework to afford metals in unusual oxidation states.[15-17] Few pincers including "PNP" have showcased the non-innocent nature of the ancillary ligand by losing electron from the nitrogen, indicating that multielectron redox can be afforded in cooperation with the ligand backbone.[18-20] However, despite some sporadic examples of direct participation of the ligand backbone in multielectron chemistry, catalytic transformations are scarce.[21] Towards this end, an 'NNN' pincer was identified, which could achieve redox transformations in a reversible manner so that a catalytic reaction can be realized. Further, aryl-aryl Kumada cross-coupling reactions were developed by using a nickel catalyst, where such a redox-active backbone played a pivotal role in steering this multielectron transformation.

Pincers are robust scaffold and has been widely utilized in multiple directions of chemistry ranging from small molecule activation, stabilizing hypervalent aluminium, bismuth compounds to making dendrimers.[22, 23] A significantly large number of pincers have been

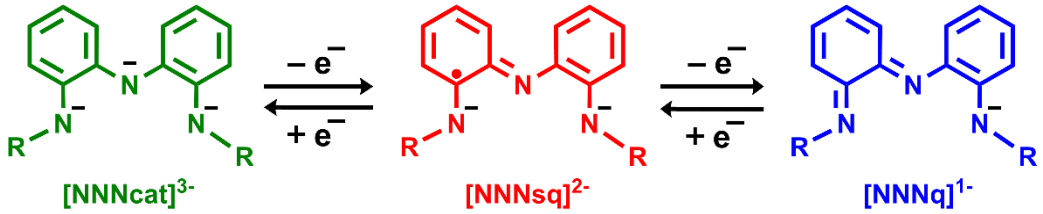

Scheme 2.1: Redox states afforded in an NNN-pincer ligand.

exploited by Milstein for borrowing hydrogen chemistry where the backbone of the ligand can undergo a reversible aromatization/dearomatization under basic conditions.[24, 25] Despite this rich chemistry afforded on this ancillary ligand, prominent examples of multielectron redox processes facilitated by the reversible redox transformation on such backbone is rare.[26] The question was, whether a NNN pincer can accommodate reversible chemical changes during a redox transformation so that such a ligand can drive some catalytic reactions. As shown in Scheme 2.1, three different redox states can be easily conceived for a NNN pincer (N^1-isopropyl-N^2-(2-(isopropylamino)phenyl)benzene-1,2-diamine) in its fully deprotonated state.[27, 28] It can be assumed that these redox states will significantly help in accomplishing demanding redox processes by direct ligand participation.

2.2. Results and Discussion

This affordability of multiple redox states gave us inspiration to utilize the backbone in multielectron redox transformations that can be realized in cross-coupling catalysis. Having this idea in mind, synthesis of a nickel complex was attempted since nickel is an abundant transition metal and is being recognized as the 'workhorse' among base metals.[29]

2.2.1. Synthesis of (NNN)H_3 Ligand and Ni(NNN) Complex 1

Towards this direction the (NNN)H_3 can be synthesized by following the literature procedures (Scheme 2.2).[27] First of all, *bis*(2-nitrophenyl) amine can be obtained *via* displacement of fluoro-group of 1-fluoro-2-nitrobenzene by 2-nitroaniline in the presence of base K_2CO_3. Both the nitro group of the starting material can be easily converted into amine by using Zn-NH_4Cl reducing agent. *Bis*(2-aminophenyl)amine can be treated with acetone in acidic medium to provide imine which can be further reduced by sodium cyanoborohydride to obtain (NNN)H_3, **1** in quantitative yield.

The protonated version of the ligand was deprotonated *in situ* upon treatment with three equivalents of ^{n}BuLi at -70 ^{o}C. Addition of a THF solution of $NiCl_2(THF)_{1.5}$ to a cold solution of the deprotonated ligand at low temperature showed a color change to dark-green which upon

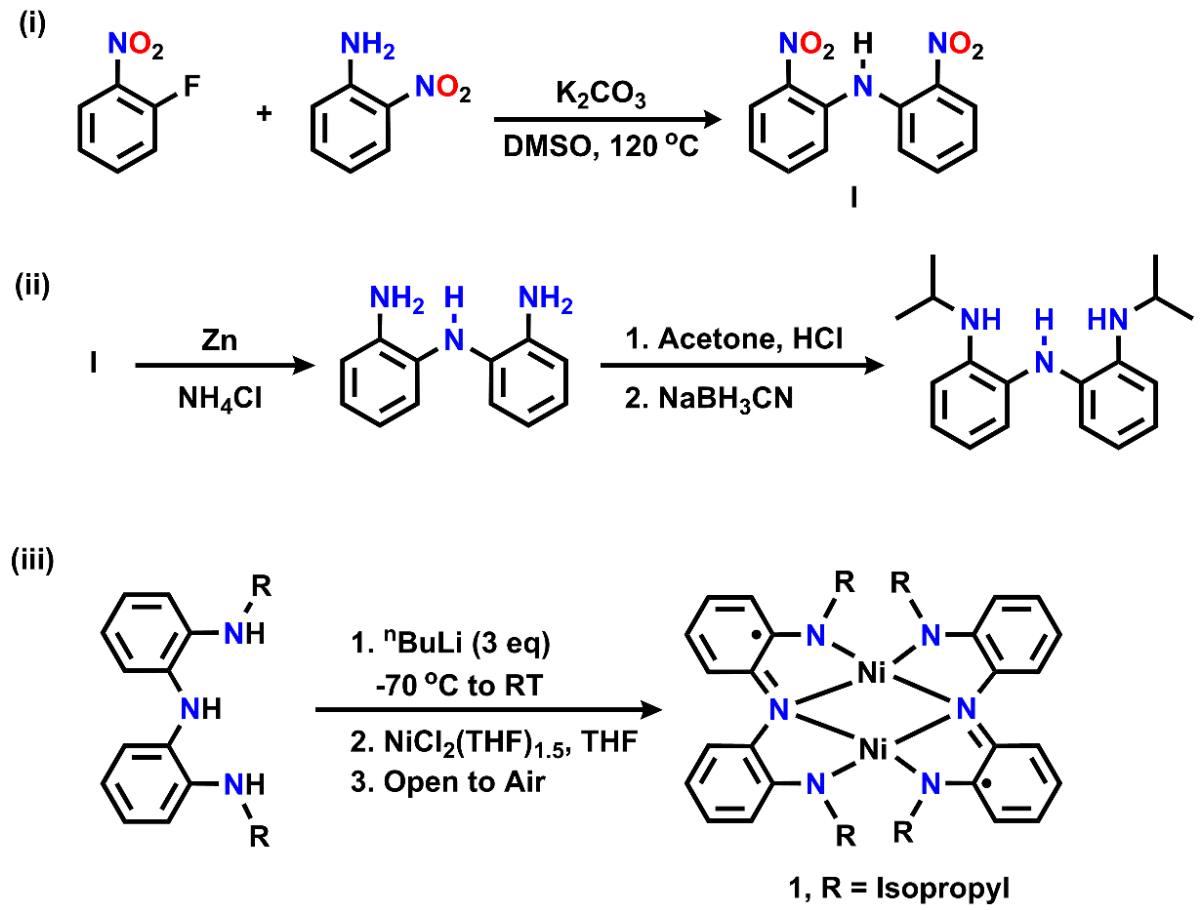

Scheme 2.2. Synthesis of $(NNN)H_3$ Ligand and Ni(NNN) Complex **1**.

exposure to air changed dramatically to a dark violet solution (Scheme 2.2). The dried product, upon attempt for crystallization from THF/pentane mixture at -40 ^{o}C temperature resulted in dark violet-colored blocks in 72% yield. Repeated attempts to collect a diffractable crystal for X-ray structure determination were fraught with poor quality of the crystal. Fortunately, X-ray diffraction study revealed that the product is a dimer in solid state (Figure 2.1). One of the amido nitrogen in the pincer backbone has bridged two nickel centers to describe a Ni_2N_2 diamond core, **1**. The metrical parameters from the structure were not interpreted due to the poor quality of the data.

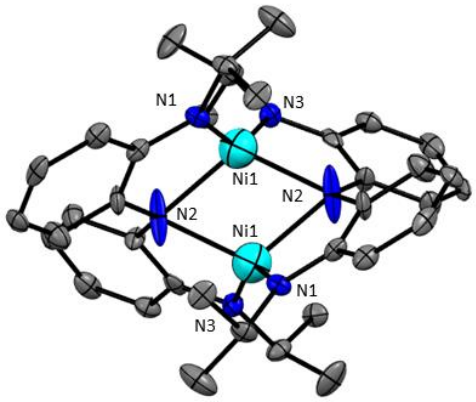

Figure 2.1: Single crystal structure of **1**

2.2.2. Characterization of Ni(NNN) Complex (1)

The diamond core arrangement closely resembles Mindiola's nickel pincer dimer molecule where two Ni^{I} centers were placed at a very close proximity, 2.32 Å.[30] The present trianionic pincer has very strong proclivity towards oxidation beacuse of its electron rich nature. So the dimeric composition consists of two Ni(II) centers bridged by two mono-oxidized pincer backbone. In other words, the pincer attained its iminosemiquinonate form via aerobic oxidation, which is also much easier than oxidizing Ni(II) to Ni(III). Our formulation is also consistent with Heyduk's observation for a similar SNS pincer backbone where aerial oxidation afforded a ligand radical owing to mono-oxidized ligand backbone.[31] Since the ligand backbone can afford one-electron oxidized state, which logically represents an iminisemiquinonate form, it provides promise to elicit redox behavior amenable to multielectron redox transformations.

2.2.2.1. ^{1}H NMR Analysis of Ni(NNN) Complex (1)

The ^{1}H NMR spectrum of **1** was conducted using deuterated benzene (C_6D_6) as a solvent at room temperature that exhibited broad peaks due to paramagnetism associated with the molecule (Figure 2.2).

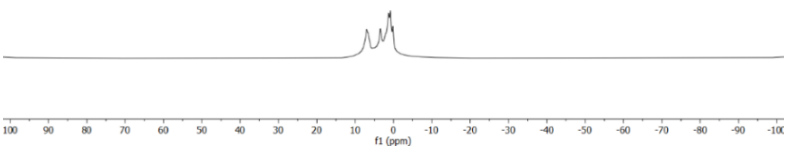

Figure 2.2: ^{1}H NMR spectrum of **1** recorded in C_6D_6.

2.2.2.2. Solution State Magnetic Moment Analysis of Ni(NNN) Complex (1) by Evans Magnetic Moment Method

Further, the paramagnetism of the molecule was interrogated by Evans magnetic moment measurement. The experiment was conducted in C_6D_6 at room temperature. Considering the dimeric molecular mass, room temperature measurement in C_6D_6 revealed a value of 1.9 μ_B. This low value is probable if a tetrahedral nickel(II) species is antiferromagnetically coupled to an organic radical, housed in the ligand backbone.

2.2.2.3. EPR Analysis of Ni(NNN) Complex (1)

To gather an evidence for the ligand-centered radical, an EPR experiment was performed at 77 K which disclosed a signal with the g value of 2.001 (Figure 2.3). This value suggests an organic radical, which is housed by the redox noninnocent ligand backbone.

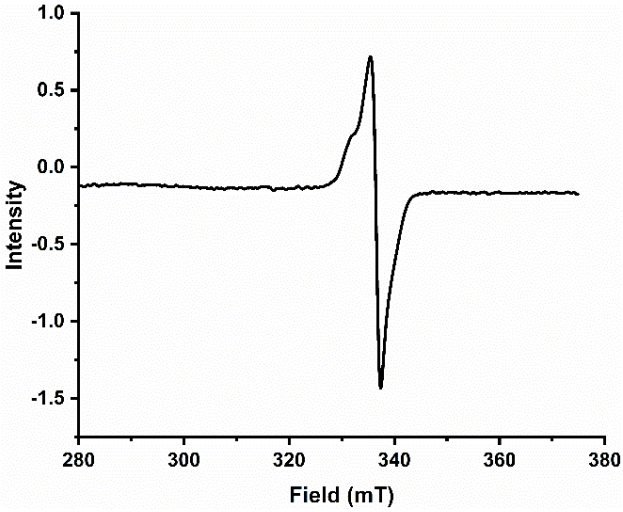

Figure 2.3: X-Band EPR spectrum of **1** at 77K.

2.3. Catalytic Reactions

The dimeric molecule **1** was used as the precatalyst for nickel catalyzed Kumada cross-coupling,[32] since it was conceived that the ligand redox non-innocence can afford such reactions following a one-electron pathway, in contrary to traditional two-electron pathways. Along this direction, catalyst **1** was tested for the cross -coupling of ArBr with an aryl Grignard, ArMgBr. Mixing a cold THF solution of the Grignard to the aryl bromide in presence of the catalyst afforded the formation of a biaryl species at –20 ^oC. The typical reaction time for such coupling reaction was 12 h. A series of optimization tests were conducted to reveal that the reaction can work well in 3 mol% loading of the catalyst and two equivalents of Grignard (entry

1, Table 2.1). Increase of catalyst loading to 5 mol% slightly increases the yield to 91%, while decreasing the catalyst loading to 2 mol% reduces the yield to 60% (entry 2 and 3, Table 2.1). Reducing the amount of Grignard to one equivalent affects the yield of the reaction, decreasing it to 29% (entry 5 and 6, Table 2.1). Increasing the temperature to zero degree and room temperature also resulted into diminished product yield (entry 7 and 8, Table 2.1). Appropriate control reactions revealed that only $NiCl_2$ as the metal precursor only afforded trace amount of product while the simple trianionic ligand did not result any product formation, under otherwise identical conditions.

Table 2.1. Optimization of reaction conditions.

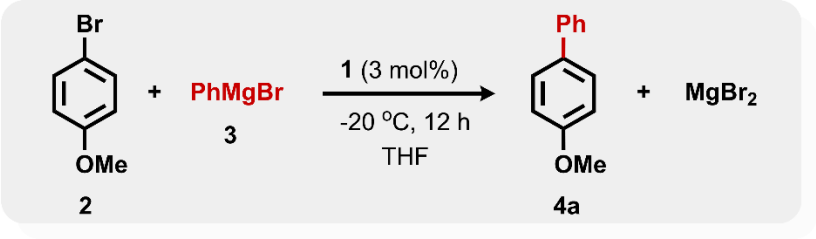

Entry	Deviation from standard conditions	% Yield[b]
1	**None**	**87(79)[c]**
2	5 mol% of **1**	91
3	2 mol% of **1**	60
4	Absence of **1**	ND
5	1.0 equiv of PhMgBr	29
6	1.5 equiv of PhMgBr	67
7	At 0 °C	28
8	At RT	21
9	$NiCl_2$ instead of **1**	Trace
10	Only ligand instead of **1**	ND

(a) 4-bromoanisole (0.2 mmol), PhMgBr (0.4 mmol), **1** (3 mol%), THF, -20 °C, 12 h. (b) GC yields. (c) Isolated yield.

2.4. Scope of Aryl-Aryl Kumada Cross-coupling Reaction by Catalyst 1

Having the optimized reaction condition in hand, the scope of reaction was explored with multiple aryl halides (Table 2.2). The methoxy substituted bromobenzene furnished the *p- and m*-methoxy biphenyl (**4a** and **4b** respectively) in 91-95% yields. The reaction provided excellent yields of multiple alkyl-substituted bromobenzenes (**4c-4e**). Interestingly, when bromo mesitylene was chosen as the coupling partner, the product 2,4,6-trimethyl-1,1'-

Table 2.2: Substrate scope of substituted aryl/heterocyclic bromide, polybrominated compounds.

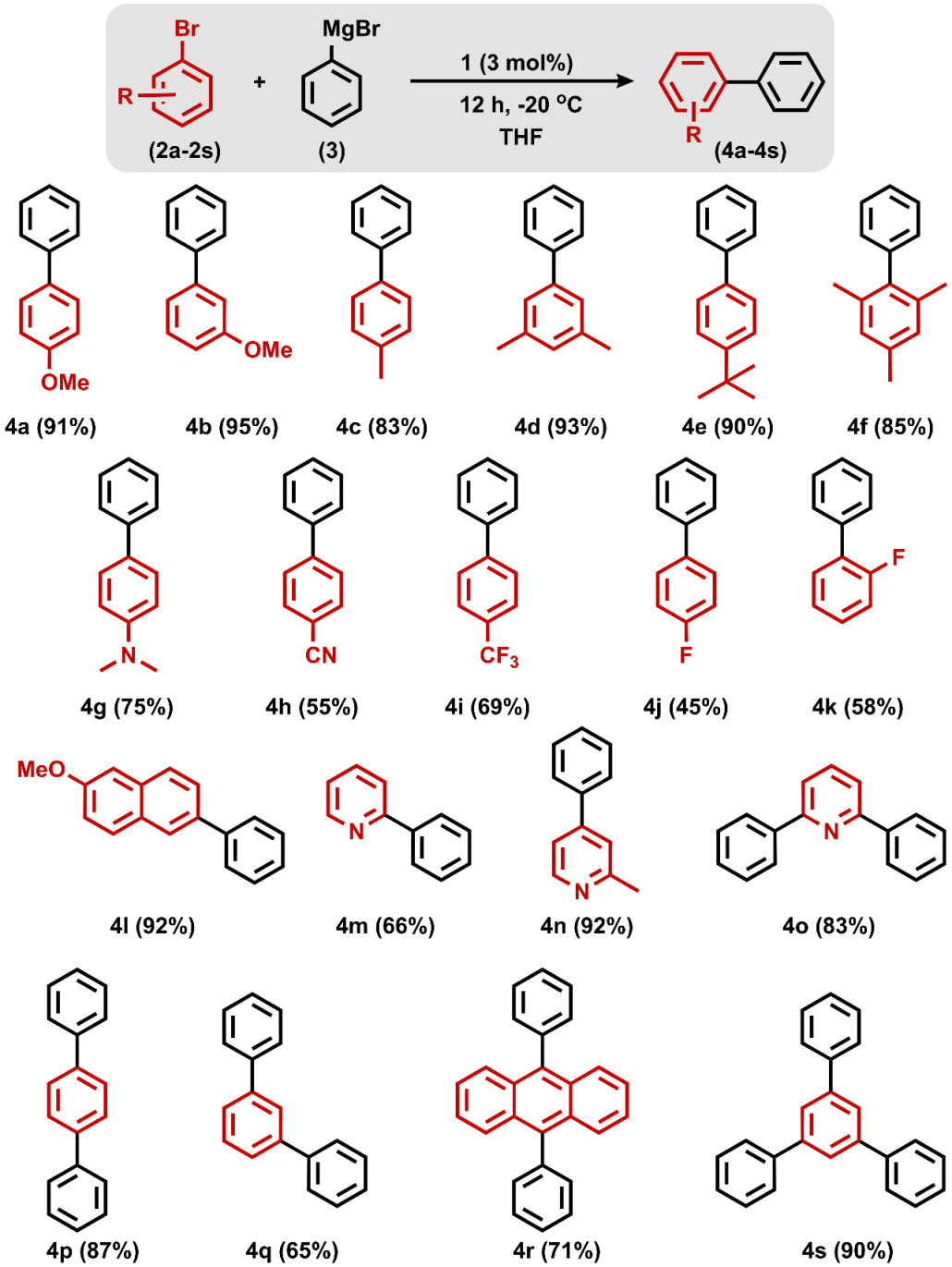

Reaction conditions: **1** (3 mol%), Aryl halide (0.5 mmol), Grignard reagent (1 mmol), THF (2 mL), -20 °C (chiller bath), 12 h, isolated yield. For di/tri-bromo aryl halides 2 equivalent Grignard reagent used with respect to each bromo group.

biphenyl, **4f** was isolated in 85% yield. Additionally, various reactive functional groups were examined for this synthetic protocol. For example, *N*,*N*-dimethyl aniline, *p*-CN, *p*-CF_3, *p*-F benzenes were all proved to be good substrates providing moderate to good (45-75%) yields

of coupling products. Similarly, naphthyl, pyridyl and picolyl bromides afforded the respective biaryl products **4l−4n** in 66-92% yields. Encouragingly, when 2,6-dibromo-pyridine was chosen as a substrate, desirably both side coupling happened to afford 2,6-diphenylpyridine (**4o**) in 83% yield. Such both side coupling was further performed on a series of substrates to isolate products **4p-4r** in 65-87% yields. Intriguingly, 1,3,5-tribromobenzene underwent the coupling reaction in all three positions to afford tetraphenyl **4s** in 90% yield.

Encouraged by the efficiency of catalyst, substrates involving less active aryl-Cl bonds was tried to examine.[33] Multiple aryl chlorides were utilized as an effective coupling partner successfully to realize the biphenyl products in moderate yields (Table 2.3). It was noted that usually the yield of the products for chloro-containing substrates are lower than the bromo-containing analogues. This also correlates well with the fact that the reduction potential of C-Cl bonds are much negative compared to C-Br bonds. Along this point of argument, it is expected that aryl iodide substrates will be relatively easy to activate, given much positive

Table 2.3: Substrate scope of substituted aryl chloride and iodides.

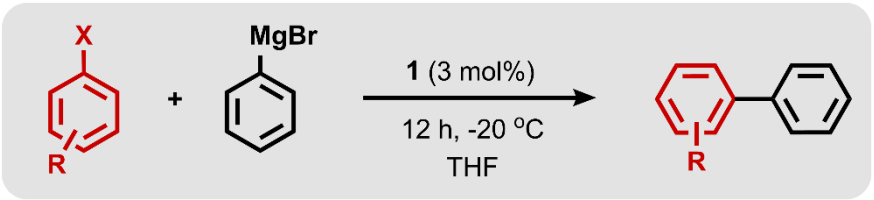

Entry	X	R	Yield
1	Cl	4-OMe	65
2	Cl	3-OMe	62
3	Cl	4-F	65
4	Cl	4-CF_3	58
5	Cl	4-Me	55
6	Cl	2,4,6-trimethyl	45
7	I	4-OMe	86
8	I	2-F	83
9	I	3,5-Dimethyl	95

Reaction conditions: 1 (3 mol%), Aryl halide (0.5 mmol), Grignard reagent (1 mmol), THF (2 mL), -20 °C (chiller bath), 12 h, isolated yield.

reduction potential to cleave a C-I bond. Indeed, three different aryl iodide substrates under the same reaction conditions afforded the respective biphenyl products in high yields (entry 7-9, Table 2.3).

2.5. Mechanistic Insights and Control Experiments

After successfully performing the aryl-aryl Kumada cross-coupling reaction, the mechanistic detail of the reaction was elucidated. In this direction, the intrigued redox responsive nature of the NNN backbone was depicted to pinpoint how this character helped in accomplishing such a multielectron transformation in tandem with 3d transition metal nickel.

2.5.1. Kinetic Study of Aryl-Aryl Kumada Cross-Coupling Reaction

In order to study the reaction kinetic, the aliquots of the reaction were taken at different time span at different temperature. In usual case where the cross-coupling reaction is performed at low temperature (-20 ^{o}C), there is an induction time of 40 minutes. Such an induction time can be avoided when the solution of **1** is heated at 60 ^{o}C for 5 minutes, and the Grignard reagent is mixed afterwards. This change in condition led to essentially instantaneous product formation as monitored by GC- analysis (Figure 2.4).

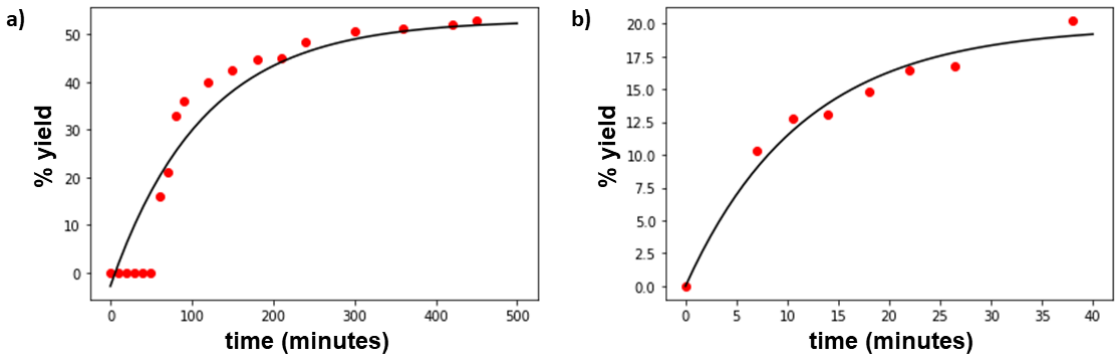

Figure 2.4: Plot for % yield of product vs time (in minutes) at (a) -20 °C temperature (b) Room temperature

2.5.2. Radical Quenching Experiment and Intermediate Trapping

The presence of the radical on the ligand backbone in **1** strongly suggests that the reaction will be radical mediated. To verify this hypothesis, the reaction was performed in the presence of a radical quencher TEMPO. Notably, the reaction completely ceases when the quencher is used in one equivalent (Scheme 2.3). Moreover, using bromo anisole as the aryl halide substrate and phenyl magnesium bromide as the representative Grignard, the TEMPO adduct of the anisole radical (**5**) was intercepted. Such a radical adduct was detected by electron spray ionization mass spectrometric technique at 264.1962 amu.

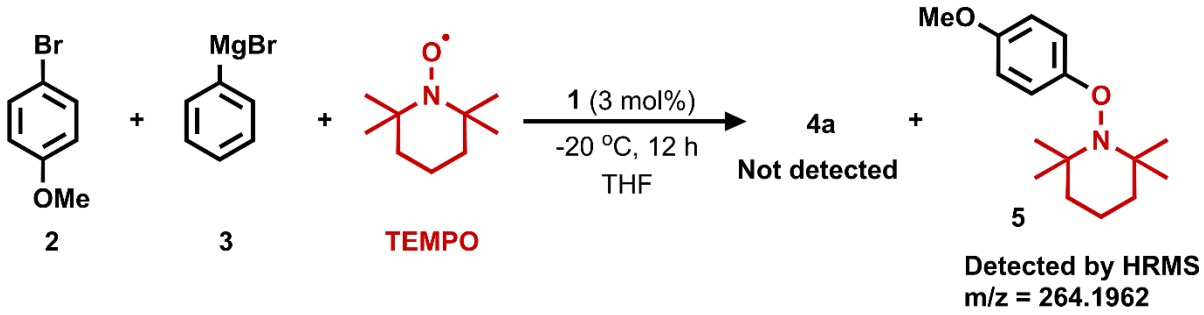

Scheme 2.3: Radical interception by TEMPO.

2.5.3. UV-Visible Analysis of Ni(NNN) (1) and Reaction Mixture

Mechanistically, we propose that the aryl magnesium bromide attacks to give a square planar four-coordinate nickel complex **1a** with phenyl group attached to nickel (Scheme 2.6). So, during attachment of the phenyl group from phenyl Grignard reagent, the ligand backbone yet remains in the iminosemiquinonate form, while $MgBr^+$ acts as the counter cation. Such 'ate' complex has been earlier documented to conduct important organometallic transformations.[34-36] We also considered the possibility of a probable oxidative addition of aryl bromide to **1** as the first step of the reaction. However, stirring the THF solution of **1** with Ar-Br, both at room temperature and at 60 °C did not provide any discernible color change of the solution. Further probation through UV-vis spectroscopy did not show any change in the spectrum of **1** (Figure 2.5), thus refuting the possibility of oxidative addition of Ar-Br as the starting point of the reaction.

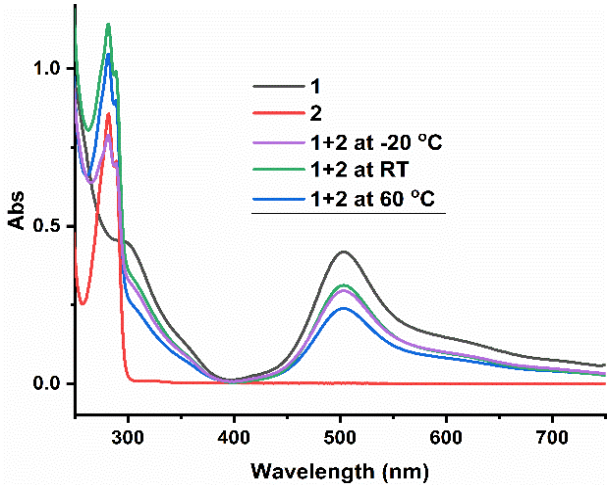

Figure 2.5. UV-Visible analysis of **1** (black line), **2** (red line) and reaction mixture at -20 ° C (violet line), room temperature (green line), 60 ° C (blue line).

2.5.4. Computational Analysis

To provide additional insight into the reaction mechanism, a high-level DFT computational study at B3LYP/6-31G* level of theory was undertaken.[37-38] Along this probation, the intermediate **1a** does a single electron transfer (SET), to homolytically cleave the aryl bromide bond so that an aryl radical and bromide anion can be generated. It is also quite probable that aryl halide reduction is facilitated by its binding to the nickel center via the halide, so that the SET process becomes inner-sphere in nature.[39] As it has been shown earlier the detection of the anisole radical from *p*-bromo-anisole substrate, which is fully consistent with SET process. It was considered that the ligand redox non-innocence plays a preponderant role in driving the SET, where the pincer backbone itself becomes converted to iminoquinone form (**1b**) (Figure 2.6). Importantly, the ligand-promoted electron transfer retains the nickel's oxidation state at +2. Moreover Br^- anion from aryl halide bond cleavage readily reacts with counter cation $MgBr^+$ of **1a** to liberate $MgBr_2$. Notably, Vicic through his earlier work proved the terpyridine ligand's predominant role in driving nickel-based alkyl-alkyl cross-coupling reaction.[40]

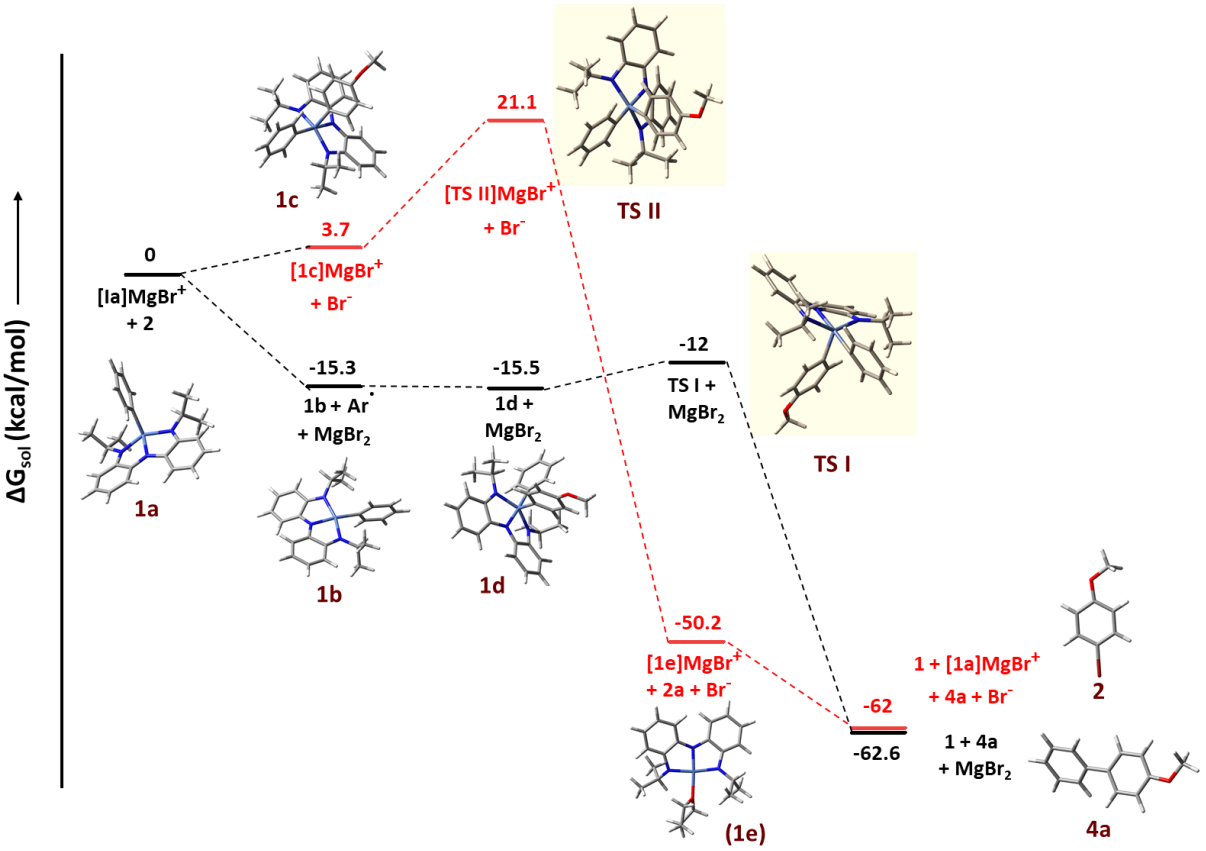

Figure 2.6: Potential energy surface at B3LYP level of theory for SET activating **2** and subsequent cross-coupling reaction to form **4a**. The red trace reflects the alternative bimetallic oxidative pathway whereas the black trace accounts for the escape-rebound pathway.

Furthermore, the SET to generate an aryl radical along with the conversion of nickel catalyst to its iminoquinone form, **1b** is further downhill by 15.3 kcal mol^{-1}. This SET process by an electron rich and hence reducing ligand backbone is a crucial step that determines the success of the catalyst. Our previous collaborative work disclosed a SET from the redox active phenalenyl backbone to homolytically cleave a Si–H bond, so that a silyl radical can pave hydrosilylation reactions via radical pathway.[41, 42] The discussed SET from the redox-active *o*-phenylenediamido backbone is an analogous event. Furthermore, it has also been observed that electron rich anion of 3,5 dimethyl pyrazole can facilitate SET process to aryldiazonium chloride to break the bond homolytically resulting the generation of aryl radical.[43] However, the reduction potential of aryldiazonium salts is much positive to a moderately strong Ar-Br bond. Following this step, the formed aryl radical is capable of attacking both the complexes **1a** and **1b** to attach both phenyl and aryl groups onto nickel following either bimetallic oxidative addition or radical rebound pathways (vide infra for details). The bimetallic oxidative addition here is used in the context of an aryl radical attacking a second molecule of (NNN)Ni species, rather than the same nickel species. Notably, this is different from traditional bimetallic sense where two metal centers simultaneously operate to carry out a chemical transformation. During the addition of aryl radical to **1a** through bimetallic pathway, a slightly high energy species of 3.7 kcal/mol is encountered corresponding to the formation of **1c** (Figure 2.6). However, on the other hand, addition of aryl radical to **1b** via radical rebound pathway leads to the formation of intermediate **1d** which is stable by 0.2 kcal/mol with respect to **1b**. Notably, during this step nickel needs to change its oxidation state to +III, since the ligand backbone already reached the highest oxidized iminoquinone form. Due to the significant energy difference between intermediates **1c** and **1d** (**1d** is lower in energy by 19.2 kcal/mol), the involvement of bimetallic pathway does not appear competitive. Also, **1a** is responsible for SET to break the Ar-X bond, and hence logically its population in the reaction medium might not be not sufficiently high to steer bimetallic reaction pathway. Finally, from the intermediate **1d**, a reductive elimination can ensue to form the new C–C bond, giving the Kumada Cross-coupled product **(4a)**. During the reductive elimination two electrons come back in the system reducing Ni (III) to Ni(II) and simultaneously reducing the ligand to its iminosemiquinonate form.[44, 45] This iminosemiquinonate form further runs the catalytic cycle. The computed barrier for the transition state, **TSI** for reductive elimination costs only 3.5 kcal mol^{-1} (Figure 2.6). In the **TSI**, the movement of the both phenyl and aryl groups are aligned to the direction of C-C bond formation and the frequency of such vibration is calculated as -199.9 cm^{-1}. At the **TSI**,

the ligand is about to be reduced and the C-N bonds in the o-iminoquinone motif starts elongating due to imminent reduction.

2.5.5. Radical Clock Experiment and Fate of Aryl Radical

Having the support from computational analysis, it was further sought-after experimental proof for such radical-promoted cross-coupling that would be predominantly steered by the ligand redox. To gather a strong evidence for SET from the ligand backbone that generates an aryl radical from the substrate aryl bromide, a radical clock substrate was selected. Along this direction, 2-hemiallyl bromobenzene was chosen as the probe molecule, as it was anticipated that the radical generation at the *ipso* position, may trigger a ring-cyclization event to leave a signature for the intermediacy of the radical (Scheme 2.4). When Kumada cross-coupling was conducted with **6**, copious amount of straight-chain product, **9** was isolated along with some amount of ring-cyclized product, **10**. This ring-cyclized product is an unambiguous proof of aryl radical generation via SET.

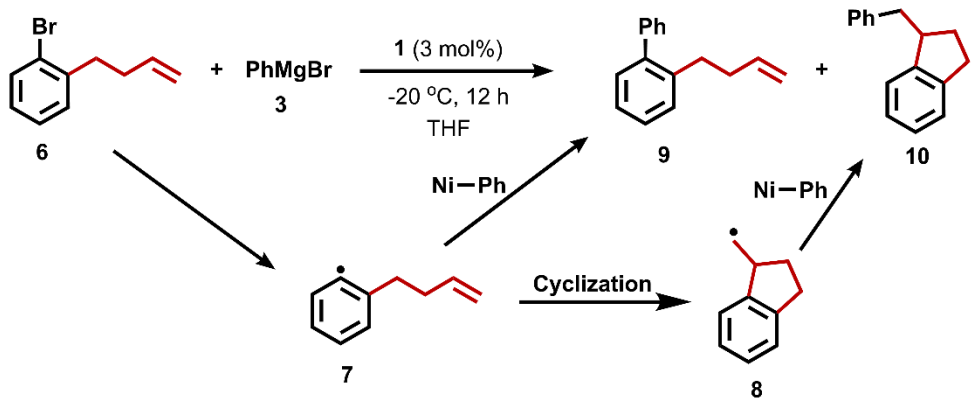

Scheme 2.4: Radical-clock experiment.

Once the aryl radical is generated, three probable pathways can be conceived for the targeted coupling: cage-rebound, escape-rebound and bimetallic oxidative addition (Scheme 2.5). The aryl radical can react in a cage-rebound fashion if the lifetime of the radical is pretty low. Indeed, Kochi postulated a cage-rebound mechanism for the oxidative addition of an aryl halide to Ni(0).[46] Alternatively, the radical could be long-lived and can come out of the solvent sphere so that further reaction by escape-rebound manner can also be imagined. In the escape-rebound pathway, the aryl radical at first escapes and then again reenters the solvent cage to recombine with L_qNi-Ph (L_q denotes the iminoquinone form of the ligand backbone) species.[47] As a third possibility, the engendered radical can react in the fashion of bimetallic oxidative addition[48, 49]

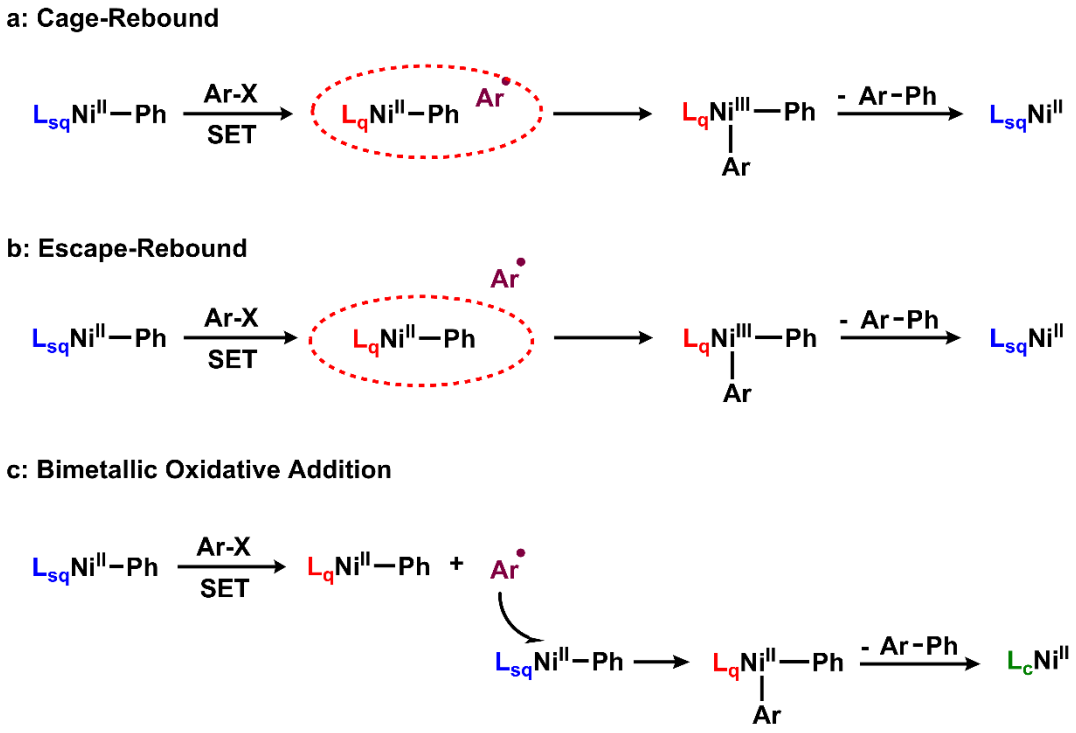

Scheme 2.5: Proposed pathways for the coupling of aryl radical. Subscripts on L symbolizes; sq = iminosemiquinonate, q = iminoquinone.

where the aryl radical can react with a second molecule of nickel species. In such case two different nickel centers would be involved to finally furnish the C–C bond. These possibilities have been also invoked during computational analysis (vide supra). The radical probe substrate and the formation of straight chain versus cyclized product provides an invaluable tool to dissect this intriguing mechanistic question and sheds further light on this radical-promoted reactivity. Usually, an unaltered ratio of straight-chain to cyclized product with increasing catalyst loading speaks for the cage-rebound mechanism. This is logical as the forged aryl radical can stay in the proximity of the metal catalyst, without leaving the solvent cage, so that the final product outcome is not dependent on catalyst loading. Conversely, if the generated radical is long-lived and hence affords enough time to come out of the solvent cage, then the ratio of the products would change on varying catalyst concentration. In essence, the ratio of **9** and **10** should be independent of catalyst concentration, if cage-rebound mechanism remains operational. In our present case, we witness a clear first-order dependence of increasing ratio of straight-chain/cyclized product (**9**/**10**) with incremental catalyst loading (Figure 2.7). This observation safely refutes the probability of any cage-bound reaction pathway. Among rest two possibilities, we prefer the escape-rebound pathway more over the bimetallic oxidative addition, since computational energy landscape argues in the favor of the former.

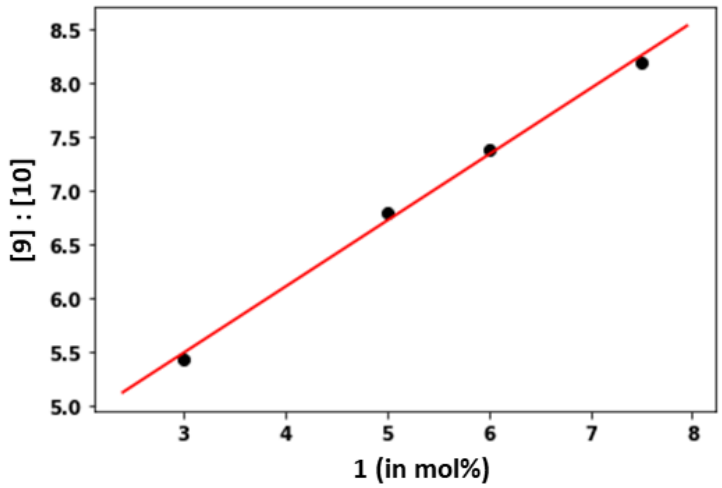

Figure 2.7: Plot for ratio of straight-chain (**9**) to cyclized (**10**) product with catalyst **1** loading.

2.6. Plausible Mechanistic Cycle

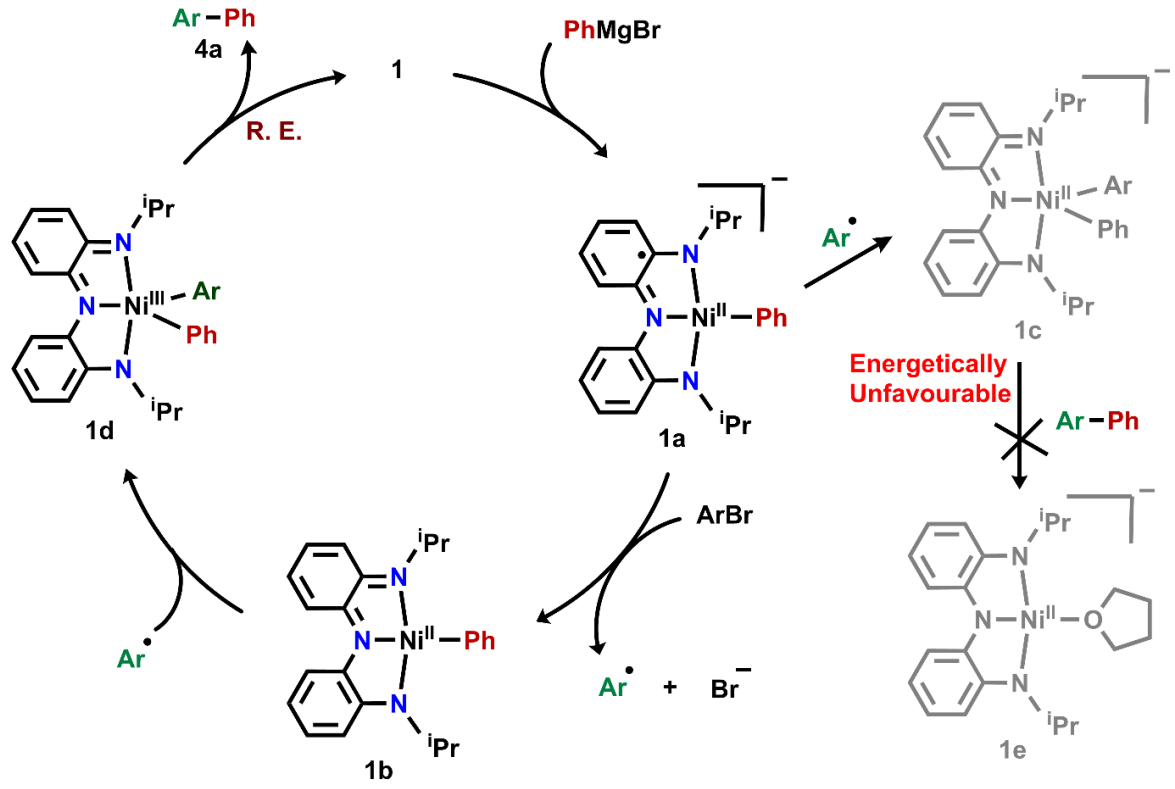

Scheme 2.6: Plausible mechanism for the reaction.

Taken all these considerations into account, the most plausible reaction pathway follows the aryl radical generation by SET and cage escape-rebound mechanism *en route* to the formation of a C–C bond. The entire process has been summarized in scheme 2.6. The pathway marked by grey shade follows the bimetallic oxidation addition that is less likely given all the evidences provided earlier. This example demonstrates an intriguing scenario where the ligand backbone

works in perfect co-operation with the metal center while the overall burden of the multielectron redox is very much shared by both.

2.7. Conclusion

In conclusion, we present an intriguing case of pincer- ligand's redox non-innocence that has been applied to C–C cross coupling catalysis. Despite the possibility of affording multielectron redox event on such a ligand motif, no straightforward catalytic example was demonstrated earlier that can prove efficient cooperation of the metal and the ligand to steer smooth functioning of the catalyst. In this work we were able to show how a 3d transition metal catalyst can be truly assisted by the ligand backbone, and the major redox processes can be facilitated by the redox reservoir property of the ligand ancillary. The presence of a crucial SET event to homolytic breaking of an aryl bromide bond and the one-electron oxidative addition onto nickel by extracting electron from the ligand backbone are two vital steps where ligand's redox participation is preeminent. This present example elegantly showcases the prowess of ligand redox noninnocence and how that can harness an efficient transformation. We do hope that more and more important catalytic reactions will start surfacing soon from many seemingly simple ligand motifs that have so far been utilized only as an ancillary.

2.8. Experimental Section

2.8.1. Materials

All reactions were carried out in flame dried glassware using air sensitive manipulations and glove box unless otherwise mentioned. Tetrahydrofuran (THF) and toluene were refluxed and freshly distilled over sodium/benzophenone and degassed using three freeze-pump-thaw cycles. Both solvents were stored over molecular sieves inside the glove box. All chemicals were purchased from Sigma-Aldrich, Avra, TCI, and GLR innovations. Deuterated solvents were purchased from Eurisotop. All chemicals were used as purchased until and unless mentioned. Progress of reactions was monitored by thin-layer chromatography using Merck 60 F_{254} precoated silica gel plate and visualized by short-wave ultraviolet light. Flash chromatography was performed with silica flash P60 silica gel (100–200 mesh).

2.8.2. Physical Measurements

All graphs are plotted using OriginPro 2021. ^{1}H and ^{13}C $\{^{1}H\}$ NMR spectra were recorded on a Bruker 400 MHz or 500 MHz spectrometer at 400/500 MHz and 101/126 MHz respectively. The residual solvent signals were taken as the reference ($CDCl_3$, 7.26 ppm for ^{1}H NMR spectra

and $CDCl_3$, 77.16 ppm for ^{13}C NMR spectra). The signals observed are described as: *s* (singlet), *d* (doublet), *t* (triplet), *q* (quartet), *m* (multiplets). All coupling constants were reported in hertz. High-resolution mass spectrometry was performed on Waters Synapt-G2S, with analyser configuration Q-ToF, ion mobility and analysed using Masslynx41. Crystals suitable for X-ray diffraction were mounted on a nylon loop in paratone oil. Diffraction data were collected using a Rigaku XtaLABmini Xray diffractometer equipped with a Mercury charge-coupled device detector and graphite monochromatic Mo Kα (λ = 0.71 Å) radiation source. For high-quality data, the crystals were cooled to 135 K with an Oxford Cryostream 700 system. The software SHELXT was used for diffractometer control, preliminary frame scans, indexing, orientation matrix calculations, least-squares refinement of cell parameters, and data collection. Data reduction and refinement was further processed using olex2. EPR spectra were recorded on Bruker EMX system. The X-band frequency was set at 9.43 GHz and the data was collected at a temperature of 77K. All reactions were carried out in flame-dried glassware using air sensitive manipulations and glove box unless otherwise mentioned. Tetrahydrofuran (THF) and toluene were refluxed and freshly distilled over sodium/benzophenone and degassed using three freeze-pump-thaw cycles. Both solvents were stored over molecular sieves inside the glove box. All chemicals were purchased from Sigma-Aldrich, Avra, TCI, and GLR innovations. Deuterated solvents were purchased from Eurisotop. All chemicals were used without further purification, unless specifically mentioned. Progress of reactions was monitored by thin-layer chromatography using Merck 60 F_{254} precoated silica gel plate and visualized by short-wave ultraviolet light. Flash chromatography was performed with silica flash P60 silica gel (100–200 mesh).

Density Functional Theory (DFT) was utilized as executed in the Gaussian09[50] quantum science program to do computational estimations. The geometry corresponding to their stationary points and transition states (TS) were optimized utilizing B3LYP functional[51,37], using a double-ζ basis set with the relativistic effective core potential of Hay and Wadt (LANL2DZ)[52, 53] for nickel and bromine elements, whereas for other elements (H, C, N, and O), 6-31G* basis set was used. The geometry optimizations were executed without introducing any symmetry constraints. Harmonic force constants were calculated at the obtained optimized geometries to characterize the stationary points as minima or first-order saddle points (TS). The harmonic vibrational frequencies determined the zero-point vibrational corrections to convert the total energies E^e to E^0. The rigid-rotor harmonic oscillator approximation evaluated the thermal and entropic contributions necessary to obtain the

enthalpies, H_{298} and Gibbs free energies, G_{298} at 298 K. To obtain accurate energies of the optimized structures, additional single point energy calculations of each optimized geometry were reevaluated using 6-311G* triple-ζ basis set[54] for atoms like H, C, N, and O. The solvent correction was done using the SMD (Solvent Model based on Density) introduced by Cramer, Marenich and Truhlar.[55]

2.8.3. Synthesis of NNN-Pincer Ligand[27]

(i) Synthesis of *Bis*(2-nitrophenyl) amine

In 100 mL round bottomed flask, 1-fluoro-2-nitrobenzene (0.9 g, 6.4 mmol), 2-nitroaniline (0.89 g, 6.4 mmol) and K_2CO_3 (1.09 g, 7.9 mmol) were dissolved in 10 mL of DMSO. The reaction mixture was stirred at a temperature of 120 °C for 36 h. The ice-chilled water (100 ml) was added to above reaction mixture and the mixture was extracted with dichloromethane (3 x 30 mL). The combined organic layer was washed with an aqueous solution of NaCl (4 x 20 mL, 15%) and dried over anhydrous $MgSO_4$. DCM was removed under a rotary evaporator. Bis(2-nitrophenyl) amine was obtained as an orange solid (1.51 g, 90%), which was used for the next step without further purification.

(ii) Synthesis of *Bis*(2-isopropylaminophenyl) amine

A 100 mL Schlenk flask equipped with a stir bar was charged with bis(2-nitrophenyl) amine (1.24 g, 4.3 mmol), Zn powder (3.712 g, 56.8 mmol) and NH_4Cl (2.78 g, 52 mmol). 40 mL of dry THF was added into the flask. A reflux condenser was attached to the Schlenk flask under N_2 flow. The reaction mixture was refluxed at a temperature of 65 °C for 16 h. At the completion of the reaction, the reaction mixture was filtered and the filtrate was removed under high vacuum to obtain yellow-brown oil. After that, yellow-brown oil was dissolved in 40 mL of degassed methanol under N_2 atmosphere. Acetone (0.64 mL, 8.6 mmol) and HCl (0.7 mL, 37%) were added to above reaction mixture. The reaction mixture immediately turned to green from brown on addition of HCl. It was stirred for 30 min at room temperature, followed by careful addition of $NaBH_3CN$ (1.14 g, 18.2 mmol) at a temperature of 0 ^{0}C. After complete addition of $NaBH_3CN$, the reaction mixture turned to reddish-brown from green. It was stirred for a further 12 h at room temperature. The solvent was removed under vacuum and the resulting residue was dissolved in 40 mL of dichloromethane. It was washed with an aqueous sodium dithionite (2 x 40 mL, 1 M) and aqueous sodium bicarbonate (2 x 40 mL, 1 M) solution respectively. The combined organic layers were dried over $MgSO_4$ and the solvent was

removed under vacuum. Bis(2-isopropylaminophenyl) amine (NNN pincer) was obtained as brown oil in 75% yield.

2.8.4. The Synthesis of $Ni_2(NNN)_2$ Dimer (1)

In a flame dried Schlenk flask, bis(2-isopropylaminophenyl) amine (NNN pincer) (57 mg, 0.2 mmol) was dissolved in 3 mL of dry toluene. The above solution was cooled to a temperature of -70 °C and ^{n}BuLi (0.4 mL of 1.6 M solution in hexane, 0.6 mmol) was added dropwise. The reaction mixture was stirred for 4 h at room temperature to obtain a yellow-colored precipitate. The solvent was removed under vacuum. Inside the glove box, the yellow solid was dissolved in dry THF and cooled to a temperature of -40 °C. A cold solution of $NiCl_2(THF)_{1.5}$ (25 mg, 0.2 mmol) was added to above reaction mixture. After 30 min stirring at room temperature, dark green colour solution was obtained. The flask was taken out from glove box and the reaction mixture was exposed to air. The dark green colored solution immediately turned into intense violet colour. THF was removed under rotary evaporator. The residue was dissolved in dichloromethane and filtered through celite bed. Dichloromethane was removed under vacuum and dark violet colour residue was obtained in 72% yield (98 mg). The crystal suitable for SC-XRD data was obtained from concentrate solution of violet residue in THF/pentane at -40 °C temperature.

2.8.5. Procedure for Optimization of Reaction Conditions

An overnight dried Schlenk flask was charged with 4-bromoanisole **2** (25 µL, 0.2 mmol), catalyst **1** (4 mg, 3 mol%) and 2 mL of dry THF under N_2 atmosphere to make a clear solution. The flask was kept at a temperature of -20 ° C. Phenylmagnesium bromide **3** (0.2 mL of 2 M solution in THF, 0.4 mmol) solution was added dropwise to the reaction mixture with continuous stirring maintaining the temperature at -20 °C. After the complete addition of phenylmagnesium bromide solution, the reaction mixture turned to brown from violet. After 12 h stirring at same temperature, the solvent was removed under vacuum. The crude reaction mixture was dissolved in DCM and organic layer was washed with water. The organic layer was collected and dried over anhydrous $MgSO_4$. DCM was removed using rotary evaporator. The yield of the desired product **4a** was determined by GC analysis.

2.8.6. General Procedure for Cross-Coupling Reaction

An overnight-dried Schlenk flask was charged with aryl halide (0.5 mmol), catalyst **1** (10 mg, 3 mol%) and 4 mL of dry THF under N_2 atmosphere to make a clear solution. The flask was kept at a temperature of -20 °C. Phenyl magnesium bromide (0.5 mL of 2 M solution in THF,

1.0 mmol) solution was added dropwise to the reaction mixture with continuous stirring maintaining the temperature at -20 °C. After the complete addition of phenyl magnesium bromide solution, the reaction mixture turned to brown from violet. After 12 h stirring at same temperature, the solvent of reaction mixture was removed under vacuum. The crude reaction mixture was dissolved in DCM and organic layer was washed with water. The organic layer was collected and dried over anhydrous $MgSO_4$. DCM was removed using rotary evaporator and the desired product was separated by column chromatography using hexane:ethylacetate mixture as eluent.

2.8.7. Procedure for Kinetic Analysis of Kumada Cross Coupling by 1

As per general procedure, the Schlenk flask was charged with 4-bromoanisole (126 µL, 1.0 mmol), **1** (20 mg, 3 mol%) and 10 mL of THF under N_2 atmosphere. The reaction mixture was kept at a temperature of -20 ° C. Phenylmagnesium bromide (1 mL of 2 M solution in THF, 2.0 mmol) was added dropwise to the reaction mixture. The aliquots of 100 µL were collected from the reaction mixture with some interval of time. The progress of the reaction was analysed by GC. The increasing product concentration **4a** (in % yield) was plotted with respect to the time (in min) and no product formation was observed for the first 40 minutes.

Next, a solution of **1** (3 mol%) in THF was heated at a temperature of 60 °C for 5 minutes and 4-bromoanisole (126 µL, 1.0 mmol) was added to that solution at room temperature. The addition of phenylmagnesium bromide (1 mL of 2 M solution in THF, 2.0 mmol) was performed at room temperature. The aliquots of 100 µL from reaction mixture were taken after some interval of time and the progress of the reaction was analysed by GC technique. The increasing product **4a** concentration (in % yield) was plotted with respect to the time (in min).

2.8.8. Procedure for Radical Trapping

As per general reaction procedure, an overnight dried Schlenk flask was charged with 4-bromoanisole (25 µL, 0.2 mmol), **1** (4 mg, 3 mol%), TEMPO (31 mg, 0.2 mmol) and 2 mL of dry THF under N_2 flow. The flask was kept at a temperature of -20 °C. Phenylmagnesium bromide (200 µL of 2 M solution in THF, 0.4 mmol) solution was added dropwise to the reaction mixture with continuous stirring maintaining the temperature at -20 °C. After 12 h stirring at same temperature, there was no formation of product **4a** as assayed by TLC. The TEMPO adduct of the trapped intermediate aryl radical (**5**) was detected by high-resolution

mass spectrometry (HRMS). **HRMS** (ESI, m/z) calcd. for $C_{16}H_{26}NO_2$ $[M+H]^+$: 264.1964; found: 264.1962.

2.8.9. Radical Clock and Solvent Cage Experiment

Following the optimized reaction condition, 1-bromo-2-(but-3-en-1-yl)benzene (105 mg, 0.5 mmol), **1** (10 mg, 3 mol %) and 2 mL THF was taken in Schlenk flask under N_2 atmosphere. The flask was kept at a temperature of -20 °C. Phenylmagnesium bromide (0.5 mL of 2.0 M solution in THF, 1.0 mmol) solution was added dropwise to the reaction mixture with continuous stirring maintaining temperature at -20 °C. After 12 h stirring at same temperature, the solvent of reaction mixture was removed under vacuum. The crude reaction mixture was dissolved in DCM and organic layer was washed with water. The organic layer was collected and dried over anhydrous $MgSO_4$. DCM was removed using rotary evaporator and the desired product was separated by column chromatography. Both the acyclic **(9**) and cyclic (**10**) product were characterized by ^1H and ^{13}C NMR spectroscopy.

For solvent cage experiment, the above radical clock experiment was repeated at different catalyst loading. The acyclic (**9**) and cyclic (**10**) was quantified by GC analysis. The ration of acyclic (**9**) and cyclic (**10**) product concentration was plotted with respect to increasing catalyst loading. The linear dependency of ratio of acyclic (**9**) and cyclic (**10**) product with catalyst loading was observed.

2.8.10. Spectroscopic Characterization of Cross Coupled Product Catalysed by 1

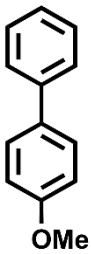

4-methoxy-1,1'-biphenyl (4a)[56]

The compound was purified by column chromatography (silica gel) with 1% mixture of ethyl acetate in hexane to give the product as a white solid (83.7 mg, 91%).

^{1}H NMR (400 MHz, $CDCl_3$) δ 7.56 (*s*, 4H), 7.44 (*s*, 2H), 7.32 (*s*, 1H), 7.00 (*d*, *J* = 8.7 Hz, 2H), 3.87 (*s*, 3H).

^{13}C NMR (101 MHz, $CDCl_3$) δ 159.2, 140.9, 133.9, 128.9, 128.3, 126.9, 114.3, 55.5.

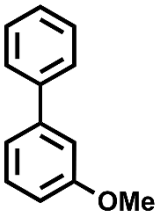

3-methoxy-1,1'-biphenyl (4b)[56]

The compound was purified by column chromatography (silica gel) with 1% mixture of ethyl acetate in hexane to give the product as a white solid (87.4 mg, 95%).

^{1}H NMR (400 MHz, $CDCl_3$) δ 7.60 (*d*, *J* = 7.4 Hz, 2H), 7.44 (*t*, *J* = 7.3 Hz, 2H), 7.36 (*s*, 2H), 7.19 (*d*, *J* = 7.6 Hz, 1H), 7.14 (*s*, 1H), 6.91 (*d*, *J* = 8.2 Hz, 1H), 3.87 (*s*, 3H).

^{13}C NMR (101 MHz, $CDCl_3$) δ 160.1, 142.9, 141.2, 129.9, 128.9, 127.6, 127.3, 119.8, 113.0, 112.8, 55.5.

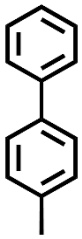

4-methyl-1,1'-biphenyl (4c)[56]

The compound was purified by column chromatography (silica gel) with hexane to give the product as a white solid (69.7 mg, 83%).

^{1}H NMR (500 MHz, $CDCl_3$) δ 7.60 – 7.56 (*m*, 2H), 7.51 – 7.47 (*m*, 2H), 7.43 (*dd*, *J* = 8.5, 7.0 Hz, 2H), 7.35 – 7.30 (*m*, 1H), 7.25 (*d*, *J* = 0.9 Hz, 1H), 7.03 (*dd*, *J* = 7.7, 1.1 Hz, 1H), 2.40 (*s*, 3H).

^{13}C NMR (126 MHz, $CDCl_3$) δ 141.3, 138.5, 137.2, 129.8, 129.6, 128.9, 127.1.

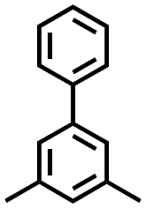

3,5-dimethyl-1,1'-biphenyl (4d)[56]

The compound was purified by column chromatography (silica gel) with hexane to give the product as a white solid (84.7 mg, 93%).

^{1}H NMR (500 MHz, $CDCl_3$) δ 7.59 (*d*, *J* = 8.3 Hz, 2H), 7.43 (*t*, *J* = 7.9 Hz, 2H), 7.34 (*t*, *J* = 7.3 Hz, 1H), 7.23 (*s*, 2H), 7.01 (*s*, 1H), 2.40 (*s*, 6H).

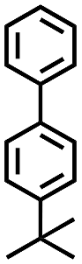

4-(tert-butyl)-1,1'-biphenyl (4e)[56]

The compound was purified by column chromatography (silica gel) with hexane to give the product as a white solid (94.6 mg, 90%).

^{1}H NMR (400 MHz, $CDCl_3$) δ 7.60 (*d*, *J* = 7.4 Hz, 2H), 7.54 (*t*, *J* = 6.3 Hz, 2H), 7.46 (*dd*, *J* = 13.9, 7.1 Hz, 4H), 7.34 (*q*, *J* = 8.3, 7.9 Hz, 1H), 1.37 (*s*, 9H).

^{13}C NMR (101 MHz, $CDCl_3$) δ 128.9, 128.8, 127.3, 127.2, 126.9, 126.8, 125.9, 125.8, 34.7, 31.5.

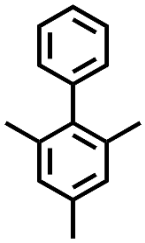

2,4,6-trimethyl-1,1'-biphenyl (4f)[56]

The compound was purified by column chromatography (silica gel) with hexane to give the product as a white solid (83.4 mg, 85%).

^{1}H NMR (400 MHz, $CDCl_3$) δ 7.47 (*t*, *J* = 7.4 Hz, 2H), 7.38 (*t*, *J* = 7.5 Hz, 1H), 7.20 (*d*, *J* = 6.7 Hz, 2H), 7.01 (*s*, 2H), 2.40 (*s*, 3H), 2.07 (*s*, 6H).

^{13}C NMR (101 MHz, $CDCl_3$) δ 141.2, 139.2, 136.7, 136.1, 129.4, 128.5, 128.2, 126.6, 21.2, 20.9.

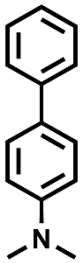

N,N-dimethyl-[1,1'-biphenyl]-4-amine (4g)[56]

The compound was purified by column chromatography (silica gel) with hexane to give the product as a white solid (74 mg, 75%).

^{1}H NMR (400 MHz, $CDCl_3$) δ 7.58 (*d*, *J* = 7.7 Hz, 2H), 7.53 (*d*, *J* = 8.1 Hz, 2H), 7.42 (*t*, *J* = 7.5 Hz, 2H), 7.29 (*d*, *J* = 7.5 Hz, 1H), 6.83 (*d*, *J* = 8.2 Hz, 2H), 3.02 (*s*, 6H).

^{13}C NMR (101 MHz, $CDCl_3$) δ 150.1, 141.3, 129.4, 128.8, 127.8, 126.4, 126.1, 112.9, 40.7.

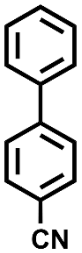

[1,1'-biphenyl]-4-carbonitrile (4h)[56]

The compound was purified by column chromatography (silica gel) with 1% ethyl acetate in hexane to give the product as a white solid (49 mg, 55%).

^{1}H NMR (400 MHz, $CDCl_3$) δ 7.73 (*d*, *J* = 7.8 Hz, 2H), 7.69 (*d*, *J* = 7.7 Hz, 2H), 7.59 (*d*, *J* = 7.2 Hz, 2H), 7.49 (*t*, *J* = 7.2 Hz, 2H), 7.44 (*d*, *J* = 6.7 Hz, 1H).

^{13}C NMR (101 MHz, $CDCl_3$) δ 145.8, 139.3, 132.7, 129.2, 128.8, 127.9, 127.4, 119.1, 111.0.

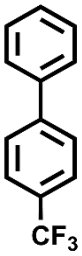

4-(trifluoromethyl)-1,1'-biphenyl (4i)[56]

The compound was purified by column chromatography (silica gel) with hexane to give the product as a white solid (76.6 mg, 69%).

^{1}H NMR (500 MHz, $CDCl_3$) δ 7.70 (*s*, 4H), 7.60 (*d*, *J* = 7.0 Hz, 2H), 7.48 (*t*, *J* = 7.5 Hz, 2H), 7.41 (*t*, *J* = 7.4 Hz, 1H).

^{13}C NMR (126 MHz, $CDCl_3$) δ 129.1, 128.3, 127.6, 127.4, 125.9, 125.9, 125.8, 125.8.

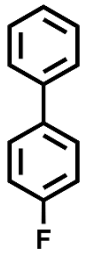

4-fluoro-1,1'-biphenyl (4j)[56]

The compound was purified by column chromatography (silica gel) with hexane to give the product as a white solid (39 mg, 45%).

^{1}H NMR (400 MHz, $CDCl_3$) δ 7.69 – 7.62 (*m*, 4H), 7.47 (*t*, *J* = 7.3 Hz, 2H), 7.37 (*t*, *J* = 7.3 Hz, 1H), 7.15 (*s*, 1H).

^{13}C NMR (101 MHz, $CDCl_3$) δ 140.8, 129.0, 127.6, 127.6, 127.5, 127.2, 115.9, 115.7.

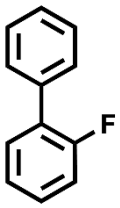

2-fluoro-1,1'-biphenyl (4k)[56]

The compound was purified by column chromatography (silica gel) with hexane to give the product as a white solid (49.9 mg, 58%).

^{1}H NMR (400 MHz, $CDCl_3$) δ 8.68 (*s*, 2H), 7.69 (*s*, 2H), 7.44 (*s*, 2H), 7.18 (*d*, *J* = 20.4 Hz, 3H).

^{13}C NMR (101 MHz, $CDCl_3$) δ 141.6, 140.7, 130.7, 130.0, 129.9, 128.0, 127.6, 127.4, 126.6, 123.4.

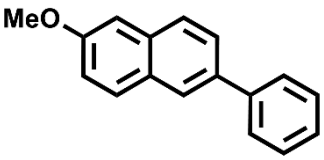

2-methoxy-6-phenylnaphthalene (4l)[57]

The compound was purified by column chromatography (silica gel) with 2% ethyl acetate in hexane to give the product as a white solid (107.8 mg, 92%).

^{1}H NMR (500 MHz, $CDCl_3$) δ 7.98 (*d*, *J* = 2.0 Hz, 1H), 7.81 (*t*, *J* = 8.0 Hz, 2H), 7.74 – 7.69 (*m*, 3H), 7.51 – 7.45 (*m*, 2H), 7.36 (*t*, *J* = 7.3 Hz, 1H), 7.20 – 7.15 (*m*, 2H), 3.95 (*s*, 3H).

^{13}C NMR (126 MHz, $CDCl_3$) δ 157.9, 141.3, 136.5, 133.9, 129.9, 129.3, 129.0, 127.4, 127.4, 127.2, 126.2, 125.8, 119.3, 105.7, 55.5.

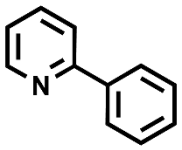

2-phenylpyridine (4m)[56]

The compound was purified by column chromatography (silica gel) with 2% ethyl acetate in hexane to give the product as a colorless oil (51.2 mg, 66%).

^{1}H NMR (400 MHz, $CDCl_3$) δ 8.70 (*d*, *J* = 4.6 Hz, 1H), 8.00 (*d*, *J* = 7.8 Hz, 2H), 7.74 (*d*, *J* = 6.3 Hz, 2H), 7.48 (*t*, *J* = 7.5 Hz, 2H), 7.42 (*t*, *J* = 7.0 Hz, 1H), 7.26 – 7.19 (*m*, 1H).

^{13}C NMR (101 MHz, $CDCl_3$) δ 157.6, 149.8, 139.5, 136.9, 129.1, 128.9, 127.0, 122.2, 120.7.

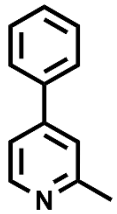

2-methyl-4-phenylpyridine (4n)[56]

The compound was purified by column chromatography (silica gel) with 2% ethyl acetate in hexane to give the product as a white solid (77.8 mg, 92%).

^{1}H NMR (500 MHz, $CDCl_3$) δ 8.53 (*d*, *J* = 5.2 Hz, 1H), 7.62 (*dd*, *J* = 8.2, 1.4 Hz, 2H), 7.51 – 7.45 (*m*, 2H), 7.43 (*d*, *J* = 7.2 Hz, 1H), 7.37 (*s*, 1H), 7.31 (*dd*, *J* = 4.9, 1.6 Hz, 1H), 2.62 (*s*, 3H).

^{13}C NMR (101 MHz, $CDCl_3$) δ 158.8, 149.5, 148.8, 138.4, 129.1, 129.0, 127.0, 121.3, 118.9, 24.5.

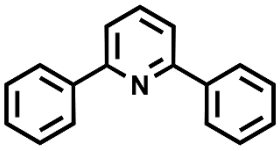

2,6-diphenylpyridine (4o)[58]

The compound was purified by column chromatography (silica gel) with hexane to give the product as a white solid (96 mg, 83%).

^{1}H NMR (500 MHz, $CDCl_3$) δ 8.16 (*d*, *J* = 7.0 Hz, 4H), 7.85 – 7.80 (*m*, 1H), 7.70 (*d*, *J* = 8.2 Hz, 2H), 7.51 (*t*, *J* = 7.5 Hz, 4H), 7.45 – 7.40 (*m*, 2H).

^{13}C NMR (126 MHz, $CDCl_3$) δ 157.0, 139.6, 137.6, 129.1, 128.8, 127.1, 118.8.

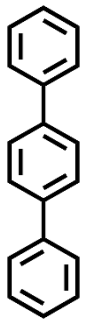

1,1':4',1''-terphenyl (4p)[56]

The compound was purified by column chromatography (silica gel) with hexane to give the product as a white solid (100.2 mg, 87%). **^{1}H NMR** (400 MHz, $CDCl_3$) δ 7.69 (*s*, 4H), 7.65 (*d*, *J* = 7.8 Hz, 4H), 7.47 (*t*, *J* = 7.6 Hz, 4H), 7.37 (*t*, *J* = 7.3 Hz, 2H).

^{13}C NMR (101 MHz, $CDCl_3$) δ 140.8, 140.2, 129.0, 127.6, 127.5, 127.2.

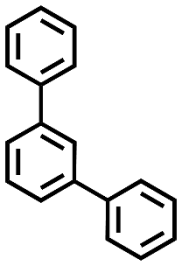

1,1':3',1''-terphenyl (4q)[58]

The compound was purified by column chromatography (silica gel) with hexane to give the product as a white solid (74.8 mg, 65%).

^{1}H NMR (500 MHz, $CDCl_3$) δ 7.82 (*t*, *J* = 1.6 Hz, 1H), 7.68 – 7.64 (*m*, 4H), 7.61 – 7.57 (*m*, 2H), 7.52 (*dd*, *J* = 8.3, 6.8 Hz, 1H), 7.50 – 7.44 (*m*, 4H), 7.41 – 7.36 (*m*, 2H).

^{13}C NMR (101 MHz, CDCl3) δ 141.9, 141.3, 129.3, 129.0, 127.6, 127.4, 126.3, 126.3.

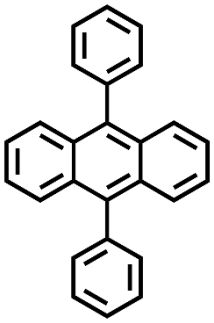

9,10-diphenylanthracene (4r)[59]

The compound was purified by column chromatography (silica gel) with hexane to give the product as a white solid (117.3 mg, 71%). **^{1}H NMR** (400 MHz, $CDCl_3$) δ 7.78 – 7.67 (*m*, 4H), 7.59 (*dd*, *J* = 15.3, 7.1 Hz, 6H), 7.49 (*d*, *J* = 6.9 Hz, 4H), 7.34 (*d*, *J* = 7.0 Hz, 4H). **^{13}C NMR** (101 MHz, $CDCl_3$) δ 139.2, 137.2, 131.5, 130.0, 128.6, 127.6, 127.1, 125.1.

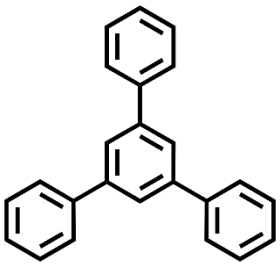

5'-phenyl-1,1':3',1''-terphenyl (4s)[60]

The compound was purified by column chromatography (silica gel) with hexane to give the product as a white solid (137.9 mg, 90%). **^{1}H NMR** (400 MHz, $CDCl_3$) δ 7.79 (*s*, 3H), 7.71 (*d*, *J* = 8.1 Hz, 6H), 7.49 (*t*, *J* = 7.4 Hz, 6H), 7.40 (*t*, *J* = 7.3 Hz, 3H).

^{13}C NMR (101 MHz, $CDCl_3$) δ 142.5, 141.3, 129.0, 127.7, 127.5, 125.3.

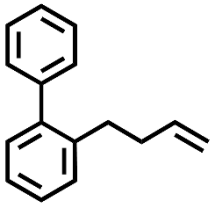

2-(but-3-en-1-yl)-1,1'-biphenyl (9)[61]

The compound was purified by column chromatography (silica gel) with hexane to give the product as a colorless oil (158.3 mg, 76%). **^{1}H NMR** (400 MHz, $CDCl_3$) δ 7.46 (*t*, *J* = 7.3 Hz, 2H), 7.38 (*dd*, *J* = 15.9, 7.1 Hz, 5H), 7.28 (*q*, *J* = 7.6, 6.0 Hz, 2H), 5.77 (*ddd*, *J* = 16.9, 10.6, 5.2 Hz, 1H), 5.00 – 4.89 (*m*, 2H), 2.79 – 2.67 (*m*, 2H), 2.26 (*q*, *J* = 7.1 Hz, 2H).

^{13}C NMR (101 MHz, $CDCl_3$) δ 142.1, 142.0, 139.4, 138.3, 130.2, 129.4, 129.3, 128.2, 127.5, 126.9, 125.9, 114.8, 35.3, 32.7.

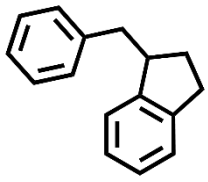

1-benzyl-2,3-dihydro-1H-indene (10)[62]

The compound was purified by column chromatography (silica gel) with hexane to give the product as a colorless oil (29.2 mg, 14%). **^{1}H NMR** (400 MHz, $CDCl_3$) δ 7.37 – 7.31 (*m*, 2H), 7.26 (*t*, *J* = 6.2 Hz, 4H), 7.23 – 7.14 (*m*, 3H), 3.53 – 3.44 (*m*, 1H), 3.19 (*dd*, *J* = 13.6, 5.7 Hz, 1H), 2.98 – 2.69 (*m*, 3H), 2.18 (*td*, *J* = 13.0, 7.9 Hz, 1H), 1.88 – 1.75 (*m*, 1H).

^{13}C NMR (101 MHz, $CDCl_3$) δ 147.0, 144.3, 141.0, 129.2, 128.4, 126.6, 126.1, 126.1, 124.7, 123.9, 46.6, 41.5, 32.1, 31.3.

2.9. References:

1. Bullock, R. M., *Catalysis Without Precious Metals*. Wiley Online Library: 2010; Vol. 15.
2. Bullock, R. M.; Chen, J. G.; Gagliardi, L.; Chirik, P. J.; Farha, O. K.; Hendon, C. H.; Jones, C. W.; Keith, J. A.; Klosin, J.; Minteer, S. D., Using Nature's Blueprint to Expand Catalysis with Earth-Abundant Metals. *Science* **2020,** *369* (6505), eabc3183.
3. Mingos, D. M. P., *The Periodic Table II: Catalytic, Materials, Biological and Medical Applications*. Springer Nature: 2020; Vol. 182.
4. Chirik, P. J.; Wieghardt, K., Radical Ligands Confer Nobility on Base-Metal Catalysts. *Science* **2010,** *327* (5967), 794-795.
5. Lyaskovskyy, V.; de Bruin, B., Redox Non-Innocent Ligands: Versatile New Tools to Control Catalytic Reactions. *ACS Catal.* **2012,** *2* (2), 270-279.
6. Kaim, W., The Shrinking World of Innocent Ligands: Conventional and Non-Conventional Redox-Active Ligands. Wiley Online Library: 2012.
7. Luca, O. R.; Crabtree, R. H., Redox-Active Ligands in Catalysis. *Chem. Soc. Rev.* **2013,** *42* (4), 1440-1459.
8. Praneeth, V. K.; Ringenberg, M. R.; Ward, T. R., Redox-Active Ligands in Catalysis. *Angew. Chem., Int. Ed.* **2012,** *51* (41), 10228-10234.
9. Singh, V.; Kundu, A.; Singh, K.; Adhikari, D., Redox Noninnocence of the Formazanate Ligand Applied to Catalytic Formation of *α*-Ketoamides. *Chem. Commun.,* **2022,** *58* (46), 6630-6633.
10. Smith, A. L.; Hardcastle, K. I.; Soper, J. D., Redox-Active Ligand-Mediated Oxidative Addition and Reductive Elimination at Square Planar Cobalt (III): Multielectron Reactions for Cross-Coupling. *J. Am. Chem. Soc.* **2010,** *132* (41), 14358-14360.
11. Pappas, I.; Treacy, S.; Chirik, P. J., Alkene Hydrosilylation Using Tertiary Silanes with α-Diimine Nickel Catalysts. Redox-Active Ligands Promote a Distinct Mechanistic Pathway from Platinum Catalysts. *ACS Catal.* **2016,** *6* (7), 4105-4109.
12. Bains, A. K.; Kundu, A.; Maiti, D.; Adhikari, D., Ligand-Redox Assisted Nickel Catalysis Toward Stereoselective Synthesis of (n+1)-Membered Cycloalkanes from 1,n-Diols with Methyl Ketones. *Chem. Sci.* **2021,** *12* (42), 14217-14223.
13. Bains, A. K.; Kundu, A.; Yadav, S.; Adhikari, D., Borrowing Hydrogen-Mediated N-Alkylation Reactions by a Well-Defined Homogeneous Nickel Catalyst. *ACS Catal.* **2019,** *9* (10), 9051-9059.

14. Singh, K.; S, V.; Adhikari, D., Visible Light Photoredox by a (ph,ArNacNac)$_2$Zn Photocatalyst: Photophysical Properties and Mechanistic Understanding. *Inorg. Chem. Front.* **2021,** *8* (8), 2078-2087.
15. Morales-Morales, D.; Jensen, C. G., *The Chemistry of Pincer Compounds*. Elsevier: 2011.
16. Press, L. P.; Kosanovich, A. J.; McCulloch, B. J.; Ozerov, O. V., High-Turnover Aromatic C–H Borylation Catalyzed by POCOP-Type Pincer Complexes of Iridium. *J. Am. Chem. Soc.* **2016,** *138* (30), 9487-9497.
17. Timpa, S. D.; Fafard, C. M.; Herbert, D. E.; Ozerov, O. V., Catalysis of Kumada–Tamao–Corriu Coupling by a (POCOP) Rh Pincer Complex. *Dalton Trans.* **2011,** *40* (20), 5426-5429.
18. Adhikari, D.; Mossin, S.; Basuli, F.; Huffman, J. C.; Szilagyi, R. K.; Meyer, K.; Mindiola, D. J., Structural, Spectroscopic, and Theoretical Elucidation of a Redox-Active Pincer-Type Ancillary Applied in Catalysis. *J. Am. Chem. Soc.* **2008,** *130* (11), 3676-3682.
19. Harkins, S. B.; Mankad, N. P.; Miller, A. J.; Szilagyi, R. K.; Peters, J. C., Probing the Electronic Structures of $[Cu_2(\mu\text{-}XR_2)]^{n+}$ Diamond Cores as a Function of the Bridging X Atom (X= N or P) and Charge (n= 0, 1, 2). *J. Am. Chem. Soc.* **2008,** *130* (11), 3478-3485.
20. Radosevich, A. T.; Melnick, J. G.; Stoian, S. A.; Bacciu, D.; Chen, C.-H.; Foxman, B. M.; Ozerov, O. V.; Nocera, D. G., Ligand Reactivity in Diarylamido/Bis (Phosphine) PNP Complexes of Mn $(CO)_3$ and Re $(CO)_3$. *Inorg. Chem.* **2009,** *48* (19), 9214-9221.
21. Belli, R. G.; Tafuri, V. C.; Joannou, M. V.; Roberts, C. C., d^0 Metal-Catalyzed Alkyl–Alkyl Cross-Coupling Enabled by a Redox-Active Ligand. *ACS Catalysis* **2022,** *12* (5), 3094-3099.
22. Peris, E.; Crabtree, R. H., Key Factors in Pincer Ligand Design. *Chem. Soc. Rev.*, **2018,** *47* (6), 1959-1968.
23. Lawrence, M. A.; Green, K.-A.; Nelson, P. N.; Lorraine, S. C., Pincer Ligands—Tunable, Versatile and Applicable. *Polyhedron* **2018,** *143*, 11-27.
24. Zell, T.; Milstein, D., Hydrogenation and Dehydrogenation Iron Pincer Catalysts Capable of Metal–Ligand Cooperation by Aromatization/Dearomatization. *Acc. Chem. Res.* **2015,** *48* (7), 1979-1994.
25. Gunanathan, C.; Milstein, D., Metal–Ligand Cooperation by Aromatization–Dearomatization: A New Paradigm in Bond Activation and "Green" Catalysis. *Acc. Chem. Res.* **2011,** *44* (8), 588-602.

26. Breitenfeld, J.; Ruiz, J.; Wodrich, M. D.; Hu, X., Bimetallic Oxidative Addition Involving Radical Intermediates in Nickel-Catalyzed Alkyl–Alkyl Kumada Coupling Reactions. *J. Am. Chem. Soc.* **2013,** *135* (32), 12004-12012.
27. Munhá, R. F.; Zarkesh, R. A.; Heyduk, A. F., Tuning the Electronic and Steric Parameters of a Redox-Active Tris(Amido) Ligand. *Inorg. Chem.* **2013,** *52* (19), 11244-11255.
28. Nguyen, A. I.; Blackmore, K. J.; Carter, S. M.; Zarkesh, R. A.; Heyduk, A. F., One-and Two-Electron Reactivity of a Tantalum(V) Complex with a Redox-Active Tris(amido) Ligand. *J. Am. Chem. Soc.* **2009,** *131* (9), 3307-3316.
29. Ananikov, V. P., Nickel: The "Spirited Horse" of Transition Metal Catalysis. *ACS Catal.* **2015,** *5* (3), 1964-1971.
30. Adhikari, D.; Mossin, S.; Basuli, F.; Dible, B. R.; Chipara, M.; Fan, H.; Huffman, J. C.; Meyer, K.; Mindiola, D. J., A Dinuclear Ni(I) System Having a Diradical Ni_2N_2 Diamond Core Resting State: Synthetic, Structural, Spectroscopic Elucidation, and reductive Bond Splitting Reactions. *Inorg. Chem.* **2008,** *47* (22), 10479-10490.
31. RoRsenkoetter, K. E.; Wojnar, M. K.; Charette, B. J.; Ziller, J. W.; Heyduk, A. F., Hydrogen-Atom Noninnocence of a Tridentate [SNS] Pincer Ligand. *Inorg. Chem.* **2018,** *57* (16), 9728-9737.
32. Joshi-Pangu, A.; Wang, C.-Y.; Biscoe, M. R., Nickel-Catalyzed Kumada Cross-Coupling Reactions of Tertiary Alkylmagnesium Halides and Aryl Bromides/Triflates. *J. Am. Chem. Soc.* **2011,** *133* (22), 8478-8481.
33. Galushko, A. S.; Prima, D. O.; Burykina, J. V.; Ananikov, V. P., Comparative Study of Aryl Halides in Pd-Mediated Reactions: Key Factors Beyond the Oxidative Addition Step. *Inorg. Chem. Front.* **2021,** *8* (3), 620-635.
34. Ogawa, H.; Minami, H.; Ozaki, T.; Komagawa, S.; Wang, C.; Uchiyama, M., How and Why Does Ni0 Promote Smooth Etheric C-O Bond Cleavage and C-C Bond Formation? A Theoretical Study. *Chem.–Eur. J.* **2015,** *21* (40), 13904-13908.
35. Borys, A. M.; Hevia, E., Diphenylacetylene Stabilised Alkali-Metal Nickelates: Synthesis, Structure and Catalytic Applications. *Dalton Trans.* **2023,** *52* (7), 2098-2105.
36. Bauer, G.; Wodrich, M. D.; Scopelliti, R.; Hu, X., Iron Pincer Complexes as Catalysts and Intermediates in Alkyl–Aryl Kumada Coupling Reactions. *Organometallics* **2015,** *34* (1), 289-298.
37. Becke, A. D., Density-Functional Thermochemistry. I. The Effect of the Exchange-Only Gradient Correction. *J. chem. Phys.* **1992,** *96* (3), 2155-2160.

38. Lee, C.; Yang, W.; Parr, R. G., Development of the Colle-Salvetti Correlation-Energy Formula into a Functional of the Electron Density. *Phys. Rev. B* **1988,** *37* (2), 785.
39. Breitenfeld, J.; Scopelliti, R.; Hu, X., Synthesis, Reactivity, and Catalytic Application of a Nickel Pincer Hydride Complex. *Organometallics* **2012,** *31* (6), 2128-2136.
40. Jones, G. D.; Martin, J. L.; McFarland, C.; Allen, O. R.; Hall, R. E.; Haley, A. D.; Brandon, R. J.; Konovalova, T.; Desrochers, P. J.; Pulay, P., Ligand Redox Effects in the Synthesis, Electronic Structure, and Reactivity of an Alkyl− Alkyl Cross-Coupling Catalyst. *J. Am. Chem. Soc.* **2006,** *128* (40), 13175-13183.
41. Bhunia, M.; Sahoo, S. R.; Shaw, B. K.; Vaidya, S.; Pariyar, A.; Vijaykumar, G.; Adhikari, D.; Mandal, S. K., Storing Redox Equivalent in the Phenalenyl Backbone Towards Catalytic Multi-Electron Reduction. *Chem. Sci.* **2019,** *10* (31), 7433-7441.
42. Vijaykumar, G.; Pariyar, A.; Ahmed, J.; Shaw, B. K.; Adhikari, D.; Mandal, S. K., Tuning the Redox Non-Innocence of a Phenalenyl Ligand Toward Efficient Nickel-Assisted Catalytic Hydrosilylation. *Chem. Sci.* **2018,** *9* (10), 2817-2825.
43. Kundu, A.; Dey, D.; Pal, S.; Adhikari, D., Pyrazole-Mediated C–H Functionalization of Arene and Heteroarenes for Aryl–(Hetero) Aryl Cross-Coupling Reactions. *J. Org.Chem.* **2021,** *86* (21), 15665-15673.
44. Zheng, B.; Tang, F.; Luo, J.; Schultz, J. W.; Rath, N. P.; Mirica, L. M., Organometallic Nickel(III) Complexes Relevant to Cross-Coupling and Carbon–Heteroatom Bond Formation Reactions. *J. Am. Chem. Soc.* **2014,** *136* (17), 6499-6504.
45. Lipschutz, M. I.; Tilley, T. D., Carbon–Carbon Cross-Coupling Reactions Catalyzed by a Two-Coordinate Nickel(II)–Bis (amido) Complex via Observable Ni^{I}, Ni^{II}, and Ni^{III} Intermediates. *Angew. Chem., Int. Ed.* **2014,** *126* (28), 7418-7422.
46. Tsou, T.; Kochi, J., Mechanism of Oxidative Addition. Reaction of Nickel(0) Complexes With Aromatic Halides. *J. Am. Chem. Soc.* **1979,** *101* (21), 6319-6332.
47. Breitenfeld, J.; Wodrich, M. D.; Hu, X., Bimetallic Oxidative Addition in Nickel-Catalyzed Alkyl–Aryl Kumada Coupling Reactions. *Organometallics* **2014,** *33* (20), 5708-5715.
48. Zhu, D.; Budzelaar, P. H., Binuclear Oxidative Addition of Aryl Halides. *Organometallics* **2010,** *29* (22), 5759-5761.
49. Velian, A.; Lin, S.; Miller, A. J.; Day, M. W.; Agapie, T., Synthesis and C− C Coupling Reactivity of a Dinuclear Ni^{I}– Ni^{I} Complex Supported by a Terphenyl Diphosphine. *J. Am. Chem. Soc.* **2010,** *132* (18), 6296-6297.

50. Frisch, M. J.; Trucks, G. W.; Schlegel, H. B.; Scuseria, G. E.; Robb, M. A.; Cheeseman, J. R.; Scalmani, G.; Barone, V.; Petersson, G. A.; Nakatsuji, H.; Li, X.; Caricato, M.; Marenich, A.V.; Bloino, J.; Janesko, B.G.; Gomperts, R.; Mennucci, B.; Hratchian, H.P.; Ortiz, J.V.; Izmaylov, A.F.; Sonnenberg, J.L.; Williams-Young, D.; Ding, F.; Lipparini, F.; Egidi, F.; Goings, J.; Peng, B.; Petrone, A.; Henderson, T.; Ranasinghe, D.; Zakrzewski, V.G.; Gao, J.; Rega, N.; Zheng, G.; Liang, W.; Hada, M.; Ehara, M.; Toyota, K.; Fukuda, R.; Hasegawa, J.; Ishida, M.; Nakajima, T.; Honda, Y.; Kitao, O.; Nakai, H.; Vreven, T.; Throssell, K.; Montgomery, Jr., J.A.; Peralta, J.E.; Ogliaro, F.; Bearpark, M.J.; Heyd, J.J.; Brothers, E.N.; Kudin, K.N.; Staroverov, V.N.; Keith, T.A.; Kobayashi, R.; Normand, J.; Raghavachari, K.; Rendell, A.P.; Burant, J.C.; Iyengar, S.S.; Tomasi, J.; Cossi, M.; Millam, J.M.; Klene, M.; Adamo, C.; Cammi, R.; Ochterski, J.W.; Martin, R.L.; Morokuma, K.; Farkas, O.; Foresman, J.B.; Fox, D.J. *Gaussian, Inc., Wallingford CT,* **2009**.
51. Becke, A. D., Density-Functional Thermochemistry. III. The Role of Exact Exchange. *J. chem. Phys.* **1993,** *98* (7), 5648-5652.
52. Hay, P. J.; Wadt, W. R., Ab Initio Effective Core Potentials for Molecular Calculations. Potentials for the Transition Metal Atoms Sc to Hg. *J. chem. Phys.* **1985,** *82* (1), 270-283.
53. Wadt, W. R.; Hay, P. J., Ab Initio Effective Core Potentials for Molecular Calculations. Potentials for Main Group Elements Na to Bi. *J. chem. Phys.* **1985,** *82* (1), 284-298.
54. Weigend, F.; Ahlrichs, R., Balanced Basis Sets of Split Valence, Triple Zeta Valence and Quadruple Zeta Valence Quality for H to Rn: Design and Assessment of Accuracy. *Phys. Chem. Chem. Phys.* **2005,** *7* (18), 3297-3305.
55. Marenich, A. V.; Cramer, C. J.; Truhlar, D. G., Universal Solvation Model Based on Solute Electron Density and on a Continuum Model of the Solvent Defined by the Bulk Dielectric Constant and Atomic Surface Tensions. *J. Phys. Chem. B,* **2009,** *113* (18), 6378-6396.
56. Liu, Z.; Wang, P.; Chen, Y.; Yan, Z.; Chen, S.; Chen, W.; Mu, T., Small Organic Molecules with Tailored Structures: Initiators in the Transition-Metal-Free C–H Arylation of Unactivated Arenes. *RSC Adv.* **2020,** *10* (25), 14500-14509.
57. Lamola, J. L.; Moshapo, P. T.; Holzapfel, C. W.; Maumela, M. C., Evaluation of P-Bridged Biaryl Phosphine Ligands in Palladium-Catalysed Suzuki–Miyaura Cross-Coupling Reactions. *RSC Adv.* **2021,** *11* (43), 26883-26891.

58. Thimma Sambamoorthy, M.; Rengan, R.; Jan Grzegorz, M., Efficient Construction of C–C bonds From Aryl Halides/Aryl Esters with Arylboronic Acids Catalysed by Palladium(II) Thiourea Complexes. *Appl Organometal Chem.* **2019,** *33* (12), e5181.
59. Talukder, M. M.; Cue, J. M. O.; Miller, J. T.; Gamage, P. L.; Aslam, A.; McCandless, G. T.; Biewer, M. C.; Stefan, M. C., Ligand Steric Effects of α-Diimine Nickel(II) and Palladium(II) Complexes in the Suzuki–Miyaura Cross-Coupling Reaction. *ACS omega* **2020,** *5* (37), 24018-24032.
60. Sun, Y.; Li, T., Fabrication and Application of Graphene Supported Diimine-Palladium Complex Catalyst for Organic Synthesis. *ChemistrySelect* **2020,** *5* (4), 1431-1438.
61. Uchiyama, N.; Shirakawa, E.; Hayashi, T., Single Electron Transfer-Induced Grignard Cross-Coupling Involving Ion Radicals as Exclusive Intermediates. *Chem. Commun.***2013,** *49* (4), 364-366.
62. Zhou, B.; Sato, H.; Ilies, L.; Nakamura, E., Iron-Catalyzed Remote Arylation of Aliphatic C–H Bond via 1, 5-Hydrogen Shift. *ACS Catal.* **2018,** *8* (1), 8-11.

Chapter 3

Part - A

Unexplored Facet of Pincer Ligands: Super-Reductant Behavior Applied to Transition-Metal-Free Catalysis

A part of this work has been published in JACS Au ***2023****, 3,* 1213−1220

3.1. Introduction

Pincers, a class of ligands affording tridentate coordination, have probably reached an iconic status in inorganic and organometallic chemistry.[1–3] Since the origin of organometallic complexes by tridentate coordination of pincer ligands in the late 1970s, it has witnessed a meteoric rise and has expanded its versatile applicability.[4–6] This category of ligands is extremely attractive due to their extensive modularity and tunability.[7] Furthermore, the ligand's robust chelating ability arises from the central coordinating motif. For example, pyridine would be lost under monodentate coordination mode, while it becomes reliably coordinated, as a part of the pincer backbone. Because of the rigid coordination architecture, sometimes, transition metal complexes bearing a pincer offer remarkable thermal stability, a property that is very much admirable in homogeneous catalysis affording molecular transformation at higher temperatures.[8–10] Having all these characteristics, pincers have been exploited to coordinate majority of metals ranging from the main group, transition metals to lanthanides[11] across the periodic table. Moreover, metal ligand cooperativity by designer pincers has been extensively exploited by Milstein's group to develop a large number of bifunctional homogeneous catalysts.[12,13]

Furthermore, pincers often enjoy extensive electron delocalization over multiple aromatic rings, which in turn decreases its highest occupied molecular orbital−lowest unoccupied molecular orbital gap. This property facilitates predominantly ligand-based filled and empty orbitals to participate in redox processes under mild potential. Such features allow further redox tuning in the pincer backbone by minor modifications. Many pincers can shuttle between multiple redox states, accessing properties akin to redox reservoirs (Scheme 3.1).[14] Recently, such properties have also been utilized by Heyduk in advancing chemistry at the metal center where the electrons are mostly provided by the pincer ligand backbone.[15,16] Scrutinizing the three stable redox states separated by one-electron processes, it was theorized that electron transfer catalysis might be possible by free ligands, (NNN)H_3 (**1**) itself, without further assistance of the metal (Scheme 3.1b). NNN pincer backbone was selected that has been used earlier by Heyduk because of its ready access to the trianionic form.[14] The electron-rich nature of the symmetric NNN pincer in its fully deprotonated trianionic form may make it moderately reducing. However, the reducing property can be considerably amplified if the molecule is excited by shining visible light. The conjugated nature of the diarylamido backbone helps in further light absorption within the visible range of electromagnetic spectra so that the excitation of the pincer becomes fully feasible under mild conditions. Leveraging this favorable

redox, the trianionic pincer has been harnessed in electron transfer catalysis and the results show that such a pincer can function as a super-reductant, a facet that has never been interrogated.

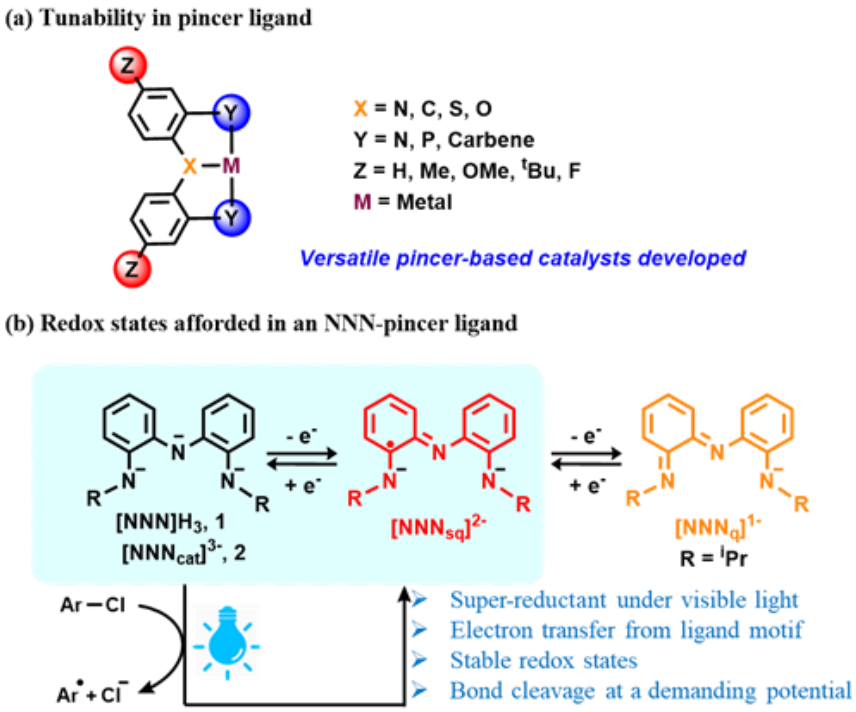

Scheme 3.1: Scope for Pincer Ligand's Non-innocence.

Examples of direct participation of pincers *via* electron transfer reactions from the ligand's backbones to promote molecular transformations are limited. In this chapter, such an electron transfer reaction from the pincer backbone without any assistance of transition metals has been disclosed. Much intriguingly, the trianionic NNN-pincer (**2**) under visible light excitation is super-reducing species that can reductively cleave even a C−Cl bond in *p*-methoxy chlorobenzene ($E_{o\ red} = -2.90$ V vs SCE).[17] It is further shown that this unprecedented electron transfer catalysis by pincer can forge a plethora of value-added heterocyclic products from substituted chlorobenzenes. However, to the best of our knowledge there is no report for such type of reactions using NNN pincer under mild photochemical conditions.

3.2. Results and Discussion

To demonstrate the pincer's electron transfer ability, the trianionic NNN-pincer (**2**) was chosen so that the parent *tris*amido and its one-electron oxidized iminosemiquinonate form can be accessed readily. The stability of both redox states avoiding any detrimental bond cleavage in the pincer's backbone ensures this proposed redox to be viable.

3.2.1. Synthesis of Trianionic NNN-Pincer 2

Towards this direction the $(NNN)H_3$, **1** can be synthesised as described in chapter 2 section 2.2.1. by following the literature procedures.[14] The parent *tris*amido form can be obtained by abstracting three protons from $(NNN)H_3$, **1** by KO^{t}Bu under inert conditions (Scheme 3.2).

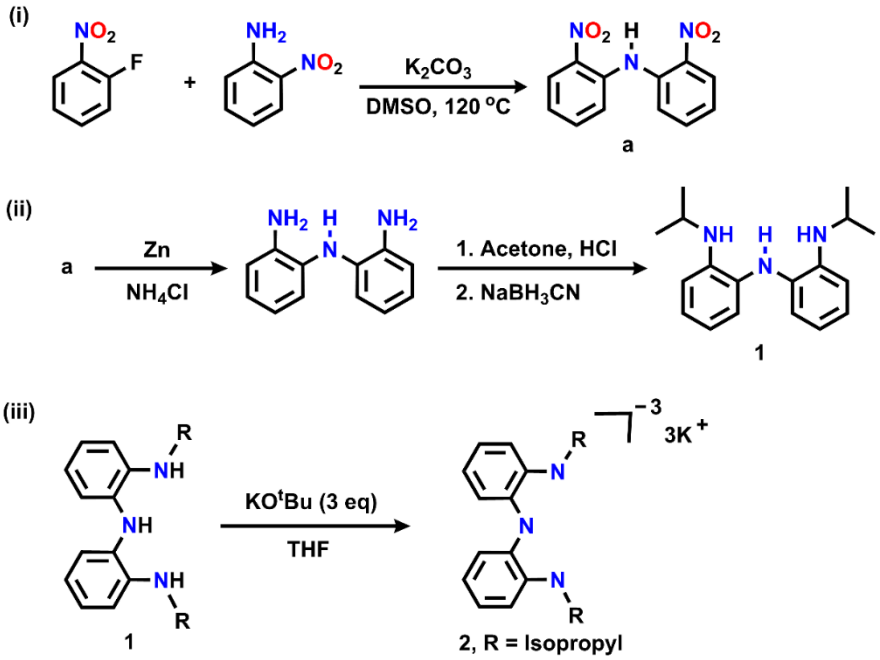

Scheme 3.2. Synthesis of $(NNN)H_3$ **1** and trianionic NNN-pincer **2**.

3.2.2. Characterization of Trianionic NNN-Pincer (2) and Single Electron Oxidised form of 2

The characterization of **2** and single electron oxidised form of **2** is essential to gain insight into the electronic structure, fate of catalyst and mechanism of reaction. Even **2** is extremely sensitive to moisture and air, appropriate physical studies were done to depict the photophysical properties. Fortunately, one electron oxidised form of **2** was detected by spectroelectrochemical EPR. Parallelly, some theoretical studies have been performed to justify the presented hypothesis.

3.2.2.1. Cyclic Voltammetry Experiment

As can be anticipated, the trianionic backbone can be oxidized at an extremely mild potential. To interrogate the electrochemical behavior of **2**, a cyclic voltammetry experiment was performed. The cyclic voltammetry analysis of the trianion **2** exhibits the first reversible oxidation wave at −0.25 V vs Fc^+/Fc couple. A second quasi-reversible oxidation was further observed at +0.04 V (vs Fc^+/Fc), (Figure 3.1). For the sake of comparison, the first oxidation

potential was converted to SCE which is found to be 0.13 V.[18] Such a mild potential indicates easy oxidation and promises the molecule to be a potent reductant.

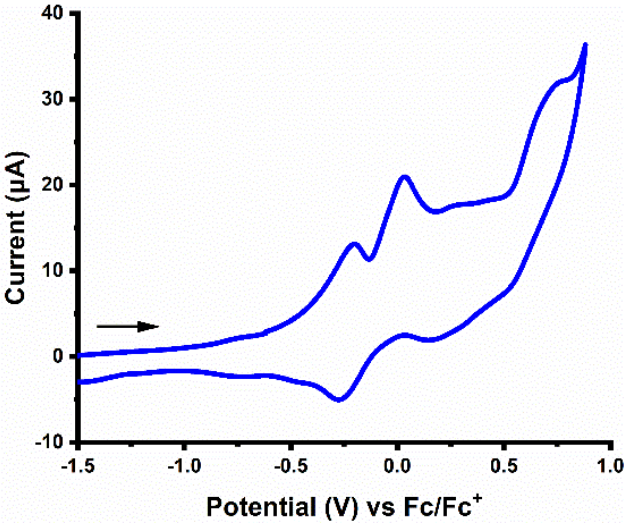

Figure 3.1. CV of 1 mM of **2** in THF along with 0.1 M solution of tetrabutyl-ammonium hexafluorophosphate salt as an electrolyte. The scan rate was 100 mVs^{-1} for the measurement.

3.2.2.2. Absorption and Emission Analysis of 2

It was envisaged that this reductive behavior can be tremendously augmented once the molecule is excited with visible light. Fascinatingly, the diaryl amido linkage absorbs significantly in the visible range of electromagnetic spectra. Having the possibility of photoexcitation of the pincer **2**, its redox and basic photochemical properties were investigated to delve into photophysical properties.

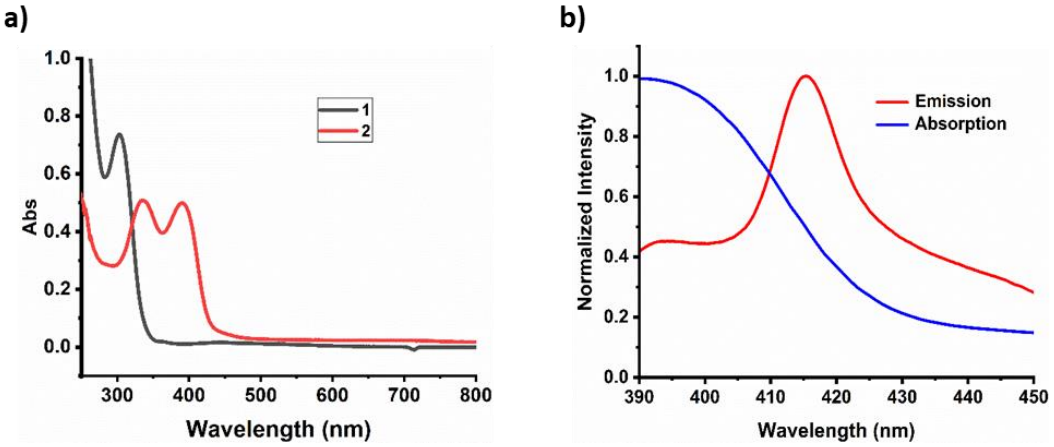

Figure 3.2. a) UV-Visible analysis of **1** and **2**. **b)** Normalized absorption and emission spectra of **2**.

Upon scrutinizing through UV-Visible spectroscopy, it was observed that the molecule **1** showed one absorption maximum at 320 nm. On the other hand, the molecule **2** absorbs at 335 and 392 nm, and the second maximum is connected to broad absorption up to 455 nm (Figure 3.2a). Furthermore, **2** is photoactive and shows an emission band at 415 nm (Figure 3.2b), when excited at a wavelength of 380 nm. The molecule is brightly fluorescing and this trait makes it propitious as a photocatalyst.

3.2.2.3. Excited State Lifetime Measurement and Average Lifetime Calculations of 2

However, efficient electron transfer from the excited state requires the same to be relatively long-lived.[19] To determine the excited state lifetime for **2**, a time-correlated single photon counting (TCSPC) measurement was performed. The decay of the fluorescence intensity was fitted with a tri-exponential function (χ^2 = 1.24) and the average fluorescence lifetime of the fluorophore was calculated as 10.2 ns (Figure 3.3). The moderately long lifetime further assures the electron transfer to be fully feasible from its excited state.[20]

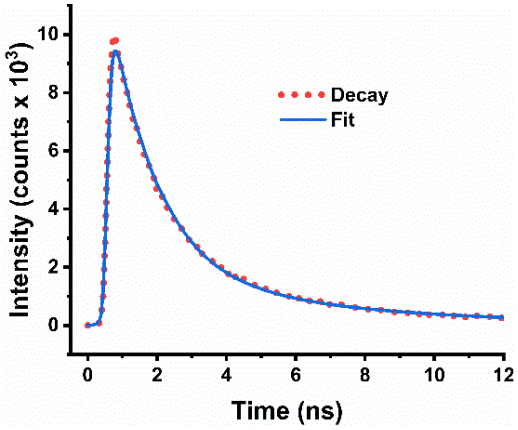

Figure 3.3: Tri-exponential fit of TCSPC data of **2** collected at its emission maxima, when excited with a 380 nm laser pulse. Data were recorded in dry and degassed THF using 1% ludox as the probe.

3.2.2.4. Calculation of Excited-State Oxidation Potential of 2

This set of photophysical data also helps us to calculate the excited-state oxidation potential of **2**. The excitation energy ($E_{o,o}$) of the molecule was estimated as 3.03 eV as derived from the intersection point of absorption and fluorescence spectral data (409 nm, Figure 3.3). Accordingly, the excited-state oxidation potential by the Relm−Weller equation[21] can be calculated as:

$$E^*_{ox} = E_{ox} - E_{0,0}$$

$$E^*_{ox} = 0.13 - (3.03) = -2.90 \text{ V vs SCE}$$

Such a large negative value of the excited-state oxidation promises the molecule to be an extremely strong photoreductant and will be able to reductively cleave the difficult-to reduce bonds.[22]

3.2.2.5. Spectroelectrochemical EPR Experiment

Since electron removal from the *bis*amido form will generate the iminosemiquinonate form, some spectroscopic signature for this redox state is required to prove this transformation. The detection of one-electron oxidized form of **2** will generate further credence for such electron transfer, on which a catalytic process can be built. Along this direction, a spectroelectrochemical EPR experiment (at −40 °C) was performed, which resulted in the detection of a complex pattern with a central g-value of 2.0043 (Figure 3.4). Moreover, the experimentally observed spectrum was successfully simulated considering the two nitrogen atoms which can be hyperfine-coupled having coupling parameters to be 11 and 6 MHz, respectively. From this spectroelectrochemical experiment, it appears that the radical in the iminosemiquinonate form is more centered in one of the arylamido rings.

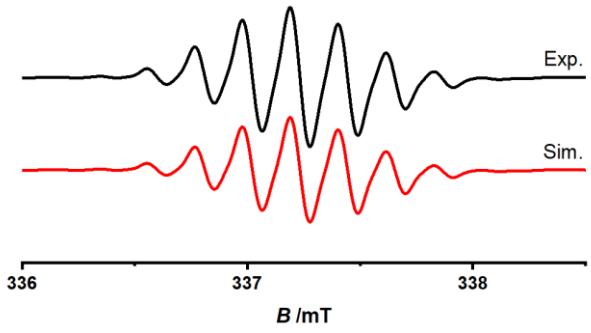

Figure 3.4. X-band (9.46 GHz) EPR signal for iminosemiquinonate form of **2** collected at -40 ˚C.

3.2.2.6. Computational Analysis

Though rather surprising, the same picture is quite reproducible from high-level DFT calculations. The iminosemiquinonate form of **2** was optimized at the M06-2X/6-31G* level of theory[23] and was analyzed further to trace the locus of the unpaired spin. Gratifyingly, the spin density calculation on the monooxidized product depicts the excess spin to be delocalized on one of the aryl amido rings (Figure 3.5).

It was discovered that the lack of a complete delocalization onto the second ring may stem from the distortion of one aryl unit from the other aryl ring of the *bis*arylamido motif. In closer inspection, the two aryl rings are distorted out of plane at least by 18° to avoid the steric clash

of *ortho* hydrogens at the two aryl units. In essence, detection of the one-electron oxidized product from **2** strongly supports the fact that the electron-rich trianionic backbone can facilitate electron transfer and generate a reasonably stable intermediate form.

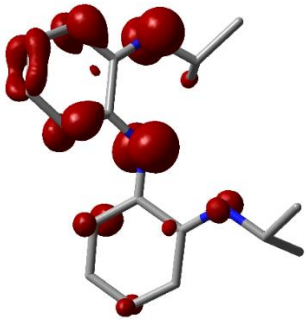

Figure 3.5. Excess α-spin density distribution for the same, calculated using the M06-2X/6-31G* level of theory (iso value 0.004 (e $bohr^{-3}$)$^{1/2}$).

3.3. Catalytic Reactions

To explore the promised super-reducing behavior for the trianionic NNN pincer ligand **2**, a substituted chlorobenzene was chosen as a model substrate, where the reductive cleavage of the C−Cl bond poses a significant challenge.[24] Sometimes, such bond cleavages demand drastic conditions of using UV light[25,26] that is carcinogenic. The C−Cl bond is very difficult to cleave primarily owing to its bond strength and demands for a strong negative reduction potential.[27] The approach of generating a super-reducing excited state is very much suitable for the activation of carbon−halogen bonds in aryl chlorides for the following reasons:

(a) Aryl chlorides do not absorb in visible light so that direct excitation is not possible.

(b) Their high reduction potentials are beyond the domain of many readily available and extremely popular photocatalysts such as $[Ru(bpy)_3]^{2+}$, $Ir(ppy)_3$, and $[Ir\text{-}(ppy)_2(dtbbpy)]^+$.[28]

(c) Strong carbon-halogen bonds and their two-step bond dissociation kinetics can deter very good electron donors to cleave the bond requiring longer reaction times.[29]

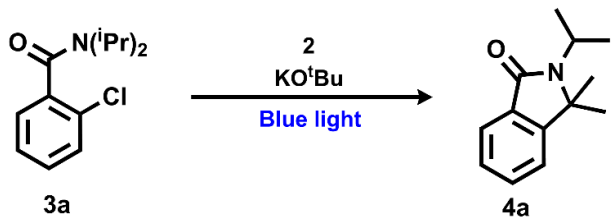

Scheme 3.3. The isoindolinone ring formation reaction catalysed by **2**.

To prove that **2** can perform productively under visible light excitation, 2-chloro-*N*,*N*-dialkylbenzamide was selected as a model substrate so that reductive cleavage of the aryl chloride bond can lead to the construction of an isoindolinone ring (Scheme 3.3).[30]

Upon extensive optimization, it was revealed that 5 mol% of the catalyst **1** can convert the chloro-substituted benzamide into the corresponding isoindolinone in 95% gas chromatography (GC) yield, with the use of 2 equivalent of base KO^{t}Bu (Table 3.1). Other bases such as DABCO and K_2CO_3 are completely ineffective, while NaO^{t}Bu affords the product in 55% yield (Table 3.1, entry 5-7). Significant reduction in yield when NaO^{t}Bu is used as a base indicates the possible role of a counter cation on the reaction.

Table 3.1. Optimization of reaction conditions.

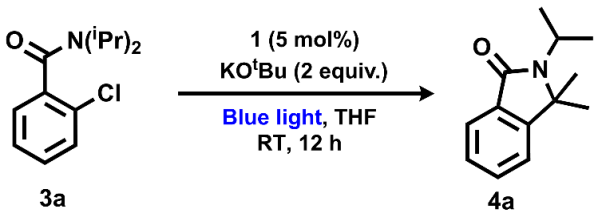

Entry	Variation from standard conditions	% Yield[b]
1	**None**	**95(91)[c]**
2	2 mol% of **1**	55
3	1.0 equiv of KO^{t}Bu	63
4	1.5 equiv of KO^{t}Bu	77
5	DABCO instead of KO^{t}Bu	Trace
6	K_2CO_3 instead of KO^{t}Bu	ND
7	NaO^{t}Bu instead of KO^{t}Bu	55
8	In white light	49
9	Absence of light	ND
10	Absence of **1**	ND
11	Absence of KO^{t}Bu	ND

Standard conditions: (a) 2- chloro-*N*,*N*-diisopropylbenzamide (0.2 mmol), KO^{t}Bu (0.4 mmol), **1** (5 mol%), and dry THF (1 mL), room temperature under a N_2 atmosphere, blue LEDs (450 nm), 12 h. [b]GC yields, [c]Isolated yield. ND = not detected.

It is notable that during this reaction, **2** is formed in situ by the deprotonation of the protonated precursor **1** so that stringent inert condition handling of **2** can be safely avoided. Instead, packing the bench-stable **1** in the reaction flask and purging the solution with nitrogen

are adequate. The optimization further discloses that blue light is the most suitable photon source, while white light gives a lower yield of the product. The reaction is completed within 12 h of reaction time. Separate experiments in absence of light, catalyst **1**, and base prove that all these components are critical for the success of the reaction. Among different solvents, THF remains ideal. Isoindoline formation is an ideal demonstration of C(sp^2)-H functionalization using photoredox processes which is a nice alternative to classical transition-metal catalyzed C−H bond activation by concerted metalation and deprotonation.[31−33] To ensure that the reaction is not facilitated by adventitious transition metals, we performed the reaction in new glassware along with an unused stir bar. The product yield was very much reproducible under such test reactions. Attempts to detect any trace metal contamination in the used KO^{t}Bu also resulted in negative observations.

3.4. Scope and Synthetic Utility of Cyclization Reaction Catalyzed by Catalyst 1

3.4.1. Scope of Intramolecular C−H Arylation of *o*-Chloro-*N*,*N*-dialkylarylamides

Having the optimized condition in hand, the scope of the reaction was tested. The substrate 2-chloro-*N*-isopropyl-*N*-alkylbenzamide (**3a**) reacted selectively to result *N*-isopropyl isoindolinone ring **4a** in very high, 92% isolated yield (Table 3.2). Further substrate scope expansion facilitated the formation of **4b–4d** in high yields of products where the substitution of nitrogen was changed. Notably, the reaction is very selective to the activation of the isopropyl group connected to nitrogen sparing methyl or even benzyl groups. As will be discussed in the following section, this stems from the stability of the tertiary carbon radical that results from the hydrogen atom abstraction from isopropyl C−H. Methyl substitutions at the benzamide ring were tolerant to the reaction condition so that isoindolinone **4e** and **4f** can be forged in 82−93% isolated yields. Interestingly, a halide substituent like fluoride also afforded the respective isoindolinone **4g** in 80% isolated yield.

Electron-donating methoxy substituents were examined further which afforded 5,6-dimethoxy-*N*-isopropyl isoindolinone, **4h** in 76% yield. More sophisticated isoindolinone architectures can also be fabricated by this method as two heterocycles **4i** and **4j** were synthesized in very high, 93% yields. If the nitrogen substituents in the benzamide are cyclohexyl rings, the appropriate C−H functionalization affords the spirocyclic product **4k** in 90% yield. Notably, such spirocyclic isoindolinone is a valuable heterocyclic motif that can improve lipophilicity, aqueous solubility, and metabolic stability.[34] Finally, a heterocyclic ring pyridine was examined as a substrate that afforded the corresponding cyclized product **4l** in

92% yield. The high yield of products in reasonable reaction time makes pincer **1** a rival for the iridium photocatalyst that was utilized earlier to forge isoindolinone under photothermal reaction conditions.[35] Further advantage of our method over the previous iridium-based protocol is that high temperature is not a need.

Table 3.2. Scope of Intramolecular C−H Arylation of *o*-Chloro-*N*,*N*-dialkylarylamides.

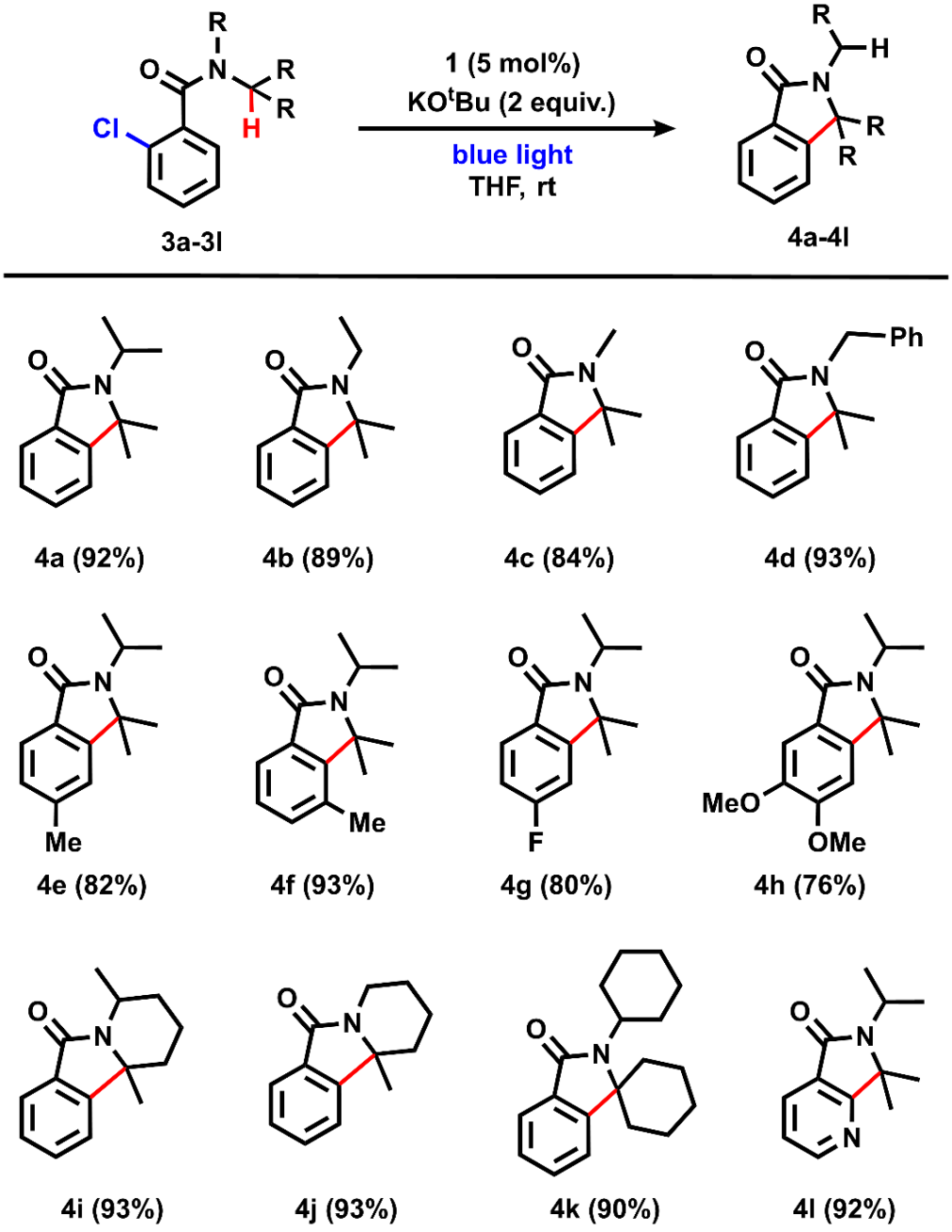

Reaction conditions: substituted *o*-Chloro-*N*,*N*-dialkylarylamides (1 equiv.), Catalyst **1** (5 mol%), KO^{t}Bu (2 equiv.), THF, Blue light, rt, 12 h, isolated yields are reported.

3.4.2. Scope of Intramolecular C−H Arylation of *N*-(*o*-chloroaryl)-*N*-methylalkylamide

After this, *N*-substituted *o*-chloroanilide was examined as a potent substrate so that a C−Cl bond can be cleaved and the subsequent cyclization can lead to value added oxindoline rings. The oxindole framework bearing a tetrasubstituted carbon center at the 3-position is regarded as a privileged motif that is often found in the core of a large class of bioactive natural products

Table 3.3. Scope of intramolecular C−H Arylation of *N*-(*o*-chloroaryl)-*N*-methylalkylamide.

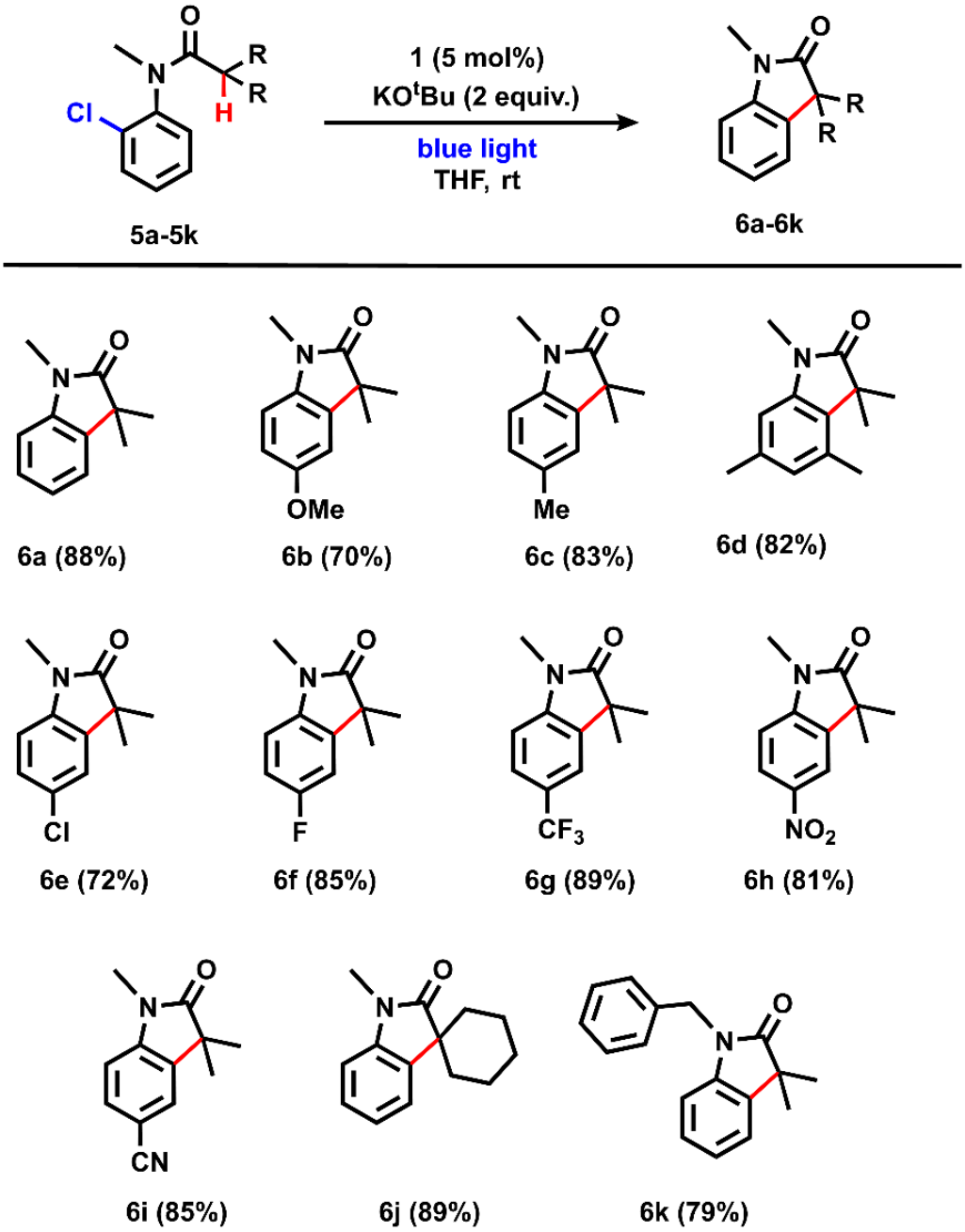

Reaction conditions: substituted *N*-(*o*-chloroaryl)-*N*-methylalkylamide (1 equiv.), Catalyst **1** (5 mol%), KO^{t}Bu (2 equiv.), THF, Blue light, rt, 12 h, isolated yields are reported.

as well as pharmaceutically important compounds.[36–38] Accordingly, *o*-anilide arylchloride was tested under the same reaction conditions to afford 3,3-dimethyloxindole **6a** in 88% yield (Table 3.3). Electron donating, methoxy or methyl substituents in the *o*-anilide aryl ring survived well through the reaction conditions to furnish products **6b−6d** in 70−83% yields. Notably, synthesis of 3,3-dialkyloxindole was earlier attempted from the aryl iodide substrate, where a precious metal photocatalyst *fac*-Ir(ppy)$_3$ was employed.[39] In case of 2,4-dichloroanilide molecules, the *o*-chloro group was selectively cleaved to provide **6e** in 72% yield. Likewise, highly electron-withdrawing trifluoromethyl group afforded 89% yield of the oxindole **6g**. Interestingly, a nitro substituent in the aryl ring was tolerant to the reaction condition and prepared the heterocycle **6h** in 81% yield. Pharmaceutically important spirocycle **6j** and *N*-benzylatedoxindole **6k** were also obtained by this method in excellent yields.

3.4.3. Cross-Coupling Reaction of Aryl Chlorides

The visible-light-induced radical reaction has to date been limited to suitably activated haloarenes possessing a C(sp^2)-X bond adjacent to a π-system, such as *α*-carbonyl, benzyl, or heteroatoms (halogen, oxygen).[40–42] To examine the full potential of the highly reducing excited state of **2**, a few unactivated aryl chlorides were chosen. To this end, it was examined a recalcitrant *p*-methoxy arylchloride whose reduction potential challenges even the class of very reducing photocatalysts.[43]

Accordingly, different unactivated chlorobenzene substrates were chosen and used for C−C cross-coupling reactions with benzene. As shown in Table 3.4, a plethora of biphenyl motifs[44,45] were synthesized following the photochemical process. Firstly, chlorobenzene was tested that provided targeted biphenyl **9a** in 72% yield (Table 3.4). Most notably, a highly challenging *p*-methoxy chlorobenzene whose reduction potential to cleave the C−Cl bond is demanding −2.90 V vs SCE was examined that afforded the respective biphenyl **9b** in 69% yield. On the other hand, chlorobenzene containing methyl and nitrile group at para position provided **9c** and **9d** in 63% and 75% respectively. When nitrile group was placed at the ortho position of chlorobenzene not much deviation in the yield of respective biphenyl **9e** was observed, 72% yield. Other polycyclic aromatic halides, like 2-chloronaphthalene provided **9f** in 72% yield. Interestingly, 9,10-dichloro anthracene was an effective coupling partner so that two phenyl groups can be easily installed at the respective positions to give 9,10- diphenyl anthracene **9g** in 71% yield. A pyridyl ring was tolerant to the reaction condition to afford product **9h** in moderate, 66% yield. Additionally, aryl chlorides involving thiophene and *N*-

methyl pyrrole as substrates afforded the C−C cross-coupled product **9i–9l** in 69−81% yields. The three different classes of the reaction, starting from varying strengths of aryl chloride bonds, attest the tremendous reducing power of the excited **2** and to steer subsequent ring cyclization or cross-coupling reactions.

Table 3.4. Cross-coupling Reaction of Benzene, *N*-Methylpyrrole and Thiophene with Aryl Chlorides

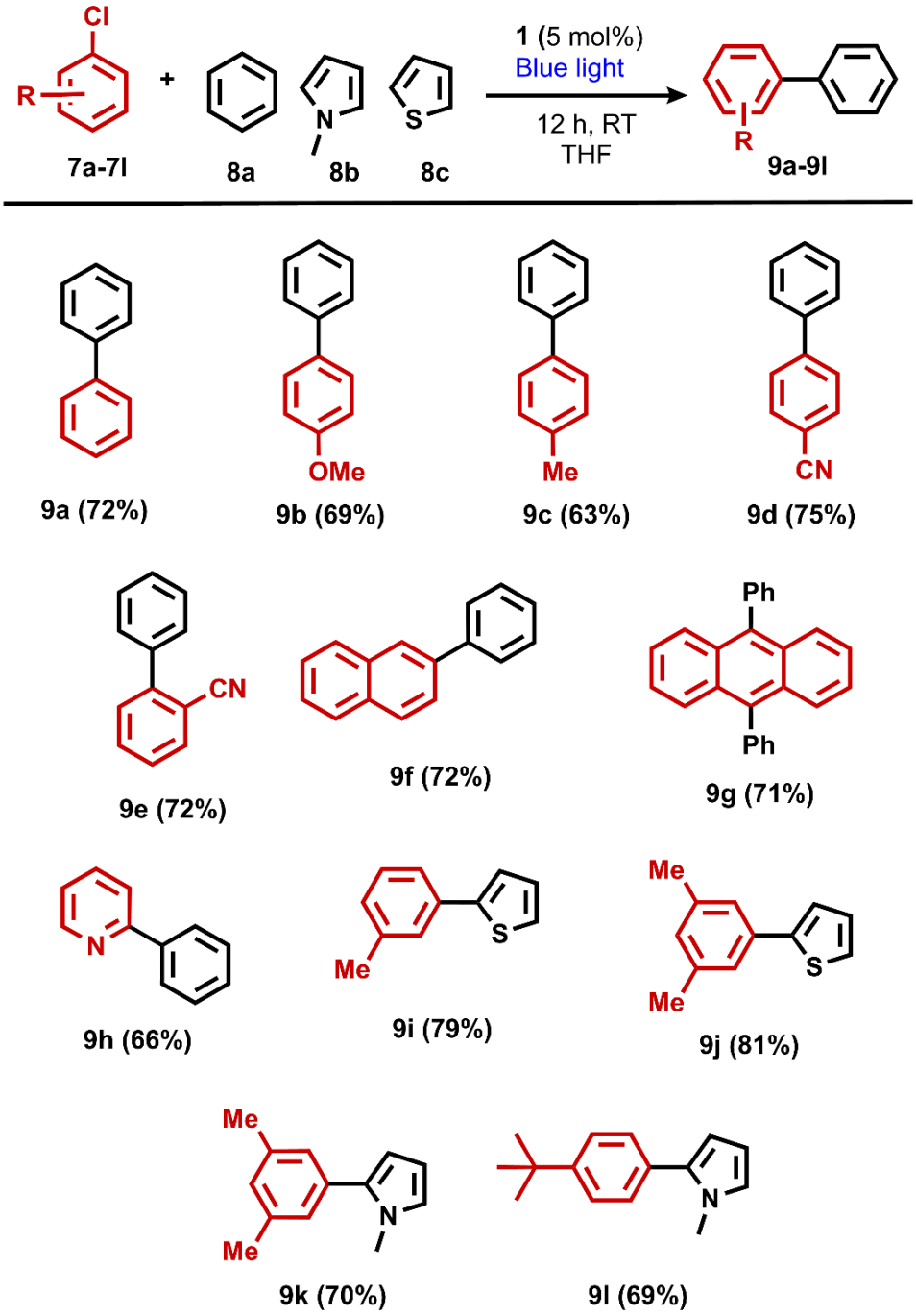

Reaction conditions: substituted *Chlorobenzene* (1 equiv.), Catalyst **1** (5 mol%), KO^{t}Bu (2 equiv.), **8a/8b/8c** (10 equiv.), THF, Blue light, rt, 12 h, isolated yields are reported.

3.5. Mechanistic Insights and Control Experiments

3.5.1. Radical Quenching Experiment and Intermediate Trapping

As the reaction involves radicals, a radical quenching experiment was performed with TEMPO. As expected, the reaction completely shuts down upon addition of TEMPO in 1.0 equivalent. Moreover, as a compelling evidence to the aryl radical generation, *p*-OMe aryl radicals were successfully intercepted as its TEMPO adduct (Scheme 3.4). The adduct was detected by high-resolution mass spectrometry showing its signature at 264.1962 amu.

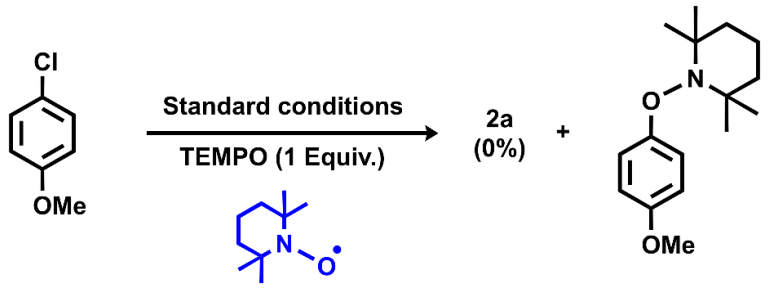

Scheme 3.4. Tapping of intermediate using TEMPO radical.

3.5.2. Stern-Volmer Experiment

As already discussed, the highly reducing excited state of **2** (having E_{ox}^{*} = −2.90 V vs SCE) is capable of cleaving an unactivated C−Cl bond of aryl chloride. To unambiguously prove that the electron transfer happens at the excited state of **2**, a Stern−Volmer luminescence quenching experiment was performed. Gratifyingly, fluorescence intensity of the photocatalyst gradually decreased with increasing concentration of aryl chloride and such a decrease generated a clear straight-line pattern from the Stern−Volmer plot (Figure 3.6).

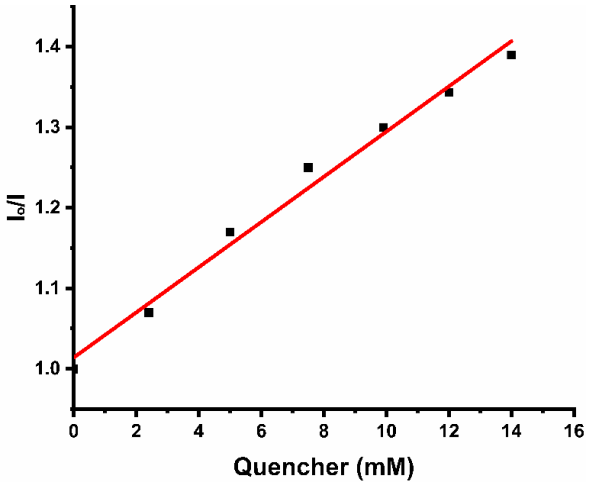

Figure 3.6. Stern–Volmer plot for electron transfer from **2*** to the 2-chloro-*N*-isopropyl-*N*-alkylbenzamide.

3.5.3. Electron Transfer Rate Constant Calculations

Incorporating the lifetime of the fluorophore, that has been measured earlier, the electron transfer rate as 2.74×10^{9} M^{-1} s^{-1} was calculated. The electron transfer rate constant suggests the process to be only limited by diffusion of the quencher and the fluorophore. In comparison, a previous photocatalyst $CzEPAIPN^{\cdot-}$ transfers electron to aryl chloride at a rate of 1.5×10^{7} M^{-1} s^{-1}.[22] When compared, the electron transfer rate in our chosen pincer backbone is two orders of magnitude faster that also likely reflects in the reduced reaction time (12 h).

3.6. Plausible Mechanistic Cycle under Photoexcitation

Taken the photophysical and redox properties of the photocatalyst molecule together, the reaction mechanism for the annulation reaction upon C−H functionalization has been delineated here. The photoexcitation of **2** prompts the electron transfer to rupture the C−Cl bond, generating an aryl radical. It is expected that losing one electron from the system will generate a dianionic radical, which is moderately stable that likely reflects in its extremely mild first oxidation potential. Notably, the electron transfer from the pincer backbone is reminiscent of Murphy's super electron donors, although those worked under stoichiometric conditions.[46,47]

The radical anion of Ar−Cl dissociates into an aryl radical, which undergoes a 1,5-hydrogen atom transfer (HAT) process.[48−50] In general, the 1,5-HAT processes are favored over 1,6-HAT because of their optimum chair like six membered cyclic transition state, thus favoring the annulation in this mode.[51] The newly generated alkyl radical **11** after HAT attacks the aryl ring to generate an intermediate **12** (Scheme 3.5.). In the presence of a strong base $KO^{t}Bu$, deprotonation can pursue to leave a radical anion of this species which is a strong reductant to give the electron back to the iminosemiquinonate form of the photocatalyst to bring back the *bis*amido form. Therefore, the facile redox interconversion between *bis*amido and iminosemiquinonate helps run the catalytic cycle.

It is also notable that **2** essentially pushes the limit of accessible reduction potential to break the electron rich aryl chloride bond. Earlier important discoveries including sensitization-induced electron transfer (SenI-ET)[52] or consecutive photoinduced electron transfer (ConPET)[53] have been attempted to break strong bonds. Although conceptually seminal, majority of the ConPET catalysts effectively cleaved electron-poor aryl chlorides.[54] In this report, it has been shown that a simple anionic pincer can strategically reach such a limit upon visible light excitation.

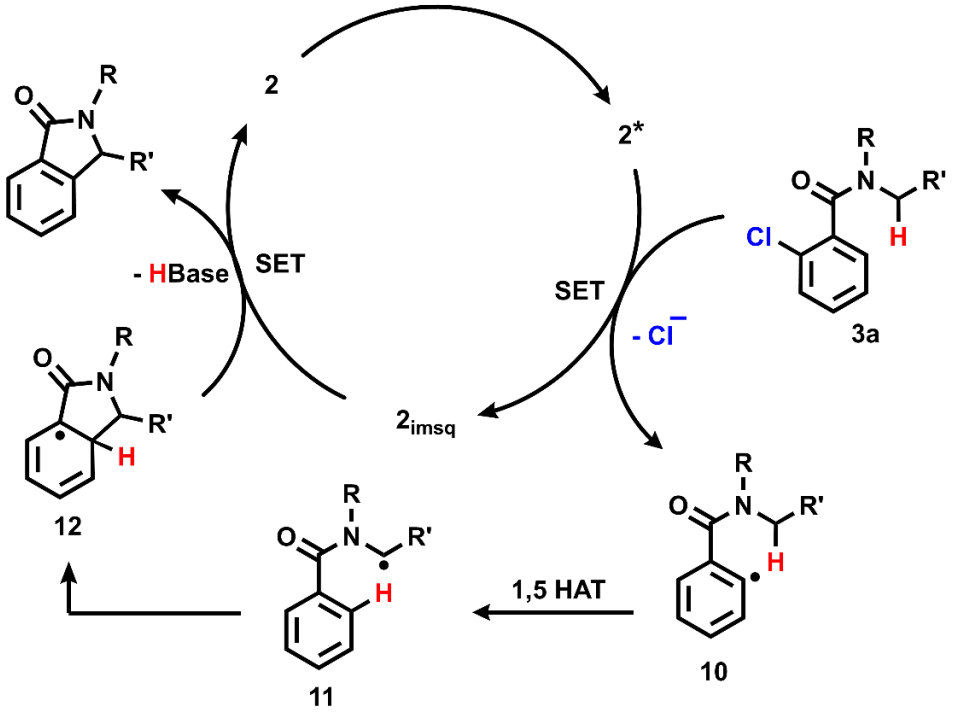

Scheme 3.5. Plausible mechanistic cycle under photoexcitation.

3.7. Fate of Catalyst 2 During or After the Reactions

Further a curious question raised in our mind that what about the fate of the pincer photocatalyst and whether such radical generation in the backbone may lead to an *N*-isopropyl bond cleavage. Such bond rupture would be detrimental to the catalyst longevity. To analyse such situation, at the end of the reaction and standard work-up, the solution was analyzed through GC−MS, the protonated pincer backbone was identified. This observation indicates that catalyst molecules remain intact at the end of the cycle. However, the challenging separation of the catalyst from the homogeneous solution mixture and our inability to quantify the amount of protonated ligands does not completely refute some possibility of the *N*-alkyl bond cleavage.

3.8. Conclusions

In summary, we have unraveled a completely new aspect of a trianionic pincer ligand, where the electron-rich pincer steers electron transfer to substrate molecules. This is a rare report where the NNN pincer backbone can drive a strong bond cleavage and subsequent C−H functionalization without any assistance of a transition metal ion. The excited state of the molecule can be easily reached by shining blue light upon it. The molecule is an extreme photoreductant that is capable of reductively cleaving even very electron-rich aryl halides, essentially pushing the limit of a strong bond cleavage. Following this protocol, we have synthesized a wide array of benzannulated rings under mild reaction conditions and short

reaction times. This reduction became possible due to the easy access of the two redox states by the pincer, whose important intermediate form has been detected spectroscopically. We believe that direct redox participation of many such ligands will surface in future where their redox properties can be modulated by shining visible light and a tremendous amount of chemistry can be developed even under metal-free conditions.

3.9. Experimental Section

3.9.1. Methods and Materials

All operations were carried out in flame-dried glassware using a N_2- gas-filled glovebox or high-vacuum standard Schlenk techniques under a nitrogen gas atmosphere unless mentioned otherwise. THF was refluxed and freshly distilled over sodium/benzophenone and degassed using three freeze−pump−thaw cycles. Starting materials and reagents were purchased from commercial sources and used without further purification. Tetrabutylammonium hexafluorophosphate ($TBAPF_6$) was recrystallized from hot ethanol and ferrocene was purified by sublimation before its use in cyclic voltammetry (CV) experiments. Progress of reactions was monitored by thin-layer chromatography using a Merck 60 F254 precoated silica gel plate and visualized by short-wave ultraviolet light. Flash chromatography was performed with Silica Flash P60 silica gel (100−200 mesh).

3.9.2. Instrumentation and Physical Measurements

Absorption spectra were recorded using a LAB-INDIA UV/Vis Spectrophotometer UV 3000 in a UV cuvette of path length 10 mm fitted with a cap. The graphs are plotted using Originpro8. ^1H and $^{13}C\{^1H\}$ NMR spectra are recorded on a Bruker 400 MHz spectrometer at the frequencies of 400 and 101 MHz, respectively. All chemical shifts are reported in parts per million (ppm) with respect to the ^1H (residual) chemical shifts of the *d*-solvent. The residual solvent signals are taken as the reference ($CDCl_3$, 7.26 ppm for ^1H NMR spectra and $CDCl_3$, 77.16 ppm for ^{13}C NMR spectra). The signals observed are described as *s* (singlet), *d* (doublet), *t* (triplet), *q* (quartet), and *m* (multiplets). All coupling constants were reported in Hertz (Hz). High-resolution mass spectroscopy was performed on Waters Synapt-G2S, analyzer configuration Q-ToF with ion mobility and analyzed using Masslynx41. Cyclic voltammetry experiments were performed on a Keithley 2450 potentiostat. For the measurement, the electrode setup consisted of a glassy carbon working electrode, a Pt wire as the counter electrode, and Ag/Ag^+ (3 M KCl) as the reference electrode. Emission spectra were collected

by a Fluoromax-4 (Horiba Jobin Yvon, NJ) spectrofluorophotometer. The analyte solution was placed in a quartz cuvette equipped with a screw cap having a path length of 10 mm.

Caution! The glovebox and high vacuum Schlenk line should be used with great care and safety. THF distillation setup contains sodium metal, which is very reactive metal to air and moisture and well-known for their explosive nature. Therefore, these types of setups must be used in a limited quantity and handled with care and safety.

3.9.3. Synthesis of Trianoinic NNN^{3-} Ligand (2)

In a flame dried Schlenk flask, *bis*(2-isopropylaminophenyl) amine (**1**) (57 mg, 0.2 mmol) was dissolved in 3 mL of dry THF. The above solution was cooled to a temperature of 0 °C and KO^tBu (68 mg, 0.6 mmol) was added. The reaction mixture was stirred for 4 h at room temperature to obtain a yellow-colored solution. The reaction mixture was filtered through celite bed inside the glove box. The solvent was removed under vacuum. The potassium salt of trianoinic NNN^{3-} (**2**) was obtained as yellow-colored solid in 88% yield.

3.9.4. Cyclic Voltammetry Experiment for 2

Voltammetry experiments were performed on CHI-610 electrochemical workstation from CH Instruments (USA). A homogeneous solution of **2** (1 mM) along with 0.1 M solution of tetrabutyl-ammonium hexafluorophosphate salt as an electrolyte was prepared in dry and degassed THF. For the measurement, the three-electrode setup consisted of a glassy carbon working electrode, a Pt-wire as counter electrode, and an Ag/AgCl (1M KCl) as the reference electrode was inserted inside the above solution. The CV spectrum was recorded at a scan rate of 100 mVs^{-1} for the measurement.

3.9.5. UV-Visible Measurements

A homogeneous solution was prepared by suspending a finely ground sample of **1** and **2** in dry and degassed THF at room temperature. The UV-Visible spectrum of the resulting solutions was recorded with the help of a LAB-INDIA UV/VIS Spectrophotometer UV 3000 in an UV-cuvette of path length 10 mm fitted with cap.

3.9.6. Time-Correlated Single Photon Counting (TCSPC) Experiment Details for 2

Condition	Dry and degassed THF
τ_1	2.67 ns
τ_2	5.34 ns

τ_3	10.68 ns
χ^2	1.24

Average excited state lifetime was calculated using equation 1.

$$\tau = \frac{\sum_{i=1}^{n} \alpha_i \tau_i^2}{\sum_{i=1}^{n} \alpha_i \tau_i} \quad \text{……. (eq. 1)}$$

where α_i and τ_i denote the amplitude fractions and lifetimes respectively and n is the number of lifetime components. For catalyst **2**, with amplitude fractions $\alpha_1 = 4.12\times10^{-2}$, $\alpha_2 = 0.20\times10^{-2}$, $\alpha_3 = 18.02\times10^{-2}$ and their respective lifetime contribution; $\tau_1 = 2.67$ ns, $\tau_2 = 5.34$ ns, $\tau_3 = 10.68$ ns. Using equation 1, the average lifetime was found to be 10.2 ns.

3.9.7. Details of Spectroelectrochemical EPR Experiment

The spectroelectrochemistry is an important technique where electrochemically generated transient species can be interrogated by an array of spectroscopic techniques. Kaim and Fiedler have written a fantastic tutorial review on this topic for the curious readers.[55] The spectroelectrochemical EPR cell consists of a three-electrode assembly with a narrow teflon-coated Pt wire as a working electrode, a naked Pt wire as counter electrode and a coated Ag wire as pseudo reference electrode. The working electrode was coated with a teflon tube with a coated and uncoated diameter of 0.18 and 0.13 mm, respectively to prevent seepage of solvent. The entire assembly is then placed in a standard quartz tube with an electrolyte solution to be used in a Magnettech MS-5000 device. Approximately 1 cm of the bottom of the coated Pt-working electrode was stripped and positioned vertically at the lowest point of the tube so that the redox species of interest is generated at the bottom and well separated from the counter electrode. The narrow diameter of the electrodes allows very little to negligible diffusion of the electrogenerated species, while the teflon-coating helps to prevent any short-circuiting. Three narrow electrodes were soldered to a three-core wire attached to a hollow Teflon tube, which is then sealed with an O-ring and collet to allow measurements at low-temperatures. The potential of the cell is controlled by the Autolab potentiostat PGSTAT101. The spectra of the electrogenerated species of interest were recorded at regular intervals. To ensure efficient electrolysis, final spectra were collected after about 30 minutes.

EPR spectra at X-band frequency (ca. 9.5 GHz) were obtained with a Magnettech MS-5000 benchtop EPR spectrometer equipped with a rectangular TE 102 cavity. The measurements were carried out in synthetic quartz glass tubes. For EPR spectroelectrochemistry, a three-electrode setup was employed using two teflon-coated platinum wires (0.005" bare, 0.008" coated) as working (or a teflon-coated gold wire (0.003" bare, 0.0055" coated) as working electrode) and platinum as counter electrode and a teflon-coated silver wire (0.005" bare, 0.007" coated) as *pseudo*-reference electrode. The low temperature EPR-experiment was performed at -40 °C under constant flow of liquid nitrogen.

3.9.8. ICP-MS Analysis for KO^{t}Bu to Evaluate Metal Contamination

This analysis was conducted on iCAP RQ instrument. The contents of transition metal elements (Pd, Fe, Co, Ni and Cu) were found to be less than detection limit (0.1 ppm).

Table 3.5: ICP-MS analysis on the contents (in ppm) of transition metals in KO^{t}Bu

Entry	Metals	contents (in ppm)
1	Palladium	ND
2	Iron	0.165
3	Cobalt	ND
4	Nickel	ND
5	Copper	ND

ND: Not detected

Additionally, KO^{t}Bu from different commercial sources such as Alfa Aesar, Sigma Aldrich, TCI were used in a new set of glassware. In all cases, the yield of the reaction was reproducible under standard reaction conditions. These results strongly suggest that the reaction is not catalyzed by the adventitious presence of transition metals.

3.9.9. Trapping of Intermediates using TEMPO Radical

An overnight-dried Schlenk flask with magnetic stirring bar was charged with 4-chloroanisole (48 µl, 0.2 mmol), catalyst **1** (6 mg, 10 mol%). 1 mL of dry benzene was added to make a brown-colored solution under N_2 atmosphere. The color of the reaction mixture instantly changed to yellowish brown after the addition of KO^{t}Bu (44 mg, 0.4 mmol) into the reaction flask. After that TEMPO (32 mg, 0.2 mmol) was added to above reaction mixture. The flask was kept under blue light at room temperature. After 12 h of stirring, the reaction was stopped.

The TEMPO adduct of *p*-OMe aryl radical was analysed by high-resolution mass spectrometry (HRMS).

HRMS (ESI, m/z) calcd. for $C_{16}H_{26}NO_2$ $[M+H]^+$: 264.1964; found: 264.1962.

3.9.10. Stern–Volmer Experiment

In a nitrogen filled glove box, 10^{-3} M solution of catalyst **2** was prepared in 1 mL of dry and degassed THF. Double dilution was done to give 10^{-6} M stock solution in 2 mL THF. Different quencher concentrations of (0.001 M – 0.005 M) were prepared and used. The fluorescence measurement was performed in a 10 mm, 4 mL screw-cap quartz cuvette. Emission intensity at 415 nm was recorded for each solution upon excitation at 380 nm. Integrated fluorescence intensities were plotted against absolute quencher concentration using Stern-Volmer equation (equation 2).

$$I_o/I = 1 + K[Q] = 1 + k_q\,\tau[Q] \qquad \text{(eq. 2)}$$

where, I_o = fluorescence intensity of **2** in absence of quencher, I = fluorescence intensity in the presence of quencher and [Q] is the concentration of quencher, K = Stern–Volmer constant which is the product of average radiative lifetime (τ) and quenching rate constant (k_q). From the plot of I_o/I vs quencher concentration [Q], K = Stern–Volmer constant was found to be 28 M^{-1} and corresponding to Stern–Volmer constant K, electron transfer rate (k_q) = 2.74×10^9 $M^{-1}s^{-1}$ was obtained.

3.9.11. General Procedure for Reaction

The oven-dried Schlenk flask with magnetic stirring bar was charged with 2-chloro-*N*,*N*-dialkylbenzamide (0.2 mmol), catalyst **1** (6 mg, 10 mol%) and KO^tBu (0.4 mmol) under N_2 atmosphere. 1 ml of dry and degassed THF was added to above reaction mixture. The reaction mixture was stirred under blue light at room temperature for 12 hours. After the completion of the reaction, the solvent was removed under rotary evaporator. The desired product was isolated by column chromatography using hexane/ethylacetate mixture. The isolated pure product was further analysed by ^1H and ^{13}C NMR spectroscopies.

3.9.12. Spectroscopic Characterization of Cross Coupled Product Catalysed by 1

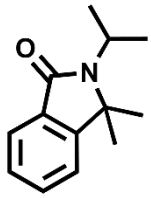

2-isopropyl-3,3-dimethylisoindolin-1-one (4a)[56]

The compound was purified by column chromatography (silica gel) with 10% mixture of ethyl acetate in hexane to give the product as a white solid (93 mg, 92%).

^{1}H NMR (400 MHz, $CDCl_3$) δ_{ppm} 7.74 (*d*, *J* = 7.5 Hz, 1H), 7.47 (*t*, *J* = 7.5 Hz, 1H), 7.36 (*t*, *J* = 7.5 Hz, 1H), 7.31 (*d*, *J* = 7.6 Hz, 1H), 3.62 (*hept*, *J* = 6.8 Hz, 1H), 1.53 (*d*, *J* = 6.8 Hz, 6H), 1.44 (*s*, 6H).

^{13}C NMR (101 MHz, $CDCl_3$) δ_{ppm} 167.35, 151.37, 132.11, 131.35, 127.97, 123.29, 120.72, 63.40, 44.68, 25.56, 20.62.

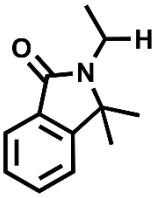

2-ethyl-3,3-dimethylisoindolin-1-one (4b)[57]

The compound was purified by column chromatography (silica gel) with 10% mixture of ethyl acetate in hexane to give the product as a white solid (84 mg, 89%).

^{1}H NMR (400 MHz, $CDCl_3$) δ_{ppm} 7.78 (*d*, *J* = 7.5 Hz, 1H), 7.50 (*t*, *J* = 7.5, 1.2 Hz, 1H), 7.41 – 7.33 (*m*, 2H), 3.49 (*q*, *J* = 7.2 Hz, 2H), 1.46 (*s*, 6H), 1.28 (*t*, *J* = 7.2 Hz, 3H).

^{13}C NMR (101 MHz, $CDCl_3$) δ_{ppm} 167.33, 151.62, 131.41, 131.03, 127.89, 123.39, 120.59, 62.76, 33.96, 25.95, 14.72.

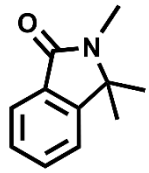

2,3,3-trimethylisoindolin-1-one (4c) [57]

The compound was purified by column chromatography (silica gel) with 10% mixture of ethyl acetate in hexane to give the product as a white solid (73 mg, 84%).

^{1}H NMR (400 MHz, $CDCl_3$) δ_{ppm} 7.80 (*dt*, *J* = 7.5, 1.1 Hz, 1H), 7.51 (*td*, *J* = 7.4, 1.2 Hz, 1H), 7.40 (*t*, *J* = 7.5 Hz, 2H), 3.01 (*s*, 3H), 1.43 (*s*, 6H).

^{13}C NMR (101 MHz, $CDCl_3$) δ_{ppm} 167.29, 151.58, 131.52, 130.94, 128.01, 123.58, 120.74, 62.13, 24.98, 23.92.

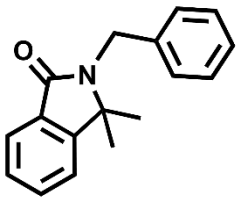

2-benzyl-3,3-dimethylisoindolin-1-one (4d) [56]

The compound was purified by column chromatography (silica gel) with 10% mixture of ethyl acetate in hexane to give the product as a white solid (116 mg, 93%).

^{1}H NMR (400 MHz, $CDCl_3$) δ_{ppm} 7.90 (*d*, *J* = 8.6 Hz, 1H), 7.55 (*t*, *J* = 7.5 Hz, 1H), 7.45 (*t*, *J* = 7.5 Hz, 1H), 7.37 (*dd*, *J* = 7.3, 2.6 Hz, 3H), 7.32 – 7.27 (*m*, 3H), 7.23 (*t*, *J* = 7.2 Hz, 1H), 4.75 (*s*, 2H), 1.36 (*s*, 6H).

^{13}C NMR (101 MHz, $CDCl_3$) δ_{ppm} 168.01, 152.02, 138.76, 131.86, 130.50, 128.55, 128.11, 127.83, 127.26, 123.92, 120.74, 63.27, 42.72, 26.43.

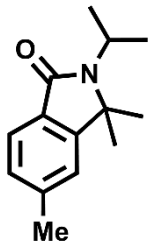

2-isopropyl-3,3,5-trimethylisoindolin-1-one (4e)[56]

The compound was purified by column chromatography (silica gel) with 10% mixture of ethyl acetate in hexane to give the product as a white solid (89 mg, 82%).

^{1}H NMR (400 MHz, $CDCl_3$) δ_{ppm} 7.62 (*d*, *J* = 7.7 Hz, 1H), 7.18 (*d*, *J* = 7.7 Hz, 1H), 7.11 (*s*, 1H), 3.60 (*hept*, *J* = 6.9 Hz, 1H), 2.42 (*s*, 3H), 1.55 – 1.50 (*m*, 6H), 1.45 – 1.41 (*m*, 6H).

^{13}C NMR (101 MHz, $CDCl_3$) δ_{ppm} 167.41, 151.72, 141.79, 129.53, 128.88, 123.02, 121.20, 63.13, 44.55, 25.54, 22.02, 20.61.

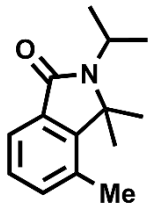

2-isopropyl-3,3,6-trimethylisoindolin-1-one (4f)[58]

The compound was purified by column chromatography (silica gel) with 10% mixture of ethyl acetate in hexane to give the product as a white solid (100 mg, 93%).

^{1}H NMR (400 MHz, $CDCl_3$) δ_{ppm} 7.62 (*d*, *J* = 6.8 Hz, 1H), 7.32 – 7.23 (*m*, 2H), 3.62 (*hept*, *J* = 6.8 Hz, 1H), 2.47 (*s*, 3H), 1.56 (*s*, 3H), 1.55 (*s*, 3H), 1.53 (*s*, 6H).

^{13}C NMR (101 MHz, $CDCl_3$) δ_{ppm} 167.28, 148.15, 133.81, 132.73, 131.61, 127.98, 120.94, 64.28, 44.30, 22.93, 20.56, 18.75.

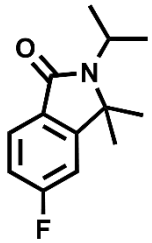

5-fluoro-2-isopropyl-3,3-dimethylisoindolin-1-one (4g)[58]

The compound was purified by column chromatography (silica gel) with 10% mixture of ethyl acetate in hexane to give the product as a white solid (88 mg, 80%).

^{1}H NMR (400 MHz, $CDCl_3$) δ_{ppm} 7.71 (*dd*, *J* = 8.3, 5.0 Hz, 1H), 7.06 (*td*, *J* = 8.8, 8.3, 2.3 Hz, 1H), 6.99 (*dd*, *J* = 8.2, 2.2 Hz, 1H), 3.60 (*hept*, *J* = 6.8 Hz, 1H), 1.52 (*d*, *J* = 6.9 Hz, 6H), 1.45 (*s*, 6H).

^{13}C NMR (101 MHz, $CDCl_3$) δ_{ppm} 166.36, 163.87 ($^{1}J_{C-F}$= 251 Hz), 153.69($^{3}J_{C-F}$= 9 Hz), 128.02($^{4}J_{C-F}$= 2 Hz), 125.28($^{3}J_{C-F}$= 9 Hz), 115.47($^{2}J_{C-F}$= 24 Hz), 108.03($^{2}J_{C-F}$= 23 Hz), 63.04, 44.77, 25.45, 20.56. ^{19}F NMR (376 MHz, $CDCl_3$) δ -108.04.

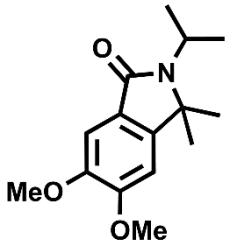

2-isopropyl-5,6-dimethoxy-3,3-dimethylisoindolin-1-one (4h)[57]

The compound was purified by column chromatography (silica gel) with 15% mixture of ethyl acetate in hexane to give the product as a white solid (100 mg, 76%).

^{1}H NMR (400 MHz, $CDCl_3$) δ_{ppm} 7.23 (*s*, 1H), 6.76 (*s*, 1H), 3.94 (*s*, 3H), 3.91 (*s*, 3H), 3.61 (*p*, *J* = 6.8 Hz, 1H), 1.53 (*d*, *J* = 6.9 Hz, 6H), 1.44 (*s*, 6H).

^{13}C NMR (101 MHz, $CDCl_3$) δ_{ppm} 167.49, 152.41, 149.52, 144.85, 124.29, 104.97, 102.96, 62.95, 56.32, 44.70, 25.65, 20.69.

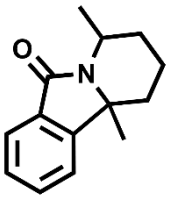

4,10b-dimethyl-1,3,4,10b-tetrahydropyrido[2,1-a]isoindol-6(2H)-one (4i)[56]

The compound was purified by column chromatography (silica gel) with 10% mixture of ethyl acetate in hexane to give the product as a white solid (100 mg, 93%).

^{1}H NMR (400 MHz, $CDCl_3$) δ_{ppm} 7.82 (*d*, *J* = 7.5 Hz, 1H), 7.50 (*t*, *J* = 7.5 Hz, 1H), 7.40 (*t*, *J* = 7.5 Hz, 1H), 7.32 (*d*, *J* = 7.5 Hz, 1H), 4.85 (*t*, *J* = 6.7 Hz, 1H), 2.09 (*ddt*, *J* = 30.1, 13.6, 3.4 Hz, 2H), 1.75 – 1.61 (*m*, 2H), 1.56 (*s*, 3H), 1.37 (*d*, *J* = 7.3 Hz, 3H), 1.34 – 1.15 (*m*, 2H).

^{13}C NMR (101 MHz, $CDCl_3$) δ_{ppm} 166.89, 152.95, 131.49, 130.56, 127.90, 123.83, 120.36, 61.45, 43.47, 36.16, 30.00, 25.55, 19.71, 16.53.

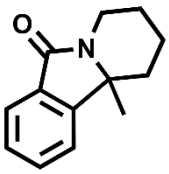

10b-methyl-1,3,4,10b-tetrahydropyrido[2,1-a]isoindol-6(2H)-one (4j)[56]

The compound was purified by column chromatography (silica gel) with 10% mixture of ethyl acetate in hexane to give the product as a colorless oil (93 mg, 93%).

^{1}H NMR (400 MHz, $CDCl_3$) δ_{ppm} 7.84 (*d*, *J* = 7.5 Hz, 1H), 7.51 (*td*, *J* = 7.4, 1.3 Hz, 1H), 7.45 – 7.35 (*m*, 2H), 4.40 (*dd*, *J* = 13.9, 4.5 Hz, 1H), 2.95 (*td*, *J* = 13.2, 3.2 Hz, 1H), 2.09 (*dd*, *J* = 13.0, 1.5 Hz, 1H), 1.89 – 1.68 (*m*, 3H), 1.45 (*s*, 3H), 1.35 – 1.17 (*m*, 2H).

^{13}C NMR (101 MHz, $CDCl_3$) δ_{ppm} 165.83, 152.53, 131.36, 131.00, 127.94, 123.86, 120.55, 60.93, 36.56, 36.30, 25.54, 21.11, 20.45.

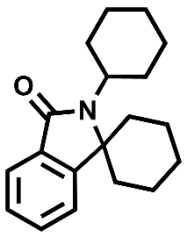

2'-cyclohexylspiro[cyclohexane-1,1'-isoindolin]-3'-one (4k)[56]

The compound was purified by column chromatography (silica gel) with 10% mixture of ethyl acetate in hexane to give the product as a white solid (127 mg, 90%).

^{1}H NMR (400 MHz, $CDCl_3$) δ_{ppm} 7.81 (*dd*, *J* = 7.6, 1.8 Hz, 1H), 7.76 (*d*, *J* = 6.5 Hz, 1H), 7.45 (*pd*, *J* = 7.3, 1.5 Hz, 2H), 3.12 (*tt*, *J* = 12.0, 3.8 Hz, 1H),

2.63 (*q*, *J* = 12.0 Hz, 2H), 1.99 – 1.82 (*m*, 9H), 1.66 (*s*, 2H), 1.59 (*d*, *J* = 13.8 Hz, 2H), 1.48 (*d*, *J* = 6.7 Hz, 2H), 1.42 – 1.23 (*m*, 4H).

^{13}C NMR (101 MHz, $CDCl_3$) δ_{ppm} 167.33, 150.18, 132.79, 130.43, 127.80, 123.50, 123.30, 66.12, 53.14, 33.20, 30.14, 26.72, 25.36, 24.79, 22.65.

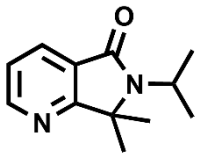

6-isopropyl-7,7-dimethyl-6,7-dihydro-5H-pyrrolo[3,4-b]pyridin-5-one (4l)[57]

The compound was purified by column chromatography (Alumina gel) with 10% mixture of ethyl acetate in hexane to give the product as a white solid (94 mg, 92%).

^{1}H NMR (400 MHz, $CDCl_3$) δ_{ppm} 8.67 (*dd*, *J* = 4.9, 1.6 Hz, 1H), 8.03 (*dd*, *J* = 7.6, 1.6 Hz, 1H), 7.33 (*dd*, *J* = 7.6, 4.9 Hz, 1H), 3.68 (*hept*, *J* = 6.8 Hz, 1H), 1.56 (*d*, *J* = 6.8 Hz, 6H), 1.52 (*s*, 6H).

^{13}C NMR (101 MHz, $CDCl_3$) δ_{ppm} 169.49, 165.52, 152.10, 131.55, 125.59, 123.26, 64.58, 45.04, 23.89, 20.65.

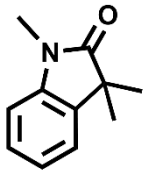

1,3,3-trimethylindolin-2-one (6a)[59]

The compound was purified by column chromatography (silica gel) with 5% mixture of ethyl acetate in hexane to give the product as a colorless oil (77 mg, 88%).

^{1}H NMR (400 MHz, $CDCl_3$) δ_{ppm} 7.27 – 7.21 (*m*, 1H), 7.19 (*d*, *J* = 7.3 Hz, 1H), 7.04 (*t*, *J* = 7.5 Hz, 1H), 6.83 (*d*, *J* = 7.8 Hz, 1H), 3.20 (*s*, 3H), 1.35 (*s*, 6H).

^{13}C NMR (101 MHz, $CDCl_3$) δ_{ppm} 181.20, 142.49, 135.65, 127.58, 122.40, 122.15, 107.95, 44.02, 26.08, 24.28.

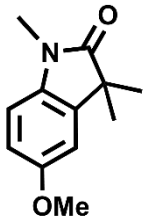

5-methoxy-1,3,3-trimethylindolin-2-one (6b)[59]

The compound was purified by column chromatography (silica gel) with 10% mixture of ethyl acetate in hexane to give the product as a colorless oil (72 mg, 70%).

^{1}H NMR (400 MHz, $CDCl_3$) δ_{ppm} 6.81 (*d*, *J* = 2.3 Hz, 1H), 6.76 (*dd*, *J* = 8.4, 2.4 Hz, 1H), 6.73 (*d*, *J* = 8.3 Hz, 1H), 3.78 (*s*, 3H), 3.17 (*s*, 3H), 1.34 (*s*, 6H).

^{13}C NMR (101 MHz, $CDCl_3$) δ_{ppm} 181.10, 156.14, 137.30, 136.22, 111.61, 110.12, 108.31, 55.86, 44.68, 26.35, 24.47.

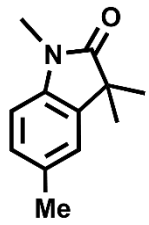

1,3,3,5-tetramethylindolin-2-one (6c)[59]

The compound was purified by column chromatography (silica gel) with 5% mixture of ethyl acetate in hexane to give the product as a yellow oil (78 mg, 83%).

^{1}H NMR (400 MHz, $CDCl_3$) δ_{ppm} 7.06 (*ddd*, *J* = 7.8, 1.7, 0.9 Hz, 1H), 7.03 – 7.01 (*m*, 1H), 6.73 (*d*, *J* = 7.8 Hz, 1H), 3.19 (*s*, 3H), 2.35 (*s*, 3H), 1.35 (*s*, 6H).

^{13}C NMR (101 MHz, $CDCl_3$) δ_{ppm} 181.49, 140.35, 136.00, 132.12, 127.95, 123.28, 107.86, 44.35, 26.35, 24.52, 21.23.

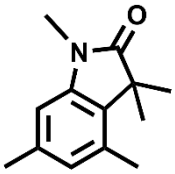

1,3,3,4,6-pentamethylindolin-2-one (6d)

The compound was purified by column chromatography (silica gel) with 5% mixture of ethyl acetate in hexane to give the product as a white solid (83 mg, 82%).

^{1}H NMR (400 MHz, $CDCl_3$) δ_{ppm} 6.65 (*s*, 1H), 6.53 (*s*, 1H), 3.18 (*s*, 3H), 2.35 (*s*, 3H), 2.34 (*s*, 3H), 1.43 (*s*, 6H).

^{13}C NMR (101 MHz, $CDCl_3$) δ_{ppm} 181.65, 143.01, 137.44, 133.69, 129.68, 125.52, 106.75, 44.69, 26.22, 22.51, 21.51, 21.48, 18.01, 17.97.

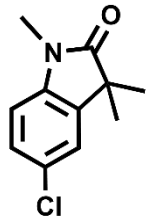

5-chloro-1,3,3-trimethylindolin-2-one (6e)[59]

The compound was purified by column chromatography (silica gel) with 5% mixture of ethyl acetate in hexane to give the product as a yellow solid (75 mg, 72%).

^{1}H NMR (400 MHz, $CDCl_3$) δ_{ppm} 7.22 (*dd*, *J* = 8.2, 2.2 Hz, 1H), 7.16 (*d*, *J* = 2.0 Hz, 1H), 6.75 (*d*, *J* = 8.2 Hz, 1H), 3.19 (*s*, 3H), 1.35 (*s*, 6H).

^{13}C NMR (101 MHz, $CDCl_3$) δ_{ppm} 180.91, 141.30, 137.57, 127.96, 127.67, 123.04, 109.06, 44.56, 26.43, 24.37.

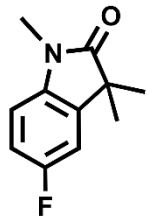

5-fluoro-1,3,3-trimethylindolin-2-one (6f)[59]

The compound was purified by column chromatography (silica gel) with 5% mixture of ethyl acetate in hexane to give the product as a yellow solid (82 mg, 85%).

^{1}H NMR (400 MHz, $CDCl_3$) δ_{ppm} 6.98 – 6.89 (*m*, 2H), 6.74 (*dd*, *J* = 9.2, 4.2 Hz, 1H), 3.18 (*s*, 3H), 1.34 (*s*, 6H).

^{13}C NMR (101 MHz, $CDCl_3$) δ_{ppm} 181.04, 158.28 (d, $^1J_{C-F}$= 241 Hz), 138.58(d, $^4J_{C-F}$ = 2 Hz), 137.51(d, $^3J_{C-F}$ = 8 Hz), 113.69($^2J_{C-F}$ = 24 Hz), 110.48($^2J_{C-F}$ = 24 Hz), 108.46($^3J_{C-F}$ = 8 Hz), 44.73, 26.41, 24.35. ^{19}F NMR (376 MHz, $CDCl_3$) δ -120.90.

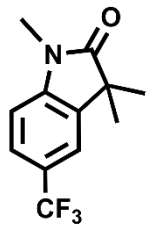

1,3,3-trimethyl-5-(trifluoromethyl)indolin-2-one (6g)[59]

The compound was purified by column chromatography (silica gel) with 5% mixture of ethyl acetate in hexane to give the product as a white solid (108 mg, 89%).

^{1}H NMR (400 MHz, $CDCl_3$) δ_{ppm} 7.54 (*ddd*, *J* = 8.2, 1.9, 1.0 Hz, 1H), 7.42 (*d*, *J* = 1.8 Hz, 1H), 6.91 (*d*, *J* = 8.2 Hz, 1H), 3.24 (*s*, 3H), 1.39 (*s*, 6H).

^{13}C NMR (101 MHz, $CDCl_3$) δ_{ppm} 181.34, 145.75, 136.42, 125.60(*q*, $^3J_{C-F}$ = 4 Hz), 124.70(*q*, $^2J_{C-F}$ = 32 Hz), 123.25(*q*, $^1J_{C-F}$ = 272 Hz), 119.45(*q*, $^3J_{C-F}$ = 4 Hz), 107.87, 44.30, 26.52, 24.35. ^{19}F NMR (376 MHz, $CDCl_3$) δ -61.35.

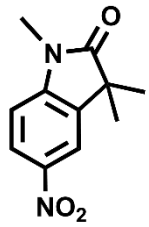

1,3,3-trimethyl-5-nitroindolin-2-one (6h)[59]

The compound was purified by column chromatography (silica gel) with 10% mixture of ethyl acetate in hexane to give the product as a yellow solid (89 mg, 81%).

^{1}H NMR (400 MHz, $CDCl_3$) δ_{ppm} 8.22 (*dd*, *J* = 8.6, 2.2 Hz, 1H), 8.07 (*d*, *J* = 2.2 Hz, 1H), 6.94 (*d*, *J* = 8.6 Hz, 1H), 3.28 (*d*, *J* = 1.1 Hz, 3H), 1.41 (*d*, *J* = 1.3 Hz, 6H).

^{13}C NMR (101 MHz, $CDCl_3$) δ_{ppm} 181.28, 148.44, 143.44, 136.46, 125.20, 118.29, 107.68, 44.22, 26.67, 24.15.

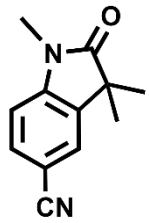

1,3,3-trimethyl-2-oxoindoline-5-carbonitrile (6i)[59]

The compound was purified by column chromatography (silica gel) with 10% mixture of ethyl acetate in hexane to give the product as a white solid (85 mg, 85%).

^{1}H NMR (400 MHz, $CDCl_3$) δ_{ppm} 7.59 (*dd*, *J* = 8.1, 1.6 Hz, 1H), 7.44 (*d*, *J* = 1.6 Hz, 1H), 6.91 (*d*, *J* = 8.1 Hz, 1H), 3.24 (*s*, 3H), 1.38 (*s*, 6H).

^{13}C NMR (101 MHz, $CDCl_3$) δ_{ppm} 181.01, 146.66, 136.79, 133.28, 125.83, 119.41, 108.57, 105.66, 44.11, 26.56, 24.26.

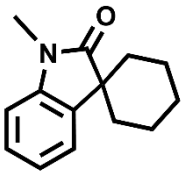

1'-methylspiro[cyclohexane-1,3'-indolin]-2'-one (6j)[56]

The compound was purified by column chromatography (silica gel) with 5% mixture of ethyl acetate in hexane to give the product as a white solid (94 mg, 89%).

^{1}H NMR (400 MHz, $CDCl_3$) δ_{ppm} 7.46 (*d*, *J* = 7.4 Hz, 1H), 7.29 (*d*, *J* = 7.7 Hz, 1H), 7.05 (*t*, *J* = 7.0 Hz, 1H), 6.85 (*d*, *J* = 7.7 Hz, 1H), 3.20 (*s*, 3H), 1.94 (*ddd*, *J* = 13.9, 6.7, 3.3 Hz, 2H), 1.90 – 1.82 (*m*, 2H), 1.82 – 1.67 (*m*, 4H), 1.67 – 1.60 (*m*, 2H), 1.56 (*dq*, *J* = 12.8, 3.4 Hz, 2H).

^{13}C NMR (101 MHz, $CDCl_3$) δ_{ppm} 180.88, 142.94, 135.52, 127.56, 124.03, 122.05, 108.02, 47.62, 33.11, 26.30, 25.31, 21.34.

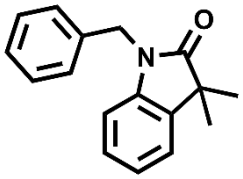

1-benzyl-3,3-dimethylindolin-2-one (6k)[59]

The compound was purified by column chromatography (silica gel) with 5% mixture of ethyl acetate in hexane to give the product as a white solid (99 mg, 79%).

^{1}H NMR (400 MHz, $CDCl_3$) δ_{ppm} 7.35 – 7.26 (*m*, 5H), 7.24 (*dd*, *J* = 7.3, 1.5 Hz, 1H), 7.15 (*td*, *J* = 7.7, 1.3 Hz, 1H), 7.07 – 7.02 (*m*, 1H), 6.75 (*d*, *J* = 7.3 Hz, 1H), 4.94 (*s*, 2H), 1.47 (*s*, 6H).

^{13}C NMR (101 MHz, $CDCl_3$) δ_{ppm} 181.50, 141.68, 136.13, 135.80, 128.81, 127.63, 127.58, 127.20, 122.57, 122.38, 109.13, 44.23, 43.55, 24.59.

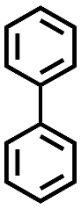

Biphenyl (9a)[60]

The compound was purified by column chromatography (silica gel) with hexane to give the product as a white solid (55 mg, 72%).

^{1}H NMR (400 MHz, $CDCl_3$) δ_{ppm} 7.67 – 7.59 (*m*, 4H), 7.47 (*q*, *J* = 5.1, 3.0 Hz, 4H), 7.38 (*dd*, *J* = 7.8, 4.4 Hz, 2H).

^{13}C NMR (101 MHz, $CDCl_3$) δ_{ppm} 141.36, 128.89, 127.39, 127.31.

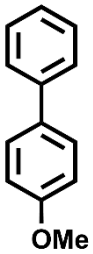

4-methoxy-1,1'-biphenyl (9b)[60]

The compound was purified by column chromatography (silica gel) with 1% mixture of ethyl acetate in hexane to give the product as a white solid (64 mg, 69%).

^{1}H NMR (400 MHz, $CDCl_3$) δ_{ppm} 7.60 – 7.54 (*m*, 4H), 7.45 (*dd*, *J* = 8.3, 6.8 Hz, 2H), 7.36 – 7.31 (*m*, 1H), 7.04 – 6.99 (*m*, 2H), 3.88 (*s*, 3H).

^{13}C NMR (101 MHz, $CDCl_3$) δ_{ppm} 159.26, 140.95, 133.90, 128.86, 128.29, 126.88, 126.79, 114.32, 55.50.

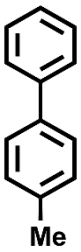

4-methyl-1,1'-biphenyl (9c)[60]

The compound was purified by column chromatography (silica gel) with hexane to give the product as a white solid (53 mg, 63%).

^{1}H NMR (400 MHz, $CDCl_3$) δ_{ppm} 7.63 (*dd*, *J* = 8.3, 1.4 Hz, 2H), 7.54 (*d*, *J* = 8.2 Hz, 2H), 7.47 (*dd*, *J* = 8.4, 6.9 Hz, 2H), 7.39 – 7.34 (*m*, 1H), 7.29 (*d*, *J* = 7.8 Hz, 2H), 2.44 (*s*, 3H).

^{13}C NMR (101 MHz, $CDCl_3$) δ_{ppm} 141.28, 138.48, 137.15, 129.61, 128.85, 127.13, 127.11, 21.23.

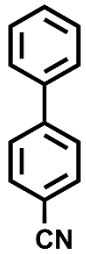

[1,1'-biphenyl]-4-carbonitrile (9d)[60]

The compound was purified by column chromatography (silica gel) with 1% ethyl acetate in hexane to give the product as a white solid (68 mg, 75%).

^{1}H NMR (400 MHz, $CDCl_3$) δ_{ppm} 7.73 (*d*, *J* = 8.4 Hz, 2H), 7.69 (*d*, *J* = 8.4 Hz, 2H), 7.59 (*d*, *J* = 7.3 Hz, 2H), 7.49 (*t*, *J* = 7.4 Hz, 2H), 7.43 (*t*, *J* = 7.3 Hz, 1H).

^{13}C NMR (101 MHz, $CDCl_3$) δ_{ppm} 145.81, 139.30, 132.74, 129.25, 128.80, 127.87, 127.37, 119.12, 111.01.

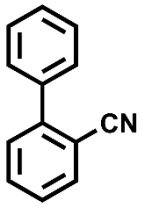

[1,1'-biphenyl]-2-carbonitrile (9e)[61]

The compound was purified by column chromatography (silica gel) with 1% ethyl acetate in hexane to give the product as a white solid (68 mg, 72%).

^{1}H NMR (400 MHz, $CDCl_3$) δ_{ppm} 7.77 (*dd*, *J* = 7.7, 1.3 Hz, 1H), 7.65 (*td*, *J* = 7.7, 1.4 Hz, 1H), 7.61 – 7.55 (*m*, 2H), 7.55 – 7.42 (*m*, 5H).

^{13}C NMR (101 MHz, $CDCl_3$) δ_{ppm} 145.54, 138.19, 133.82, 132.92, 130.16, 128.83, 128.81, 128.79, 127.63, 118.83, 111.30.

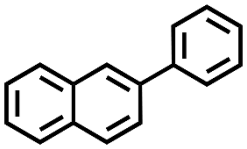

2-phenylnaphthalene (9f)[62]

The compound was purified by column chromatography (silica gel) with 2% ethyl acetate in hexane to give the product as a white solid (73 mg, 72%).

^{1}H NMR (400 MHz, CDCl3) δ_{ppm} 8.07 (*s*, 1H), 7.96 – 7.87 (*m*, 3H), 7.80 – 7.72 (*m*, 3H), 7.52 (*td*, J = 8.6, 7.7, 4.8 Hz, 4H), 7.41 (*t*, J = 7.4 Hz, 1H).

^{13}C NMR (101 MHz, $CDCl_3$) δ_{ppm} 141.25, 138.68, 133.80, 132.74, 128.99, 128.55, 128.33, 127.78, 127.57, 127.48, 126.42, 126.06, 125.94, 125.73.

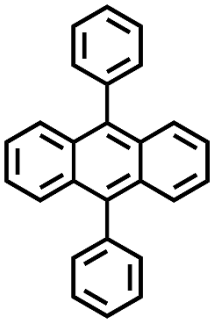

9,10-diphenylanthracene (9g)[63]

The compound was purified by column chromatography (silica gel) with hexane to give the product as a white solid (117 mg, 71%).

^{1}H NMR (400 MHz, $CDCl_3$) δ_{ppm} 8.52 (*dq*, *J* = 8.9, 1.0 Hz, 4H), 8.45 (*s*, 2H), 8.00 (*dd*, *J* = 8.5, 1.1 Hz, 4H), 7.61 (*ddd*, *J* = 8.9, 6.6, 1.3 Hz, 4H), 7.51 (*ddd*, *J* = 7.9, 6.6, 1.2 Hz, 4H).

^{13}C NMR (101 MHz, $CDCl_3$) δ_{ppm} 132.31, 130.73, 128.75, 127.78, 127.35, 127.25, 125.80, 122.50.

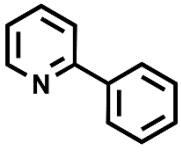

2-phenylpyridine (9h)[64]

The compound was purified by column chromatography (silica gel) with 2% ethyl acetate in hexane to give the product as a colorless oil (51.2 mg, 66%).

^{1}H NMR (400 MHz, $CDCl_3$) δ_{ppm} 8.73 (*d*, *J* = 4.9 Hz, 1H), 8.05 – 7.98 (*m*, 2H), 7.80 – 7.73 (*m*, 2H), 7.54 – 7.48 (*m*, 2H), 7.48 – 7.41 (*m*, 1H), 7.25 (*ddd*, *J* = 6.3, 4.8, 2.3 Hz, 1H).

^{13}C NMR (101 MHz, $CDCl_3$) δ_{ppm} 157.60, 149.80, 139.53, 136.87, 129.07, 128.87, 127.03, 122.22, 120.70.

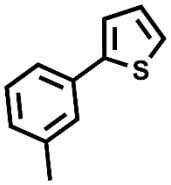

2-(m-tolyl)thiophene (9i)[60]

The compound was purified by column chromatography (silica gel) with hexane to give the product as a white solid (69 mg, 79%).

^{1}H NMR (400 MHz, $CDCl_3$) δ_{ppm} 7.44 (*d*, *J* = 7.0 Hz, 2H), 7.33 – 7.30 (*m*, 1H), 7.28 (*d*, *J* = 5.0 Hz, 1H), 7.15 – 7.07 (*m*, 2H), 2.41 (*s*, 3H).

^{13}C NMR (101 MHz, $CDCl_3$) δ_{ppm} 144.71, 138.65, 134.44, 128.91, 128.40, 128.07, 126.83, 124.77, 123.23, 123.10, 21.60.

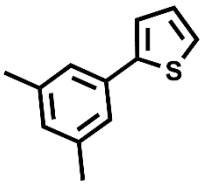

2-(3,5-dimethylphenyl)thiophene (9j)[60]

The compound was purified by column chromatography (silica gel) with hexane to give the product as a white solid (76 mg, 81%).

^{1}H NMR (400 MHz, $CDCl_3$) δ_{ppm} 7.32 (*dd*, *J* = 3.6, 1.2 Hz, 1H), 7.30 (*d*, *J* = 1.2 Hz, 3H), 7.10 (*dd*, *J* = 5.1, 3.6 Hz, 1H), 6.97 (*s*, 1H), 2.39 (*s*, 6H).

^{13}C NMR (101 MHz, $CDCl_3$) δ_{ppm} 144.84, 138.54, 134.36, 129.34, 128.00, 124.60, 124.00, 123.00, 21.46, 21.43.

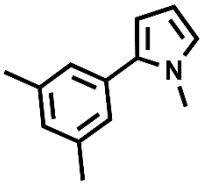

2-(3,5-dimethylphenyl)-1-methyl-1H-pyrrole (9k)[65]

The compound was purified by column chromatography (silica gel) with hexane to give the product as a white solid (65 mg, 70%).

^{1}H NMR (400 MHz, $CDCl_3$) δ_{ppm} 7.03 (*d*, *J* = 1.6 Hz, 2H), 6.96 (*s*, 1H), 6.70 (*t*, *J* = 2.3 Hz, 1H), 6.19 (*d*, *J* = 2.3 Hz, 2H), 3.66 (*s*, 3H), 2.35 (*s*, 6H).

^{13}C NMR (101 MHz, $CDCl_3$) δ_{ppm} 137.82, 134.83, 133.24, 128.48, 126.56, 123.38, 108.43, 107.65, 35.06, 21.38.

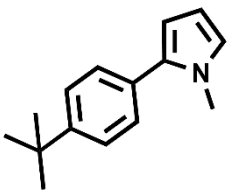

2-(4-(tert-butyl)phenyl)-1-methyl-1H-pyrrole (9l)[66]

The compound was purified by column chromatography (silica gel) with hexane to give the product as a white solid (73 mg, 69%).

^{1}H NMR (400 MHz, $CDCl_3$) δ_{ppm} 7.45 – 7.42 (*m*, 2H), 7.37 – 7.33 (*m*, 2H), 6.72 (*t*, *J* = 2.3 Hz, 1H), 6.21 (*t*, *J* = 2.2 Hz, 2H), 3.68 (*s*, 3H), 1.37 (*s*, 12H).

^{13}C NMR (101 MHz, $CDCl_3$) δ_{ppm} 149.77, 134.74, 130.58, 128.48, 125.40, 123.44, 108.48, 107.76, 35.19, 34.68, 31.49.

Chapter-3

Part-B

Trianionic NNN Pincer : A Photo-Redox catalyst for Transition-Metal-Free Reductive Cyclisation of Organic Halides to Access Indolines and Oxindoles.

3.10. Introduction

Over the decades, the generation of radical species has been extensively studied and exploited.[67] Instead of various approaches, radical mediated transformation holds a significant place to access the synthesis of these type of unique heterocycles. However, generation of free radicals generally needs high activation energy or drastic reaction conditions. Intriguingly, the field of photocatalysis is rapidly growing area of research as an alternate of such high energy demanding transformations.[68-70] As a consequence of this, the use of visible-light as a source of energy for promoting chemical transformation has emerged as an interesting topic in organic synthesis.[71] Over the past decade, MacMillan[72,73], Yoon[74,75], Stephenson[76-78] have done extensive work on heavy metal (Ir, Pt, Ru) based complexes ($[Ru(bpy)_3]^{2+}$ fac-$Ir(ppy)_3$ $[Ir(ppy)_2(bpy)]^+$ etc.) and organo-photocatalyst which has been widely used over wide range of applications in organic synthesis, like C–C bond formation, [2 + 2] enone cycloadditions[75], reductive dehalogenation of activated alkyl halides[78] etc.

Heterocyclic scaffolds are predominant components of a variety of important natural products and prevalent structural motifs in biologically active molecules, agrochemicals and designed materials.[79-82] In particular, indolines and oxindoles are privileged scaffolds in pharmaceutical[83, 84] and naturally occurring alkaloids.[85] Under this scenario, various efforts have been made to develop an efficient and sustainable protocols to synthesize these potent molecules.

The organic halides as radical precursors hold a significant place in efficient organic synthesis.[86-88] In this direction, Chulbom Lee and co-workers first time reported a visible-light-induced photocatalytic reductive transformation of organohalides (X= I and Br) towards the synthesis of indolines using $[(ppy)_2Ir(dtbbpy)]PF_6$ as a photocatalyst (Scheme 1).[88] They demonstrated a crucial role of DIPEA acting as a reductant and a source hydrogen atom. In the same direction, Chi-Ming Che has communicated a bis-NHC Ir(III) complexes photocatalyst towards the synthesis of indolines.[89] In 2017, Gwilherm Evano and co-workers has also described a protocol to synthesize indoline from aromatic iodide with $[(DPEphos)(bcp)Cu]PF_6$ photocatalyst.[90] As bromides are found to be less active towards indoline synthesis, a strong reducing photocatalyst is required to active such aryl halides. Recently, this concern has been addressed by Barriault and co-workers using dinuclear gold(I) complexes ($[Au_2(dppm)_2]OTf_2$) as photo-catalysts but this gold complex shows absorption in the high energy UV region, which may leads to the destructive or undesired side reactions.[91] Although, metal promoted

photoredox strategies shows their excellence in small molecule activation but such catalysts also revealed some drawbacks such as cost and environmental incompatibility.

In this context, metal free photochemical protocols are much reliable alternate to overcomes these issues. In 2018, Márcio has explored a strategy to synthesis indoline by photoirradiation electron donor–acceptor (EDA) complex but this protocol is not much atom economic as excess of additive is needed.[92] Nevertheless, in spite of the considerable development has been made in this field, the design of general and mild photochemical strategies that improves efficiency, lower cost and decrease waste are highly desirable.

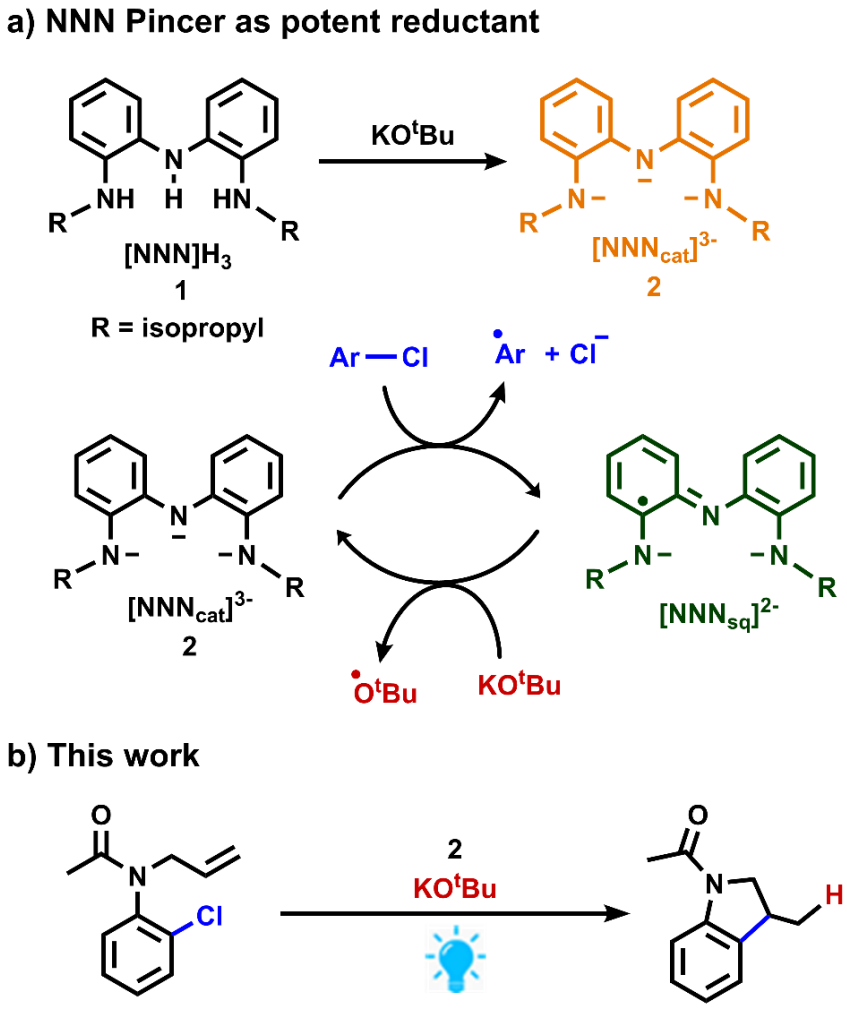

Scheme 3.6. (a) Redox behaviour of NNN pincer (b) Our work.

Recently, our group has described that a simple organic molecule in its anionic form is capable of catalysing light induced C–C bond formation from unactivated aryl halides under mild conditions.[60,93,94]

3.11. Results and Discussion

In our previous part of this chapter, the electron tranfer ability of pincer's was demonstrated, the parent trisamido assigned as trianionic NNN-pincer (2) and its one-electron oxidized iminosemiquinonate form could be accessed readily (scheme 3.6).

To our advantage, again trianionic pincer **2** was used as photocatalyst under photochemical condition towards the synthesis of Indolines and oxindoles. Following the same strategy, a series of indolines and oxindoles was synthesized using a photocatalytic intramolecular reductive cyclization reaction. This reaction uses several *N*-substituted chloroanilines in the presence of trianionic NNN pincer as an organic photocatalyst. More importantly, the KO^{t}Bu not only acts as base to deprotonate the $NNNH_3$ (**1**) but also behave as reductant to bring back the oxidised trianionic NNN pincer (**2$_{imq}$**) into **2** and complete the catalytic cycle. Importantly, the redox behaviour of KO^{t}Bu have been thoroughly investigated by Murphy group.[95] Further, it was observed that the KO^{t}Bu oxidised at mild oxidation potential (+0.10 V vs SCE) in DMF solvent.[96] Interestingly, the tert-butoxide radical is short living species which eventually generate acetone as the byproduct.[95] Gratifyingly, this by product behaves as hydrogen atom transfer (HAT) source[97] which finally affords the privileged indoline and oxindole Scaffolds. So, KO^{t}Bu make an endeavour to ensure that its can acts as a base, a reductant and a hydrogen atom transfer (HAT) source. On the other hand, aryl chlorides are used which are significantly abundant and cheaper starting material correlated to aryl iodides and aryl bromides.[98] A major consideration of this exercise is to utilize a cheap, abundant starting materials and metal free organic photocatalyst which falls in visible region to avoids deleterious side reactions. To the best of our knowledge, this is the first example of metal free visible-light-driven radical cyclization for synthesis of indolines and oxindoles using organic chlorides via last stage hydrogen atom transfer.

3.12. Catalytic Applications

Initially, a *N*-allyl-*N*-(2-chlorophenyl)acetamide **3** was taken as model substrate to setup the best reaction conditions. Pleasingly, 1-(3-methylindolin-1-yl)ethan-1-one 4**a** was formed in quantitative yield (98% by NMR analysis) with only 5 mol% loading of the $NNNH_3$ pincer catalyst **1** (Table 3.6, entry 2). On reducing the catalyst loading to 2 mol% the yield of reaction was diminished to 59%. Further, lowing the base equivalence results into lowering of overall yield of the reaction (Table 3.6, entry 3-4). A set of optimization studies fix the parameters for the best reaction condition and establishes that the reaction is complete in 6 h at room

temperature. Instead of KO^{t}Bu, we also examined some organic bases such as NEt_3, DABCO, and DIPEA (Table 3.6, entry 5). No desired product was observed as assay by thin layer chromatography which might be due to inability of such weak bases to generate the active trianionic NNN pincer **2**.

Furthermore, K_2CO_3 also found ineffective base for this transformation. Although, the possibility of activation of substrate by KO^{t}Bu is negligible, but to be sure a reaction was set only in the presence of KO^{t}Bu, which resulted a negative. Ultimately, last three entry 8-10 in table 3.6 conclude that catalyst **1**, KO^{t}Bu, light are predominant component of the reaction to be successful.

Table 3.6. Optimization studies.

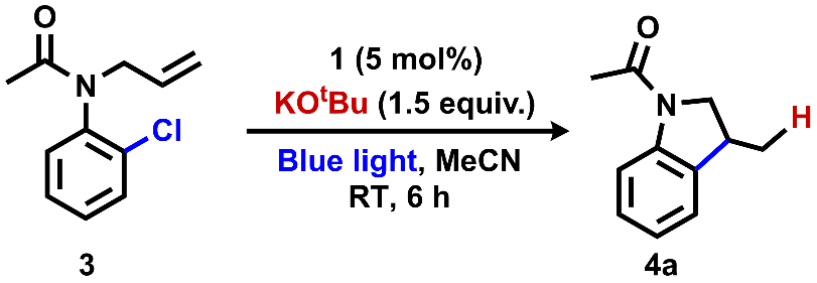

Entry	Variation from standard conditions	% Yield[b]
1	None	98(93)[c]
2	2 mol% of **1**	59
3	1.0 equiv of KO^{t}Bu	68
4	0.5 equiv of KO^{t}Bu	38
5	Only NEt_3/DABCO/DIPEA	ND
6	K_2CO_3 instead of KO^{t}Bu	12
7	Only KO^{t}Bu	ND
8	Absence of light	ND
9	Absence of **1**	ND
10	Absence of KO^{t}Bu	ND

Standard conditions: (a) *N*-allyl-*N*-(2-chlorophenyl)acetamide (0.2 mmol), KO^{t}Bu (0.3 mmol), **1** (5 mol%), and dry MeCN (1 mL), room temperature under a N_2 atmosphere, blue LEDs (450 nm), 6 h. [b]NMR yields, [c]Isolated yield. ND = not detected.

3.12.1. Scope of the Reaction Catalyzed by Catalyst 1

3.12.1.1. Scope for Reductive Cyclization of *N*-allyl-*N*-(2-chlorophenyl)acetamide

After the extensive study of best optimization conditions, the synthetic utility of this protocols was extended to various substrate having different functional group. The isolated yield of the product **4a** was determined to be 93% upon appropriate column-chromatographic separation (Table 3.7). Identically, -Me, -^{t}Bu containing *N*-allyl-*N*-(2-chlorophenyl)acetamide afforded **4b-4c** in 89-84% isolated yields. Electron donating group such as *p*-OMe is well tolerated to provide **4d** in 83% yield.

Table 3.7. Substrate Scope for Reductive Cyclization of *N*-allyl-*N*-(2-chlorophenyl)acetamide

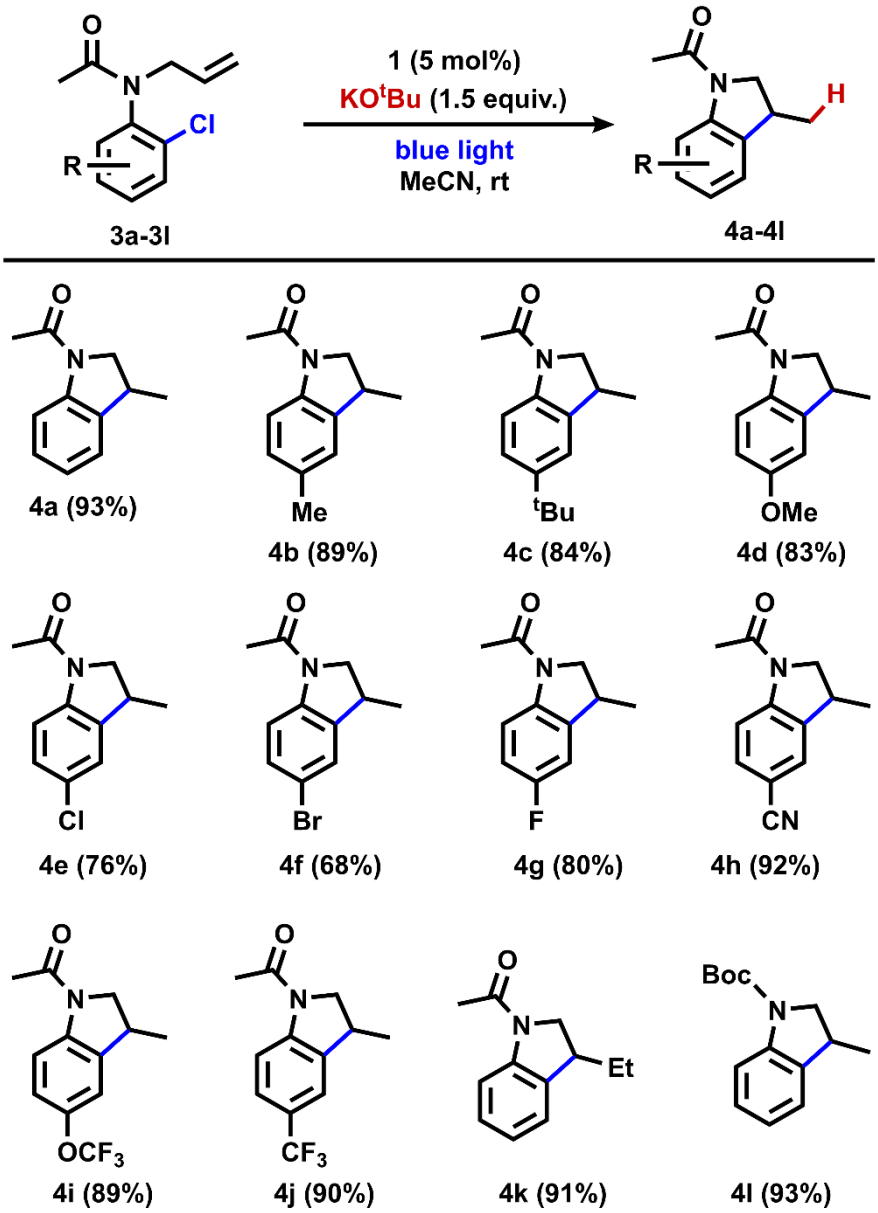

To generate the variety of halogen containing desired product like 1-(5-chloro-3-methylindolin-1-yl)ethan-1-one **4e** and 1-(5-bromo-3-methylindolin-1-yl)ethan-1-one **4f**, we chose *N*-allyl-*N*-(2-bromo-4-chlorophenyl)acetamide and *N*-allyl-*N*-(2-iodo-4-bromophenyl)acetamide as iodo and bromo aryls are easy to activate because of low reduction potential as compare to chloro one . The reaction was ceased after 3 hours in order to avoid the activation of halogen at para position. Fortunately, both the desired products **4e** and **4f** was obtained in 76-68%. A variety of electron withdrawing groups involving *p*-F, *p*-CN responded very well under the set of reaction conditions and afforded 80% and 92% isolated yield of **4g** and **4h** respectively. Similarly, *p*-OCF_3 and *p*-CF_3 provided **4i** and **4j** in 89-90% isolated yield. Instead of terminal *N*-allyl, internal olefin like *N*-crotonyl motifs such as *N*-(but-2-en-1-yl)-*N*-(2-chlorophenyl)acetamide were well behaved, afforded 4k in 91% isolated yield. After that *N*-Boc functionalitieswas examined, tert-butyl allyl(2-chlorophenyl)carbamate, since these functional groups possess much synthetic utility. Interestingly, these groups were well tolerated to afford 93% yields of the desired product **4l**.

3.12.1.2. Scope for Reductive Cyclization of *N*-allyl-*N*-(2-chlorophenyl)acetamide

As the substituted oxindole framework are privileged motif that is often found in the core of a large class of bioactive natural products as well as pharmaceutically important compounds.[99-101] In our synthetic effort, *N*-(2-chlorophenyl)-*N*-alkylmethacrylamide was chosen as the substrate, so that a reductive cleavage of C-Cl bond can engender a aryl radical. The oxindole 3,3'-dimethyl oxindole, **6a** was conveniently synthesized in very high, 92% yield when the catalyst loading was only 5 mol% (Table 3.8). Similarly, electron donating groups such as -OMe, -Me, substitutions were compatible with the process to furnish oxindoles (**6b-6d**) in 88-76% yields. The chloro- substitution on the aryl ring of amides was retained during the synthesis to result oxindole **6e** in 73% yield when *N*-(2-bromo-4-chlorophenyl)-*N*-methylmethacrylamide was used in place of 2-chloro acryamide. Similarly, strong electron withdrawing groups such as -F, -CF_3 and CN substitutions were compatible with the process to furnish oxindoles (**6f-6h**) in 92-82% yields. After that we introduced nitro functionalities at para position of respective chloromethacrylamide, since these functional groups possess much synthetic utility. Interestingly, nitro substitution was well tolerated to afford **6i** in 75% yield. Additionally, the protocol was tested on different *N*-alkylated methaacrylamide, *N*-benzyl, *N*-ethyl, *N*-isopropyl while the cyclized products **6j-6l** were obtained in 81-74% yield.

Table 3.8. Substrate Scope for Reductive Cyclization of *N*-(2-chlorophenyl)-*N*-alkylmethacrylamide

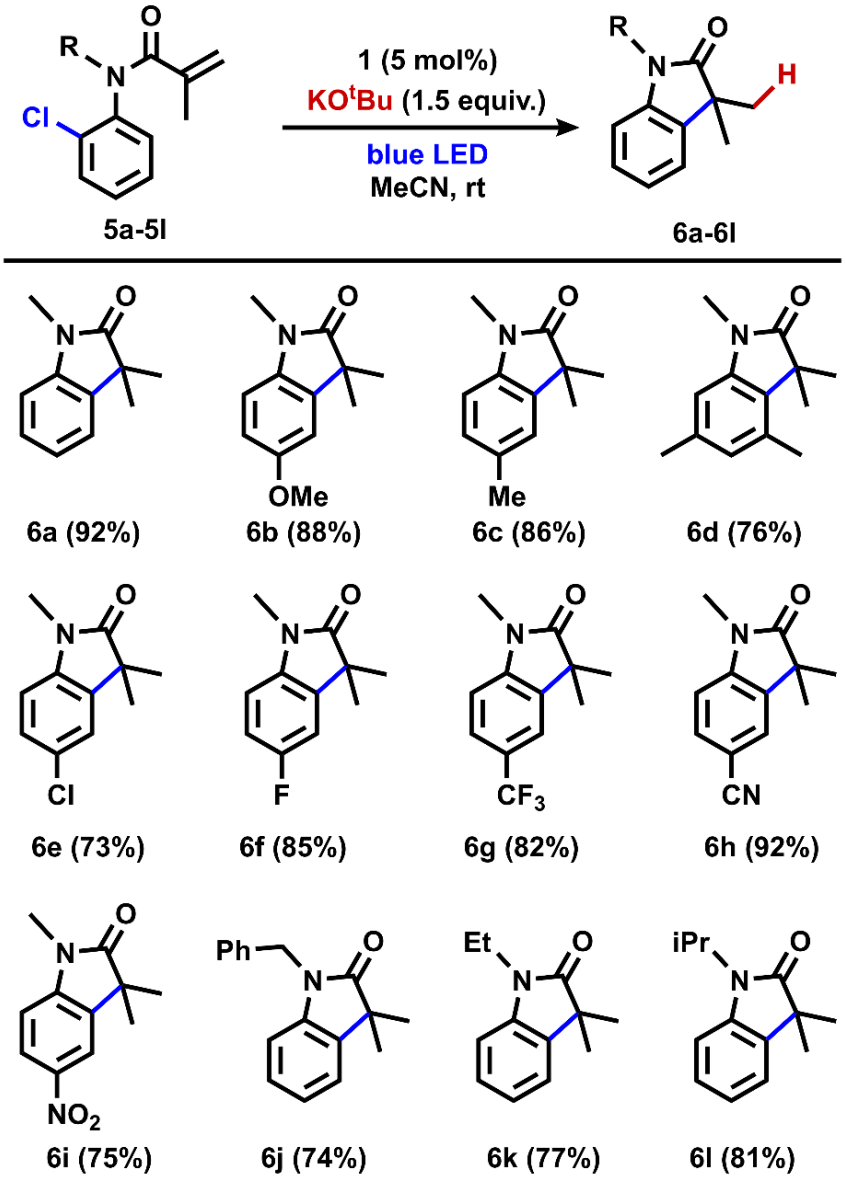

3.13. Mechanistic Investigations

As, an intrigued nature of the redox noninnocence of the trianionic NNN pincer has been discussed and how that can promote the catalytic efficiency for the chosen photo-redox catalyst in this report. The electron transfer step from the catalyst was further interogated, that reductive cleaves the C-Cl bond of an aryl amide. The measured excited state reduction potential for trianionic NNN pincer **2,** -2.90 V vs SCE, suggests the electron transfer from catalyst to sigma antibonding orbital of C-Cl is thermodynamically favorable. So, the NNN pincer can easily activate the aryl C-Cl bond via transfer single electron to sigma antibonding of C-Cl to generate resulted aryl radical. This generated radical is one the key step in various organic transformation to make the valuable products.

3.13.1. TEMPO Quenching Experiment

The reductive cleavage of C-Cl bond will generate the putative aryl radical. To find a compelling proof for its generation, the radical intermediate was intercepted with a readily available TEMPO radical. Predominantly, one equivalent of the radical trap TEMPO was added to the reaction mixture. Fortunately, the TEMPO was able to capture this radical intermediate in the form of adduct **7** (Scheme 3a). The adduct **7** was detected by high-resolution mass spectrometry. Further, methyl radical is also a side product of tertiary butoxide radical that was also form an adduct with TEMPO **8** (Scheme 3.7b). The signature of methyl radical TEMPO was also seen in HRMS.

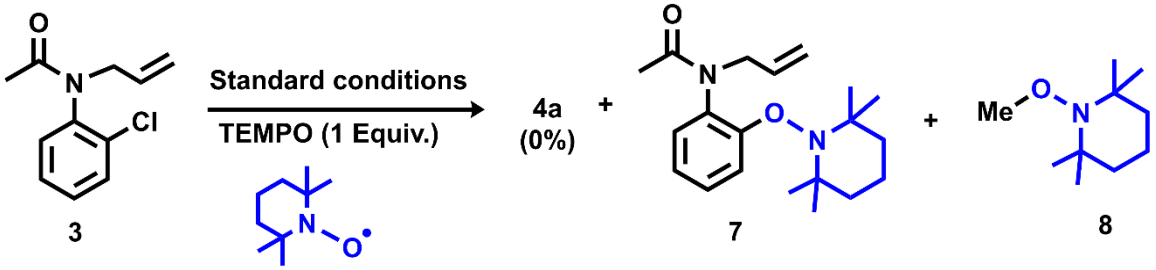

Scheme 3.7. (a) Trapping of aryl radical intermediate using TEMPO radical.

3.14. Plausible Catalytic Cycle

Mechanistically, the trianionic NNN pincer **2** is pushed up to excited state by shining the light on it (Scheme 3.8). After that, excited NNN pincer (**2**) transfer single electron to sigma antibonding orbital of C-Cl bond leading to bond cleavage to give a aryl radical at C2 position of aryl ring. Further, the corresponding aryl radical is generated through the reductive cleavage of the C–Cl bond, generating 5-*exo* cyclization products. Further, the corresponding aryl radical is sufficiently living to undergo 5-exo cyclization with terminal olefinic arm and generates terminal alkyl radical species (II). This may be due to the fact that 5-exo cyclization is kinetically more favourable in comparison to 6-endo cyclization via the radical pathway.[102]

A question arises that how the iminosemiquinonate form $\mathbf{2_{imq}}$ is going back to iminocatecholate **2**. Interestingly, trianionic NNN pincer **2** undergoes reversible one electron redox at a potential of 0.13 V vs SCE and oxidation potential of potassium tert-butoxide (E_{ox} = 0.1 V vs SCE)[96] also lies in the range of this potential window. So, the KO^{t}Bu is sufficiently reducing to reduce the one-electron oxidized backbone of **2** (i.e., $\mathbf{2_{imq}}$), so that the parent unoxidized form **2** is back and eliminates a tert-butoxide radical (Scheme 4). Interestingly, the reversibility of trianionic NNN pincer was further proved by sperate reduction of oxidised

trianionic NNN pincer i.e., $\mathbf{2_{imq}}$ using KO^{t}Bu as reductant. In order to prepare iminosemiquinonate from $\mathbf{2_{imq}}$, the trianionic NNN pincer was prepared by treatment of 3 equivalent of KO^{t}Bu, which results into a yellow color solid. Further, the one electron oxidised form of trianionic NNN pincer i.e., $\mathbf{2_{imq}}$ was generated using one equivalent of silver triflate, resulting a green color solid. After that, in order to regain the fully reduced form of trianionic NNN pincer **2**, the above green colour solid was treated with KO^{t}Bu. Fortunately, after 3 hours of stirring at room temperature under dark conditions, the similar yellow color compound was regained. So, the redox potential values and separate reduction of $\mathbf{2_{imq}}$ with KO^{t}Bu is concrete proof of insitu reduction of $\mathbf{2_{imq}}$ to **2** during the catalytic cycle.

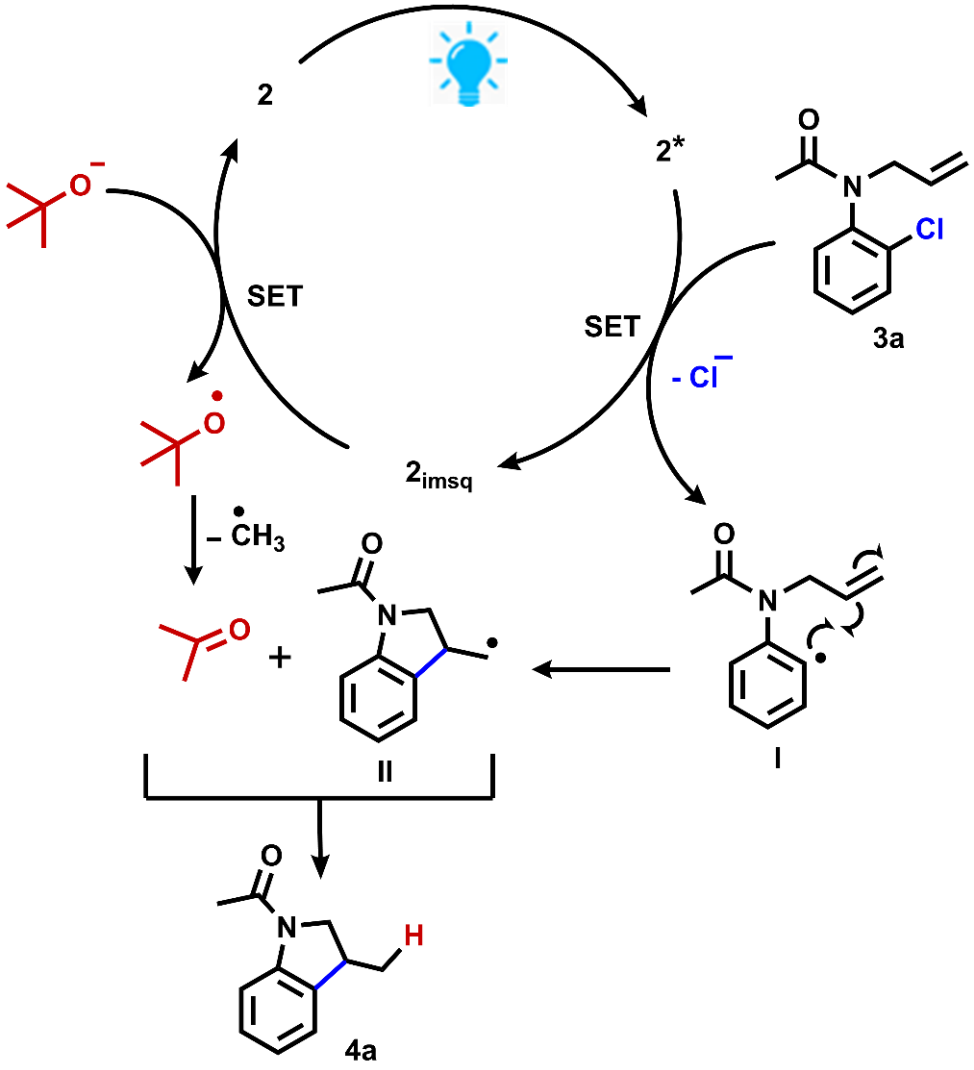

Scheme 3.8. Plausible catalytic cycle.

After supplying the redox noninnocent NNN pincer supplies electron during the reductive cleavage of C-Cl, oxidized NNN pincer behaves as an electron sink and gets the electron back.

In essence the role of KO^{t}Bu is more to providing help to iminosemiquinonate from $\mathbf{2_{imq}}$ to come back to 2 via electron transfer processes by forming tert-butoxide radical. The KO^{t}Bu plays a preponderant role and overall tunes the redox transformation. Upon electron transfer, once the **2** is generated in the presence of a KO^{t}Bu, the tert-butoxide radical is generated which immediately affords acetone via methyl radical elimination.[95] Impressively, acetone is also well established as source of hydrogen atom.[97] Finally, the hydrogen atom abstraction happens to provide desired product. An alternative possibility of HAT by solvent was also considered. In such case, it is logical to perform deuterium labelling experiment. For the sake of argument, a quantitative reaction was set in the presence of deuterated acetonitrile. From ^{1}H NMR analysis, there was no deuterium incorporation was observed which conclude that the last stage hydrogen atom transfer is taking place from insitu generated acetone instead of solvent acetonitrile.

3.15. Conclusions

In Conclusion, we have synthesis indolines and oxindoles exclusively via photo-induced cyclization of substituted aryl chlorides. Electron rich and conjugated behaviour of trianionic NNN pincer in fully deprotonated form provide easily accessible redox states. Low oxidation potential at ground state is further enhanced once the molecule is excited by light irradiation that facilitates subsequent electron transfer from electron rich trianionic NNN pincer backbone. KO^{t}Bu plays three major role, activation of catalyst, resuscitate the pincer from oxidized form and fount of hydrogen atom transfer. A plethora of challenging indoline and oxindoles has been accomplished by this methodology proving the great utility of metal free catalysis when both catalyst and KO^{t}Bu plays a predominant role. A series of controls and intermediate isolation provide reliable evidences for reductive cleavage of the substrate and fate of KO^{t}Bu.

3.16. Experimental Section

3.16.1. General Procedure for Optimization of Reaction Condition

An adequately dried Schlenk flask (overnight at 120 °C oven) with magnetic stirring bar was charged with *N*-allyl-*N*-(2-chlorophenyl)acetamide 3 (42 mg, 0.2 mmol), catalyst 1 (3 mg, 5 mol%). 1 mL of dry acetonitrile was added to make a brown-colored solution under N_2 atmosphere. The color of the reaction mixture instantly changed to yellowish brown upon the addition of KO^{t}Bu (34 mg, 0.3 mmol) into the reaction flask. The flask was kept under blue light (450 nm, 15 W) at room temperature. The Schlenk flask was placed 6-7 inch away from the light source. After 6 hours of stirring, the solvent was removed under vacuum. The crude

reaction mixture was dissolved in DCM and organic layer was washed with water. The organic layer was collected and dried over anhydrous MgSO4. DCM was removed using rotary evaporator. The yield of the desired product 1-(3-methylindolin-1-yl)ethan-1-one **4a** was determined by NMR analysis.

3.16.2. Procedure for Trapping of Intermediates using TEMPO Radical

An overnight-dried Schlenk flask with magnetic stirring bar was charged with *N*-allyl-*N*-(2-chlorophenyl)acetamide **3** (42 mg, 0.2 mmol), catalyst **1** (3 mg, 5 mol%). 1 mL of dry acetonitrile was added to make a brown colored solution under N_2 atmosphere. The color of the reaction mixture instantly changed to yellowish brown after the addition of KO^tBu (34 mg, 0.4 mmol) into the reaction flask. After that TEMPO (32 mg, 0.2 mmol) was added to above reaction mixture. The flask was kept under blue light at room temperature. After 6 h of stirring, the reaction was ceased. The TEMPO adduct of *N*-allyl-*N*-(phenyl)acetamide radical was analysed by High-Resolution Mass Spectrometry (HRMS).

For **7**, HRMS (ESI, m/z) calcd. for $C_{20}H_{31}N_2O_2$ $[M + H]^+$: 331.2386; found: 331.2381.

For **8**, HRMS (ESI, m/z) calcd. for $C_{10}H_{22}NO$ $[M + H]^+$: 172.1701; found: 172.1691.

3.16.3. General Procedure for Reaction

The oven-dried Schlenk flask with magnetic stirring bar was charged with 2-chloro-N,N-dialkylbenzamide (0.2 mmol), catalyst **1** (3 mg, 5 mol%) and KO^tBu (0.4 mmol) under N_2 atmosphere. 1 ml of dry and degassed THF was added to above reaction mixture. The reaction mixture was stirred under blue light at room temperature for 12 hours. After the completion of the reaction, the solvent was removed under rotary evaporator. The desired product was isolated by column chromatography using hexane/ethylacetate mixture. The isolated pure product was further analysed by ^1H and ^{13}C NMR spectroscopies.

3.16.4. Spectroscopic Characterization of Cyclized Products

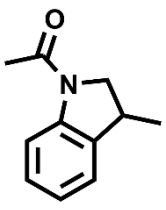

1-(3-methylindolin-1-yl)ethan-1-one (4a)[92]

The compound was purified by column chromatography (silica gel) with 10% mixture of ethyl acetate in hexane to give the product as a white solid (86 mg, 98%).

^{1}H NMR (400 MHz, $CDCl_3$) δ 8.19 (*d*, *J* = 8.1 Hz, 1H), 7.21 (*d*, *J* = 7.6 Hz, 1H), 7.19 – 7.14 (*m*, 1H), 7.04 (*t*, *J* = 7.6 Hz, 1H), 4.21 (*t*, *J* = 9.5

Hz, 1H), 3.57 (*dd*, *J* = 9.9, 6.7 Hz, 1H), 3.50 (*dd*, *J* = 15.9, 6.6 Hz, 1H), 2.22 (*s*, 3H), 1.36 (*d*, *J* = 6.8 Hz, 3H).

^{13}C NMR (101 MHz, $CDCl_3$) δ 168.80, 142.48, 136.42, 127.85, 123.83, 123.48, 116.99, 57.06, 34.87, 24.38, 20.40.

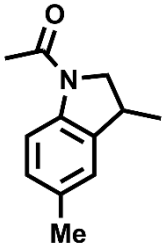

1-(3,5-dimethylindolin-1-yl)ethan-1-one (4b)[92]

The compound was purified by column chromatography (silica gel) with 10% mixture of ethyl acetate in hexane to give the product as a white solid (84 mg, 89%).

^{1}H NMR (400 MHz, $CDCl_3$) δ 8.05 (*d*, *J* = 8.2 Hz, 1H), 7.00 (*d*, *J* = 5.5 Hz, 1H), 6.96 (*s*, 1H), 4.18 (*t*, *J* = 9.7 Hz, 1H), 3.55 (*dd*, *J* = 10.0, 6.7 Hz, 1H), 3.45 (*dq*, *J* = 13.7, 6.9 Hz, 1H), 2.31 (*s*, 3H), 2.20 (*s*, 3H), 1.33 (*d*, *J* = 6.8 Hz, 3H).

^{13}C NMR (101 MHz, $CDCl_3$) δ 168.42, 140.17, 136.51, 133.41, 128.24, 124.11, 116.67, 57.17, 34.81, 24.23, 21.16, 20.35.

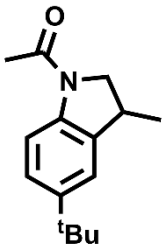

1-(5-(tert-butyl)-3-methylindolin-1-yl)ethan-1-one (4c)

The compound was purified by column chromatography (silica gel) with 10% mixture of ethyl acetate in hexane to give the product as a white solid (97 mg, 84%).

^{1}H NMR (400 MHz, $CDCl_3$) δ 8.09 (*d*, *J* = 8.5 Hz, 1H), 7.23 (*dd*, *J* = 8.5, 2.0 Hz, 1H), 7.17 (*t*, *J* = 1.5 Hz, 1H), 4.20 (*t*, *J* = 9.6 Hz, 1H), 3.56 (*dd*, *J* = 10.0, 6.8 Hz, 1H), 3.48 (*dq*, *J* = 13.8, 6.9 Hz, 1H), 2.20 (*s*, 3H), 1.37 (*d*, *J* = 6.8 Hz, 3H), 1.31 (*s*, 9H).

^{13}C NMR (101 MHz, $CDCl_3$) δ 168.42, 147.04, 140.16, 136.12, 124.69, 120.30, 116.43, 57.27, 35.05, 34.63, 31.67, 24.21, 20.37.

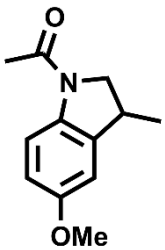

1-(5-methoxy-3-methylindolin-1-yl)ethan-1-one (4d)

The compound was purified by column chromatography (silica gel) with 10% mixture of ethyl acetate in hexane to give the product as a white solid (85 mg, 83%).

^{1}H NMR (400 MHz, $CDCl_3$) δ 8.12 – 8.07 (*m*, 1H), 6.72 (*ddd*, *J* = 7.1, 2.7, 0.8 Hz, 2H), 4.20 (*dd*, *J* = 10.1, 9.3 Hz, 1H), 3.78 (*s*, 3H), 3.56 (*dd*,

J = 10.1, 6.8 Hz, 1H), 3.46 (*dd*, *J* = 15.9, 6.7 Hz, 1H), 2.19 (*s*, 3H), 1.34 (*d*, *J* = 6.9 Hz, 3H).

^{13}C NMR (101 MHz, $CDCl_3$) δ 168.05, 156.53, 138.08, 136.27, 117.60, 112.04, 109.95, 57.23, 55.74, 34.99, 24.07, 20.23.

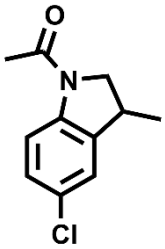

1-(5-chloro-3-methylindolin-1-yl)ethan-1-one (4e)[92]

The compound was purified by column chromatography (silica gel) with 10% mixture of ethyl acetate in hexane to give the product as a white solid (80 mg, 76%).

^{1}H NMR (400 MHz, $CDCl_3$) δ 8.10 (*d*, *J* = 8.6 Hz, 1H), 7.14 (*dd*, *J* = 8.6, 2.2 Hz, 1H), 7.11 – 7.08 (*m*, 1H), 4.21 (*t*, *J* = 9.8 Hz, 1H), 3.58 (*dd*, *J* = 10.1, 6.8 Hz, 1H), 3.47 (*dq*, *J* = 13.9, 7.0 Hz, 1H), 2.20 (*s*, 3H), 1.34 (*d*, *J* = 6.9 Hz, 3H).

^{13}C NMR (101 MHz, $CDCl_3$) δ 168.78, 141.12, 138.33, 128.64, 127.72, 123.77, 117.87, 57.12, 34.74, 24.20, 20.23.

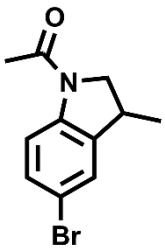

1-(5-bromo-3-methylindolin-1-yl)ethan-1-one (4f)[103]

The compound was purified by column chromatography (silica gel) with 10% mixture of ethyl acetate in hexane to give the product as a white solid (86 mg, 68%).

^{1}H NMR (400 MHz, $CDCl_3$) δ 8.05 (*d*, *J* = 8.6 Hz, 1H), 7.30 – 7.27 (*m*, 1H), 7.24 (*t*, *J* = 1.6 Hz, 1H), 4.20 (*t*, *J* = 9.7 Hz, 1H), 3.57 (*dd*, *J* = 10.1, 6.8 Hz, 1H), 3.48 (*dt*, *J* = 9.3, 6.7 Hz, 1H), 2.20 (*s*, 3H), 1.34 (*d*, *J* = 6.9 Hz, 3H).

^{13}C NMR (101 MHz, $CDCl_3$) δ 168.85, 141.60, 138.72, 130.66, 126.68, 118.35, 116.19, 57.08, 34.72, 24.24, 20.26.

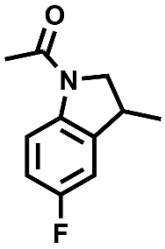

1-(5-fluoro-3-methylindolin-1-yl)ethan-1-one (4g)[92]

The compound was purified by column chromatography (silica gel) with 10% mixture of ethyl acetate in hexane to give the product as a white solid (77 mg, 80%).

^{1}H NMR (400 MHz, $CDCl_3$) δ 8.13 (*dd*, *J* = 8.7, 4.9 Hz, 1H), 6.90 – 6.82 (*m*, 2H), 4.22 (*t*, *J* = 9.8 Hz, 1H), 3.59 (*dd*, *J* = 10.2, 6.8 Hz, 1H), 3.48 (*dq*, *J* = 14.3, 7.0 Hz, 1H), 2.20 (*s*, 3H), 1.34 (*d*, *J* = 6.9 Hz, 3H).

^{13}C NMR (101 MHz, $CDCl_3$) δ 168.49, 160.78(*d*, $^1J_{C-F}$= 242 Hz), 138.58(*d*, $^3J_{C-F}$= 8 Hz), 138.50(*d*, $^3J_{C-F}$= 8 Hz), 117.86(*d*, $^3J_{C-F}$= 8 Hz), 114.13(*d*, $^3J_{C-F}$= 23 Hz), 110.91(*d*, $^3J_{C-F}$= 24 Hz), 57.24, 34.85, 24.11, 20.17.

^{19}F NMR (376 MHz, $CDCl_3$) δ -119.20.

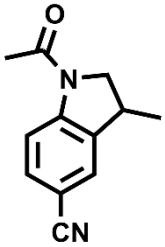

1-acetyl-3-methylindoline-5-carbonitrile (4h)[92]

The compound was purified by column chromatography (silica gel) with 15% mixture of ethyl acetate in hexane to give the product as a white solid (92 mg, 92%).

^{1}H NMR (400 MHz, $CDCl_3$) δ 8.26 (*d*, *J* = 8.4 Hz, 1H), 7.51 (*dd*, *J* = 8.3, 1.7 Hz, 1H), 7.41 (*s*, 1H), 4.28 (*t*, *J* = 9.9 Hz, 1H), 3.65 (*dd*, *J* = 10.1, 6.7 Hz, 1H), 3.53 (*d*, *J* = 6.9 Hz, 1H), 2.25 (*s*, 3H), 1.38 (*d*, *J* = 6.9 Hz, 3H). **^{13}C NMR** (101 MHz, $CDCl_3$) δ 169.57, 146.17, 137.47, 133.08, 127.27, 119.47, 117.19, 106.61, 57.12, 34.54, 24.45, 20.33.

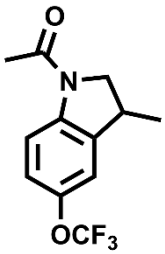

1-(3-methyl-5-(trifluoromethoxy)indolin-1-yl)ethan-1-one (4i)[103]

The compound was purified by column chromatography (silica gel) with 10% mixture of ethyl acetate in hexane to give the product as a white solid (115 mg, 89%).

^{1}H NMR (400 MHz, $CDCl_3$) δ 8.19 (*d*, *J* = 8.7 Hz, 1H), 7.00 (*s*, 1H), 4.25 (*t*, *J* = 9.8 Hz, 1H), 3.62 (*dd*, *J* = 10.1, 6.8 Hz, 1H), 3.51 (*d*, *J* = 7.0 Hz, 1H), 2.22 (*s*, 3H), 1.37 (*d*, *J* = 6.8 Hz, 3H).

^{13}C NMR (101 MHz, $CDCl_3$) δ 168.84, 145.29, 145.27, 141.13, 138.22, 121.91, 120.65, 119.36, 117.55, 116.80, 57.25, 34.79, 29.82, 24.19, 20.17.

^{19}F NMR (376 MHz, $CDCl_3$) δ -58.13.

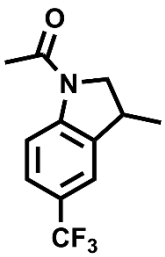

1-(3-methyl-5-(trifluoromethyl)indolin-1-yl)ethan-1-one(4j)[103]

The compound was purified by column chromatography (silica gel) with 10% mixture of ethyl acetate in hexane to give the product as a white solid (109 mg, 90%).

^{1}H NMR (400 MHz, $CDCl_3$) δ 8.25 (*d*, *J* = 8.4 Hz, 1H), 7.45 (*d*, *J* = 8.5 Hz, 1H), 7.37 (*s*, 1H), 4.26 (*t*, *J* = 9.8 Hz, 1H), 3.64 (*dd*, *J* = 10.1, 6.8 Hz, 1H), 3.53 (*d*, *J* = 6.9 Hz, 1H), 2.24 (*s*, 3H), 1.38 (*d*, *J* = 6.8 Hz, 3H).

^{13}C NMR (101 MHz, $CDCl_3$) δ 169.35, 145.27, 137.03, 125.58, 120.59, 116.68, 57.24, 34.67, 32.04, 29.82, 24.37, 20.29, 14.25.

^{19}F NMR (376 MHz, $CDCl_3$) δ -61.59.

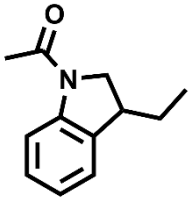

1-(3-ethylindolin-1-yl)ethan-1-one(4k)[92]

The compound was purified by column chromatography (silica gel) with 10% mixture of ethyl acetate in hexane to give the product as a white solid (86 mg, 91%).

^{1}H NMR (400 MHz, $CDCl_3$) δ 8.19 (*d*, *J* = 8.1 Hz, 1H), 7.18 (*dd*, *J* = 17.5, 8.0 Hz, 2H), 7.02 (*t*, *J* = 7.5 Hz, 1H), 4.18 – 4.09 (*m*, 1H), 3.67 (*dd*, *J* = 10.3, 5.9 Hz, 1H), 3.33 (*tt*, *J* = 9.5, 5.3 Hz, 1H), 2.22 (*s*, 3H), 1.84 (*td*, *J* = 8.1, 7.3, 3.6 Hz, 1H), 1.64 – 1.54 (*m*, 1H), 0.98 (*t*, *J* = 7.4 Hz, 3H).

^{13}C NMR (101 MHz, $CDCl_3$) δ 168.78, 142.81, 135.05, 127.87, 123.91, 123.66, 116.98, 54.80, 41.57, 28.22, 24.37, 11.27.

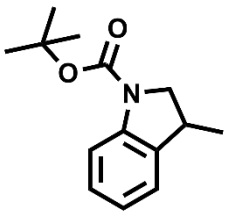

tert-butyl 3-methylindoline-1-carboxylate(4l)[90]

The compound was purified by column chromatography (silica gel) with 1% mixture of ethyl acetate in hexane to give the product as a white solid (108 mg, 93%).

^{1}H NMR (400 MHz, $CDCl_3$) δ 7.15 (*dd*, *J* = 18.5, 7.5 Hz, 3H), 6.95 (*t*, *J* = 7.4 Hz, 1H), 4.14 (*t*, *J* = 10.3 Hz, 1H), 3.50 (*t*, *J* = 9.9 Hz, 1H), 3.39 (*dt*, *J* = 9.4, 6.8 Hz, 1H), 1.57 (*s*, 9H), 1.32 (*d*, *J* = 6.9 Hz, 3H).

^{13}C NMR (101 MHz, $CDCl_3$) δ 152.66, 127.61, 123.64, 122.31, 114.68, 55.72, 34.13, 28.56, 20.37.

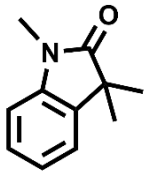

1,3,3-trimethylindolin-2-one (6a)[59]

The compound was purified by column chromatography (silica gel) with 5% mixture of ethyl acetate in hexane to give the product as a colorless oil (81 mg, 92%).

^{1}H NMR (400 MHz, $CDCl_3$) δ 7.27 – 7.21 (*m*, 1H), 7.19 (*d*, *J* = 7.3 Hz, 1H), 7.04 (*t*, *J* = 7.5 Hz, 1H), 6.83 (*d*, *J* = 7.8 Hz, 1H), 3.20 (*s*, 3H), 1.35 (*s*, 6H).

^{13}C NMR (101 MHz, $CDCl_3$) δ 181.20, 142.49, 135.65, 127.58, 122.40, 122.15, 107.95, 44.02, 26.08, 24.28.

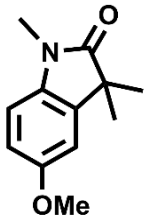

5-methoxy-1,3,3-trimethylindolin-2-one (6b)[59]

The compound was purified by column chromatography (silica gel) with 10% mixture of ethyl acetate in hexane to give the product as a colorless oil (90 mg, 88%).

^{1}H NMR (400 MHz, $CDCl_3$) δ 6.81 (*d*, *J* = 2.3 Hz, 1H), 6.76 (*dd*, *J* = 8.4, 2.4 Hz, 1H), 6.73 (*d*, *J* = 8.3 Hz, 1H), 3.78 (*s*, 3H), 3.17 (*s*, 3H), 1.34 (*s*, 6H).

^{13}C NMR (101 MHz, $CDCl_3$) δ 181.10, 156.14, 137.30, 136.22, 111.61, 110.12, 108.31, 55.86, 44.68, 26.35, 24.47.

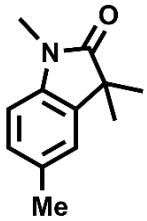

1,3,3,5-tetramethylindolin-2-one (6c)[59]

The compound was purified by column chromatography (silica gel) with 5% mixture of ethyl acetate in hexane to give the product as a yellow oil (80 mg, 86%).

^{1}H NMR (400 MHz, $CDCl_3$) δ 7.06 (*ddd*, *J* = 7.8, 1.7, 0.9 Hz, 1H), 7.03 – 7.01 (*m*, 1H), 6.73 (*d*, *J* = 7.8 Hz, 1H), 3.19 (*s*, 3H), 2.34 (*s*, 3H), 1.35 (*s*, 6H).

^{13}C NMR (101 MHz, $CDCl_3$) δ 181.41, 140.29, 135.93, 132.05, 127.90, 123.22, 107.81, 44.29, 26.29, 24.48, 24.46, 21.18.

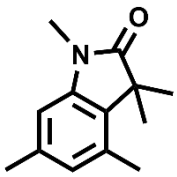

1,3,3,4,6-pentamethylindolin-2-one (6d)[104]

The compound was purified by column chromatography (silica gel) with 5% mixture of ethyl acetate in hexane to give the product as a white solid (77 mg, 76%).

^{1}H NMR (400 MHz, $CDCl_3$) δ 6.65 (*s*, 1H), 6.53 (*s*, 1H), 3.18 (*s*, 3H), 2.35 (*s*, 3H), 2.34 (*s*, 3H), 1.43 (*s*, 6H).

^{13}C NMR (101 MHz, $CDCl_3$) δ 181.85, 143.16, 137.60, 133.88, 129.84, 125.64, 106.87, 44.85, 26.39, 22.64, 21.63, 18.13.

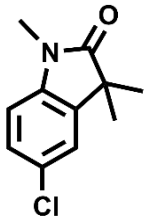

5-chloro-1,3,3-trimethylindolin-2-one (6e)[59]

The compound was purified by column chromatography (silica gel) with 5% mixture of ethyl acetate in hexane to give the product as a yellow solid (76 mg, 73%).

^{1}H NMR (400 MHz, $CDCl_3$) δ 7.22 (*dd*, *J* = 8.2, 2.2 Hz, 1H), 7.16 (*d*, *J* = 2.0 Hz, 1H), 6.75 (*d*, *J* = 8.2 Hz, 1H), 3.19 (*s*, 3H), 1.35 (*s*, 6H).

^{13}C NMR (101 MHz, $CDCl_3$) δ 180.93, 141.30, 137.57, 127.97, 127.67, 123.05, 109.07, 44.58, 26.45, 24.38.

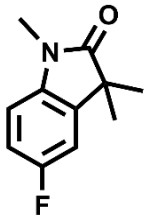

5-fluoro-1,3,3-trimethylindolin-2-one (6f)[59]

The compound was purified by column chromatography (silica gel) with 5% mixture of ethyl acetate in hexane to give the product as a yellow solid (82 mg, 85%).

^{1}H NMR (400 MHz, $CDCl_3$) δ 6.98 – 6.89 (*m*, 2H), 6.74 (*dd*, *J* = 9.2, 4.2 Hz, 1H), 3.20 (*s*, 3H), 1.36 (*s*, 6H).

^{13}C NMR (101 MHz, $CDCl_3$) δ 181.10, 158.33 (*d*, $^{1}J_{C\text{-}F}$= 241 Hz), 138.64(*d*, $^{4}J_{C\text{-}F}$= 2 Hz), 137.55(*d*, $^{3}J_{C\text{-}F}$= 8 Hz), 113.74(*d*, $^{2}J_{C\text{-}F}$= 24 Hz), 110.54(*d*, $^{2}J_{C\text{-}F}$= 24 Hz), 108.50(*d*, $^{3}J_{C\text{-}F}$= 8 Hz), 44.79, 26.48, 24.41.

^{19}F NMR (376 MHz, $CDCl_3$) δ -120.90.

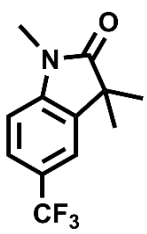

1,3,3-trimethyl-5-(trifluoromethyl)indolin-2-one (6g)[59]

The compound was purified by column chromatography (silica gel) with 5% mixture of ethyl acetate in hexane to give the product as a white solid (100 mg, 82%).

^{1}H NMR (400 MHz, $CDCl_3$) δ 7.54 (*d*, *J* = 9.0 Hz, 1H), 7.42 (*s*, 1H), 6.91 (*d*, *J* = 8.2 Hz, 1H), 3.24 (*s*, 3H), 1.39 (*s*, 6H).

^{13}C NMR (101 MHz, $CDCl_3$) δ 181.36, 145.74, 136.41, 125.64(*q*, $^{3}J_{C-F}$= 4 Hz), 124.70(*q*, $^{2}J_{C-F}$= 32 Hz), 123.24(*q*, $^{1}J_{C-F}$= 272 Hz), 119.45(*q*, $^{3}J_{C-F}$= 4 Hz), 107.88, 44.31, 26.53, 24.34.

^{19}F NMR (376 MHz, $CDCl_3$) δ -61.34.

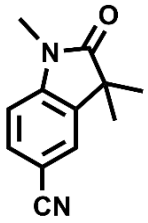

1,3,3-trimethyl-2-oxoindoline-5-carbonitrile (6i)[59]

The compound was purified by column chromatography (silica gel) with 10% mixture of ethyl acetate in hexane to give the product as a white solid (92 mg, 92%).

^{1}H NMR (400 MHz, $CDCl_3$) δ 7.60 (*dd*, *J* = 8.1, 1.6 Hz, 1H), 7.45 (*d*, *J* = 1.6 Hz, 1H), 6.91 (*d*, *J* = 8.1 Hz, 1H), 3.24 (*s*, 3H), 1.39 (*s*, 6H).

^{13}C NMR (101 MHz, $CDCl_3$) δ 181.04, 146.69, 136.83, 133.31, 125.86, 119.44, 108.58, 105.71, 44.15, 26.59, 24.30.

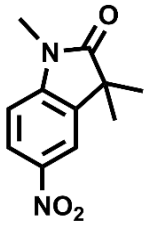

1,3,3-trimethyl-5-nitroindolin-2-one (6h)[59]

The compound was purified by column chromatography (silica gel) with 10% mixture of ethyl acetate in hexane to give the product as a yellow solid (82 mg, 75%).

^{1}H NMR (400 MHz, $CDCl_3$) δ 8.20 (*dd*, *J* = 8.6, 2.2 Hz, 1H), 8.05 (*d*, *J* = 2.2 Hz, 1H), 6.92 (*d*, *J* = 8.6 Hz, 1H), 3.26 (*d*, *J* = 1.1 Hz, 3H), 1.39 (*d*, *J* = 1.3 Hz, 6H).

^{13}C NMR (101 MHz, $CDCl_3$) δ 181.28, 148.44, 143.44, 136.46, 125.20, 118.29, 107.68, 44.22, 26.67, 24.15.

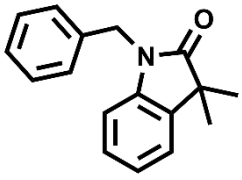

1-benzyl-3,3-dimethylindolin-2-one (6k)[59]

The compound was purified by column chromatography (silica gel) with 5% mixture of ethyl acetate in hexane to give the product as a white solid (93 mg, 74%).

^{1}H NMR (400 MHz, $CDCl_3$) δ 7.30 (*dd*, *J* = 13.8, 6.7 Hz, 5H), 7.22 (*d*, *J* = 7.3 Hz, 1H), 7.14 (*t*, *J* = 7.1 Hz, 1H), 7.03 (*t*, *J* = 7.5 Hz, 1H), 6.72 (*d*, *J* = 7.8 Hz, 1H), 4.92 (*s*, 2H), 1.44 (*s*, 6H).

^{13}C NMR (101 MHz, $CDCl_3$) δ 181.60, 141.79, 136.21, 135.92, 128.90, 127.70, 127.66, 127.29, 122.63, 122.46, 109.21, 44.33, 43.65, 24.68.

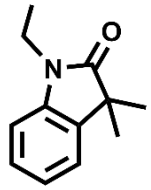

1-ethyl-3,3-dimethylindolin-2-one (6l)[105]

The compound was purified by column chromatography (silica gel) with 5% mixture of ethyl acetate in hexane to give the product as a white solid (73 mg, 77%).

^{1}H NMR (400 MHz, $CDCl_3$) δ 7.26 (*dd*, *J* = 7.7, 1.3 Hz, 1H), 7.23 – 7.19 (*m*, 1H), 7.05 (*td*, *J* = 7.5, 1.0 Hz, 1H), 6.87 (*dd*, *J* = 7.8, 0.8 Hz, 1H), 3.76 (*q*, *J* = 7.2 Hz, 2H), 1.36 (*s*, 6H), 1.26 (*t*, *J* = 7.2 Hz, 3H).

^{13}C NMR (101 MHz, $CDCl_3$) δ 168.84, 145.29, 145.27, 141.13, 138.22, 121.91, 120.65, 119.36, 117.55, 116.80, 57.25, 34.79, 29.82, 24.19, 20.17.

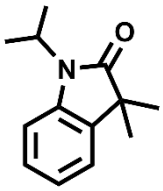

1-isopropyl-3,3-dimethylindolin-2-one (6m)[105]

The compound was purified by column chromatography (silica gel) with 5% mixture of ethyl acetate in hexane to give the product as a white solid (82 mg, 81%).

^{1}H NMR (400 MHz, $CDCl_3$) δ 7.22 (*ddd*, *J* = 8.5, 7.5, 1.2 Hz, 2H), 7.03 (*t*, *J* = 7.4 Hz, 2H), 4.66 (*hept*, *J* = 7.1 Hz, 1H), 1.48 (*d*, *J* = 7.1 Hz, 6H), 1.35 (*s*, 6H).

^{13}C NMR (101 MHz, $CDCl_3$) δ 181.17, 141.29, 136.53, 127.44, 122.66, 121.99, 110.01, 43.97, 43.53, 24.63, 19.56.

3.17. References:

1. Peris, E.; Crabtree, R. H. Key Factors in Pincer Ligand Design. *Chem. Soc. Rev.* **2018**, *47*, 1959−1968.
2. Alig, L.; Fritz, M.; Schneider, S. First-Row Transition Metal (De)Hydrogenation Catalysis Based on Functional Pincer Ligands. *Chem. Rev.* **2019**, *119*, 2681−2751.
3. Szabo, K. J.; Wendt, O. F. Pincer and Pincer-type Complexes: Applications in Organic Synthesis and Catalysis; John Wiley & Sons: **2014**.
4. Ozerov, O. V. Rigid PNP Pincer ligands and Their Transition Metal Complexes. In the Chemistry of Pincer Compounds, Morales-Morales, D.; Jensen, C. M., Eds.; Elsevier: Amsterdam, **2007**.
5. Eberhardt, N. A.; Guan, H. Reduction of CO_2 Mediated or Catalyzed by Pincer Complexes. In Pincer Compounds: Chemistry and Applications, Morales-Morales, D., Ed.; Elsevier: Amsterdam, **2018**.
6. Ito, J. I.; Nishiyama, H. Chiral Pincer Complexes for Asymmetric Reactions. In Pincer Compounds: Chemistry and Applications, Morales-Morales, D., Ed.; Elsevier: Amsterdam, **2018**.
7. Roddick, D. M. Tuning of PCP Pincer Ligand Electronic and Steric Properties. In Organometallic Pincer Chemistry, van Koten, G.; Milstein, D., Eds.; Springer Berlin Heidelberg: Berlin, Heidelberg, **2013**; pp. 49−88.
8. Valdés, H.; García-Eleno, M. A.; Canseco-Gonzalez, D.; Morales-Morales, D. Recent Advances in Catalysis with Transition-Metal Pincer Compounds. *ChemCatChem* **2018**, *10*, 3136−3172.
9. St. John, A.; Goldberg, K. I.; Heinekey, D. M. Pincer Complexes as Catalysts for Amine Borane Dehydrogenation. In Organometallic Pincer Chemistry, van Koten, G.; Milstein, D., Eds.; Springer Berlin Heidelberg: Berlin, Heidelberg, **2013**; pp. 271−287.
10. Szabó, K. J. Pincer Complexes as Catalysts in Organic Chemistry. In Organometallic Pincer Chemistry, van Koten, G.; Milstein, D., Eds.; Springer Berlin Heidelberg: Berlin, Heidelberg, **2013**; pp. 203−241.
11. Freeman, G. R.; Williams, J. A. G. Metal Complexes of Pincer Ligands: Excited States, Photochemistry, and Luminescence. In Organometallic Pincer Chemistry, van Koten, G.; Milstein, D., Eds.; Springer Berlin Heidelberg: Berlin, Heidelberg, **2013**; pp. 89−129.

12. Poverenov, E.; Milstein, D. Noninnocent Behavior of PCP and PCN Pincer Ligands of Late Metal Complexes. In Organometallic Pincer Chemistry, van Koten, G.; Milstein, D., Eds.; Springer Berlin Heidelberg: Berlin, Heidelberg, **2013**; pp. 21−47.
13. Khusnutdinova, J. R.; Milstein, D. Metal−Ligand Cooperation. *Angew. Chem., Int. Ed.* **2015**, 54, 12236−12273.
14. Munhá, R. F.; Zarkesh, R. A.; Heyduk, A. F. Tuning the Electronic and Steric Parameters of a Redox-Active Tris(amido) Ligand. *Inorg. Chem.* **2013**, *52*, 11244−11255.
15. Haneline, M. R.; Heyduk, A. F. C−C Bond-Forming Reductive Elimination from a Zirconium(IV) Redox-Active Ligand Complex. *J. Am. Chem. Soc.* **2006**, *128*, 8410−8411.
16. Singh, K.; Kundu, A.; Adhikari, D. Ligand-Based Redox: Catalytic Applications and Mechanistic Aspects. *ACS Catal.* **2022**, *12*, 13075−13107.
17. Chmiel, A. F.; Williams, O. P.; Chernowsky, C. P.; Yeung, C. S.; Wickens, Z. K. Non-innocent Radical Ion Intermediates in Photoredox Catalysis: Parallel Reduction Modes Enable Coupling of Diverse Aryl Chlorides. *J. Am. Chem. Soc.* **2021**, *143*, 10882−10889.
18. Pavlishchuk, V. V.; Addison, A. W. Conversion Constants for Redox Potentials Measured versus Different Reference Electrodes in Acetonitrile Solutions at 25 °C. *Inorg. Chim. Acta* **2000**, *298*, 97−102.
19. Arias-Rotondo, D. M.; McCusker, J. K. The Photophysics of Photoredox Catalysis: A Roadmap for Catalyst Design. *Chem. Soc. Rev.* **2016**, *45*, 5803−5820.
20. Wenger, O. S. Photoactive Complexes with Earth-Abundant Metals. *J. Am. Chem. Soc.* **2018**, *140*, 13522−13533.
21. Rehm, D.; Weller, A. Kinetics of Fluorescence Quenching by Electron and H-Atom Transfer. *Isr. J. Chem.* **1970**, *8*, 259−271.
22. Xu, J.; Cao, J.; Wu, X.; Wang, H.; Yang, X.; Tang, X.; Toh, R. W.; Zhou, R.; Yeow, E. K. L.; Wu, J. Unveiling Extreme Photoreduction Potentials of Donor−Acceptor Cyanoarenes to Access Aryl Radicals from Aryl Chlorides. *J. Am. Chem. Soc.* **2021**, *143*, 13266−13273.
23. Zhao, Y.; Truhlar, D. G. The M06 Suite of Density Functionals for Main Group Thermochemistry, Thermochemical Kinetics, Non-covalent Interactions, Excited States, and Transition Elements: Two New Functionals and Systematic Testing of Four

M06-Class Functionals and 12 other Functionals. *Theor. Chem. Acc.* **2008**, *120*, 215−241.

24. Shon, J.-H.; Kim, D.; Rathnayake, M. D.; Sittel, S.; Weaver, J.; Teets, T. S. Photoredox Catalysis on Unactivated Substrates with Strongly Reducing Iridium Photosensitizers. *Chem. Sci.* **2021**, *12*, 4069−4078.
25. Mfuh, A. M.; Doyle, J. D.; Chhetri, B.; Arman, H. D.; Larionov, O. V. Scalable, Metal- and Additive-Free, Photoinduced Borylation of Haloarenes and Quaternary Arylammonium Salts. *J. Am. Chem. Soc.* **2016**, *138*, 2985−2988.
26. Qiao, Y.; Yang, Q.; Schelter, E. J. Photoinduced Miyaura Borylation by a Rare-Earth-Metal Photoreductant: The Hexachlorocerate(III) Anion. *Angew. Chem., Int. Ed.* **2018**, *57*, 10999−11003.
27. Cybularczyk-Cecotka, M.; Szczepanik, J.; Giedyk, M. Photocatalytic Strategies for the Activation of Organic Chlorides. *Nat. Catal.* **2020**, *3*, 872−886.
28. Koike, T.; Akita, M. Visible-Light Radical Reaction Designed by Ru- and Ir-Based Photoredox Catalysis. *Inorg. Chem. Front.* **2014**, *1*, 562−576.
29. Blanksby, S. J.; Ellison, G. B. Bond Dissociation Energies of Organic Molecules. *Acc. Chem. Res.* **2003**, *36*, 255−263.
30. Wertjes, W. C.; Wolfe, L. C.; Waller, P. J.; Kalyani, D. Nickel or Phenanthroline Mediated Intramolecular Arylation of sp^3 C−H Bonds Using Aryl Halides. *Org. Lett.* **2013**, *15*, 5986−5989.
31. Wagner, A. M.; Hickman, A. J.; Sanford, M. S. Platinum-Catalyzed C−H Arylation of Simple Arenes. *J. Am. Chem. Soc.* **2013**, *135*, 15710−15713.
32. Gensch, T.; Hopkinson, M. N.; Glorius, F.; Wencel-Delord, J. Mild Metal-Catalyzed C−H Activation: Examples and Concepts. *Chem. Soc. Rev.* **2016**, *45*, 2900−2936.
33. Wedi, P.; Farizyan, M.; Bergander, K.; Mück-Lichtenfeld, C.; van Gemmeren, M. Mechanism of the Arene-Limited Nondirected C−H Activation of Arenes with Palladium. *Angew. Chem., Int. Ed*. **2021**, *60*, 15641−15649.
34. Degorce, S. L.; Bodnarchuk, M. S.; Scott, J. S. Lowering Lipophilicity by Adding Carbon: AzaSpiroHeptanes, a logD Lowering Twist. *ACS Med. Chem. Lett.* **2019**, *10*, 1198−1204.
35. Dai, P.; Ma, J.; Huang, W.; Chen, W.; Wu, N.; Wu, S.; Li, Y.; Cheng, X.; Tan, R. Photoredox C−F Quaternary Annulation Catalyzed by a Strongly Reducing Iridium Species. *ACS Catal.* **2018**, *8*, 802−806.

36. Zhou, F.; Liu, Y.-L.; Zhou, J. Catalytic Asymmetric Synthesis of Oxindoles Bearing a Tetrasubstituted Stereocenter at the C-3 Position. *Adv. Synth. Catal.* **2010**, *352*, 1381−1407.
37. Marti, C.; Carreira, E. M. Construction of Spiro[pyrrolidine-3,3′-oxindoles] − Recent Applications to the Synthesis of Oxindole Alkaloids. *Eur. J. Org. Chem.* **2003**, *2003*, 2209−2219.
38. Hibino, S.; Choshi, T. Simple indole alkaloids and those with a nonrearranged monoterpenoid unit. *Nat. Prod. Rep.* **2001**, *18*, 66−87.
39. Chen, J.-Q.; Wei, Y.-L.; Xu, G.-Q.; Liang, Y.-M.; Xu, P.-F. Intramolecular 1,5-H Transfer Reaction of Aryl Iodides Through Visible Light Photoredox Catalysis: A Concise Method for the Synthesis of Natural Product Scaffolds. *Chem. Commun.* **2016**, *52*, 6455−6458.
40. Nguyen, J. D.; Tucker, J. W.; Konieczynska, M. D.; Stephenson, C. R. J. Intermolecular Atom Transfer Radical Addition to Olefins Mediated by Oxidative Quenching of Photoredox Catalysts. *J. Am. Chem. Soc.* **2011**, *133*, 4160−4163.
41. Maji, T.; Karmakar, A.; Reiser, O. Visible-Light Photoredox Catalysis: Dehalogenation of Vicinal Dibromo-, α-Halo-, and α,α-Dibromocarbonyl Compounds. *J. Org. Chem.* **2011**, *76*, 736−739.
42. Pham, P. V.; Nagib, D. A.; MacMillan, D. W. C. Photoredox Catalysis: A Mild, Operationally Simple Approach to the Synthesis of α-Trifluoromethyl Carbonyl Compounds. *Angew. Chem., Int. Ed.* **2011**, *50*, 6119−6122.
43. MacKenzie, I. A.; Wang, L.; Onuska, N. P. R.; Williams, O. F.; Begam, K.; Moran, A. M.; Dunietz, B. D.; Nicewicz, D. A. Discovery and Characterization of an Acridine Radical Photoreductant. *Nature* **2020**, *580*, 76−80.
44. Deprez, P.; Guillaume, J.; Becker, R.; Corbier, A.; Didierlaurent, S.; Fortin, M.; Frechet, D.; Hamon, G.; Heckmann, B.; Heitsch, H. Sulfonylureas and Sulfonylcarbamates as New Non-Tetrazole Angiotensin II Receptor Antagonists. Discovery of a Highly Potent Orally Active (Imidazolylbiphenylyl)sulfonylurea (HR 720). *J. Med. Chem.* **1995**, *38*, 2357−2377.
45. Dey, D.; Kundu, A.; Roy, M.; Pal, S.; Adhikari, D. Aromatization as the Driving Force for Single Electron Transfer Towards C−C Cross-Coupling Reactions. *Catal. Sci. Technol.* **2022**, *12*, 1934−1940.

46. Cahard, E.; Schoenebeck, F.; Garnier, J.; Cutulic, S. P. Y.; Zhou, S.; Murphy, J. A. Electron Transfer to Benzenes by Photoactivated Neutral Organic Electron Donor Molecules. *Angew. Chem., Int. Ed.* **2012**, *51*, 3673−3676.
47. Doni, E.; Murphy, J. A. Evolution of Neutral Organic Superelectron-Donors and Their Applications. *Chem. Commun.* **2014**, *50*, 6073−6087.
48. Schmidt, V. A.; Quinn, R. K.; Brusoe, A. T.; Alexanian, E. J. Site-Selective Aliphatic C−H Bromination using N-Bromoamides and Visible Light. *J. Am. Chem. Soc.* **2014**, *136*, 14389−14392.
49. Shields, B. J.; Doyle, A. G. Direct C(sp^3)−H Cross Coupling Enabled by Catalytic Generation of Chlorine Radicals. *J. Am. Chem. Soc.* **2016**, *138*, 12719−12722.
50. Sharma, A.; Hartwig, J. F. Metal-Catalysed Azidation of Tertiary C−H Bonds Suitable for Late-Stage Functionalization. *Nature* **2015**, *517*, 600−604.
51. Morcillo, S. P.; Dauncey, E. M.; Kim, J. H.; Douglas, J. J.; Sheikh, N. S.; Leonori, D. Photoinduced Remote Functionalization of Amides and Amines Using Electrophilic Nitrogen Radicals. *Angew. Chem., Int. Ed.* **2018**, *57*, 12945−12949.
52. Ghosh, I.; Shaikh, R. S.; König, B. Sensitization-Initiated Electron Transfer for Photoredox Catalysis. *Angew. Chem., Int. Ed.* **2017**, *56*, 8544−8549.
53. Ghosh, I.; Ghosh, T.; Bardagi, J. I.; König, B. Reduction of Aryl Halides by Consecutive Visible Light-Induced Electron Transfer Processes. *Science* **2014**, *346*, 725−728.
54. Ghosh, I.; König, B. Chromoselective Photocatalysis: Controlled Bond Activation through Light-Color Regulation of Redox Potentials. *Angew. Chem., Int. Ed.* **2016**, *55*, 7676−7679.
55. Kaim, W.; Fiedlerb, J. Spectroelectrochemistry: The Best of Two Worlds. *Chem. Soc. Rev.* **2009**, *38*, 3373–3382.
56. Cecotka, M. C.; Predygier, J.; Crespi, S.; Szczepanik, J.; Giedyk, M. Photocatalysis in Aqueous Micellar Media Enables Divergent C−H Arylation and N-Dealkylation of Benzamides. *ACS Catal.* **2022**, *12*, 3543−3549.
57. Bhakuni, B. S.; Yadav, A.; Kumar, S.; Patel, S.; Sharma, S.; Kumar, S. KO^{t}Bu-Mediated Synthesis of Dimethylisoindolin-1-ones and Dimethyl-5-phenylisoindolin-1-ones: Selective C−C Coupling of an Unreactive Tertiary sp^3 C−H Bond. *J. Org. Chem.* **2014**, *79*, 2944−2954.

58. Wertjes, W. C.; Wolfe, L. C.; Waller, P. J.; Kalyani, D. Nickel or Phenanthroline Mediated Intramolecular Arylation of sp^3 C-H Bonds Using Aryl Halides. *Org. Lett.* **2013**, *15*, 5986−5989.
59. Wu, S.; Zhao, Q.; Wu, C.; Wang, C.; Lei, H. Transition-Metal-Free Oxindole Synthesis: Quinone–K2CO3 Catalyzed Intramolecular Radical Cyclization. *Org. Chem. Front.* **2022**, *9*, 2593–2599.
60. Dey, D.; Kundu, A.; Mandal, B.; Roy, M.; Adhikari, D. Deciphering the Single Electron Transfer Ability of Fluorene Under Photoredox Conditions. *Catal. Sci. Technol.* **2022**, *12*, 7322–7327.
61. Zhou, C.; Liu, Q.; Li, Y.; Zhang, R.; Fu, X.; Duan, C. Palladium-Catalyzed Desulfitative Arylation by C−O Bond Cleavage of Aryl Triflates with Sodium Arylsulfinates. *J. Org. Chem.* **2012**, *77*, 10468−10472.
62. Lamola, J. L.; Moshapo, P. T.; Holzapfel, C. W.; Maumela, M. C. Evaluation of P-bridged Biaryl Phosphine Ligands in Palladium-Catalysed Suzuki–Miyaura Cross-Coupling Reactions. *RSC Adv*. **2021**, *11*, 26883−26891.
63. Talukder, M. M.; Cue, J. M. O.; Miller, J. T.; Gamage, P. L.; Aslam, A.; McCandless, G. T.; Biewer, M. C.; Stefan, M. C. Ligand Steric Effects of α-Diimine Nickel(II) and Palladium(II) Complexes in the Suzuki–Miyaura Cross-Coupling Reaction. *ACS Omega* **2020**, *5*, 24018−24032.
64. Liu, Z.; Wang, P.; Chen, Y.; Yan, Z.; Chen, S.; Chen, W.; Mu, T. Small Organic Molecules with Tailored Structures: Initiators in the Transition-Metal-Free C–H Arylation of Unactivated Arenes. *RSC Adv.* **2020**, 10, 14500–14509.
65. Yu, F.; Mao, R.; Yu, M.; Gu, X.; Wang, Y. Generation of Aryl Radicals from Aryl Halides: Rongalite-Promoted Transition-Metal-Free Arylation. *J. Org. Chem.* **2019**, *84*, 9946−9956.
66. Shen, N.; Li, R.; Liu, C.; Shen, X.; Guan, W.; Shang, R., Photocatalytic Cross-Couplings of Aryl Halides Enabled by o-Phosphinophenolate and o-Phosphinothiophenolate. *ACS Catal.* **2022**, *12*, 2788−2795.
67. Neumann, M.; Füldner, S.; König, B.; Zeitler, K., Metal-free, Cooperative Asymmetric Organophotoredox Catalysis with Visible Light. *Angew. Chem., Int. Ed.* **2011,** *50* (4), 951-954.
68. Romero, N. A.; Nicewicz, D. A., Organic Photoredox Catalysis. *Chem. Rev.* **2016,** *116* (17), 10075-10166.

69. Shaw, M. H.; Twilton, J.; MacMillan, D. W., Photoredox Catalysis in Organic Chemistry. *J. Org. Chem.* **2016,** *81* (16), 6898-6926.
70. Stephenson, C. R.; Yoon, T. P.; MacMillan, D. W., *Visible Light Photocatalysis in Organic Chemistry*. John Wiley & Sons: 2018.
71. Brown, D. G.; Sanguantrakun, N.; Schulze, B.; Schubert, U. S.; Berlinguette, C. P., Bis (tridentate) Ruthenium–terpyridine Complexes Featuring Microsecond Excited-state Lifetimes. *J. Am. Chem. Soc.* **2012,** *134* (30), 12354-12357.
72. Prier, C. K.; Rankic, D. A.; MacMillan, D. W., Visible Light Photoredox Catalysis with Transition Metal Complexes: Applications in Organic Synthesis. *Chem. Rev.* **2013,** *113* (7), 5322-5363.
73. Nicewicz, D. A.; MacMillan, D. W., Merging Photoredox Catalysis with Organocatalysis: The Direct Asymmetric Alkylation of Aldehydes. *Science* **2008,** *322* (5898), 77-80.
74. Lu, Z.; Yoon, T. P., Visible Light Photocatalysis of [2+ 2] Styrene Cycloadditions by Energy Transfer. *Angew. Chem., Int. Ed.* **2012,** *124* (41), 10475-10478.
75. Ischay, M. A.; Anzovino, M. E.; Du, J.; Yoon, T. P., Efficient Visible Light Photocatalysis of [2+ 2] Enone Cycloadditions. *J. Am. Chem. Soc.* **2008,** *130* (39), 12886-12887.
76. Tucker, J. W.; Nguyen, J. D.; Narayana, J. M.; Krabbe, S. W.; Stephenson, C. R., Tin-free Radical Cyclization Reactions Initiated by Visible Light Photoredox Catalysis. *Chem. Commun.* **2010,** *46* (27), 4985-4987.
77. Narayanam, J. M.; Stephenson, C. R., Visible Light Photoredox Catalysis: Applications in Organic Synthesis. *Chem. Soc. Rev.* **2011,** *40* (1), 102-113.
78. Narayanam, J. M. R.; Tucker, J. W.; Stephenson, C. R. J., Electron-Transfer Photoredox Catalysis: Development of a Tin-Free Reductive Dehalogenation Reaction. *J. Am. Chem. Soc.* **2009,** *131* (25), 8756-8757.
79. Guo, X.-X.; Gu, D.-W.; Wu, Z.; Zhang, W., Copper-catalyzed C–H Functionalization Reactions: Efficient Synthesis of Heterocycles. *Chem. Rev.* **2015,** *115* (3), 1622-1651.
80. Eftekhari-Sis, B.; Zirak, M.; Akbari, A., Arylglyoxals in Synthesis of Heterocyclic Compounds. *Chem. Rev.* **2013,** *113* (5), 2958-3043.
81. Candeias, N. R.; Branco, L. C.; Gois, P. M.; Afonso, C. A.; Trindade, A. F., More Sustainable Approaches for the Synthesis of N-based Heterocycles. *Chem. Rev.* **2009,** *109* (6), 2703-2802.

82. Carson, C. A.; Kerr, M. A., Heterocycles from Cyclopropanes: Applications in Natural Product Synthesis. *Chem. Soc. Rev.* **2009,** *38* (11), 3051-3060.
83. Wilson, J. E.; Kurukulasuriya, R.; Reembark, M.; Reiter, M.; Zwicker, A.; Zhao, K.; Zhang, F.; Anand, R.; Colandrea, V. J.; Cumiskey, A.-M., Discovery of Novel Indoline Cholesterol Ester Transfer Protein Inhibitors (CETP) Through a Structure-guided Approach. *ACS Med. Chem. Lett.* **2016,** *7* (3), 261-265.
84. Mayer, P.; Brunel, P.; Imbert, T., A New Efficient Synthesis of Efaroxan. *Bioorg. Med. Chem. Lett.* **1999,** *9* (20), 3021-3022.
85. Zhang, D.; Song, H.; Qin, Y., Total Synthesis of Indoline Alkaloids: A Cyclopropanation Strategy. *Acc. Chem. Res.* **2011,** *44* (6), 447-457.
86. Juliá, F.; Constantin, T.; Leonori, D., Applications of Halogen-Atom Transfer (XAT) for the Generation of Carbon Radicals in Synthetic Photochemistry and pPhotocatalysis. *Chem. Rev.* **2021,** *122* (2), 2292-2352.
87. Nguyen, J. D.; D'amato, E. M.; Narayana, J. M.; Stephenson, C. R., Engaging Unactivated Alkyl, Alkenyl and Aryl Iodides in Visible-Light-Mediated Free Radical Reactions. *Nat. Chem.* **2012,** *4* (10), 854-859.
88. Kim, H.; Lee, C., Visible-Light-Induced Photocatalytic Reductive Transformations of Organohalides. *Angew. Chem., Int. Ed.* **2012,** *51* (49), 12303-12306.
89. Yang, C.; Mehmood, F.; Lam, T. L.; Chan, S. L.-F.; Wu, Y.; Yeung, C.-S.; Guan, X.; Li, K.; Chung, C. Y.-S.; Zhou, C.-Y.; Zou, T.; Che, C.-M., Stable Luminescent Iridium(iii) Complexes with bis(N-heterocyclic carbene) Ligands: Photo-Stability, Excited State Properties, Visible-Light-Driven Radical Cyclization and CO_2 Reduction, and Cellular Imaging. *Chem. Sci.* **2016,** *7* (5), 3123-3136.
90. Michelet, B.; Deldaele, C.; Kajouj, S.; Moucheron, C.; Evano, G., A General Copper Catalyst for Photoredox Transformations of Organic Halides. *Org. Lett.* **2017,** *19* (13), 3576-3579.
91. Zidan, M.; McCallum, T.; Swann, R.; Barriault, L., Formal Bromine Atom Transfer Radical Addition of Nonactivated Bromoalkanes Using Photoredox Gold Catalysis. *Org. Lett.* **2020,** *22* (21), 8401-8406.
92. Caiuby, C. A. D.; Ali, A.; Santana, V. T.; de S. Lucas, F. W.; Santos, M. S.; Corrêa, A. G.; Nascimento, O. R.; Jiang, H.; Paixão, M. W., Intramolecular Radical Cyclization Approach to Access Highly Substituted Indolines and 2,3-Dihydrobenzofurans Under Visible-Light. *RSC Adv.* **2018,** *8* (23), 12879-12886.

93. Dey, D.; Kundu, A.; Roy, M.; Singh, V.; Maji, S.; Adhikari, D., Single Electron Transfer Catalysis by Diphenylthiourea Under Visible Light Photoredox Conditions. *Org. Chem. Front.* **2023,** *10* (20), 5248-5253.
94. Dey, D.; Kundu, A.; Roy, M.; Pal, S.; Adhikari, D., Aromatization as the Driving Force for Single Electron Transfer Towards C–C Cross-Coupling Reactions. *Catal. Sci. Technol.* **2022,** *12* (6), 1934-1940.
95. Barham, J. P.; Coulthard, G.; Emery, K. J.; Doni, E.; Cumine, F.; Nocera, G.; John, M. P.; Berlouis, L. E.; McGuire, T.; Tuttle, T., KO^{t}Bu: A Privileged Reagent for Electron Transfer Reactions? *J. Am. Chem. Soc.* **2016,** *138* (23), 7402-7410.
96. Yi, H.; Jutand, A.; Lei, A., Evidence for the Interaction Between ^{t}BuOK and 1, 10-Phenanthroline to form the 1, 10-Phenanthroline Radical Anion: A Key Step for the Activation of Aryl Bromides by Electron Transfer. *Chem. Commun.* **2015,** *51* (3), 545-548.
97. Tanielian, C.; Cougnon, F.; Seghrouchni, R., Acetone, a Substrate and a New Solvent in Decatungstate Photocatalysis. *J. Mol. Catal. A: Chem.* **2007,** *262* (1-2), 164-169.
98. Huang, L.; Ackerman, L. K.; Kang, K.; Parsons, A. M.; Weix, D. J., LiCl-Accelerated Multimetallic Cross-Coupling of Aryl Chlorides with Aryl Triflates. *J. Am. Chem. Soc.* **2019,** *141* (28), 10978-10983.
99. Zhou, F.; Liu, Y. L.; Zhou, J., Catalytic Asymmetric Synthesis of oOxindoles Bearing a Tetrasubstituted Stereocenter at the C-3 Position. *J. Adv. Synth. Catal.* **2010,** *352* (9), 1381-1407.
100. Marti, C.; Carreira, E. M., Construction of Spiro [pyrrolidine-3, 3′-oxindoles]− Recent Applications to the Synthesis of Oxindole Alkaloids. *Eur. J. Org. Chem.* **2003,** *2003* (12), 2209-2219.
101. Hibino, S.; Choshi, T., Simple Indole Alkaloids and those with a Nonrearranged Monoterpenoid Unit. *Nat. Prod. Rep.* **2001,** *18* (1), 66-87.
102. Pan, Q.; Ping, Y.; Wang, Y.; Guo, Y.; Kong, W., Ni-Catalyzed Ligand-Controlled Regiodivergent Reductive Dicarbofunctionalization of Alkenes. *J. Am. Chem. Soc.* **2021,** *143* (27), 10282-10291.
103. Cao, M.; Wang, H.; Ma, Y.; Tung, C.-H.; Liu, L. Site- and Enantioselective Manganese-Catalyzed Benzylic C–H Azidation of Indolines. *J. Am. Chem. Soc.* **2022**, *144*, 15383– 15390.

104. Singh, V.; Singh, R.; Hazari, A. S.; Adhikari, D. Unexplored Facet of Pincer Ligands: Super-Reductant Behavior Applied to Transition-Metal-Free Catalysis. *JACS Au* **2023**, *3*, 1213– 1220.

105. Ren, Y. Z.; Fang, C. Z.; Zhang, B. B.; He, L.; Tu, Y. L.; Chen, X. Y. Photocatalytic Charge-Transfer Complex Enables Hydroarylation of Alkenes for Heterocycle Synthesis. *Org. Lett.* **2023**, *25*, 3585– 3589.

Chapter 4

Redox Non-Innocence of Formazanate Ligand Applied to Catalytic Formation of α-Ketoamides

A part of this work has been published in Chem. Commun., **2022**, *58,* 6630–6633

4.1. Introduction

The use of organic ligand motifs to store redox equivalents is a preeminent theme in enzymatic reactions and has inspired chemists to mimic such systems for efficient chemical transformations.[1–4] The ability of some ligands to store and deliver redox equivalents has opened up new avenues in catalysis, where crucial steps are mostly regulated by ligand-dominated redox processes.[5–9] This fact also has a significant implication in sustainable catalysis, where 3d transition metals can be utilized in opposition to their rare, expensive and toxic heavy metal congeners.[10,11] A good covalency between the 3d metal and the ligand backbone can emulate the overall two-electron behaviour of their heavier analogues. This fact has created tremendous momentum in identifying suitable redox-active ligands that in conjunction with 3d transition metals can perform chemical reactions in a catalytic fashion.[12–15]

Among different classes of redox-active backbones, formazanates hold a special place.[16,17] They were introduced as close analogues to ubiquitous β-diketiminates, where more heteroatoms were placed in the ligand architecture, so that the delocalized π^* orbitals could be further lowered in energy. Through a number of elegant studies, the redox non-innocent nature of formazanates has been firmly established.[18,19] Furthermore, coordination to main group metals and non-metals with formazanates has been introduced to obtain impressive photophysical properties of the synthesized molecules.[20,21] The ligand-based redox events have been carefully evaluated to precisely determine the electronic structures of the complexes.[19,22–24] Conversely, despite their proven roles as redox reservoirs, experimental demonstration of catalytic activity eliciting from the redox non-innocence of the formazanate ligands remains elusive.

In this chapter, an iron formazanate complex was used to demonstrate the catalytic reactivity, where a crucial redox step is dictated by the ligand's ability to store and release electrons in a reversible manner and stabilize it by the extended delocalization, over its backbone (Scheme 4.1). Although, iron formazanate complex (**1**) has already been prepared and characterised by Gilroy group[25,26] in 2008 but catalytic activity of the earlier reported an iron formazanate complex (**1**) equipped with redox non-innocent formazanate ligands was not explored. This example fulfills the promised conjecture that redox non-innocence of formazanate can lead to efficient catalytic reactions. The single electron transfer is facilitated

due to the redox non-innocence of the formazanate backbone, where the oxidation is fully ligand-centered.

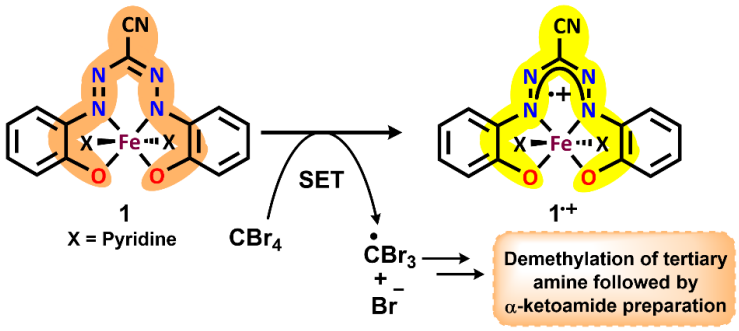

Scheme 4.1. Redox non-innocence of iron-formazanate complex to promote single electron transfer and reductive cleavage of tetrabromomethane.

α-Ketoamides are an important class of functional group in medicinal chemistry as drug molecules, biologically relevant, synthetic intermediates for many organic transformations, as building blocks and in metal complexes. Orexin receptor antagonists, cytokine inhibitors, epoxide hydrolase inhibitors, are well known bioactive *α*-ketoamides (Scheme 4.2).[27]

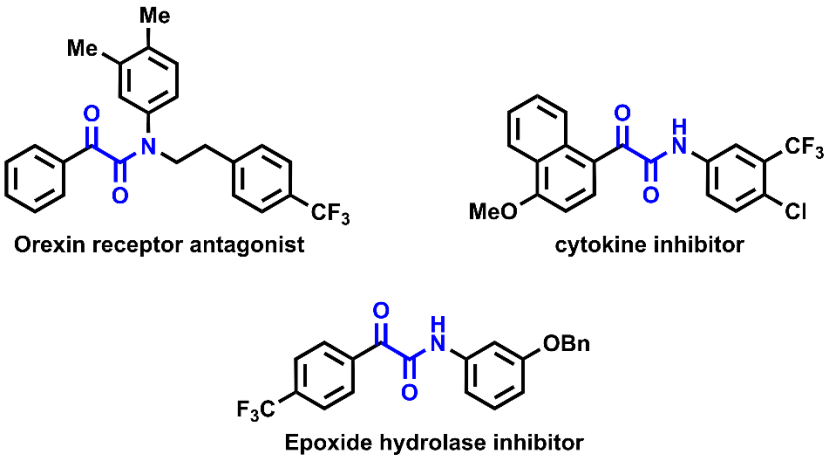

Scheme 4.2. Examples of bioactive *α*-ketoamide.

Due to the biological and synthetic demands, significant efforts have been dedicated for the construction of these structural motifs. For instance, in 1982 the Yamamoto group[28] reported a catalytic double carbonylation of organohalogen compounds promoted by palladium complexes resulting into *α*-ketoamides on reaction with secondary amines (Scheme 4.3). In this direction, the Wang group[29] reported synthesis of *α*-ketoamides from *α*-ketoacids with tertiary amines using silver catalyst *via N*-dealkylation of tertiary amines. However, a strong oxidant $K_2S_2O_8$ was used at high temperature (120 °C). Since tertiary amines are easily

available, often a demethylation route is followed to prepare a secondary amine. Recently, a photochemical route employing $Ru(bpy)_3(PF_6)_2$ as the photocatalyst has been examined to carry out such a demethylation reaction.[30]

The present investigated method that relies on the redox non-innocence of the formazanate, is thermal and obviates the need of expensive ruthenium photocatalysts. In this chapter, a single electron transfer (SET) approach for highly selective mono-demethylation of *tert*-amine to generate secondary amine and subsequent coupling with α-ketocarboxylic acids to form α-ketoamides was explored. However, to the best of our knowledge there is no report for the such type of reaction using iron metal complex under mild thermal conditions.

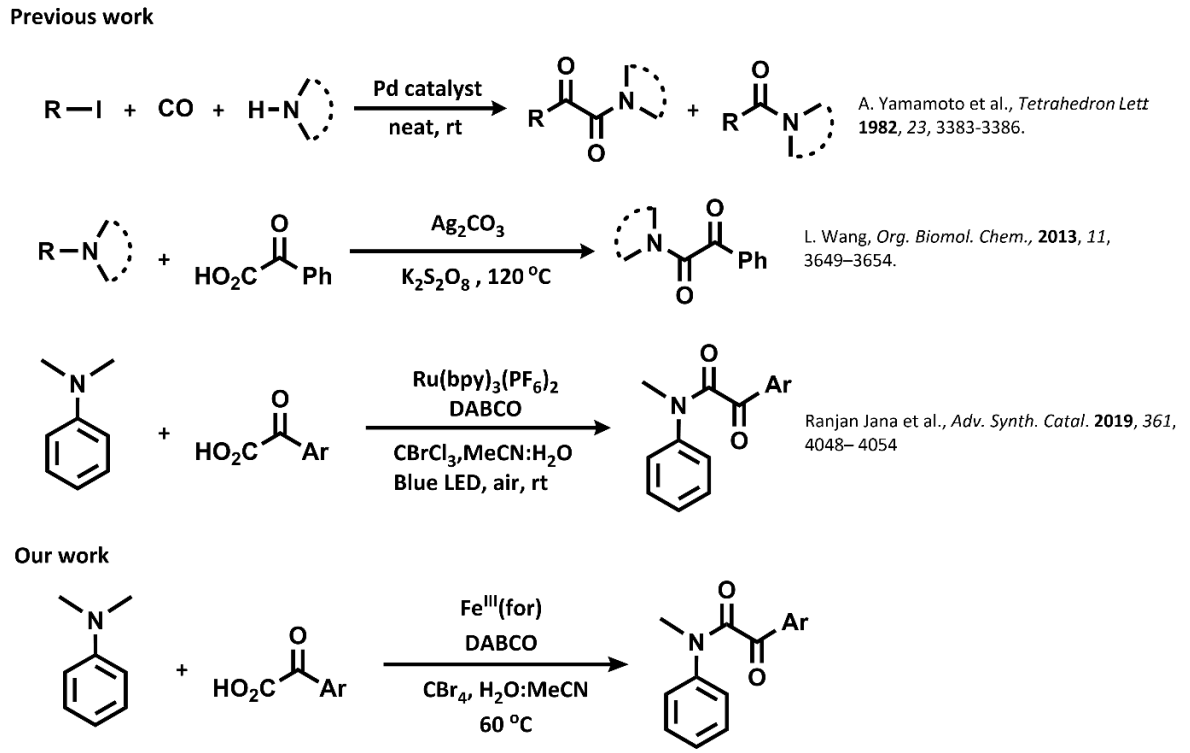

Scheme 4.3. Literature reports and the present method for α-ketoamide synthesis.

4.2. Results and Discussion

In the pursuit of demonstrating redox transformations led by a formazanate backbone, 1,5-*bis*(2-hydroxyphenyl)-3-cyanoformazan ligand was chosen. Such a trianionic N_2O_2 ligand backbone offers four coordination sites for the central metal and facilitates electronic conjugation to be further extended to the phenolate groups. The CN group placed at the third position of the ligand will exert only the inductive effect as it is placed on the nodal plane of the ligand's LUMO (Figure 4.1b). The great utility of the ligand backbone in the redox

transformations lies in the accessibility of high-lying filled (e^- donor) and low-lying empty (e^- acceptor) orbitals of *Π*-symmetry.[31]

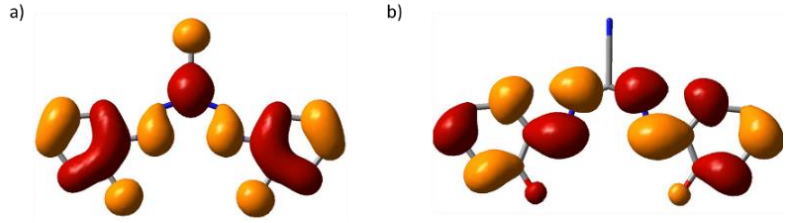

Figure 4.1. a) HOMO of formazanate ligand. b) LUMO of formazanate ligand.

4.2.1. Synthesis of Formazanate Ligand and Iron(III) Complex 1

The formazanate ligand (**L**) and an iron(III) complex **1** (Scheme 4.4) were prepared following the literature procedure.[25,26] The reaction of cyanoacetic acid with diazonium salt of *o*-hydroxy aniline at low temperature in strong alkaline medium resulted in formazanate ligand (**L**). All the protons from ligand were abstracted by sodium hydride. The anhydrous ferric chloride salt was added to the fully deprotonated ligand in the presence of pyridine. In this complex **1**, iron is coordinated to two nitrogen atoms and two oxygen atoms from the phenolate arm in a *pseudo*-octahedral environment, where two pyridyl ligands are coordinated axially and the iron center is lying in the same plane as the formazan (scheme 4.4). Each of the coordinated pyridine is oriented such that their ring planes bisect the N_2-Fe-N_4 bond angle.

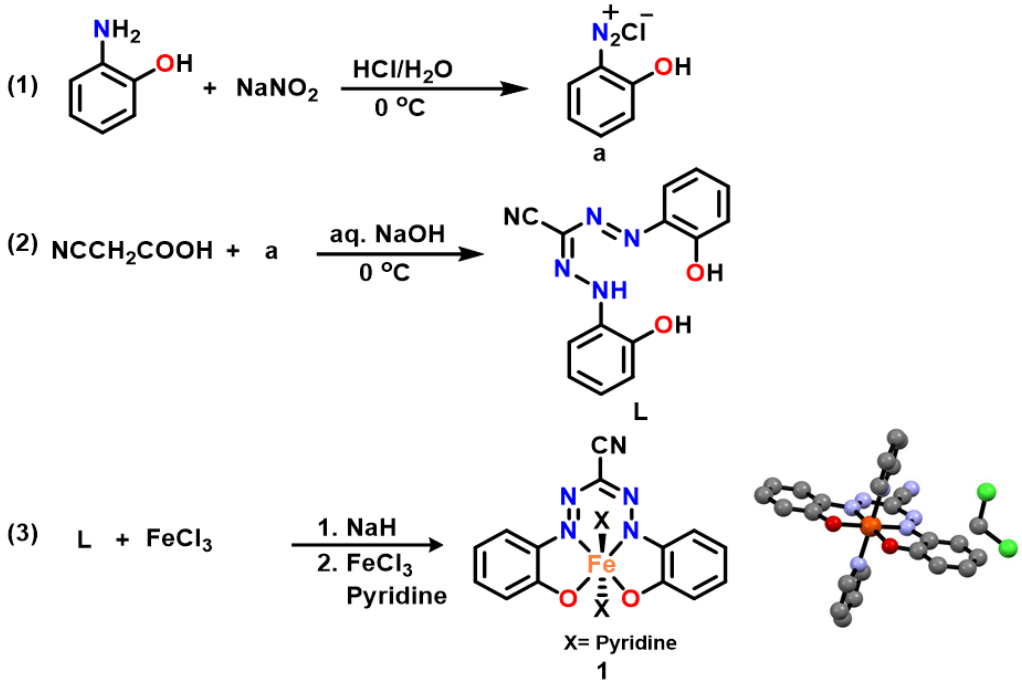

Scheme 4.4. Synthesis of 3-cyano-1,5-dihydroxyphenylformazan (**L**) and iron(3-cyano-1,5-(2-hydroxyphenylformazanato)-*bis*-pyridine (**1**). The crystal structure was reproduced from ref. 26.

This iron (III) complex **1** was employed for the demethylation of a tertiary amine, with the hope that ligand based redox heavily drives this chemistry. The high-lying *Π*-orbital suggests that reductive redox behaviour offered by the complex will be very much ligand-centered.

4.2.2. Catalytic Application

α-ketoamides were prepared from *α*-ketoacid in the presence of tertiary amine (*N*,*N*-dimethyl aniline) by using **1** as a catalyst wherein the tertiary amine is acting as a nitrogen source.[32] Gratifyingly, a model reaction with *N*,*N*-dimethyl aniline and *α*-ketoacid in the presence of tetrabromomethane yielded the desired amide product, **5a** in an 89% yield (Scheme 4.5).

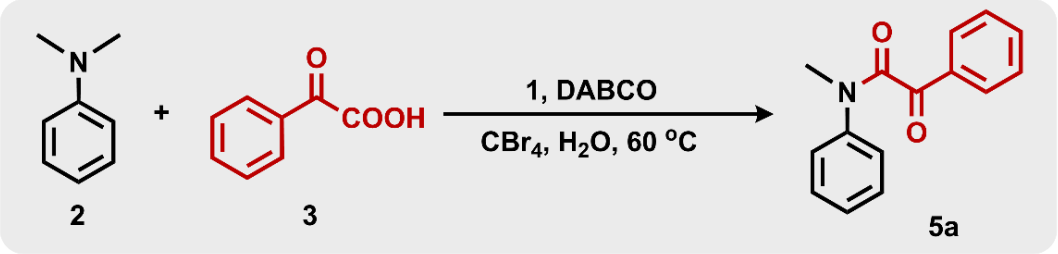

Scheme 4.5. The *α*-ketoamide formation reaction catalysed by **1**.

A series of optimization studies disclosed that the two equivalents base DABCO was required for an efficient reaction, which primarily deprotonated the carboxylic acid to its respective carboxylate salt. The reaction temperature and time were optimized to be 60 °C and 12 h (Table 4.1). Encouragingly, water can be chosen as the reaction medium, with a slight mixing of acetonitrile (0.1 mL) to augment the solubility of catalyst **1**. The catalytic performance of the chosen molecule is very commendable, since only 2 mol% loading of the catalyst was sufficient to carry out the reaction successfully (Table 4.1, entry 3). Only water as a solvent did not provided the appropriate result due to low solubility of metal complex **1** (Table 4.1, entry 4).

When a strong oxidant $Na_2S_2O_8$ was used in place of CBr_4, the desired product was not observed (Table 4.1, entry 11) clearly indicating that $CBr_3^{\cdot}$ radical from CBr_4 have a crucial role in this catalysis. Other oxidant like molecular oxygen, $CBrCl_3$, TBHP were not as effective as CBr_4 (Table 4.1, entry 12–15). DABCO was found to be more efficient base as compared to other organic bases (Table 4.1, entry 16–18). The simple iron(III) precursor $FeCl_3$ did not

catalyze the reaction, proving that the entire metal complex is required and the ligand has a special role in completing the transformation.

Table 4.1. Optimization of reaction conditions.

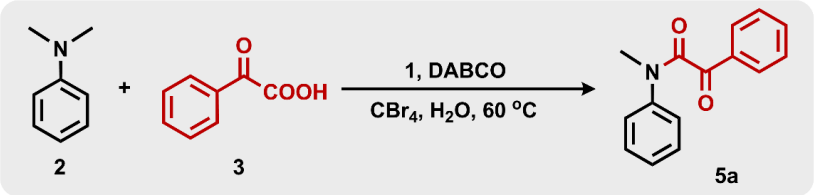

Entry	Acid (3) equiv	Catalyst Loading (mol%)	Oxidant	Base	Yield[a]
1	1	2	CBr_4	DABCO	65
2	1.5	2	CBr_4	DABCO	77
3	**2**	**2**	**CBr_4**	**DABCO**	**89**
4	2	2	CBr_4	DABCO	68[b]
5	2	1	CBr_4	DABCO	62
6	2	0.5	CBr_4	DABCO	24
7	2	-	CBr_4	DABCO	ND
8	2	2	CBr_4	DABCO	25[c]
9	2	2	-	DABCO	ND
10	2	2	CBr_4	-	18
11	2	2	$Na_2S_2O_8$	DABCO	ND
12	2	2	O_2	DABCO	ND
13	2	2	$CBrCl_3$	DABCO	25
15	2	2	TBHP	DABCO	trace
16	2	2	CBr_4	DBU	29
17	2	2	CBr_4	2,6 Lutidine	29
18	2	2	CBr_4	NEt_3	20
19	2	$FeCl_3$	CBr_4	DABCO	trace

Note: a) GC yield b) reaction using H_2O as the only solvent. c) at room temperature.

4.2.2.1. Scope and Synthetic Utility of Demethylation Amidation Reaction by Catalyst 1

Having the mechanistic details sketched, the scope of the reaction was elaborated. As described in Table 4.2, an array of amines was tested for the demethylative amidation reaction. The *para*-substitutions of this *N*,*N*-dimethyl aniline by –Br, –Cl, –OMe, and -Me were all well tolerated and furnished the *α*-ketoamide products (**5b–5e**) in 59–92% yields. Similarly, the *ortho*- and *meta*-substituted anilines were introduced in the amide products **5f–5h** in 47–69% isolated

yields. A more challenging aliphatic amine such as diethylmethyl amine afforded the product **5i** in 70% yield. Similarly, *N*-methylpyrolidine or *N*-methylpiperidine were equally effective in introducing the amides on the carboxylic acid to forge products **5j** and **5k** in 67 and 62% yields, respectively. Finally, a morpholine amine was successfully installed in the amide product **5l** in 55% yield.

Table 4.2. Substrate scope for demethylative amidation varying *N*,*N*-dimethylaniline, *α*-ketoacid and benzoic acid.

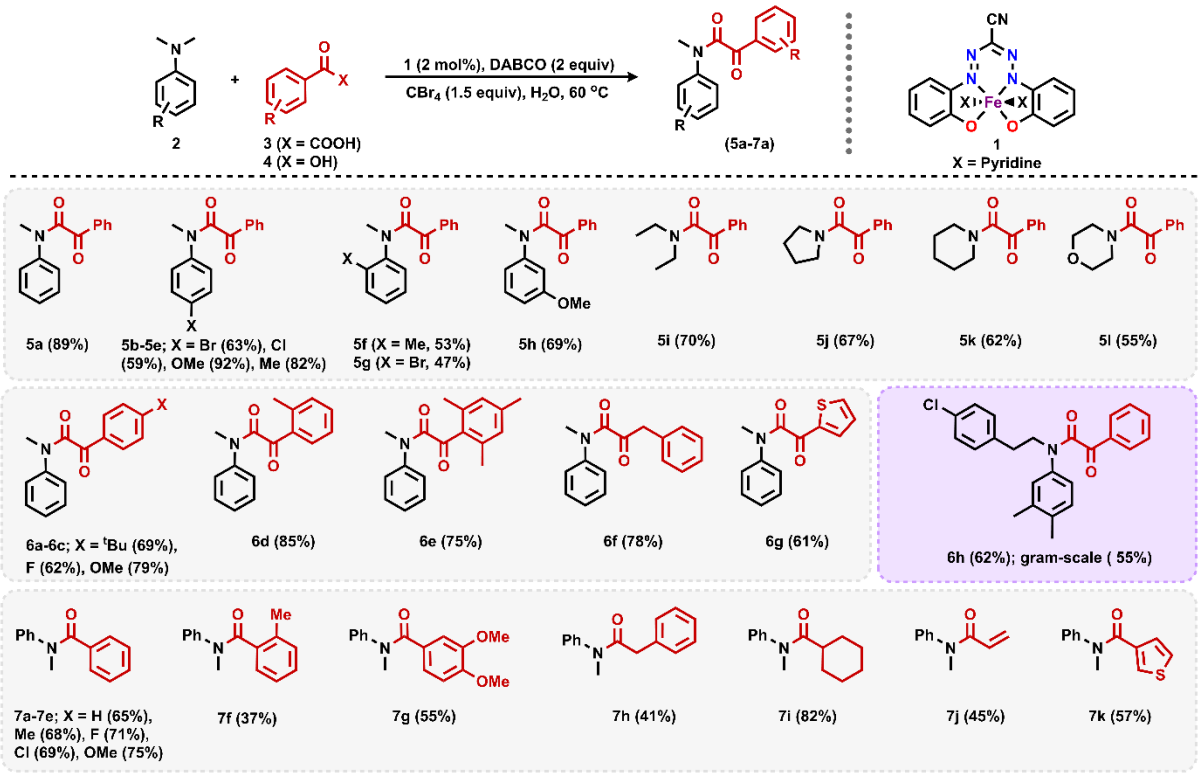

Reaction conditions: substituted *N*,*N*-dimethylanilne (1 equiv), substituted *α*-ketoacid/benzoic acid (2 equiv), DABCO (2 equiv), CBr_4 (1.5 equiv) and **1** (2 mol%) in solvent (H_2O:MeCN ; 1:0.05), 6 h, isolated yields are reported.

Next, the scope of different carboxylic acids for this amidation reaction was examined. Accordingly, *para*-substitution of *α*-keto benzoic acid by –^{t}Bu, –F, and OMe groups was well suited for this reaction and afforded products **6a–6c** in 62–79% yields. *ortho*-methyl and 1,3,5-trimethyl substitution in the keto benzoic acid was also suitable for the reaction furnishing the desired amide products **6d** and **6e** in 85% and 75% yields, respectively. Interestingly, a heterocycle thiophene in the *α*-keto acid was well tolerated so that the amide product **6g** can be isolated in 61% yield. Finally, to test the efficiency of the developed protocol, an orexin

receptor antagonist[38] molecule (**6h**) was synthesized in a few steps (see the details in the experimental Section 2.6.8). An ethynyl-substituted aniline was deployed to forge this value-added molecule in 62% yield, where the demethylation is carried out by the redox-active formazanate backbone. The method was further effective in scaling-up the reaction, as the preparation afforded a 55% yield of the antagonist in a gram-scale reaction.

Additionally, the demethylation reaction was connected to simple amidation. Along this goal, a large number of substituted benzoic acids (**7a–7g**), cyclohexylcarboxylic acid (**7i**), acrylic acid (**7j**) and thiophenecarboxylic acid (**7k**) were converted to their corresponding amide derivatives in good yields starting from a tertiary amine. A vast substrate scope including both general carboxylic acids and α-keto acids likely attests the generality of this synthetic method.

4.3. Mechanistic Insights and Control Experiments

4.3.1. Cyclic Voltammetry Experiment

To interrogate the electrochemical behaviour of **1**, a cyclic voltammetry experiment was performed. The iron complex in acetonitrile solvent showed a quasi-reversible oxidation wave at a mild potential of 0.36 V (vs. $Fc^{0/+}$) (Figure 4.2). The quasi-reversible behaviour, as reflected in the low current during the cathodic wave might be indicative of limited chemical stability of the oxidized radical cation, $\mathbf{1}^{\cdot+}$ in its solution state, especially at a slow scan rate. Notably, the oxidation potential for complex **1** is also in close proximity to the redox-inert Al^{+3} complex with the same ligand backbone, strongly indicating a ligand-centered oxidation.[33]

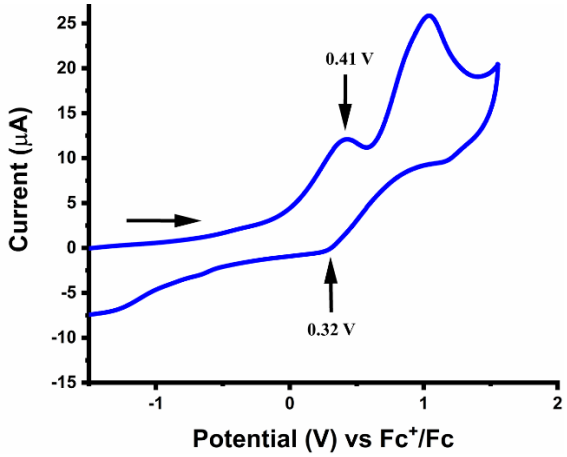

Figure 4.2. CV of 1 mM of **1** dissolved in acetonitrile along with 0.1 M solution of tetrabutyl-ammonium hexafluorophosphate salt as an electrolyte. The scan rate was 50 mVs^{-1} for the measurement.

4.3.2. Chemical Synthesis of Oxidized Radical Cation $\mathbf{1}^{\cdot+}$

To get more information about the oxidised form of **1** (**1**$^{\cdot+}$), we attempted the chemical synthesis of oxidized radical cation **1**$^{\cdot+}$. Due to the large reduction potential of AgOTf, this oxidant has been used in many organometallic transformations. So, to oxidize **1**, AgOTf was chosen as an oxidant. Addition of one equivalent of silver triflate to a THF solution of **1** resulted in a rapid colour change from blue to maroon red (Scheme 4.6). The oxidized product was separated by filtration from the by-product metallic silver. The oxidized molecule is air sensitive in nature, but can remain stable for weeks in the solid state under an inert atmosphere.

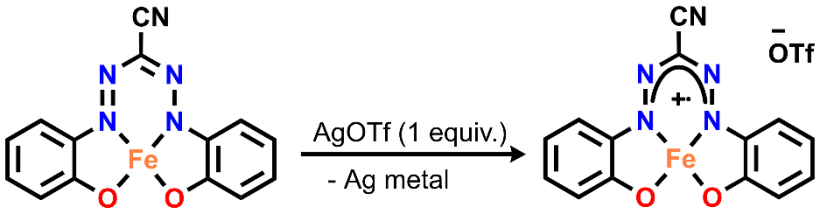

Scheme 4.6. Synthesis of (**1**$^{\cdot+}$). Axial coordinated pyridyl ligand has been omitted for clarity.

4.4. Characterization of 1$^{\cdot+}$

The characterization of oxidised iron complex **1**$^{\cdot+}$ is essential to gain insight into the electronic structure, fate of the catalyst and mechanistic insight of reaction. Unfortunately, due the high sensitivity and insignificant life time of oxidised iron complex **1**$^{\cdot+}$ inside the solution, the single crystal of this metal complex could not be obtained for single crystal x-ray diffraction (SC-XRD) studies. In order to elaborate the electronic structure of **1**$^{\cdot+}$ some physical and theoretical experiments were performed.

4.4.1. UV–Visible Analysis of 1$^{\cdot+}$

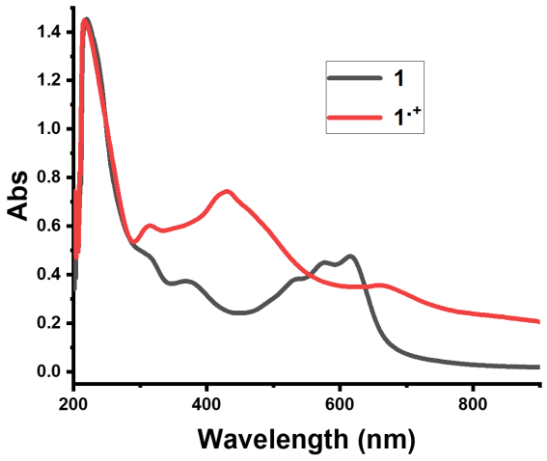

Figure 4.3. UV–Vis plot for **1** (grey line) and oxidised product $\mathbf{1}^{\cdot+}$ (red line) recorded in dry and degassed THF at room temperature.

The electronic spectra of complexes **1** and $\mathbf{1}^{\cdot+}$ are presented in Figure 4.3. As previously discussed, the absorption spectra of **1** was similar to the literature report.[26] The spectra of the complex have absorption peaks in the UV (λ_{max}) 335 nm and in the visible (λ_{max}) 392 and 631 nm. Upon scrutinizing through UV–Visible spectroscopy, it is observed that the complex $\mathbf{1}^{\cdot+}$ absorbs at 455 and this broad absorption is connected to a second short band up to 600 nm.

4.4.2. Magnetic Moment Measurement of Oxidised Iron Complex $\mathbf{1}^{\cdot+}$

The magnetic moment is a useful tool to know the number of unpaired electrons in any system. A crucial information regarding the nature of unpaired electron can also be obtained, like how the unpaired electrons are coupled to each other. If the two-electron system is considered then there are two possibilities:

(a) Both the electrons are strongly antiferromagnetically coupled. So, in that case both the unpaired electrons have equal but opposite spin quantum numbers. That means, total spin is zero and total spin quantum number represents singlet state (Figure 4.4).

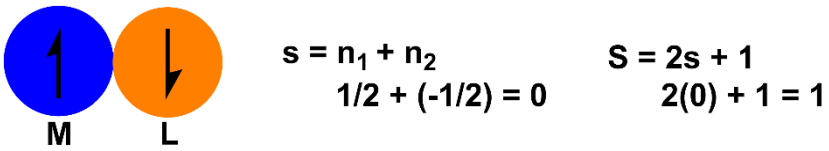

Figure 4.4. Strong antiferromagnetic coupling of electrons.

(b) Both the electrons are weakly antiferromagnetically coupled or not coupled. In that case both the electrons have some antiferromagnetic coupling but still both the spin vectors do not neutralise the overall spin magnetic moment. On the other hand, if there is very minute antiferromagnetic coupling or electrons are not coupled, then the overall spin is one and total spin quantum number represents triplet state (Figure 4.5).

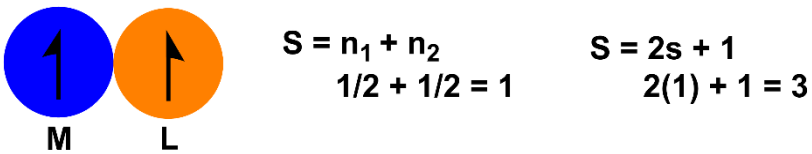

Figure 4.5. Weak antiferromagnetic coupling/ uncoupled electrons.

The solid-state magnetic moments for complex **1** has already been reported in literature.[26] The room-temperature magnetic moment of **1** is 1.82 μB, indicating that the Fe(III) ion is low-spin with one unpaired electron in one of the *d*-orbital. On the other hand, the room temperature magnetic moment measurement of $\mathbf{1}^{\cdot+}$ in the solution state by Evans magnetometry[34,35] revealed a value of 2.6(2) μB, which is very close to the spin-only value for two unpaired electrons. The value closely represents the triplet state that has been confirmed from computational analysis.

4.5. Computational Analysis

The electronic structure of **1** and its oxidized counterpart $\mathbf{1}^{\cdot+}$ were investigated computationally (Figure 4.6a). On comparing the metrical parameters of single crystal X-ray diffraction (SC-XRD) data analysis of **1** and computationally optimised $\mathbf{1}^{\cdot+}$, no deviation in bond length of formazanate backbone was observed. The spin density distribution in the triplet state clearly shows an excess spin density in both iron and the formazanate backbone (Figure 4.6b). The calculations clearly support the major locus of the oxidation to be the ligand backbone. DFT calculations at the B3LYP level for $\mathbf{1}^{\cdot+}$ disclosed a triplet ground state with an antiferromagnetically coupled, open-shell singlet, to be only 0.3 kcal mol^{-1} higher in energy (Figure 4.6c).

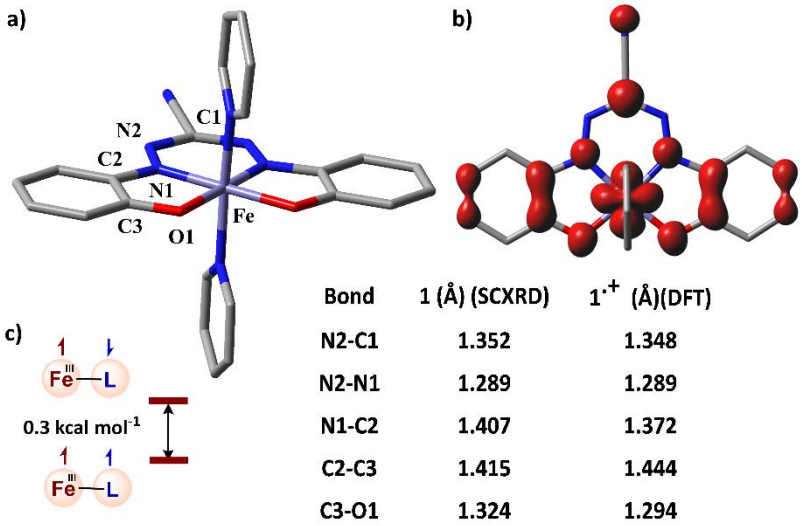

Bond	1 (Å) (SCXRD)	$1^{\cdot+}$ (Å)(DFT)
N2-C1	1.352	1.348
N2-N1	1.289	1.289
N1-C2	1.407	1.372
C2-C3	1.415	1.444
C3-O1	1.324	1.294

Figure 4.6. (a) Computationally optimized $\mathbf{1}^{\cdot+}$ at its triplet state. (b) Excess alpha spin density distribution of $\mathbf{1}^{\cdot+}$ at the triplet state. (c) Energy difference between open-shell singlet and triplet state of $\mathbf{1}^{\cdot+}$.

This broken symmetry, BS(1,1) solution[36] for the open-shell singlet represents an extremely weakly coupled ligand and iron *d*-electron with a negligible overlap integral of 0.0005 (Figure

4.7 and 4.8). We anticipate such a weak coupling originates from the heavily delocalized nature of the ligand-based unpaired spin.

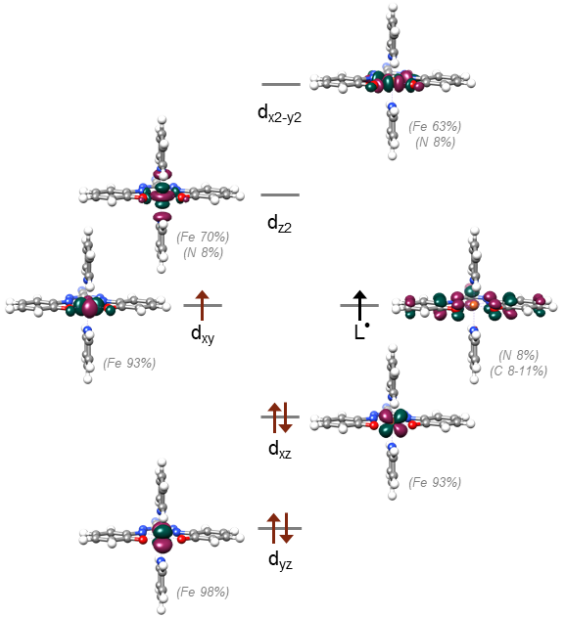

Figure 4.7. MO for S=1 state, $\mathbf{1}^{\bullet+}$.

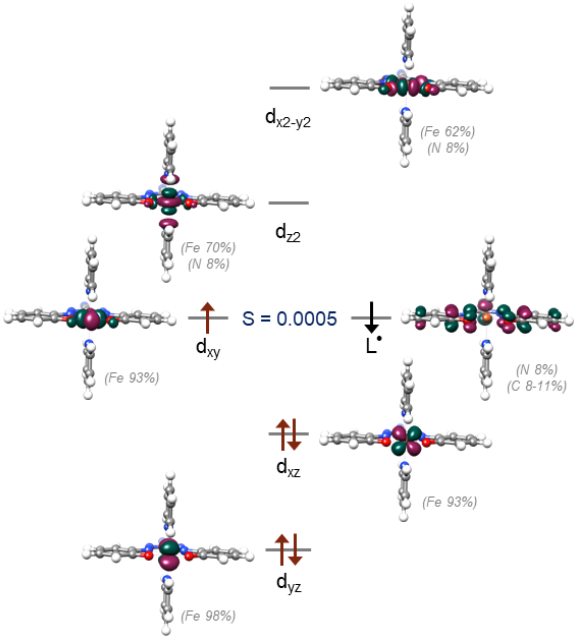

Figure 4.8. MO for open-shell singlet structure, $\mathbf{1}^{\bullet+}$.

4.6. Control experiments

4.6.1. Trapping of Radical Intermediates

To prove the intermediacy of carboxylate radical during the reaction, a radical trap 1,1-diphenylethene was incorporated resulting in the trapping of intermediate which was confirmed by high resolution mass spectrometry showing its signature peak at 347.1254 amu (Scheme 4.7a). Furthermore, as a conclusive proof of the radical-mediated reaction, the reaction stops completely when TEMPO is introduced in the reaction mixture. Moreover, under such

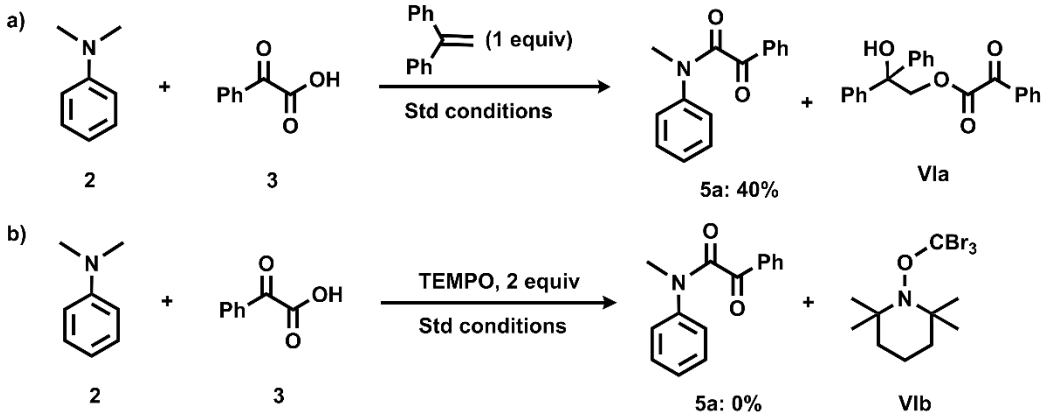

Scheme 4.7. (a) Trapping of carboxyl radical adduct. (b) Trapping of tribromomethane radical.

conditions, a $CBr_3^{\cdot}$ radical was intercepted as its TEMPO adduct and was detected by ESI mass spectrometry (Scheme 4.7b) showing its signature at 405.9030 amu.

The trapping of such crucial intermediates provides compelling evidence for the radical reaction and the generation of key intermediates where reductive cleavage is advanced by the single electron transfer from the formazanate ligand backbone.

4.6.2. Kinetics of Reaction

A kinetic experiment was performed by taking the aliquots from the reaction mixture under the optimised reaction conditions. It was observed that the product yield was getting saturated after 2 hours. Gratifyingly, the reaction followed the *pseudo*-first-order rate kinetics (Figure 4.9).

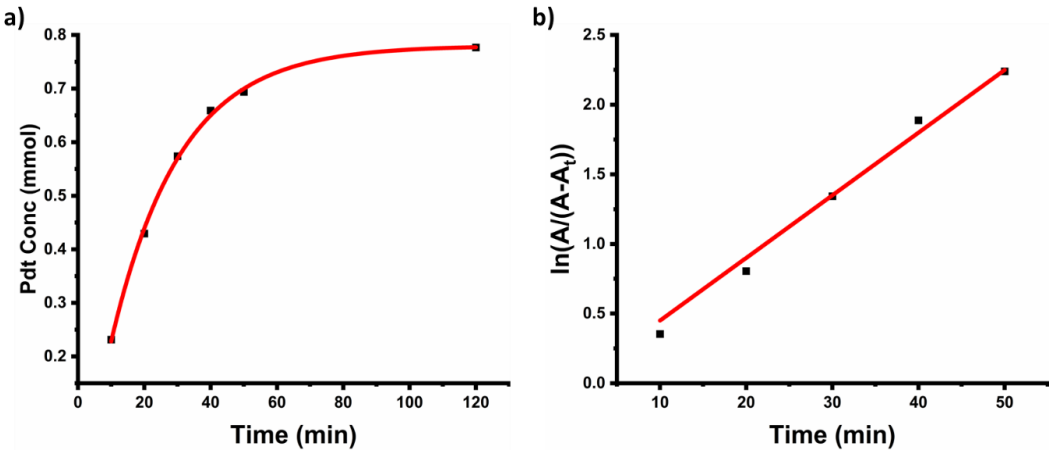

Figure 4.9. a) Growth of product *vs* time (min). b) *Pseudo*-first order plot.

4.7. Proposed Reaction Mechanism

Mechanistically, this electron reservoir property of the formazanate helps in reducing CBr_4 to generate the $CBr_3^{\cdot}$ radical, which can be the starting point for the catalytic reaction. Furthermore, the quasi-reversible oxidation wave suggests that the formazanate backbone may accept the electron back during the catalytic cycle.

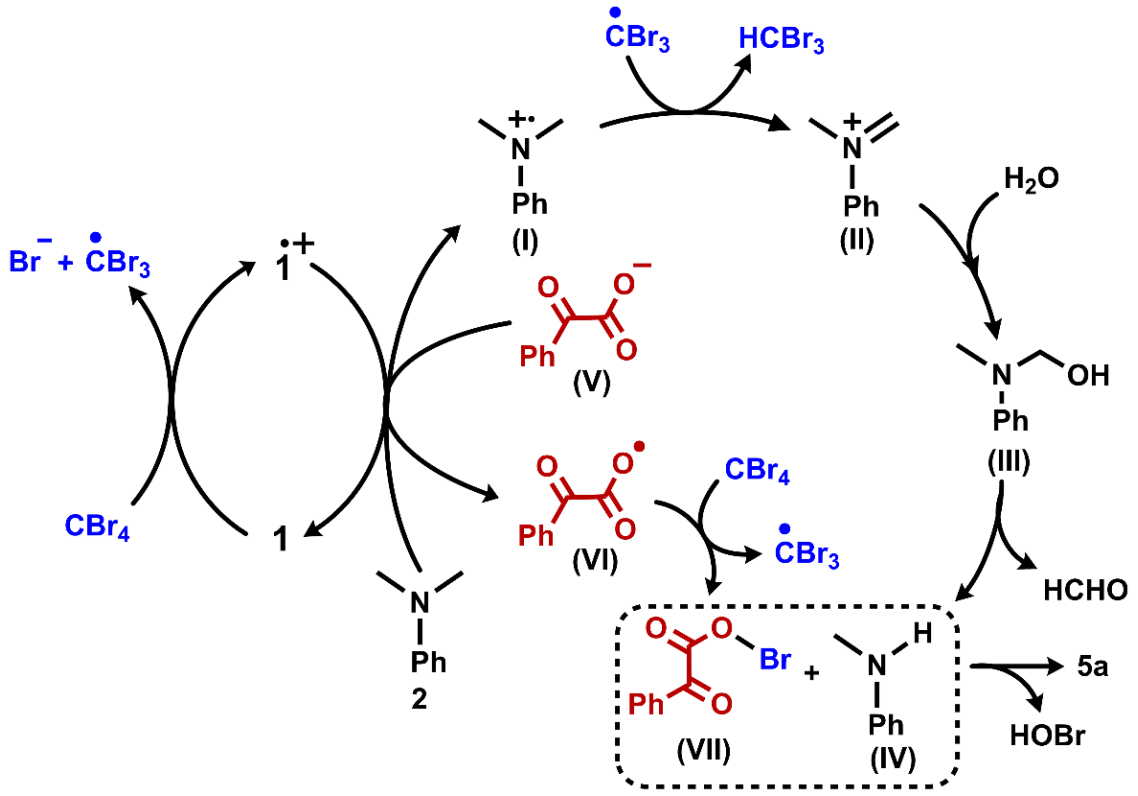

Scheme 4.8. Plausible catalytic cycle for the formation of α-ketoamide.

Both the carboxylate anion of α-ketoacid (V) or tertiary amine (**2**) can donate one electron back to $\mathbf{1}^{\cdot+}$ to reduce it (Scheme 4.8). The depletion of the electron density in the formazanate backbone makes it sufficiently electron hungry so that mild reductants (such as amine and carboxylates) can reduce it, regenerating the catalyst. In the meantime, $CBr_3^{\cdot}$ would be able to abstract a hydrogen atom from the methyl group of the tertiary amine radical cation (I) so that an amidinium species (II) results. Such an amidinium cation (II) can be readily hydrolysed to afford a tertiary amine (III) where one of the arms is an alcohol. This species is very prone to release formaldehyde so that a secondary amine (IV), *N*-methyl aniline, results. In essence, demethylation of a tertiary amine is facilitated by the electron transfer from the parent amine to the electron-depleted, oxidized formazanate ligand backbone.[37]

Meanwhile, the carboxylate salt (V) is also mildly reducing, which can reduce the oxidized formazanate backbone and generate a carboxyl radical species (VI). The proof of intermediacy of VI and $CBr_3^{\cdot}$ radical during the reaction has been discussed in intermediate trapping experiment (Scheme 4.7). The CBr_4 can react with the carboxylic radical to form an α-keto carboxylic acid bromide (VII), which upon nucleophilic attack by the secondary amine generates the desired α-ketoamide product (**5a**).

4.8. Conclusions

To summarize, this report showcases the rare example of formazanate redox non-innocence applied in catalysis.[39] An iron formazanate reductively cleaves a C–Br bond where the oxidation is accommodated in the *p*-delocalized ligand framework. The electronic structure analysis of the radical cation clearly supports the ligand's participation in crucial redox steps en route to demethylation of a tertiary amine. We hope more well-known redox-active ligands will be delivering important redox transformations to steer catalysis in the future.

4.9. Experimental Section

4.9.1. Chemicals and Reagents

All reactions were carried out using air sensitive manipulations and glove box unless otherwise mentioned. The solvents used were of analytical grade and purified wherever necessary as per the standard literature protocol. Tetrahydrofuran (THF) was refluxed and freshly distilled over sodium/benzophenone and degassed using three freeze-pump-thaw cycles. All chemicals were purchased from Sigma-Aldrich, Avra, TCI, Alfa Aesar and GLR innovations. CD_3CN and $CDCl_3$ were purchased from Euroisotope. All chemicals were used as purchased until and

unless mentioned. Progress of reactions was monitored by thin-layer chromatography (TLC) using Merck 60 F254 precoated silica gel plate and visualized by short-wave ultraviolet light. Flash chromatography was performed with Silica Flash P60 silica gel (100–200 mesh).

4.9.2. Instrumentation and Physical Measurements

Absorption spectra were recorded using LAB-INDIA UV/VIS Spectrophotometer UV 3000 in an UV-cuvette of path length 10 mm fitted with cap. The graphs were plotted using Originpro8. ^{1}H and ^{13}C $\{^{1}H\}$ NMR spectra were recorded on a Bruker 400 MHz spectrometer at 400 MHz and 101 MHz respectively. The residual solvent signals were taken as the reference ($CDCl_3$, 7.26 ppm for ^{1}H NMR spectra and $CDCl_3$, 77.16 ppm for ^{13}C NMR spectra). The signals observed are described as: *s* (singlet), *d* (doublet), *t* (triplet), *q* (quartet), *m* (multiplets). All coupling constants were reported in hertz. High-resolution mass spectrometry was performed on Waters Synapt-G2S, with analyser configuration Q-ToF, ion mobility and analysed using Masslynx41. Cyclic Voltammetry experiments were performed CHI-610 electrochemical workstation from CH Instruments (USA). For the measurement, the three-electrode setup consisted of a glassy carbon working electrode, a Pt-wire as counter electrode, and an Ag/AgCl (1M KCl) as the reference electrode.

All DFT calculations have been carried out using the ORCA 4.2.1 program[40]. Geometry optimizations and single point calculations were carried out by employing the B3LYP[41,42] functional. All atoms were described by the def2-TZVP[43,44] basis set. Vibrational calculations were done to ensure that the geometries are true minima.

Caution! The Glovebox and high vacuum Shlenk line should be used with great care and safety. THF distillation setup contains sodium metal, which is very reactive metal to air and moisture and well-known for their explosive nature. Therefore, these types of setups must be used in a limited quantity and handled with care and safety.

4.9.3. Synthesis of Formazanate Ligand (L) and Iron(3-cyano-1,5-(2-hydroxyphenyl-formazanato)-*bis*-pyridine (1)

4.9.3.1. Synthesis of Ligand 3-cyano-1,5-dihydroxyphenylformazan (L)

The ligand **L** was prepared by following the literature protocol with slight modifications.[25] To a solution of *o*-aminophenol (4.36 g, 40 mmol) in 12 M concentrated hydrochloric acid (10 mL) and water (10 mL) at -5 °C, as solution of sodium nitrite (3.00 g, 43 mmol) in water was added in small portions over a period of 10 min. After 15 min of stirring, the mixture was added

to a second solution containing cyanoacetic acid (1.70 g, 20 mmol), sodium hydroxide (8.00 g, 200 mmol) and water (100 mL) at 0 °C over a period of 30 min. The resulting dark red solid was isolated *via* filtration and purified *via* flash column chromatography (neutral alumina and dichloromethane). The eluate was concentrated *in* V*acuo* to afford **L** as a dark red gummy solid. The above gummy solid was triturated using hexane, which resulted into a dark red powder. This powder was used as such for synthesis of iron metal complex without any further purifications.

4.9.3.2. Synthesis of Iron(3-cyano-1,5-(2-hydroxyphenylformazanato)-*bis*-pyridine (1)

Formazan ligand **L** (250 mg, 0.88 mmol) was dissolved in freshly distilled THF (10 mL) under argon and treated with sodium hydride (108 mg of 60% emulsion in oil, 2.7 mmol) before being left to stir for 16 h, changing in colour from red to dark blue. Iron(III) chloride (144 mg, 0.88 mmol) and pyridine (0.36 mL, 4.5 mmol) were added, and the reaction was left to stir for 16 h, at which time the solution was a dark blue colour. The mixture was then filtered and the solvent was removed under vacuum. Trituration with hexanes allowed for **1** to be isolated as a dark blue solid, yield: 304 mg (70% based on ligand **L**). The formation of metal complex was confirmed by UV–Visible analysis of prepared complex. Similar UV–Visible spectrum was obtained as reported in literature.[26]

4.9.3.3. Synthesis of Mono-Oxidised Iron(3-cyano-1,5-(2-hydroxyphenylformazanato)-*bis*-pyridine ($\mathbf{1}^{\cdot+}$)

In a Schlenk flask **1** (246 mg, 0.5 mmol) was dissolved in 5 mL of THF and silver triflate (129 mg, 0.5 mmol) was added to the solution. During the addition, the colour of the reaction mixture turned to brown from greenish blue over the course of 1 h. The reaction mixture was further stirred for 12 h at room temperature. At the completion of the reaction, the reaction mixture was filtered and the filtrate was removed under high vacuum. The oxidized product was isolated (205 mg, 83% yield). UV–Vis spectroscopic data was collected for both **1** and $\mathbf{1}^{\cdot+}$ under inert conditions.

4.9.4. Intermediate Trapping

(a) Carboxyl Radical Trapping

Following the standard reaction conditions, a 20 mL vial was charged with *N*,*N*-dimethylaniline (26 μL, 0.2 mmol), α-ketocarboxylic acids (60 mg, 0.4 mmol), DABCO (45 mg, 0.4 mmol) and 1,1-Diphenylethylene (36 μL, 0.2 mmol). 2 mL of distilled water was

added to the vial to make a clear solution. A solution of tetrabromomethane (99 mg, 0.3 mmol) in 100 μL of acetonitrile was added to the reaction mixture. The above reaction mixture was loaded with catalyst **1** (2 mol%, 4.9 mg) and was stirred at 60 $^{\circ}$C temperature. After 6 h, the product **5a** was obtained in 40% yield and the carboxyl radical adduct (**VIa**) (scheme 4.7a) was analysed by High-resolution mass spectrometry. (ESI mode, m/z) calcd. for $C_{22}H_{19}O_4$ $[M+H]^+$: 347.1283; found: 347.1254.

(b) CBr_3 Radical Trapping

Following the standard reaction conditions, a 20 mL vial was charged with *N*,*N*-dimethylaniline (26 μL, 0.2 mmol), α-ketocarboxylic acids (60 mg, 0.4 mmol), DABCO (45 mg, 0.4 mmol) and TEMPO (62 mg, 0.4 mmol)). 2 mL of distilled water was added to the vial to make a clear solution. A solution of tetrabromomethane (99 mg, 0.3 mmol) in 100 μL of acetonitrile was added to the reaction mixture. The above reaction mixture was loaded with catalyst **1** (2 mol%, 4.9 mg) and was stirred at a temperature of 60 °C. After 6 h, there is no formation of product as assayed by TLC. The $CBr_3^{\cdot}$ radical adduct (**VIb**) (scheme 4.7b) was detected by high-resolution mass spectrometry (HRMS). HRMS (ESI, m/z) calcd. for $C_{10}H_{19}Br_3NO$ $[M+H]^+$: 405.9017; found: 405.9030.

4.9.7. General Procedure for Demethylative Amidation Catalyzed by 1

Using the optimized condition, the reaction was carried out with *N*,*N*-dimethylaniline (65 μL, 0.5 mmol), α-ketocarboxylic acids (150 mg, 1.0 mmol) and DABCO (112 mg, 1.0 mmol). 2 mL of distilled water was added to the vial to make a clear solution. A solution of tetrabromomethane (248 mg, 0.75 mmol) in 100 μL of acetonitrile was added to the reaction mixture. The above reaction mixture was loaded with catalyst **1** (2 mol%, 4.9 mg) and was stirred at a temperature of 60 °C. After 6 h, the reaction aqueous layer was extracted with ethyl acetate and dried over anhydrous $MgSO_4$. Ethyl acetate was removed under reduced pressure and the desired product was separated from crude mixture by flash column chromatography using silica as stationary phase and hexane:ethylacetate as eluent. All products were characterized by ^{1}H and ^{13}C NMR spectroscopic techniques.

4.9.8. Gram-Scale Synthesis of Orexin Receptor Agonist[38]

As per general optimised reaction conditions, a 100 mL round bottomed flask was charged with *N*-(4-chlorophenethyl)-*N*-methylaniline (1.23 g, 5 mmol), 2-oxo-2-phenylacetic acid (1.5 g, 10 mmol), DABCO (1.12 g, 10 mmol) and 40 mL of distilled water was added to make a clear solution. A solution of tetrabromomethane (2.5 g, 7.5 mmol) in 2 mL of acetonitrile was added

to the reaction mixture. The above reaction mixture was loaded with catalyst **1** (2 mol%, 49 mg) and was stirred at 60 °C temperature. After 6 h, the reaction aqueous layer was extracted with ethyl acetate and dried over anhydrous $MgSO_4$. Ethyl acetate was removed under reduced pressure and the desired product was separated from crude mixture by flash column chromatography using silica as stationary phase and hexane:ethylacetate (9:1) as eluent. The pure product orexin receptor agonist (**6h**) was obtained in 55% yield (0.99 g) as a white solid. **^{1}H NMR** (400 MHz, $CDCl_3$) δ_{ppm} 7.64 – 7.60 (*m*, 2H), 7.57 – 7.52 (*m*, 1H), 7.39 (*t*, *J* = 7.7 Hz, 2H), 7.31 (*d*, *J* = 8.3 Hz, 2H), 7.21 (*d*, *J* = 8.4 Hz, 2H), 6.93 (*d*, *J* = 7.9 Hz, 1H), 6.78 (*d*, *J* = 2.4 Hz, 1H), 6.68 (*dd*, *J* = 7.9, 2.4 Hz, 1H), 4.21 – 4.15 (*m*, 2H), 2.92 (*t*, *J* = 7.4 Hz, 2H), 2.15 (*s*, 3H), 2.09 (*s*, 3H). **^{13}C NMR** (101 MHz, $CDCl_3$) δ_{ppm} 190.7, 167.0, 138.2, 137.2, 136.8, 136.7, 134.2, 133.7, 132.5, 130.7, 130.5, 129.4, 128.7, 128.7, 128.7, 125.1, 48.8, 33.0, 19.8, 19.4.

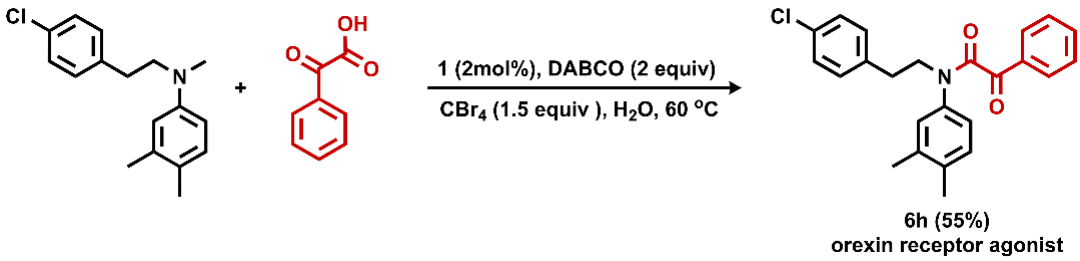

Scheme 4.9. Gram-scale synthesis of orexin receptor agonist (**6h**) by **1**.

4.9.9. Spectroscopic Characterization for Demethylative Amidation Products

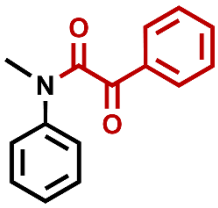

***N*-Methyl-2-oxo-*N*,2-diphenylacetamide (5a)**

The general procedure was followed. Column chromatography (SiO_2, eluting with 85:15 hexane/ethyl acetate) afforded the desired product as a yellow solid (107 mg, yield 89%).

^{1}H NMR (400 MHz, $CDCl_3$) δ_{ppm} 7.88 – 7.82 (*m*, 2H), 7.59 – 7.53 (*m*, 1H), 7.43 (*q*, *J* = 7.9 Hz, 2H), 7.35 (*d*, *J* = 8.7 Hz, 1H), 7.25 – 7.11 (*m*, 3H), 7.01 (*d*, *J* = 8.7 Hz, 1H), 3.48 and 3.45 (*s*, 3H, N-CH_3, major and minor, conformers).

^{13}C NMR (101 MHz, $CDCl_3$) δ_{ppm} 190.9, 167.2, 141.2, 134.6, 133.6, 129.6, 129.5, 128.9, 128.4, 126.8, 36.3.

HRMS (ESI, m/z) calcd. for $C_{15}H_{14}NO_2$ $[M+H]^+$: 240.1024; found: 290.1026.

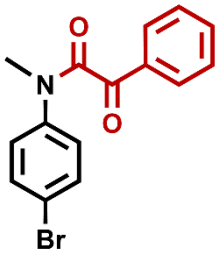

***N*-(4-bromophenyl)-*N*-methyl-2-oxo-2-phenylacetamide (5b)**

The general procedure was followed. Column chromatography (SiO_2, eluting with 85:15 hexane/ethyl acetate) afforded the desired product as a yellow gummy liquid (100 mg, 63%).

^{1}H NMR (400 MHz, $CDCl_3$) δ_{ppm} 7.85 (*dd*, *J* = 7.3, 1.3 Hz, 2H), 7.58 (*t*, *J* = 7.4 Hz, 1H), 7.44 (*t*, *J* = 7.6 Hz, 2H), 7.20 (*d*, *J* = 8.8 Hz, 2H), 7.07 (*d*, *J* = 8.8 Hz, 2H), 3.45 (*s*, 3H).

^{13}C NMR (101 MHz, $CDCl_3$) δ_{ppm} 190.7, 167.0, 139.8, 134.6, 134.0, 133.4, 129.8, 129.5, 129.0, 128.2, 36.3.

HRMS (ESI, m/z) calcd. for $C_{15}H_{13}BrNO_2$ $[M+H]^+$: 318.0130; found: 318.0147.

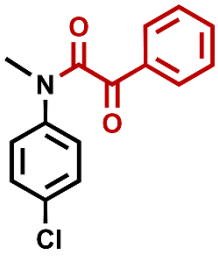

***N*-(4-chlorophenyl)-*N*-methyl-2-oxo-2-phenylacetamide (5c**

The general procedure was followed. Column chromatography (SiO_2, eluting with 85:15 hexane/ethyl acetate) afforded the desired product as a yellow gummy liquid (81 mg, 59%).

^{1}H NMR (400 MHz, $CDCl_3$) δ_{ppm} 7.85 (*d*, *J* = 7.5 Hz, 2H), 7.58 (*t*, *J* = 7.4 Hz, 1H), 7.44 (*t*, *J* = 7.8 Hz, 2H), 7.34 (*d*, *J* = 8.7 Hz, 2H), 7.01 (*d*, *J* = 8.7 Hz, 2H), 3.44 (*s*, 3H).

^{13}C NMR (101 MHz, $CDCl_3$) δ_{ppm} 190.6, 166.9, 140.3, 134.6, 133.3, 132.8, 129.5, 129.0, 128.4, 122.0, 36.3.

HRMS (ESI, m/z) calcd. for $C_{15}H_{13}ClNO_2$ $[M+H]^+$: 274.0635; found: 274.0639.

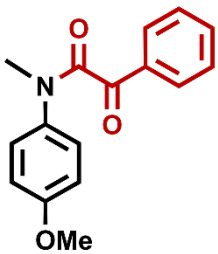

***N*-(4-methoxyphenyl)-*N*-methyl-2-oxo-2-phenylacetamide (5d)**

The general procedure was followed. Column chromatography (SiO_2, eluting with 80:20 hexane/ethyl acetate) afforded the desired product as a yellow gummy liquid (124 mg, 92%).

^{1}H NMR (400 MHz, $CDCl_3$) δ_{ppm} 7.83 (*d*, *J* = 7.8 Hz, 2H), 7.56 (*t*, *J* = 7.4 Hz, 1H), 7.43 (*t*, *J* = 6.8 Hz, 2H), 7.05 (*d*, *J* = 6.5 Hz, 2H), 6.72 (*d*, *J* = 6.5 Hz, 2H), 3.71 (*s*, 3H), 3.43 (*s*, 3H).

^{13}C NMR (101 MHz, $CDCl_3$) δ_{ppm} 191.3, 167.4, 159.2, 134.4, 133.7, 133.6, 129.5, 128.9, 128.5, 114.7, 55.5, 36.6.

HRMS (ESI, m/z) calcd. for $C_{16}H_{16}NO_3$ $[M+H]^+$: 270.1130; found: 270.1136.

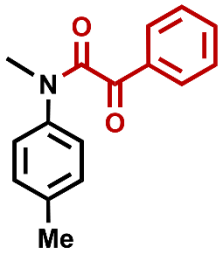

***N*-methyl-2-oxo-2-phenyl-*N*-(*p*-tolyl)acetamide (5e)**

The general procedure was followed. Column chromatography (SiO_2, eluting with 85:15 hexane/ethyl acetate) afforded the desired product as a yellow gummy liquid (104 mg, 82%).

^{1}H NMR (400 MHz, $CDCl_3$) δ_{ppm} 7.89 – 7.82 (*m*, 2H), 7.55 (*t*, *J* = 7.5 Hz, 1H), 7.42 (*t*, *J* = 7.7 Hz, 2H), 7.01 (*s*, 4H), 3.45 (*s*, 3H), 2.23 (*s*, 3H).

^{13}C NMR (101 MHz, $CDCl_3$) δ_{ppm} 191.0, 167.2, 138.5, 138.2, 134.3, 133.5, 130.2, 129.5, 128.8, 126.6, 36.3, 21.1.

HRMS (ESI, m/z) calcd. for $C_{16}H_{16}NO_2$ $[M+H]^+$: 254.1181; found: 254.1198.

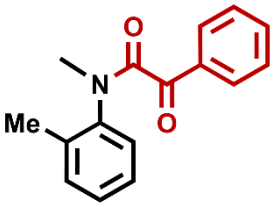

***N*-methyl-2-oxo-2-phenyl-*N*-(o-tolyl)acetamide (5f)**

The general procedure was followed. Column chromatography (SiO_2, eluting with 90:10 hexane/ethyl acetate) afforded the desired product as a yellow oil (67 mg, 53%).

^{1}H NMR (400 MHz, $CDCl_3$) δ_{ppm} 7.85 – 7.79 (*m*, 2H), 7.55 (*t*, *J* = 7.4 Hz, 1H), 7.41 (*t*, *J* = 7.8 Hz, 2H), 7.19 – 7.11 (*m*, 2H), 6.97 (*dd*, *J* = 4.7, 1.8 Hz, 2H), 3.36 (*s*, 3H), 2.30 (*s*, 3H).

^{13}C NMR (101 MHz, $CDCl_3$) δ_{ppm} 190.7, 167.1, 139.5, 136.7, 134.3, 133.4, 131.6, 129.4, 129.2, 129.2, 128.8, 128.7, 126.9, 35.4, 17.8.

HRMS (ESI, m/z) calcd. for $C_{16}H_{16}NO_2$ $[M+H]^+$: 254.1181; found: 254.1171.

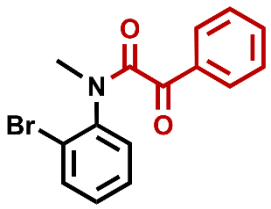

***N*-(2-bromophenyl)-*N*-methyl-2-oxo-2-phenylacetamide (5g)**

The general procedure was followed. Column chromatography (SiO_2, eluting with 85:15 hexane/ethyl acetate) afforded the desired product as a white solid (75 mg, 47%).

^{1}H NMR (400 MHz, $CDCl_3$) δ_{ppm} 7.89 (*dd*, *J* = 8.4, 1.3 Hz, 2H), 7.57 – 7.50 (*m*, 2H), 7.42 (*t*, *J* = 7.8 Hz, 2H), 7.29 (*dd*, *J* = 7.8, 1.8 Hz, 1H), 7.25 – 7.20 (*m*, 1H), 7.13 (*td*, *J* = 7.6, 1.8 Hz, 1H), 3.42 (*s*, 3H).

^{13}C NMR (101 MHz, $CDCl_3$) δ_{ppm} 190.2, 166.8, 139.9, 134.5, 134.0, 133.0, 131.3, 130.4, 129.9, 128.7, 128.6, 123.1, 35.6.

HRMS (ESI, m/z) calcd. for $C_{15}H_{13}BrNO_2$ $[M+H]^+$: 318.0130; found: 318.0144

_N_-(3-methoxyphenyl)-_N_-methyl-2-oxo-2-phenylacetamide (5h)

The general procedure was followed. Column chromatography (SiO_2, eluting with 80:20 hexane/ethyl acetate) afforded the desired product as a yellow oil (93 mg, 69%).

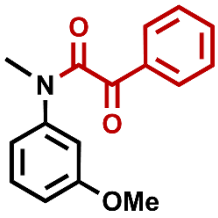

^{1}H NMR (400 MHz, $CDCl_3$) δ_{ppm} 7.92 – 7.84 (*m*, 2H), 7.58 (*t*, *J* = 7.4 Hz, 1H), 7.45 (*t*, *J* = 7.7 Hz, 2H), 7.13 (*t*, *J* = 8.1 Hz, 1H), 6.76 – 6.68 (*m*, 2H), 6.65 (*t*, *J* = 2.3 Hz, 1H), 3.61 (*s*, 3H), 3.48 (*s*, 3H).

^{13}C NMR (101 MHz, $CDCl_3$) δ_{ppm} 190.8, 167.2, 160.4, 142.4, 134.4, 133.8, 130.4, 129.6, 128.9, 118.8, 114.2, 112.3, 55.4, 36.3.

HRMS (ESI, m/z) calcd. for $C_{16}H_{16}NO_3$ $[M+H]^+$: 270.1130; found: 270.1124.

_N,N_-diethyl-2-oxo-2-phenylacetamide (5i)

The general procedure was followed. Column chromatography (SiO_2, eluting with 85:15 hexane/ethyl acetate) afforded the desired product as a yellow liquid (72 mg, 70%).

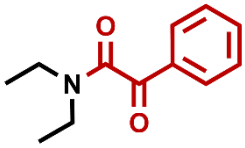

^{1}H NMR (400 MHz, $CDCl_3$) δ_{ppm} 7.93 (*dd*, *J* = 8.3, 1.3 Hz, 2H), 7.67 – 7.59 (*m*, 1H), 7.50 (*dd*, *J* = 8.4, 7.1 Hz, 2H), 3.56 (*q*, *J* = 7.2 Hz, 2H), 3.23 (*q*, *J* = 7.1 Hz, 2H), 1.28 (*t*, *J* = 7.2 Hz, 3H), 1.15 (*t*, *J* = 7.1 Hz, 3H).

^{13}C NMR (101 MHz, $CDCl_3$) δ_{ppm} 191.7, 166.8, 134.7, 133.3, 129.7, 129.1, 42.2, 38.9, 14.2, 13.0.

HRMS (ESI, m/z) calcd. for $C_{12}H_{16}NO_2$ $[M+H]^+$: 206.1181; found: 206.1194.

1-phenyl-2-(pyrrolidin-1-yl)ethane-1,2-dione (5j)

The general procedure was followed. Column chromatography (SiO_2, eluting with 85:15 hexane/ethyl acetate) afforded the desired product as a yellow liquid (68 mg, 67%).

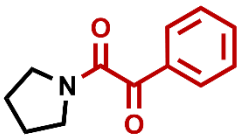

^{1}H NMR (400 MHz, $CDCl_3$) δ_{ppm} 7.98 (*d*, *J* = 7.5 Hz, 2H), 7.62 (*t*, *J* = 7.4 Hz, 1H), 7.49 (*t*, *J* = 7.6 Hz, 2H), 3.64 (*t*, *J* = 6.6 Hz, 2H), 3.41 (*t*, *J* = 6.4 Hz, 2H), 1.98 – 1.89 (*m*, 4H).

^{13}C NMR (101 MHz, $CDCl_3$) δ_{ppm} 191.7, 165.0, 134.7, 133.0, 130.0, 129.0, 46.8, 45.3, 26.0, 24.1.

HRMS (ESI, m/z) calcd. for $C_{12}H_{14}NO_2$ $[M+H]^+$: 204.1024; found: 204.1035.

1-phenyl-2-(piperidin-1-yl)ethane-1,2-dione (5k)

The general procedure was followed. Column chromatography (SiO_2, eluting with 85:15 hexane/ethyl acetate) afforded the desired product as a yellow liquid (67 mg, 62%).

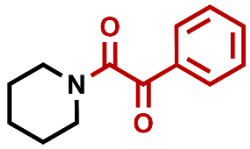

^{1}H NMR (400 MHz, $CDCl_3$) δ_{ppm} 7.99 – 7.90 (*m*, 2H), 7.66 – 7.59 (*m*, 1H), 7.50 (*t*, *J* = 7.7 Hz, 2H), 3.73 – 3.66 (*m*, 2H), 3.33 – 3.24 (*m*, 2H), 1.68 (*p*, *J* = 2.9 Hz, 4H), 1.58 – 1.49 (*m*, 2H).

^{13}C NMR (101 MHz, $CDCl_3$) δ_{ppm} 192.1, 165.5, 134.8, 133.3, 129.7, 129.1, 47.1, 42.2, 26.3, 25.5, 24.5.

HRMS (ESI, m/z) calcd. for $C_{13}H_{16}NO_2$ $[M+H]^+$: 218.1181; found: 218.1172.

1-Morpholino-2-phenylethane-1,2-dione (5l)

The general procedure was followed. Column chromatography (SiO_2, eluting with 75:25 hexane/ethyl acetate) afforded the desired product as a yellow liquid (60 mg, 55%).

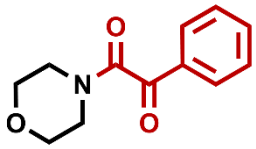

^{1}H NMR (400 MHz, $CDCl_3$) δ_{ppm} 7.95 – 7.89 (*m*, 2H), 7.62 (*t*, *J* = 7.4 Hz, 1H), 7.48 (*t*, *J* = 7.8 Hz, 2H), 3.76 (*s*, 4H), 3.61 (*t*, *J* = 4.8 Hz, 2H), 3.37 – 3.32 (*m*, 2H).

^{13}C NMR (101 MHz, $CDCl_3$) δ_{ppm} 191.2, 165.5, 135.0, 133.0, 129.6, 129.1, 66.7, 66.6, 46.2, 41.6.

HRMS (ESI, m/z) calcd. for $C_{12}H_{14}NO_3$ $[M+H]^+$: 220.0974; found: 220.0994.

2-(4-(Tert-butyl)phenyl)-*N*-methyl-2-oxo-*N*-phenylacetamide (6a)

The general procedure was followed. Column chromatography (SiO_2, eluting with 90:10 hexane/ethyl acetate) afforded the desired product as a yellow solid (94 mg, 69%).

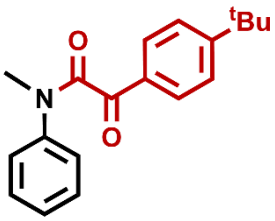

^{1}H NMR (400 MHz, $CDCl_3$) δ_{ppm} 7.79 (*d*, *J* = 8.8 Hz, 2H), 7.44 (*d*, *J* = 8.8 Hz, 2H), 7.27 – 7.19 (*m*, 3H), 7.17 – 7.13 (*m*, 2H), 3.48 (*s*, 3H), 1.31 (*s*, 9H).

^{13}C NMR (101 MHz, $CDCl_3$) δ_{ppm} 190.5, 167.4, 158.3, 141.5, 131.1, 129.6, 129.5, 128.1, 126.8, 125.9, 36.3, 35.4, 31.1.

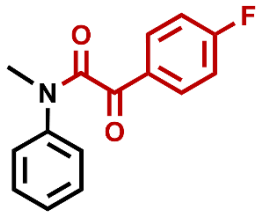

2-(4-Fluorophenyl)-*N*-methyl-2-oxo-*N*-phenylacetamide (6b)

The general procedure was followed. Column chromatography (SiO_2, eluting with 85:15 hexane/ethyl acetate) afforded the desired product as a yellow gummy liquid (80 mg, 62%).

^{1}H NMR (400 MHz, $CDCl_3$) δ_{ppm} 7.88 (*dd*, *J* = 8.9, 5.3 Hz, 2H), 7.26 – 7.18 (*m*, 3H), 7.15 – 7.05 (*m*, 4H), 3.47 and 3.32 (*s*, 3H, *N*-CH_3, Major and Minor conformers).

^{13}C NMR (101 MHz, $CDCl_3$) δ_{ppm} 189.2, 167.7, 166.9, 165.1, 141.2, 132.3, 132.2, 129.7, 128.3, 126.8, 116.3, 116.1, 36.3.

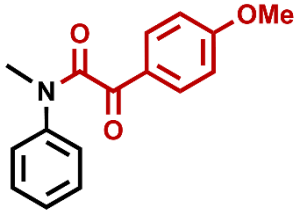

2-(4-Methoxyphenyl)-*N*-methyl-2-oxo-*N*-phenylacetamide (6c)

The general procedure was followed. Column chromatography (SiO_2, eluting with 80:20 hexane/ethyl acetate) afforded the desired product as a yellow gummy liquid (110 mg, 79%).

^{1}H NMR (400 MHz, $CDCl_3$) δ_{ppm} 7.83 (*d*, *J* = 9.0 Hz, 2H), 7.22 (*dd*, *J* = 10.6, 7.1 Hz, 3H), 7.13 (*dd*, *J* = 8.1, 1.6 Hz, 2H), 6.90 (*d*, *J* = 8.9 Hz, 2H), 3.85 (*s*, 3H), 3.47 (*s*, 3H).

^{13}C NMR (101 MHz, $CDCl_3$) δ_{ppm} 189.6, 167.5, 164.5, 141.5, 132.0, 129.6, 128.1, 126.8, 114.2, 55.7, 36.3.

HRMS (ESI, m/z) calcd. for $C_{16}H_{16}NO_3$ $[M+H]^+$: 270.1130; found: 270.1124.

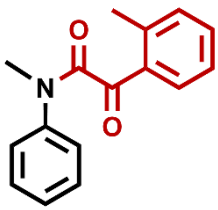

N-Methyl-2-oxo-N-phenyl-2-(o-tolyl)acetamide (6d)

The general procedure was followed. Column chromatography (SiO_2, eluting with 80:15 hexane/ethyl acetate) afforded the desired product as a yellow solid (67 mg, 85%).

^{1}H NMR (400 MHz, $CDCl_3$) δ_{ppm} 7.79 (*dd*, *J* = 7.8, 1.6 Hz, 1H), 7.36 (*td*, *J* = 7.5, 1.5 Hz, 1H), 7.25 (*t*, *J* = 7.2 Hz, 1H), 7.23 – 7.16 (*m*, 3H), 7.13 – 7.06 (*m*, 3H), 3.43 (*s*, 3H), 2.26 (*s*, 3H).

^{13}C NMR (101 MHz, $CDCl_3$) δ_{ppm} 193.3, 167.6, 141.1, 140.7, 133.1, 132.3, 132.2, 131.8, 129.5, 128.1, 127.1, 125.8, 36.2, 21.2.

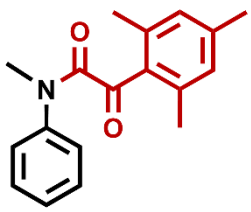

2-mesityl-*N*-methyl-2-oxo-*N*-phenylacetamide (6e)

The general procedure was followed. Column chromatography (SiO_2, eluting with 80:20 hexane/ethyl acetate) afforded the desired product as a pale-yellow solid (67 mg, 75%).

^{1}H NMR (400 MHz, $CDCl_3$) δ_{ppm} 7.21 (*dd*, *J* = 5.3, 1.9 Hz, 3H), 7.08 – 7.02 (*m*, 2H), 6.69 (*s*, 2H), 3.37 (*s*, 3H), 2.21 (*s*, 3H), 2.18 (*s*, 6H).
^{13}C NMR (101 MHz, $CDCl_3$) δ_{ppm} 194.4, 167.0, 141.5, 141.4, 137.7, 133.0, 129.7, 129.4, 128.1, 127.0, 37.8, 21.2, 20.8.
HRMS (ESI, m/z) calcd. for $C_{18}H_{20}NO_2$ $[M+H]^+$: 282.1494; found: 282.1465.

_N_-methyl-_N_,2-diphenylacetamide (6f)

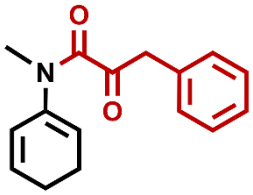

The general procedure was followed. Column chromatography (SiO_2, eluting with 80:20 hexane/ethyl acetate) afforded the desired product as a yellow gummy liquid (99 mg, 78%).
^{1}H NMR (400 MHz, $CDCl_3$) δ_{ppm} 7.32 – 7.21 (*m*, 7H), 7.06 – 7.01 (*m*, 2H), 6.82 (*dd*, *J* = 7.6, 2.1 Hz, 2H), 3.89 (*s*, 2H), 3.29 (*s*, 3H).
^{13}C NMR (101 MHz, $CDCl_3$) δ_{ppm} 197.0, 166.9, 141.3, 131.7, 130.1, 129.5, 128.8, 128.2, 127.5, 126.7, 47.0, 36.8.

_N_-Methyl-2-oxo-_N_-phenyl-2-(thiophen-2-yl)acetamide (6g)

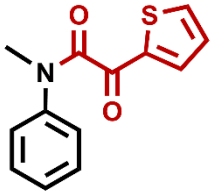

The general procedure was followed. Column chromatography (SiO_2, eluting with 80:20 hexane/ethyl acetate) afforded the desired product as a yellow solid (75 mg, 61%).
^{1}H NMR (400 MHz, $CDCl_3$) δ_{ppm} 7.85 (*d*, *J* = 3.9 Hz, 1H), 7.72 (*d*, *J* = 6.1 Hz, 1H), 7.30 (*d*, *J* = 7.3 Hz, 3H), 7.20 – 7.14 (*m*, 3H), 3.48 (*s*, 3H).
^{13}C NMR (101 MHz, $CDCl_3$) δ_{ppm} 182.7, 166.1, 141.7, 140.8, 136.0, 135.6, 132.9, 129.7, 128.6, 128.2, 126.6, 36.8, 29.8.

_N_-methyl-_N_-phenylbenzamide (7a)

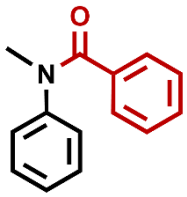

The general procedure was followed. Column chromatography (SiO_2, eluting with 80:20 hexane/ethyl acetate) afforded the desired product as a yellow solid (69 mg, 65%).
^{1}H NMR (400 MHz, $CDCl_3$) δ_{ppm} 7.29 (*d*, *J* = 6.8 Hz, 2H), 7.24 – 7.18 (*m*, 3H), 7.17 – 7.09 (*m*, 3H), 7.02 (*d*, *J* = 7.2 Hz, 2H), 3.49 (*s*, 3H).
^{13}C NMR (101 MHz, $CDCl_3$) δ_{ppm} 170.7, 144.9, 135.9, 129.6, 129.2, 128.8, 127.8, 127.0, 126.5, 38.5.

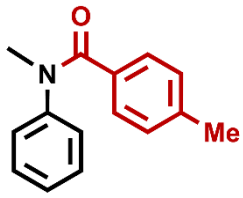

_N_,4-dimethyl-_N_-phenylbenzamide (7b)

The general procedure was followed. Column chromatography (SiO_2, eluting with 80:20 hexane/ethyl acetate) afforded the desired product as a yellow solid (77 mg, 68%).

^{1}H NMR (400 MHz, $CDCl_3$) δ_{ppm} 7.25 – 7.11 (*m*, 5H), 7.03 (*d*, *J* = 7.1 Hz, 2H), 6.95 (*d*, *J* = 8.1 Hz, 2H), 3.48 (*s*, 3H), 2.24 (*s*, 3H).

^{13}C NMR (101 MHz, $CDCl_3$) δ_{ppm} 170.8, 145.3, 139.9, 133.0, 129.2, 129.0, 128.5, 127.0, 126.4, 38.6, 21.4.

HRMS (ESI, m/z) calcd. for $C_{15}H_{16}NO$ $[M+H]^+$: 226.1232; found: 226.1222.

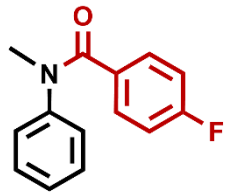

4-fluoro-_N_-methyl-_N_-phenylbenzamide (7c)

The general procedure was followed. Column chromatography (SiO_2, eluting with 80:15 hexane/ethyl acetate) afforded the desired product as a yellow solid (81 mg, 71%).

^{1}H NMR (400 MHz, $CDCl_3$) δ_{ppm} 7.26 (*dd*, *J* = 15.2, 8.4 Hz, 4H), 7.15 (*t*, *J* = 6.8 Hz, 1H), 7.05 (*d*, *J* = 8.2 Hz, 2H), 6.67 (*d*, *J* = 8.8 Hz, 2H), 3.74 (*s*, 3H), 3.50 (*s*, 3H).

^{13}C NMR (101 MHz, $CDCl_3$) δ_{ppm} 170.4, 160.7, 145.5, 131.0, 129.3, 128.0, 126.9, 126.4, 113.1, 55.3, 38.7.

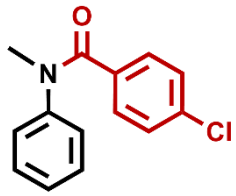

4-chloro-_N_-methyl-_N_-phenylbenzamide (7d)

The general procedure was followed. Column chromatography (SiO_2, eluting with 85:15 hexane/ethyl acetate) afforded the desired product as a yellow solid (85 mg, 69%).

^{1}H NMR (400 MHz, $CDCl_3$) δ_{ppm} 7.23 (*dd*, *J* = 8.3, 3.5 Hz, 4H), 7.19 – 7.11 (*m*, 3H), 7.02 (*d*, *J* = 7.8 Hz, 2H), 3.49 (*s*, 3H).

^{13}C NMR (101 MHz, $CDCl_3$) δ_{ppm} 169.4, 144.6, 135.7, 134.3, 130.3, 129.4, 128.0, 126.9, 126.8, 38.5.

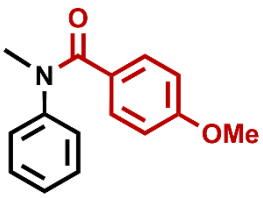

4-methoxy-_N_-methyl-_N_-phenylbenzamide (7e)

The general procedure was followed. Column chromatography (SiO_2, eluting with 75:25 hexane/ethyl acetate) afforded the desired product as a yellow solid (90 mg, 75%).

^{1}H NMR (400 MHz, $CDCl_3$) δ_{ppm} 7.26 (*dd*, *J* = 15.2, 8.4 Hz, 4H), 7.15 (*t*, *J* = 6.8 Hz, 1H), 7.05 (*d*, *J* = 8.2 Hz, 2H), 6.67 (*d*, *J* = 8.8 Hz, 2H), 3.74 (*s*, 3H), 3.50 (*s*, 3H).

^{13}C NMR (101 MHz, $CDCl_3$) δ_{ppm} 170.4, 160.7, 145.5, 131.0, 129.3, 128.0, 126.9, 126.4, 113.1, 55.3, 38.7.

_N_,2-dimethyl-_N_-phenylbenzamide (7f)

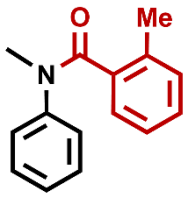

The general procedure was followed. Column chromatography (SiO_2, eluting with 80:20 hexane/ethyl acetate) afforded the desired product as a yellow solid (42 mg, 37%).

^{1}H NMR (400 MHz, $CDCl_3$) δ_{ppm} 7.51 (*d*, *J* = 2.0 Hz, 1H), 7.27 (*d*, *J* = 4.6 Hz, 4H), 7.18 (*t*, *J* = 7.4 Hz, 1H), 7.12 – 7.05 (*m*, 3H), 6.31 (*d*, *J* = 8.5 Hz, 1H), 3.47 (*s*, 3H), 2.83 (*d*, *J* = 3.9 Hz, 3H).

^{13}C NMR (101 MHz, $CDCl_3$) δ_{ppm} 169.4, 147.1, 145.7, 134.0, 130.4, 129.40, 126.9, 126.4, 124.2, 108.8, 38.9, 30.4.

3,4-dimethoxy-_N_-methyl-_N_-phenylbenzamide (7g)

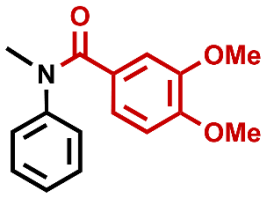

The general procedure was followed. Column chromatography (SiO_2, eluting with 80:20 hexane/ethyl acetate) afforded the desired product as a yellow gummy liquid (149 mg, 55%).

^{1}H NMR (400 MHz, $CDCl_3$) δ_{ppm} 7.25 – 7.19 (*m*, 2H), 7.16 – 7.10 (*m*, 1H), 7.03 (*d*, *J* = 8.1 Hz, 2H), 6.91 (*dd*, *J* = 8.3, 2.1 Hz, 1H), 6.82 (*d*, *J* = 2.1 Hz, 1H), 6.61 (*d*, *J* = 8.4 Hz, 1H), 3.78 (*s*, 3H), 3.61 (*s*, 3H), 3.47 (*s*, 3H).

^{13}C NMR (101 MHz, $CDCl_3$) δ_{ppm} 170.19, 150.26, 147.94, 145.67, 129.35, 127.89, 126.91, 126.47, 122.91, 112.49, 109.96, 55.90, 55.77, 38.77.

_N_-methyl-_N_,2-diphenylacetamide (7h)

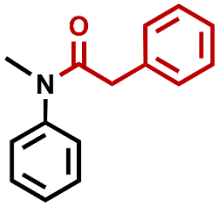

The general procedure was followed. Column chromatography (SiO_2, eluting with 85:15 hexane/ethyl acetate) afforded the desired product as a yellow oil. (46 mg, 41%).

^{1}H NMR (400 MHz, $CDCl_3$) δ_{ppm} 7.43 – 7.35 (*m*, 3H), 7.21 (*dd*, *J* = 10.5, 7.0 Hz, 3H), 7.12 (*d*, *J* = 7.7 Hz, 2H), 7.05 (*d*, *J* = 6.6 Hz, 2H), 3.46 (*s*, 2H), 3.28 (*s*, 3H).

^{13}C NMR (101 MHz, $CDCl_3$) δ_{ppm} 171.2, 144.1, 135.6, 129.8, 129.2, 128.4, 128.1, 127.8, 126.7, 41.0, 37.8.

HRMS (ESI, m/z) calcd. for $C_{15}H_{16}NO$ $[M+H]^+$: 226.1232; found: 226.1254.

***N*-methyl-*N*-phenylcyclohexanecarboxamide (7i)**

The general procedure was followed. Column chromatography (SiO_2, eluting with 80:15 hexane/ethyl acetate) afforded the desired product as a yellow liquid (89 mg, 82%).

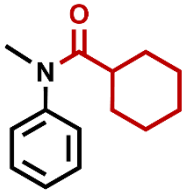

^{1}H NMR (400 MHz, $CDCl_3$) δ_{ppm} 7.39 (*t*, *J* = 7.6 Hz, 2H), 7.32 (*t*, *J* = 7.4 Hz, 1H), 7.15 (*d*, *J* = 7.7 Hz, 2H), 3.21 (*s*, 3H), 2.16 (*s*, 1H), 1.62 (*d*, *J* = 13.0 Hz, 4H), 1.50 (*q*, *J* = 12.7, 11.2 Hz, 3H), 1.15 (*q*, *J* = 13.0 Hz, 1H), 0.94 (*t*, *J* = 12.9 Hz, 2H).

^{13}C NMR (101 MHz, $CDCl_3$) δ_{ppm} 176.5, 144.3, 129.8, 127.7, 127.3, 41.4, 37.5, 29.5, 25.7, 25.6.

HRMS (ESI, m/z) calcd. for $C_{14}H_{20}NO$ $[M+H]^+$: 218.1545; found: 218.1540.

***N*-methyl-*N*-phenylacrylamide (7j)**

The general procedure was followed. Column chromatography (SiO_2, eluting with 80:20 hexane/ethyl acetate) afforded the desired product as a white solid (36 mg, 45%).

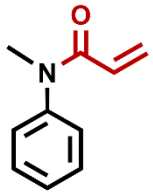

^{1}H NMR (400 MHz, $CDCl_3$) δ_{ppm} 7.41 (*t*, *J* = 7.4 Hz, 2H), 7.33 (*t*, *J* = 7.5 Hz, 1H), 7.22 – 7.14 (*m*, 2H), 6.37 (*dd*, *J* = 16.8, 2.1 Hz, 1H), 6.07 (*dd*, *J* = 16.8, 10.3 Hz, 1H), 5.51 (*dd*, *J* = 10.3, 2.1 Hz, 1H), 3.36 (*s*, 3H).

^{13}C NMR (101 MHz, $CDCl_3$) δ_{ppm} 165.9, 143.6, 129.7, 128.6, 127.8, 127.6, 127.4, 37.6.

***N*-methyl-*N*-phenylthiophene-3-carboxamide (7k)**

The general procedure afforded the desired product as a yellow solid (62 mg, 57%).

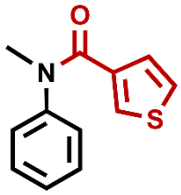

^{1}H NMR (400 MHz, $CDCl_3$) δ_{ppm} 7.34 (*t*, *J* = 7.3 Hz, 2H), 7.30 – 7.25 (*m*, 1H), 7.20 (*dd*, *J* = 3.0, 1.3 Hz, 1H), 7.17 – 7.12 (*m*, 2H), 7.03 (*dd*, *J* = 5.1, 3.0 Hz, 1H), 6.88 (*dd*, *J* = 5.1, 1.3 Hz, 1H), 3.48 (*s*, 3H).

^{13}C NMR (101 MHz, $CDCl_3$) δ_{ppm} 165.0, 144.9, 136.8, 129.9, 129.5, 128.6, 127.3, 127.2, 124.4, 38.6.

4.10. References:

1. Costas, M.; Mehn, M. P.; Jensen, M. P.; Que, L. Dioxygen Activation at Mononuclear Nonheme Iron Active Sites: Enzymes, Models, and Intermediates. *Chem. Rev.* **2004**, *104*, 939–986.
2. Rittle, J.; Green, M. T. Cytochrome P450 Compound I: Capture, Characterization, and C-H Bond Activation Kinetics. *Science* **2010**, *330*, 933–937.
3. Broere, D. L. J.; Plessius, R.; van der Vlugt, J. I. New Avenues for Ligand-mediated Processes Expanding Metal Reactivity by the use of Redox-active Catechol, *o*-aminophenol and *o*-Phenylenediamine Ligands. *Chem. Soc. Rev*. **2015**, *44*, 6886–6915.
4. Bains, A. K.; Ankit, Y.; Adhikari, D. Bioinspired Radical-Mediated Transition-Metal-Free Synthesis of N-Heterocycles under Visible Light. *ChemSusChem* **2021**, *14*, 324–329.
5. Lyaskovskyy, V.; de Bruin, B. Redox Non-Innocent Ligands: Versatile New Tools to Control Catalytic Reactions. *ACS Catal.* **2012**, *2*, 270–279.
6. Ganguly, S.; Ghosh, A. Seven Clues to Ligand Noninnocence: The Metallocorrole Paradigm. *Acc. Chem. Res.* **2019**, *52*, 2003–2014.
7. Bains, A. K.; Kundu, A.; Maiti, D.; Adhikari, D. Ligand-redox Assisted Nickel Catalysis Toward Stereoselective Synthesis of (n+1)-Membered Cycloalkanes from 1,n-diols with Methyl Ketones. *Chem. Sci.* **2021**, *12*, 14217–14223.
8. Bains, A. K.; Kundu, A.; Yadav, S.; Adhikari, D. Borrowing Hydrogen-Mediated *N*-Alkylation Reactions by a Well-defined Homogeneous Nickel Catalyst. *ACS Catal.* **2019**, *9*, 9051–9059.
9. Jain, R.; Mamun, A. A.; Buchanan, R. M.; Kozlowski, P. M.; Grapperhaus, C. A. Ligand-Assisted Metal-Centered Electrocatalytic Hydrogen Evolution upon Reduction of a Bis(thiosemicarbazonato)Ni(II) Complex. *Inorg. Chem.* **2018**, *57*, 13486–13493.
10. Bullock, R. M. Catalysis Without Precious Metals, Wiley-VCH; Weinheim, 2010.
11. Bullock, R. M. Reaction: Earth-Abundant Metal Catalysts for Energy Conversions. *Chemistry* **2017**, *2*, 444–446.
12. Sherbow, T. J.; Fettinger, J. C.; Berben, L. A. Control of Ligand *p*Ka Values Tunes the Electrocatalytic Dihydrogen Evolution Mechanism in a Redox-Active Aluminum(III) Complex. *Inorg. Chem.* **2017**, *56*, 8651–8660.
13. Andrez, J.; Guidal, V.; Scopelliti, R.; Pe´caut, J.; Gambarelli, S.; Mazzanti, M. Ligand and Metal Based Multielectron Redox Chemistry of Cobalt Supported by Tetradentate Schiff Bases. *J. Am. Chem. Soc.* **2017**, *139*, 8628–8638.

14. Singh, K.; Singh, R.; Hazari, A. S.; Adhikari, D. Bimodal Photocatalytic Behaviour of a Zinc *β*-diketiminate: Application to Trifluoromethylation Reactions. *Chem. Commun.* **2022**, *58*, 4384–4387.
15. Singh, K.; Sreedharan, V.; Adhikari, D. Visible Light Photoredox by a (^{ph,Ar}NacNac)$_2$Zn Photocatalyst: Photophysical Properties and Mechanistic Understanding. *Inorg. Chem. Front.* **2021**, *8*, 2078–2087.
16. Gilroy, J. B.; Otten, E. Formazanate Coordination Compounds: Synthesis, Reactivity, and Applications. *Chem. Soc. Rev.* **2020**, *49*, 85–113.
17. Lipunova, G. N.; Federchenko, T. G.; Chupakhin, O. N. New Aspects of the Chemistry of Formazans. *Russ. J. Gen. Chem.* **2019**, *89*, 1225–1245.
18. Chang, M. C.; Dann, T.; Day, D. P.; Lutz, M.; Wildgoose, G. G.; Otten, E. The Formazanate Ligand as an Electron Reservoir: Bis(Formazanate) Zinc Complexes Isolated in Three Redox States. *Angew. Chem., Int. Ed.* **2014**, *53*, 4118–4122.
19. Broere, D. L. J.; Mercado, B. Q.; Lukens, J. T.; Vilbert, A. C.; Banerjee, G.; Lant, H. M. C.; Lee, S. H.; Bill, E.; Sproules, S.; Lancaster, K. M.; Holland, P. L. Reversible Ligand-Centered Reductionin Low-Coordinate Iron Formazanate Complexes. *Chem. Eur. J.* **2018**, *24*, 9417–9425.
20. Novoa, S.; Paquette, J. A.; Barbon, S. M.; Maar, R. R.; Gilroy, J. B. Side-chain Boron Difluoride Formazanate Polymers *via* Ring-Opening Metathesis Polymerization. *J. Mater. Chem. C* **2016**, *4*, 3987–3994.
21. Chang, M. C.; Otten, E. Synthesis and Ligand-Based Reduction Chemistry of Boron Difluoride Complexes with Redox-Active Formazanate Ligands. *Chem. Commun.* **2014**, *50*, 7431–7433.
22. Kabir, E.; Patel, D.; Clark, K.; Teets, T. S. Spectroscopic and Electrochemical Properties of Electronically Modified Cycloplatinated Formazanate Complexes. *Inorg. Chem.* **2018**, *57*, 10906–10917.
23. Jin, D.; Sun, X.; Hinz, A.; Roesky, P. W. Rare-earth Metal Complexes with Redox-active Formazanate Ligands. *Dalton Trans.* **2022**, *51*, 5218–5226.
24. Mu, G.; Cong, L.; Wen, Z.; Wu, J. I. C.; Kadish, K. M.; Teets, T. S. Homoleptic Platinum Azo-iminate Complexes *via* Hydrogenative Cleavage of Formazans. *Inorg. Chem.* **2018**, *57*, 9468–9477.

25. Gilroy, J. B.; Otieno, P. O.; Ferguson, M. J.; McDonald, R.; Hicks, R. G. Synthesis and Characterization of 3-Cyano- and 3-Nitroformazans, Nitrogen-Rich Analogues of *β*-Diketimine Ligands. *Inorg. Chem.* **2008**, *47*, 1279–1286.
26. Gilroy, J. B.; Patrick, B. O.; McDonald, R.; Hicks, R. G. Transition Metal Complexes of 3-Cyano- and 3-Nitroformazans. *Inorg. Chem.* **2008**, *47*, 1287–1294.
27. Zhang, C.; Xu, Z.; Zhang, L.; Jiao, N. Copper-Catalyzed Aerobic Oxidative Coupling of Aryl Acetaldehydes with Anilines Leading to α-Ketoamides. *Angew. Chem. Int. Ed.* **2011**, *50*, 11088 –11092.
28. Ozawa, F.; Soyama, H.; Yamamoto, T.; Yamamoto, A. Catalytic Double Carbonylation of Organohalogen Compounds Promoted by Palladium Complexes. *Tetrahedron Lett.* **1982**, *23*, 3383–3386.
29. Zhang, X.; Yanga, W.; Wang, L. Silver-catalyzed Amidation of Benzoylformic Acids with Tertiary Amines *via* Selective Carbon–Nitrogen Bond Cleavage. *Org. Biomol. Chem.* **2013**, *11*, 3649–3654.
30. Das, P.; Begam, H. M.; Bhunia, S. K.; Jana, R. Photoredox-Catalyzed Tandem Demethylation of *N*,*N*-Dimethyl Anilines Followed by Amidation with *α*-Keto or Alkynyl Carboxylic Acids. *Adv. Synth. Catal.* **2019**, *361*, 4048–4054.
31. Mandal, A.; Schwederski, B.; Fiedler, J.; Kaim, W.; Lahiri, G. K. Evidence for Bidirectional Noninnocent Behavior of a Formazanate Ligand in Ruthenium Complexes. *Inorg. Chem.* **2015**, *54*, 8126–8135.
32. Kumar, D.; Vemula, S. R.; Cook, G. R. Recent Advances in the Catalytic Synthesis of *α*-Ketoamides. *ACS Catal.* **2016**, *6*, 4920–4945.
33. Maar, R. R.; Kenaree, A. R.; Zhang, R.; Tao, Y.; Katzman, B. D.; Staroverov, V. N.; Ding, Z.; Gilroy, J. B. Aluminum Complexes of $N_2O_2^{3-}$ Formazanate Ligands Supported by Phosphine Oxide Donors. *Inorg. Chem.* **2017**, *56*, 12436–12447.
34. Sur, S. K. Measurement of Magnetic Susceptibility and Magnetic Moment of Paramagnetic Molecules in Solution by High-Field Fourier Transform NMR Spectroscopy. *J. Magn. Reson.* **1989**, *82*, 169–173.
35. Evans, D.F. The Determination of the Pararnagnetic Susceptibility of Substances in Solution by Nuclear Magnetic Resonance. *J. Chem. Soc.* **1959**, 2003–2005.
36. Noodleman, L. Valence Bond Description of Antiferromagnetic Coupling in Transition Metal Dimers. *J. Chem. Phys.* **1981**, *74*, 5737–5743.

37. Baciocchi, E.; Bietti, M.; Gerini, M. F.; Lanzalunga, O. Electron-Transfer Mechanism in the N-Demethylation of *N*,*N*-Dimethylanilines by the Phthalimide-*N*-oxyl Radical. *J. Org. Chem.* **2005**, *70*, 5144–5149.
38. Robello, M.; Barresi, E.; Baglini, E.; Salerno, S.; Taliani, S.; Settimo, F. D. The Alpha Keto Amide Moiety as a Privileged Motif in Medicinal Chemistry: Current Insights and Emerging Opportunities. *J. Med. Chem.* **2021**, *64*, 3508–3545.
39. de Vries, F.; Otten, E. Reversible On/Off Switching of Lactide Cyclopolymerization with a Redox-Active Formazanate Ligand. *ACS Catal.* **2022**, *12*, 4125–4130.
40. Neese, F. Software Update: The ORCA Program System, Version 4.0. WIREs *Comput. Mol. Sci.* **2018**, *8*, e1327.
41. Becke, A.D. Density-functional Thermochemistry. III. The Role of Exact Exchange. *J. Chem. Phys.* **1993**, *98*, 5648–5652.
42. Lee, C.; Yang, W.; Parr, R.G. Development of the Colle-Salvetti Correlation-Energy Formula into a Functional of the Electron Density. *Phys. Rev. B* **1988**, *37*, 785–789.
43. Weigend, F.; Ahlrichs, R. Balanced Basis Sets of Split Valence, Triple Zeta Valence and Quadruple Zeta Valence Quality for H to Rn: Design and Assessment of Accuracy**.** *Phys. Chem. Chem. Phys.* **2005**, *7*, 3297–3305.
44. Schaafer, A.; Horn, H.; Ahlrichs, R. Fully Optimized Contracted Gaussian Basis Sets for Atoms Li to Kr. *J. Chem. Phys*. **1992**, *97*, 2571–2577.

Chapter 5

Exclusively Ligand Redox-Promoted C-H Tertiary Alkylation of Heteroarenes

A part of this work has been published in ACS Catal., **2024**, *14*, 8939−8948

5.1. Introduction

Catalytic processes, heavily governed by ligand-based redox is at the mainstay of 3d transition metal catalysis.[1–4] Major inspiration in this direction comes from metal-radical motifs in active sites of metalloenzymes including cytochrome P-450[5] or galactose oxidase[6]. In such cases the ligands' capability of holding an electron is judged as instrumental in dictating the final outcome of the process. Mimicking such processes derived tremendous recent attention since such redox reservoir/sink characteristics can ideally emulate two-electron processes on 3d-transition metal systems, which are as such prone to perform one-electron chemistry.[7–11] In such processes, often the ligand plays a preeminent role, far beyond their traditional participation as robust ancillary that also fine tunes the electronics at the metal coordination sphere. Recent developments showed few prominent examples where an intricate interplay of the ligand and the 3d-metal can succeed to solve challenging chemical/electrochemical processes.[12–15] Since there is a strong drive for 3d transition metal catalysis as an approach to sustainability, there is a genuine need to identifying ligand backbones that directly participate in redox reactions, thus imitating the reactivity patterns afforded by precious metals.[16–18]

Along the progress of 3d transition metal catalysis, iron is a major contributor.[19-20] It is the second most abundant element available in Earth's crust. Inexpensive iron metal salts often promote radical chemistry, and has shown its strong presence in cross-coupling chemistry and atom-transfer radical polymerization reactions.[21-24] Surprisingly, the precise role of iron's oxidation state is not thoroughly evaluated in many reactions.[25] Knowing the oxidation state of iron is important to control the processes where switching to a redox noninnocent ligand often alters spin state population in iron and change the course of a catalytic process. In this chapter, we report a redox noninnocent formazanate backbone coordinated to iron, where the complex is capable of promoting radical chemistry to conduct C-H tertiary alkylation of heteroarenes. It has been utilized in a series of chemical transformations under very small amount of catalyst loading. By thorough Mössbauer and EPR spectroscopic analysis we prove that the formazanate ligand motif helps in single electron transfer, largely retaining the iron's oxidation state throughout the catalytic cycle.

5.2. Results and Discussion

In the portfolio of redox noninnocent ligands 2-iminopyridines,[26] bis(imino)pyridines,[27] *o*-phenylenediamines,[28] dithiolenes,[29] are some of the key motifs that often drive important chemical transformations in tandem with 3d-metals. Structurally, formazanate is very close to

ubiquitous β-diketiminates,[30] although further coordination can be introduced by modifying the *N*-aryl group. Previously, the formazanate coordinated transition metal complexes have been utilized for synthesizing molecules with impressive photophysical properties.[31-32] However, their use in developing homogeneous catalysts is relatively scarce.[33-34]

5.2.1. Synthesis of Formazanate Ligand and Iron(III) Complex 1

In our work, we selected 1,5-bis(2-hydroxyphenyl)-3-phenylformazan (**L**) backbone that can afford tetradentate coordination (Scheme 5.1).[35] The synthesis of the desirable catalyst molecule starts with deprotonation of **L** by 3.1 equivalents of NaH and the coordination to Fe(III) precursor, following a literature procedure.[35] Accordingly, treatment of $FeCl_3$ in the THF solution of the deprotonated ligand backbone immediately evinces a color change from dark blue to darkgreen, that lead to the formation of $(L)Fe(THF)_2$ complex, tentatively (Scheme 5.1a).

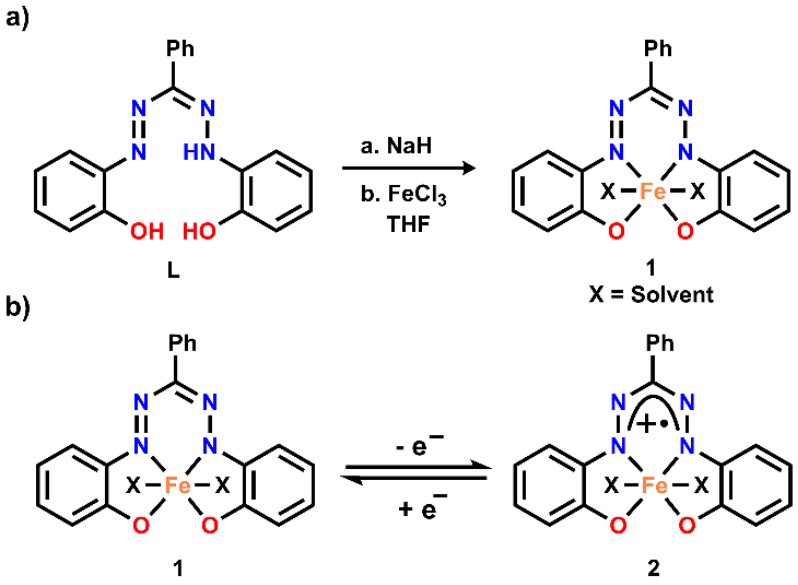

Scheme 5.1. (a) Attempted synthesis of $(L)Fe^{III}(THF)_2$ complex **1**. (b) ligand-centered reversible redox process.

It was expected that the tetradentate coordination of the azophenolate with Fe(III) will be in plane, and the two axial positions will be filled with loosely bound THF. This assignment is in line with Hick's iron formazanate complex, where a similar formazanate ligand coordinates to Fe(III), and two pyridine molecules binds axially to complete the octahedral coordination sphere.[35] Notably, the coordinated THF is a labile placeholder and its removal gives access to free binding site for an incoming substrate.

5.3. Characterization of (L)$Fe^{III}(THF)_2$ Complex (1) and Single Electron Oxidised form of 1

5.3.1. Mössbauer spectroscopic Analysis of Complex 1

To unambiguously assign the iron oxidation state in **1**, solid sample was analyzed through zero-field Mössbauer spectroscopy at a temperature of 20 K. Fitting the experimental data displayed two major subspectra in close to 1:1 ratio. The first subspectrum displays an isomer shift of δ 0.59 mm s^{-1} and quadrupole splitting, ΔE_Q of 0.85 mm s^{-1} (Figure 5.1).

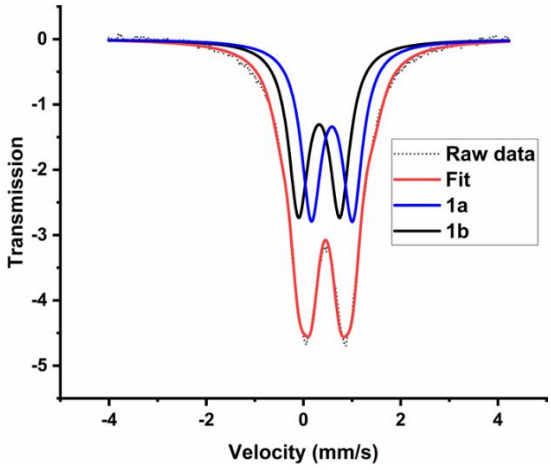

Figure 5.1. ^{57}Fe Mössbauer spectroscopic (zero-field) analysis for the Fe(III)formazanate complex **1**. The data was collected at 20 K.

This set of values strongly suggests a high-spin (HS) Fe(III) (labeled as **1a,** Scheme 5.2) molecule likely in a pseudooctahedral ligand environment. The relatively smaller quadrupole splitting parameter, that provides the measure of the asymmetry of the electric field gradient at the nucleus, suggests relatively symmetric environment akin to S = 5/2 spin state. On the other hand, the second subspectrum also discloses a well-resolved quadrupole doublet with δ 0.32 mm s^{-1} and ΔE_Q of 0.85 mm s^{-1}. The change in isomer shift compared to the first subspectrum is indicative of another HS Fe(III) (S = 5/2) (labeled as **1b**, Scheme 5.2) species in solid state.

The lower value of δ for the second species hints the iron to remain in a strong ligand environment, that prompts us to suggest the retention of a chloride ligand in an "ate" complex. The chloride is an anionic ligand and forms a much shorter, and hence stronger bond to Fe(III), in comparison to THF. Multiple attempts to crystalize the iron molecules in this speciation were futile due to the mixture of Fe(III) species in solution. Prior literature report also disclosed

the difficulty in characterizing such sample speciation via crystallography when multiple species are present due to solvent vs counter anion coordination.[36]

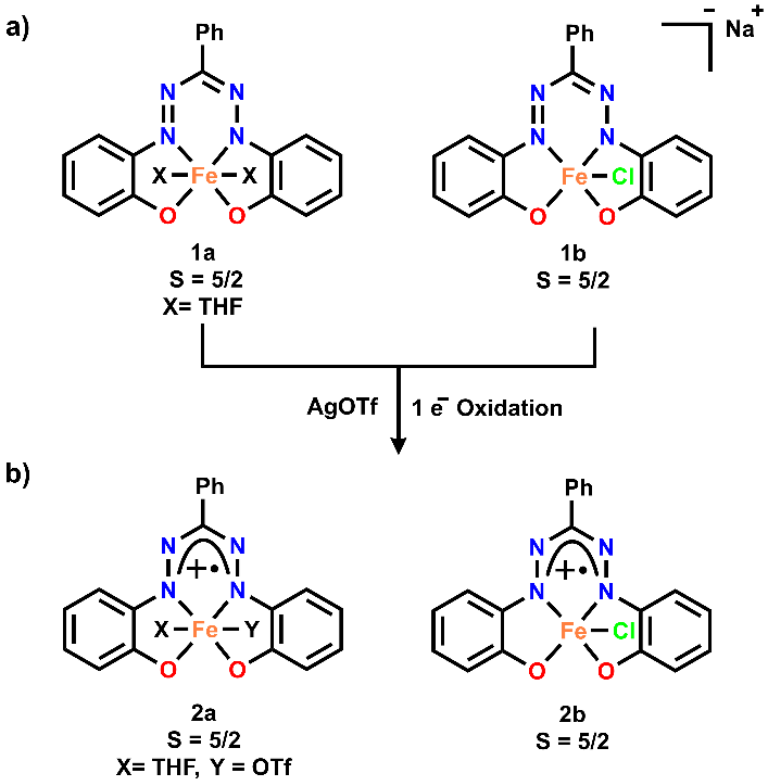

Scheme 5.2. a) Plausible Fe(III) molecules to describe the composition of **1**. b) The corresponding species upon one-electron oxidation describing composition of **2**.

5.3.2. High Resolution Mass Spectrometry Analysis of Fe(III)formazanate Complex 1

However, the synthesized iron complex contains two species. As per above discussion, the second species might be an iron complex with one of chloride ligand attached to the metal center. As, the final species is ate complex with one negative charge on the coordination sphere having sodium as counter cation. So, the ESI mass spectrometry experiment in negative mode was conducted. Fortunately, the ESI mass spectrometry identified the presence of **1b** in solution. For 1b: HRMS (ESI, m/z) calcd. for $C_{19}H_{12}ClFeN_4O_2$ $[M - H]^-$: 420.9977; found: 420.9970.

Such an iron chloride complex was also documented in a prior report where the ligand backbone involved a β-diketiminate appended with phenolic arms.[37] We note that speciation and availing multiple spin states, depending on the very small change in the ligand environment is rather common for Fe(III) complexes.[38-43]

In turn, we rely on Mössbauer, EPR and magnetic data was conto gather electronic information for the suggested Fe(III) molecules from formazanate coordination.

5.3.3. Solid State Magnetic Moment Analysis of Fe(III)formazanate Complex 1

In line with the presence of two HS Fe(III) species present in a solid mixture, a magnetic moment measurement was conducted at room temperature revealed a value of 5.8 μ_B, strongly supporting the S = 5/2 Fe(III) species being present. In essence, the sample represents a physical mixture of two different Fe(III) molecules both possessing HS iron centers.[44]

5.3.4. Cyclic Voltammetry Measurement of Fe(III)formazanate Complex 1

The formazanate backbone is redox noninnocent[45] and it is anticipated that the electron-rich nature of the backbone will prompt the oxidation majorly on the ligand backbone. A cyclic voltammetry measurement in dichloromethane solution evinced a broad quasi-reversible wave at 0.38 V (vs Fc^+/Fc couple) (Figure 2).

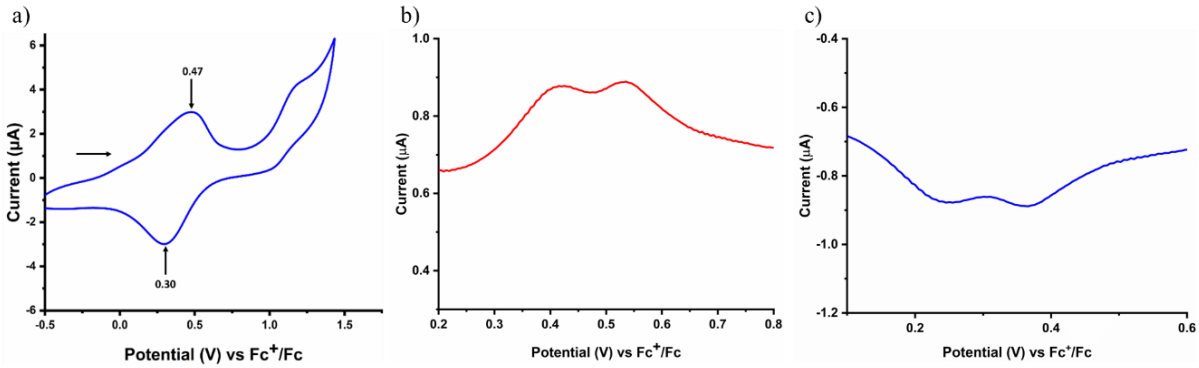

Figure 5.2. a) CV of 1 mM of **1** dissolved in dichloromethane along with 0.1 M solution of tetrabutyl-ammonium hexafluorophosphate salt as an electrolyte. The scan rate was 200 mV s^{-1}. b) DPV plot during oxidation wave c) DPV plot during reduction wave.

Such a moderate potential required to extract out one electron from the system is indicative of ligand-based oxidation since the alternative iron-centered oxidation; Fe(III)/Fe(IV) couple will demand a much positive potential. The observed potential also comes closer to the previously observed formazanate ligand oxidation for an aluminum complex.[46] The broad quasi-reversible wave also hints the presence of two species having a narrow difference in their redox potentials, Apparently, the differential pulse voltammetry (DPV) study clearly located two peaks having a difference of 120 mV in their peak potentials (Figure 5.2b). Furthermore, a second irreversible oxidation wave was located at 1.26 V, which is also in strong agreement with the prior report involving the (formazanate)Al complex.[46] The cyclic voltammetry experiment has

been repeated multiple times on different batches of sample to conclude that the presence of two Fe(III) molecules is reproducible under the preparatory method.

5.3.5. UV-Visible Analysis of Ligand (L) and Fe(III)-formazanate Complex 1

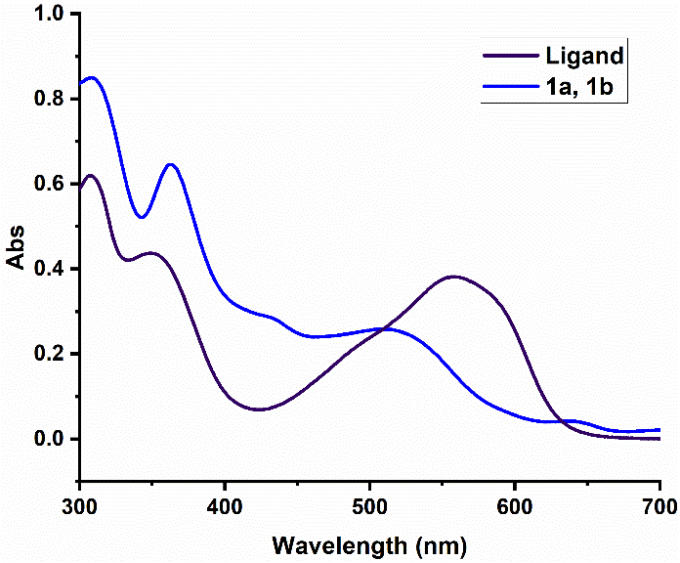

Figure 5.5. UV-Visible spectrum of Ligand (Violet line) and Fe(III) formazanate complex (Blue line)

TD-DFT was performed to analyse the nature of electronic transitions further. The TD-DFT analysis of the complex **1a** displays transitions at 357 nm, 390 nm, 440 nm, 511 nm. Similarly, the TD-DFT analysis of the complex **1b** shows transitions at 363 nm, 421 nm, 566 nm, 666 nm. Both the predicted spectra closely resemble the experimental absorption spectra of complex **1**. Along with some ligand-centered transitions, majority of transitions involve mixed metal-ligand orbitals.

5.4. Synthesis and Characterization of Oxidised Fe(III) Complex 2

5.4.1. Synthesis of Oxidized Fe(III)formazanate Complex 2

The chemical oxidation of the bulk starting complexes by AgOTf showed a rapid color change to reddish brown, and the oxidation were completed within an hour. Extracting the resulting oxidized product in THF left a dark brown colored material. ^{19}F NMR spectroscopic data was collected on the sample to find the resonance at -19 ppm (with respect to $BF_3.OEt_2$). The crude sample was subjected to HRMS for further studies. From mass spectrum, the signature of **2a**, where a triflate ligand is bound to Fe(III) was observed. Similarly, the oxidized version of **1b** was further diagnosed via mass spectrometry to retain the chloride ion (**2b**).

For **2a**: HRMS (ESI, m/z) calcd. for $C_{20}H_{14}F_3FeN_4O_5S$ $[M + H]^+$: 534.9987; found: 534.9941.

For **2b**: HRMS (ESI, m/z) calcd. for $C_{19}H_{12}ClFeN_4O_2$ $[M - H]^-$: 420.9977; found: 420.9981.

5.4.2. Mössbauer spectroscopic Analysis of Oxidised Iron(III) Complex 2

To unambiguously assign the oxidation state of the iron center, Mössbauer spectroscopic analysis was conducted. Gratifyingly, in the zero-field Mössbauer analysis, again two major subspectra were visible. The first major subspectrum displayed the isomer shift δ 0.66 mm s^{-1} with a ΔE_Q of 1.02 mm s^{-1}. The small change of the isomer shift value compared to the parent molecule suggests the iron oxidation to remain unaltered (Figure 3) proving oxidation at the formazanate backbone.[47-48] We assign this as HS, $(L^{\bullet+})Fe^{III}(THF)(OTf)$, **2a** (Scheme 2). Plausibly, the depletion of electron density in the ligand backbone reduces the sigma-electron donation to the metal center, making the s-electron density around iron nucleus less, thus shifting the chemical shift to a slightly higher value. Similarly, the fitting of the data reveals the second subspectrum that is represented by δ and ΔE_Q of 0.42 and 0.98 mm s^{-1} respectively. These values represent the HS, $(L^{\bullet+})Fe^{III}Cl(THF)$, **2b** (Scheme 5.2).

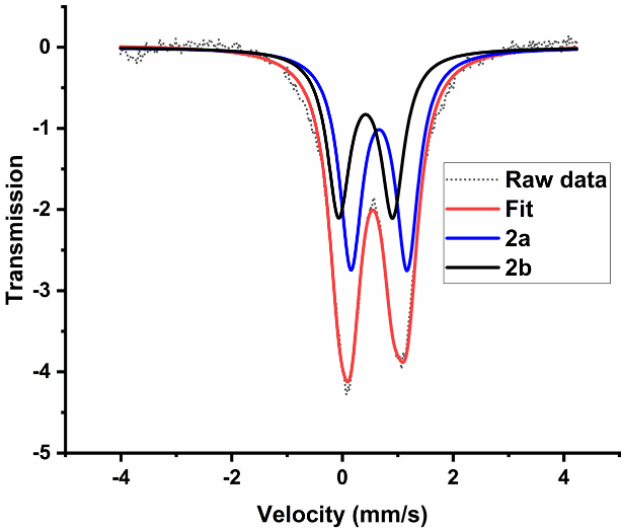

Figure 5.3. ^{57}Fe zero-field Mössbauer spectroscopic analysis (20 K) for the oxidized sample from **1**.

In the oxidized sample the two subspectra shows up in a 3:2 ratio, that concludes that the two HS iron species are likely in equilibrium at starting mixture, so that upon oxidation the relative proportion may change. The higher value of quadrupole split in the oxidized variety (both **2a** and **2b**) hints increased asymmetry in the electronic environment of the system. This likely stems from the change in electric field gradients from oxidized ligand backbone, as well as a

probable triflate binding. Indeed, the mass spectrometric analysis revealed the presence of an iron-bound triflate in **2a**.

Additionally, the ^{19}F NMR resonance appeared at δ -19 ppm, as a real broad peak. In moderately coordinating solvent, the triflate easily exchanges with the solvent that also causes such peak broadening.[49-50] However, such a weak binding of triflate does not change the spin state of the Fe(III) center.

5.4.3. EPR Analysis of Fe(III)formazanate Complex 1 and Oxidised Fe(III) Complex 2

Moreover, the X-band EPR spectroscopic determination of the iron speciation is in close agreement with the Mössbauer spectroscopic data. A THF glass of the parent sample at 4.2 K clearly evinces the signature of S = 5/2 Fe(III) species. The low temperature data shows a small signal at g = 9.76, while a strong and sharp signal at g = 5.84, 3.12 and 1.99 respectively (Figure 5.4a).[51] From the emergence of the g values for the HS molecule, it was estimated that the rhombicity (D/E) to be close to 0.1.[52] In this spectrum, few peaks are relatively broad and they represent both S = 5/2 Fe(III) species to be available in the analyzed sample, consistent with Mössbauer and CV experiments.

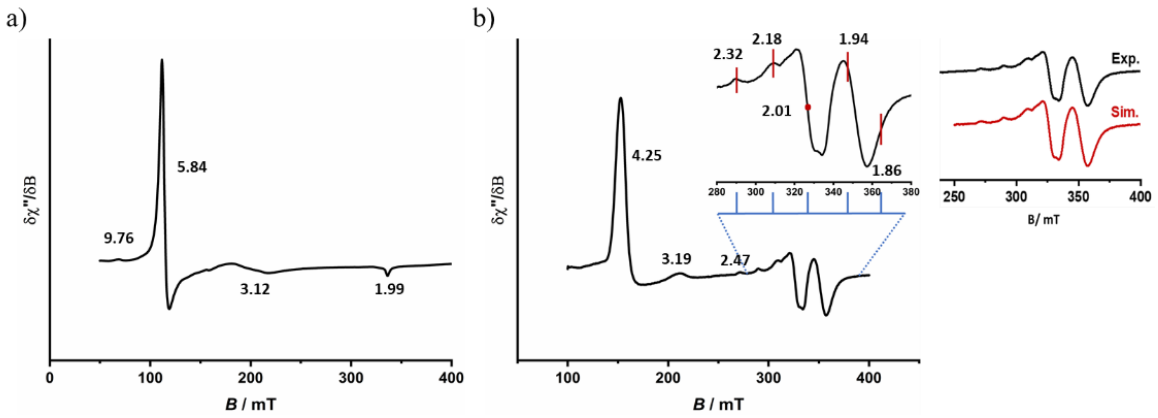

Figure 5.4. (a) X-band EPR spectrum of **1** in frozen THF at 4.2 K. (b) X-band EPR spectrum of the oxidized sample **2** in frozen THF at 4.2 K.

To unambiguously ascertain the ligand-based oxidation, the oxidized mixture was further interrogated by EPR spectroscopy. The EPR analysis on the oxidized batch discloses the presence of S= 5/2 species along with the clear signature of oxidized ligand backbone. The EPR signature for the S = 5/2 species is clear at g = 4.25, 3.19 and 1.86 that pertains to a rhombicity of 0.2. Most importantly, the formazanate ligand oxidation is prominent with the appearance of an anisotropic signal centered around g = 2.01 with visible hyperfine features.

The ligand-based SOMO for the radical cation, $\mathbf{2}^{\bullet+}$ shows major molecular orbital coefficients on two nitrogens, that are directly coordinated to Fe(III) (Figure 4b). Keeping this into account, the simulation of this part of the spectrum was attempted that found to be a good fit. Theoretically reproducing the spectrum strongly suggests the ligand-based electron to couple with two nitrogens along with iron (Figure 5.4b). However, the interaction of the ligand-based radical with the iron d-electron is very weak that is supported by the appearance of separated signal pertaining to an organic radical. Overall, the X-band EPR spectroscopic data strongly supports that the one-electron oxidation to happen on the formazanate ligand backbone, while the iron oxidation state is retained as +3. Indeed, retention of Kramer's system in the oxidized sample directly speaks for the preservation of the metal oxidation state during the process.

5.5. Computational Analysis

This ligand-based oxidation was further interrogated by DFT analysis focusing on the S = 5/2 molecule **2a** at B3LYP level of theory.[53-54] The electronic structure of the oxidized molecule **2a** can represent two different spin scenario; the structure can possess a spin-uncoupled septet state, or alternatively, the ligand-based electron may antiferromagnetically couple the S = 5/2 of iron to overall represent an open-shell quintet state (Figure 5.6). In DFT calculations, both the septet and open-shell quintet states are extremely close in energy having an energy difference of only 1.2 kcal mol^{-1} favoring the septet as ground state.

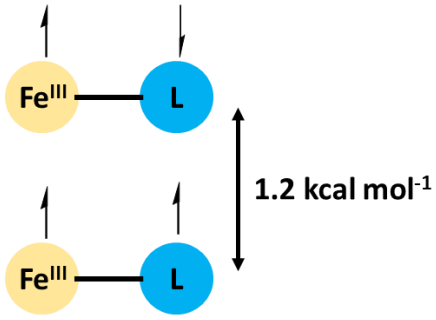

Figure 5.6. Calculated energy difference between spin-uncoupled septet state and open-shell quintet state

Notably, the open-shell quintet geometry was optimized by a BS(5,1) formalism and found to feature an extremely weakly coupled metal d-electron with ligand electron.[55] The spin densities for the both septet and BS(5,1) solution is presented in (Figure 5.7). This weak coupling aligns very well with our EPR observation, where a separate organic radical signal has been recognized along with signatures of Fe(III) center. All these spectroscopic, magnetochemical,

and computational data provide compelling proof for the formazanate ligand oxidation, with the clear retention of Fe(III) oxidation state upon oxidizing **1**.

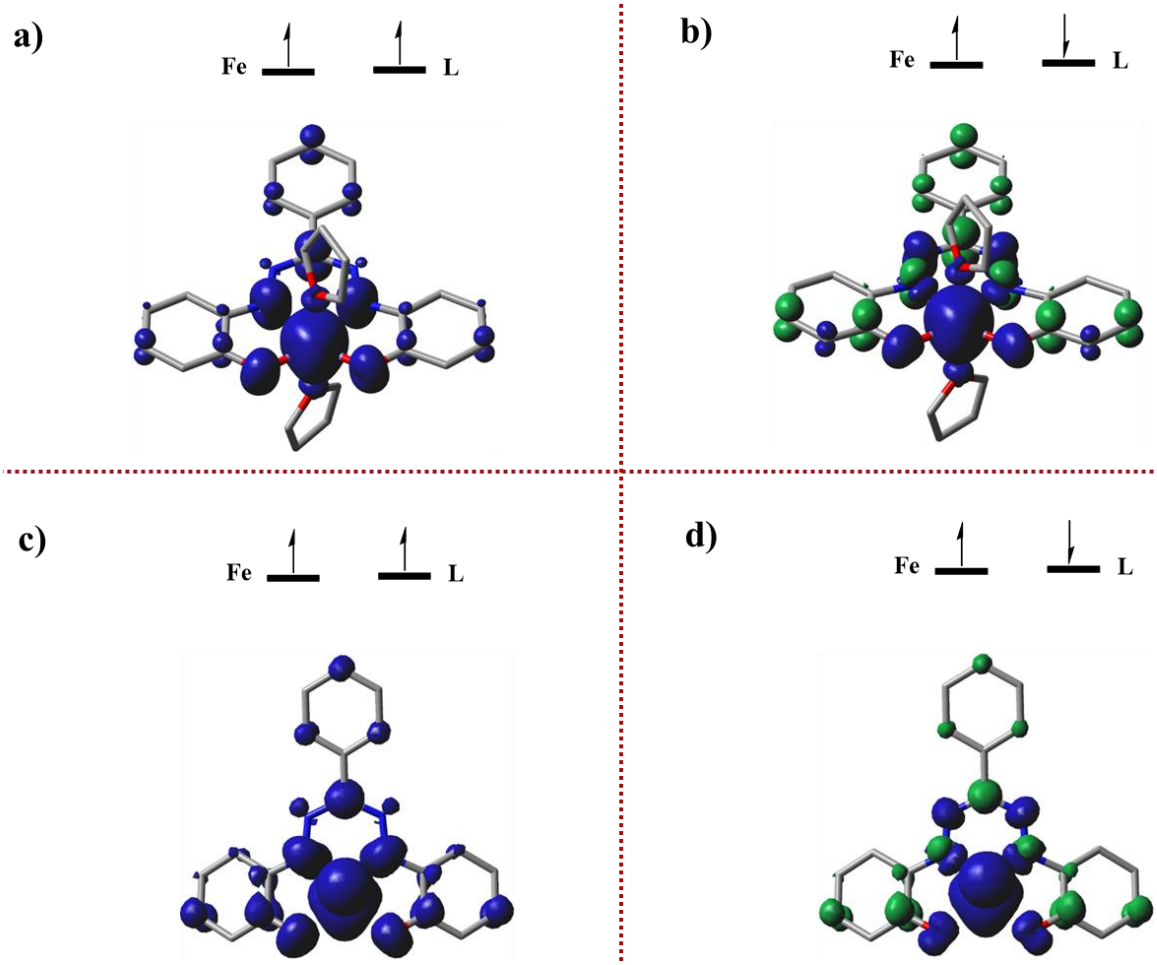

Figure 5.7. (a) Electronic description of the septet state of **2a** and Excess alpha spin density distribution of **2a** at the septet. (b) Electronic description of the quintet state originating from BS(5,1) solution of **2a** and unpaired electron spin density distribution due to unpaired electrons of **2a** at its open-shell quintet state from BS(5,1) solution. (c) Electronic description of the septet state of **2b** and Excess alpha spin density distribution of **2b** at the septet. (d) Electronic description of the quintet state originating from BS(5,1) solution of **2b** and unpaired electron spin density distribution due to unpaired electrons of **2b** at its open-shell quintet state from BS(5,1) solution.

5.6. Catalytic Applications

Upon establishing the ligand noninnocence of the formazanate backbone, the catalytic activity of **1** was explored where the chemical transformation will be facilitated by the ligand-redox property. A methodology where a quaternary carbon center can be created in a heteroarene was chosen since majority of the known processes suffer from the installation of sterically encumbering tertiary group.[56] In this domain, iron catalysts often rely on oxidative addition or

concerted metalation-deprotonation (CMD) to transform C-H bonds in the presence of an oxidant or Grignard reagent.[57] It was planned to generate a tertiary alkyl radical via single electron transfer process and utilize such a radical for C-H functionalization, so that an aromatic ring with a quaternary center can be realized. Along this direction, a tertiary α-haloester has been chosen as the substrate molecule that can be a convenient source of tertiary radical, and can alkylate a host of heterocycle rings following radical mechanism.

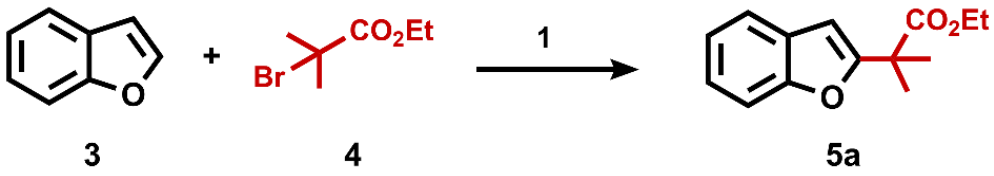

3 **4** **5a**

Scheme 5.3. C-H functionalization of heterocycle ring with tertiary alkyl ester.

5.6.1. Optimization of Reaction Conditions

Initially, a benzofuran **3** was reacted with ethyl α-bromoisobutyrate **4** in presence of 1.5 equivalent of base, triethylamine. Pleasingly, 2-alkylated benzofuran **5a** was formed in quantitative yield (98% by GC analysis) with only 1 mol% loading of the iron catalyst **1** in MeCN (Table 5.1, entry 4).

Table 5.1. Optimization of the reaction conditions

Entry	Base	Solvent	Yield (%)[b]
1	NEt_3	dioxane	84
2	NEt_3	THF	64
3	NEt_3	Toluene	21
4	**NEt_3**	**MeCN**	**98**
5	DABCO	MeCN	26
6	Na_2CO_3	MeCN	35
7	DIPEA	MeCN	92
8[c]	NEt_3	MeCN	85
9[d]	NEt_3	MeCN	30
10[e]	NEt_3	MeCN	ND
11	-	MeCN	18

[a]Reaction conditions: **3** (0.25 mmol), **4** (0.2 mmol), Catalyst **1** (1 mol%), base (0.3 mmol) in solvent at 100 °C for 12 h. [b]Yield determined by Gas chromatography. [c] Using 1 equivalent of **3**. [d] at 70 °C. [e] Without catalyst.

A set of optimization studies fix the parameters for the best reaction conditions and establishes that the reaction is completed in 12 h when heated at a temperature of 100 °C. DABCO and Na_2CO_3 were not as effective base as NEt_3. Diisopropylethylamine (DIPEA) provided almost similar yield of final product. Lowering the reaction temperature to 70 °C, diminished the yield to 30%. Catalyst and base are the crucial component of the reaction. In the absence of either of them, almost negligible product formation was observed (Table 5.1, entry 10, 11).

5.6.2. Scope and Synthetic Utility of the Reaction by Catalyst 1

5.6.2.1. Scope of Different Heterocycles, with Different Tertiary α-Bromoesters/Tertiary α-Bromoamides

With the best optimized reaction condition, the isolated yield of the product **5a** was determined to be 91% upon appropriate column-chromatographic separation (Table 5.2). Identically, -Me, -Br containing benzofurans afforded **5b**-**5c** in 78-82% isolated yields. Furthermore, aldehyde group at the C5 position of benzofuran is well tolerated to provide **5d** in 62% yield. Multiple sources of tertiary radicals involving **4**, all responded very well under this C-Br bond activation strategy and resulted products 2-alkylated benzofurans **5e**-**5h** in 69-92% isolated yields. Furthermore, the tertiary radical source spanned an amide, so that *N*-benzyl-2-bromo-2-methylpropanamide, *N*-cyclohexyl-2-bromo-2-methylpropanamide were considered as substrates. Both tertiary radical sources efficiently generated the desired radical so that a smooth alkylation was conducted on benzofuran to furnish **5j** and **5k** in 63-77% yields. Along with aliphatic esters, other aryl ester motifs as the source of tertiary alkyl radical were also well-behaved, since multiple *p*-substituted benzyl esters afforded the 2-alkylated furans in high yields. After this, aldehyde and nitro functionalities was also examined in the α-bromoester, since these functional groups possess much synthetic utility. Interestingly, these groups were well tolerated to afford 75-88% yields of the products **5m** and **5n**. It is noteworthy, that 2-substitution of a heterocycle such as furan is more challenging over the activated 3-position and the tertiary radical's stability paves an easy access to this position. By this way, the radical stability also dictates the regioselectivity of the process.

Along the same C-H functionalization by tertiary alkyl groups to other heterocycles, indoles are valuable molecules in natural products and pharmaceuticals. Henceforth, we

examined synthetic utility of this developed protocol on various substituted indoles. In all cases the tertiary alkylated indoles **7a-7d** were isolated in 62-78% yields (Table 5.2). Notably, 3-methyl indole when reacted with tertiary α-bromoesters, afforded the product **7e** in 76% yield. Additionally, the protocol was tested on sulfur containing heterocycle thiophene, while the alkylated products **9a-9c** were obtained in 69-92% yields (Table 5.2).

Table 5.2. Substrate scope of different heterocycles, with different tertiary α-bromoesters/tertiary α-bromoamides

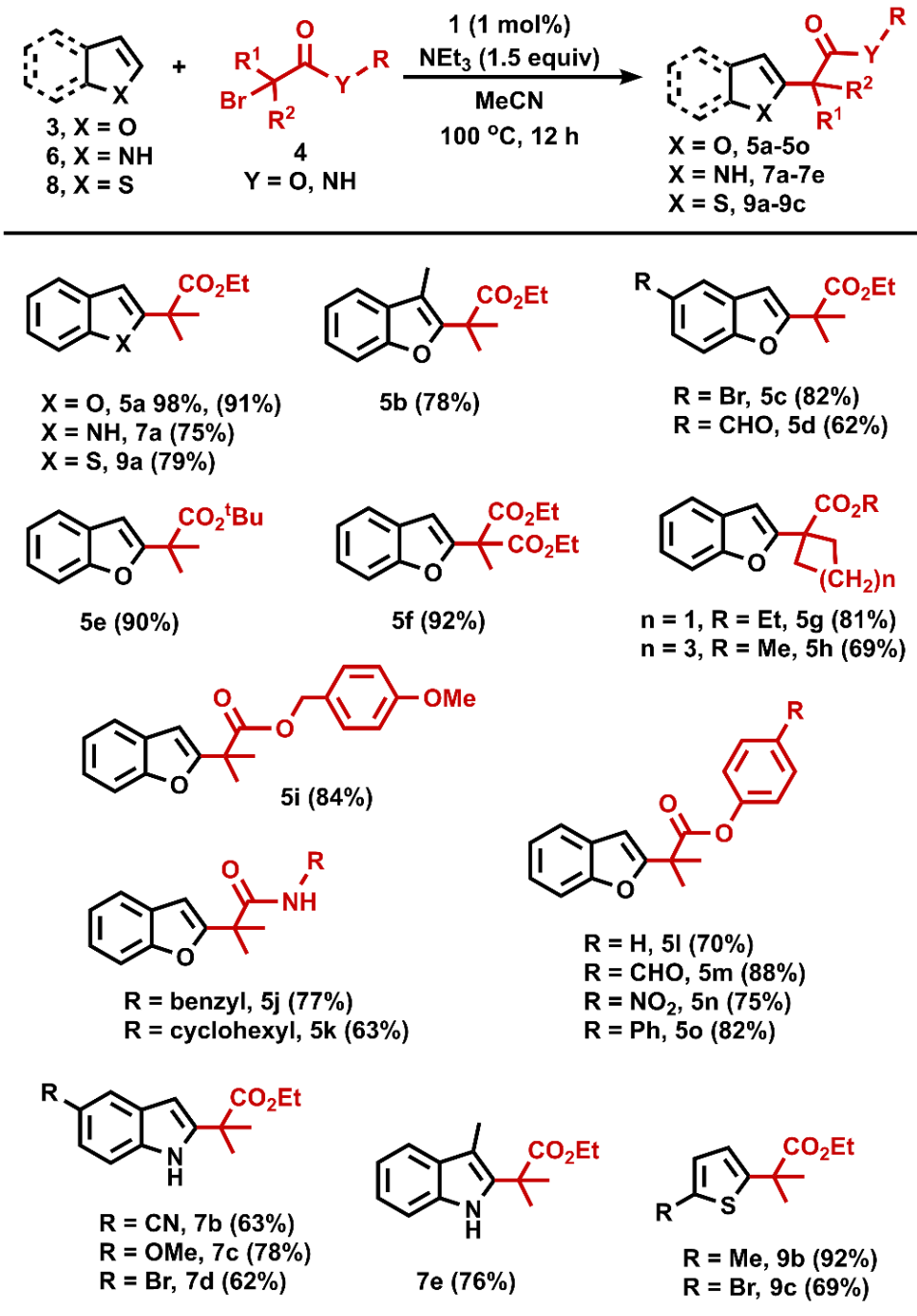

5.6.2.2. Scope of Different Tertiary α-Bromoesters/Tertiary α-Bromoamides with *p*-OMe Styrene

To expand the synthetic utility of the protocol further, we planned to alkylate styrenes with tertiary alkyl groups containing ester or amide motifs. Towards this goal, we chose *p*-OMe-styrene and reacted with an α-bromo ester to furnish the Heck-like coupling product **11a** in 94% isolated yield (Table 5.3). Changing the other substrate to *tert*-butyl ester synthesized **11b** in 67% yield. Similarly, a variety of tertiary alkyl radical sources afforded the vinylic C-H-substituted styrenes **11c**-**11e** in 81-92% isolated yields. Additionally, a *p*-OMe-styrene with a tertiary-α-bromo amide afforded product **11f** in 69% yield.

Table 5.3. Scope of different tertiary α-bromoesters/tertiary α-bromoamides with *p*-OMe styrene.

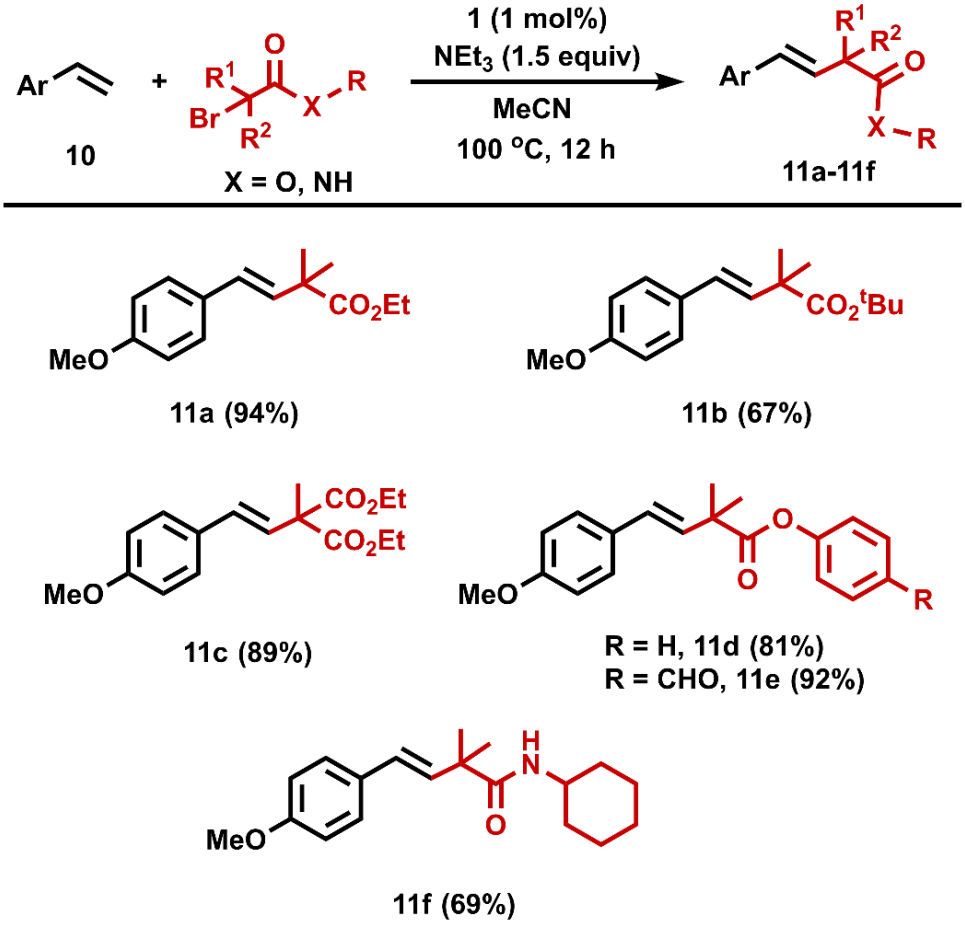

5.6.2.3. Scope of Intramolecular C−H Arylation of Tertiary α-Bromo Amides

Upon successfully synthesizing a series of C-H substituted styrenes, we harnessed this synthetic protocol by intramolecular annulation to fabricate a series of oxindoles. The oxindole scaffolds are privileged structural motifs that are encountered in a large number of bioactive targets and natural products.[58-59] Also, several tetrasubstituted oxindoles are often found in

pharmaceutically important molecules or potent oral inotropes.[59] In our synthetic effort, we chose α-bromo amides as the substrate, so that a reductive cleavage of C-Br bond can engender a tertiary radical. In agreement with the radical's stability as a deterministic factor, we observed primary and secondary bromoesters not to afford the desirable oxindole products. The putative radical cyclizes in a downstream process followed by deprotonation and electron transfer to complete the catalytic cycle. Following this, the oxindole 3,3'-dimethyl oxindole, **13a** is conveniently synthesized in a very high, 86% yield when the catalyst loading was only 1 mol% (Table 5.4). The chloro- substitution on the aryl ring of amides was retained during the synthesis to result oxindole **13b** in 91% yield. Similarly, substituents having electron donating and strongly electron withdrawing nature, such as -Me, -OMe, -F and -CF_3 were compatible with the process to furnish oxindoles (**13c**-**13f**) in 78-92% yields. Encouragingly, nitro substitution was well tolerated to synthesize **13g** in 88% yield.

Table 5.4. Scope of Intramolecular C−H Arylation of tertiary α-bromo amides

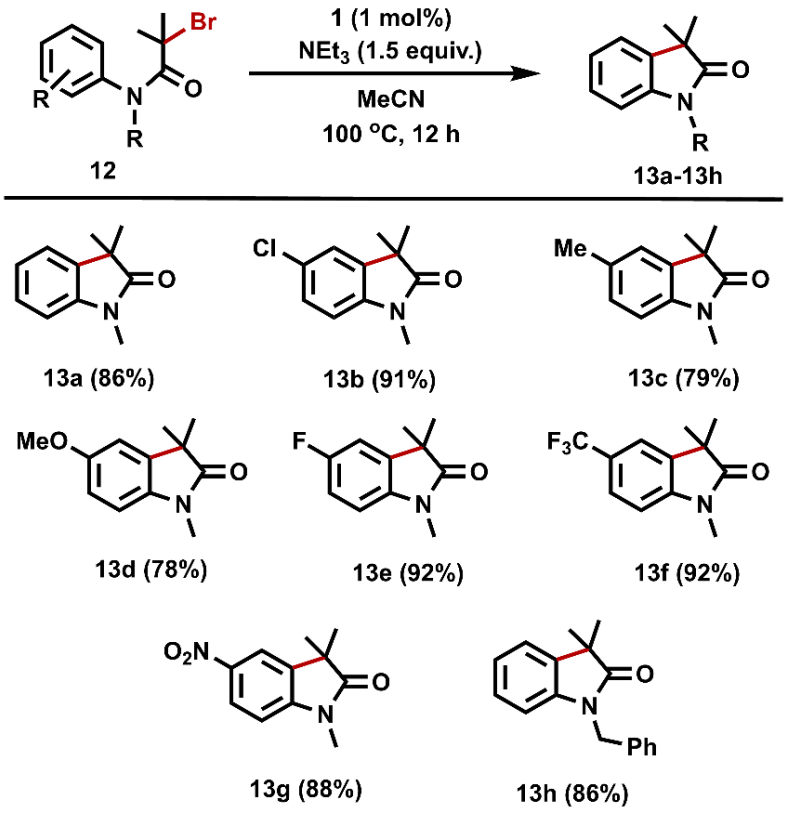

5.6.2.4. Synthetic Utility of Oxindoles

To prove the importance of synthesized oxindole product, demethylation of the *N*-Me in the indole was targeted. Gratifyingly, the demethylation was successful to result the parent indolinone **13aa** in 73% yield (Scheme 4). Furthermore, the oxindole framework can be easily

converted to thioindole motifs by the treatment of Lawesson's reagent,[60] resulting **13ab** in 91% yield.

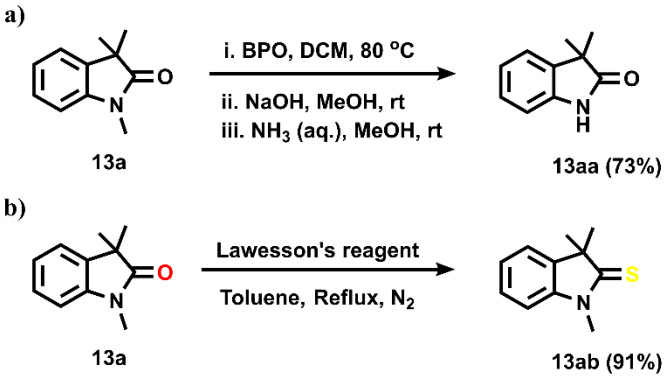

Scheme 5.4. Conversion of oxindole **13a** to, a). 3,3-dimethylindolin-2-one b). 1,3,3-trimethylindoline-2-thione.

5.7. Mechanistic Insights and Control Experiments

After successfully performing the catalytic reactions, the mechanistic detail of the reaction was elucidated. In this direction, the intrigued redox noninnocence of the formazanate backbone was depicted that promotes the catalytic efficiency for the chosen iron catalyst in this report. To understand these details, there is need to focused on the electron transfer step from the catalyst, that reductively cleaves the C-Br bond of an α-bromo ester. Since the coordination sphere of the iron in **1a** is relatively vacant, owing to the presence of labile placeholders THF, binding of the substrate to the iron center is highly possible. This substrate binding is also feasible to **1b**, possibly making it a contributor to the catalysis. Substrate binding will facilitate an inner-sphere electron transfer over the outer-sphere processes.

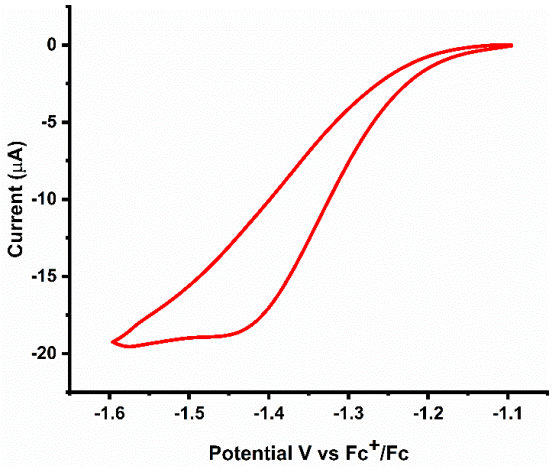

Figure 5.8. CV of 1 mM of **4** dissolved in DCM along with 0.1 M solution of tetrabutyl-ammonium hexafluorophosphate salt as an electrolyte. The scan rate was 100 mVs^{-1} for the measurement.

The measured reduction potential for the α-bromo ester, -1.07 V vs SCE (Figure 5.8), does not suggest thermodynamically favorable electron transfer in an outer-sphere manner. As soon as the α-bromo ester binds to the Lewis acidic Fe(III) center its reduction becomes much easier, and the electron transfer from the formazanate backbone happens clearly via the iron center. The reductive cleavage of C-Br bond generates the putative tertiary alkyl radical.

5.7.1. Trapping of Intermediates

To prove its generation, we added one equivalent of the radical trap TEMPO to the reaction mixture. To our pleasure, TEMPO adduct **14a** (Scheme 5.5a) of the putative tertiary radical was detected by high-resolution mass spectrometry. Furthermore, when butylated hydroxy toluene was used as the radical trap, the formed adduct was very stable. Such an adduct **15** was chromatographically isolated in 82% yield and fully characterized by NMR spectroscopies. Isolation and thorough characterization of the tertiary radical adduct is a compelling proof for the radical intermediacy in the reaction. Mechanistically, the thus formed tertiary radical will attack the benzofuran at its C2 position to generate a radical at its C3 position. Treatment of TEMPO radical with the reaction mixture was able to capture the alkyl benzofuran radical **14b** (Scheme 5.5a) that has been identified by high-resolution mass spectrometry. The resulting radical is sufficiently reducing to reduce the one-electron oxidized backbone of **2a**, so that the parent unoxidized form **1a** is back and alkyl benzofuran cation **19** (Scheme 5.6) is formed. To demonstrate that the cationic intermediate forms in a reaction mixture, this cationic intermediate can be easily intercepted with a readily available anion. Along that goal the diethylmalonate was chosen so that a stable anion can be generated in situ by the abstraction of the active methylene group by a mild base. Fortunately, the diethyl malonate arrested the putative benzofuran cation **19** (Scheme 5.6) and was able to capture this cationic intermediate in the form of **16** (Scheme 5.5c), that was further identified by HRMS.

So, the redox noninnocent formazanate supplies requisite electron during the reductive cleavage of C-Br bond, and it also behaves as an electron sink when the oxidized catalyst system gets the electron back. In essence the role of iron is more to providing the template and to help in electron transfer processes by forming a good metal-ligand covalent bond. The ligand plays a preponderant role and overall tunes the redox transformation. Upon electron transfer, once the cation is generated in presence of a base, proton abstraction happens to provide the desired product. An alternative possibility of bromide anion performing a SET to reduce **2** to

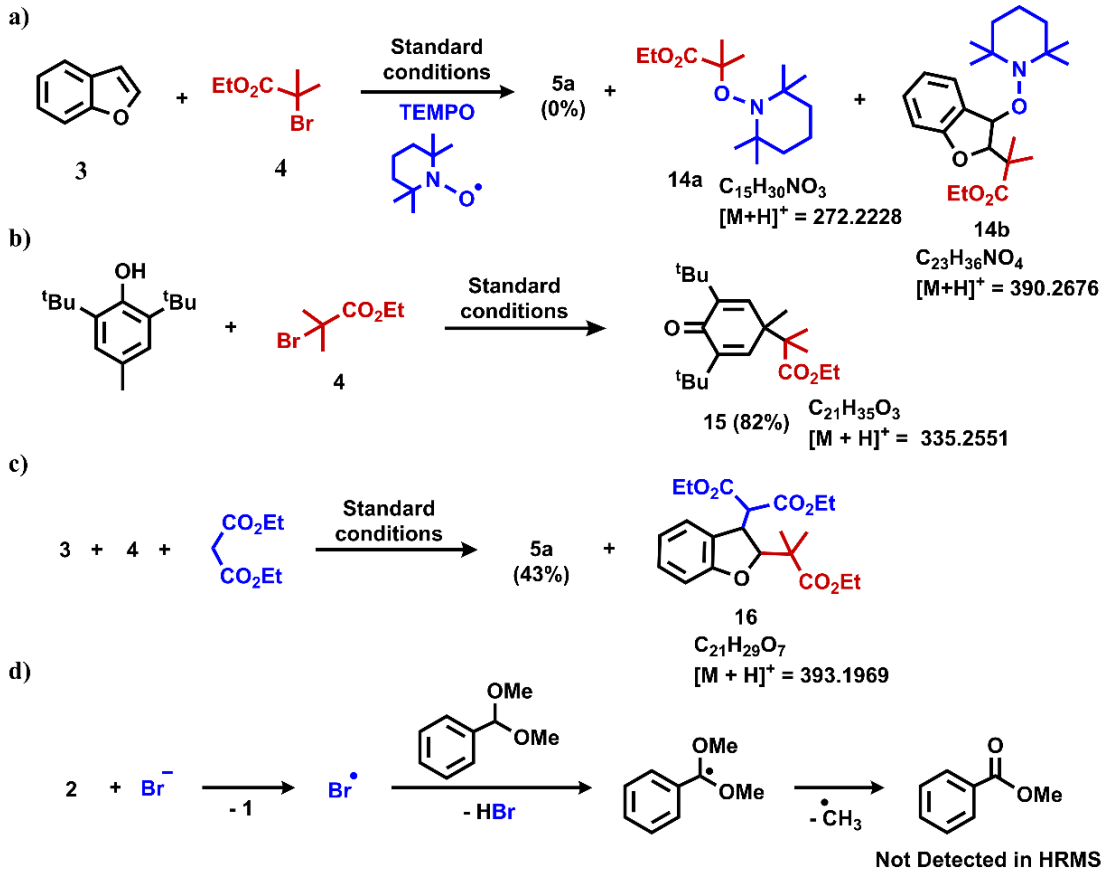

Scheme 5.5. (a) Trapping of tertiary alkyl radical, and another intermediate using TEMPO. (b) Isolation of tertiary alkyl radical adduct intercepted by butylated hydroxytoluene, BHT. (c) Trapping of alkyl benzofuran cation using diethylmalonate anion. (d) Trapping of bromine radical.

1 was also considered (Scheme 5.5d). In such case, it is logical to expect the formation of bromine radical, which did not happen. In the case of radical-promoted reaction often chain propagation step proceeds to furnish the product. However, the interception of cationic benzofuran **19** also discarded the possibility of chain propagation. Moreover, in presence of a weak base such as NEt_3, deprotonation of **18** to generate a radical anion that may promote SET does not seem plausible.

5.8. Proposed Reaction Mechanism

Mechanistically, this electron reservoir property of the formazanate helps in reducing α-bromo ester to generate the tertiary alkyl radical, which can be the starting point for the catalytic reaction. Furthermore, the generated radical coupled with benzofuran at C2 position. The quasi-reversible oxidation wave suggests that the formazanate backbone may accept the electron back during the catalytic cycle. The benzofuran radical can donate one electron back to **2** to reduce

it (Scheme 5.6). In the meantime, base would be able to abstract a proton from the benzofuran cationic intermediate and provides the final product.

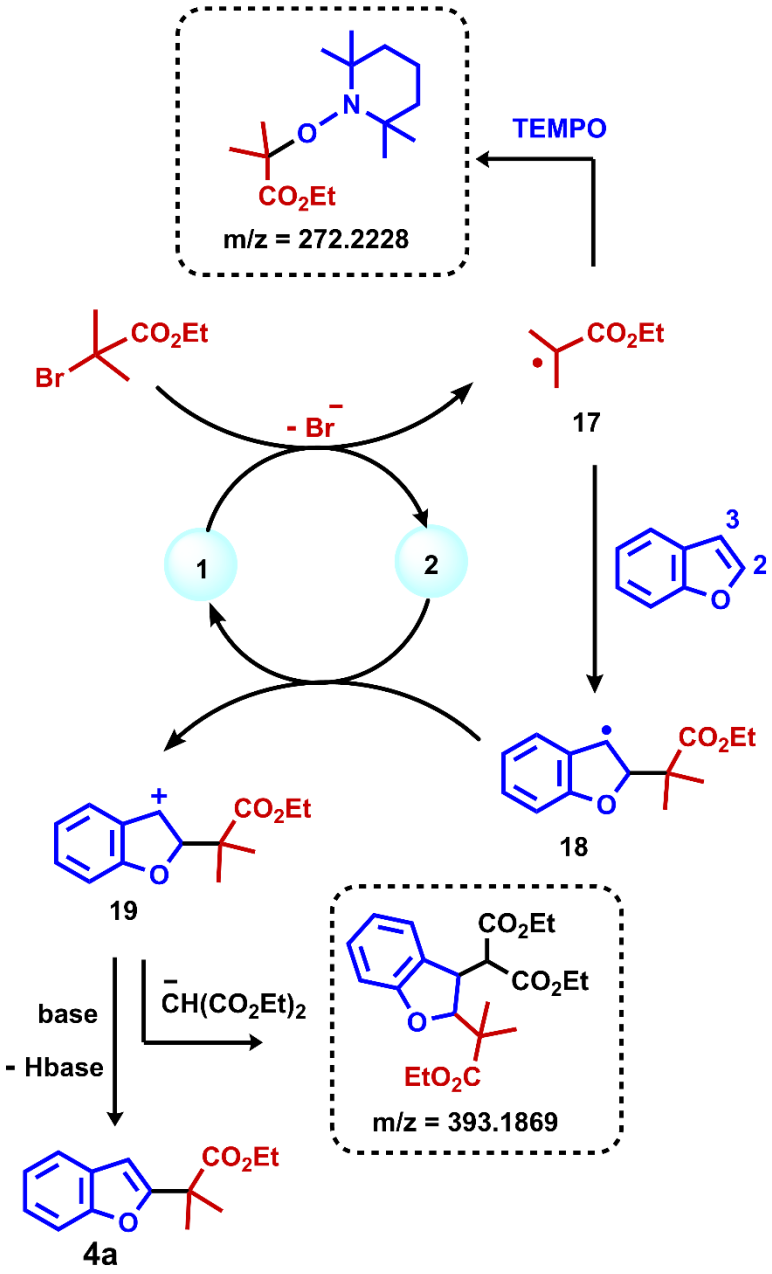

Scheme 5.6. Plausible catalytic mechanistic cycle for the reductive cleavage of α-bromo ester and radical-mediated C-H tertiary alkylation of a heteroarene.

5.9. Conclusions

In summary, an iron (III) formazanate complex was prepared, that steers tertiary alkylation of C-H bonds of heteroarene and styrene exclusively via ligand-redox process. The complex can remain as a mixture of two molecules in Fe^{III} high spin states which may be dependent on the

other ligand coordination to the iron center. Presence of a labile place holder ligand THF provides an easy access to the vacant site at the metal center that facilitates substrate binding and subsequent electron transfer from electron rich formazanate ligand backbone. The Ligand-dominated oxidation was probed by zero-field Mössbauer and EPR spectroscopies that strongly suggest the iron's retention of oxidation state to +3 upon oxidation of the complex. As such the metal center behaves as a communicating medium between the formazanate ligand backbone and the substrate, α-bromo ester. A plethora of challenging C-H alkylation by tertiary alkyl groups has been accomplished by this method proving the great utility of 3d transition metal catalysis when ligand plays a preponderant role. A series of control reactions and critical intermediate isolation provide credible evidences for ligand-based electron flow to promote the reductive cleavage of a C-Br bond of the substrate. It is believed that this example will encourage further to unravel the untapped potential of several redox active ligand backbones to facilitate important chemical transformations.

5.10. Experimental Section

5.10.1. Chemicals and Reagents

All operations were carried out in flame-dried glassware using N_2 gas filled glovebox or high-vacuum standard Schlenk techniques under nitrogen gas atmosphere until unless mentioned. THF refluxed and freshly distilled over sodium/benzophenone. and degassed using three freeze-pump-thaw cycles. Starting materials and reagents were purchased from commercial sources and used without further purification. Formazan was prepared by following literature procedures. Tetrabutylammonium hexafluorophosphate ($TBAPF_6$) was recrystallized from hot ethanol, and ferrocene was purified by sublimation before use in cyclic voltammetry (CV) experiments. Progress of reactions was monitored by thin-layer chromatography using Merck 60 F_{254} precoated silica gel plate and visualized by short-wave ultraviolet light. Flash chromatography was performed with Silica Flash P60 silica gel (100–200 mesh).

5.10.2. Instrumentation and Physical Measurements

All graphs are plotted using Originpro8. ^{1}H and ^{13}C $\{^{1}H\}$ NMR spectra were recorded on a Bruker 400 MHz spectrometer at 400 and 101 MHz respectively. All chemical shifts are reported in part per million (ppm) with respect to the ^{1}H (residual) chemical shifts of the d-solvent. The residual solvent signals were taken as the reference ($CDCl_3$, 7.26 ppm for ^{1}H NMR spectra and $CDCl_3$, 77.16 ppm for ^{13}C NMR spectra). The signals observed are described as: *s* (singlet), *d* (doublet), *t* (triplet), *q* (quartet), *m* (multiplets). All coupling constants were

reported in hertz. High resolution mass spectroscopy was performed on Waters Synapt-G2S, analyser configuration Q-ToF with ion mobility and analysed using Masslynx41. Cyclic Voltammetry experiments were performed on Keithley 2450 potentiostat. For the measurement, the electrode setup consisted of a glassy carbon working electrode, a Pt-wire as counter electrode, and an Ag^{+}/Ag (3M KCl) as the reference electrode.

^{57}Fe Mössbauer Measurement

Zero-field ^{57}Fe Mössbauer spectra were recorded on a SooCo MS6 Spectrometer at 20 K. Spectra were recorded in PTFE sample holders with about 20 mg of sample. The minimum experimental line width is 0.28 mm s^{-1}. The temperature of the samples was held constant in a Janis CCS-850 closed cycle cryostat with sample in exchange gas (helium). ^{57}Co was used as the radiation source. Isomer shifts were determined relative to α-iron. The zero-field splitting spectrum was simulated by using Lorenzian doublets, and processed with WMOSS4 software.

EPR Measurement

EPR spectra of the complexes at X-band frequency (ca. 9.43 GHz) were obtained from a Bruker EMX system ESP 300 equipped with a Hewlett-Packard Frequency counter 5350B, a Bruker ER035M gaussmeter for g values determination and a continuous flow cryostat ESR 900 from Oxford instruments for measurements at liquid helium temperature (4.2 K). During the data collection the modulation amplitude and modulation frequency were set at 4 Gauss and 100 kHz respectively.

Caution! The Glovebox and high vacuum Shlenk line should be used with great care and safety. THF distillation setup contains sodium metal, which is very reactive metal to air and moisture and well-known for their explosive nature. Therefore, these types of setups must be used in a limited quantity and handled with care and safety.

5.10.3. Procedure for Synthesis of Fe(III)-Formazanate Complex (1)

In a Schlenk flask, 3-Phenyl-1,5-dihydroxyphenylformazan (**L**) (332 mg, 1mmol) was dissolved in 10 mL of THF under nitrogen atmosphere to make a clear violet colored solution. The reaction mixture was kept at a temperature of -78 °C. Sodium hydride (126 mg of 60% dispersion in mineral oil, 3.1 mmol) was slowly added to the above reaction mixture, the solution turned into dark blue over the stirring of 10 minutes. The reaction mixture was stirred for an additional 1 hour at room temperature. After that, a solution of anhydrous $FeCl_3$ (162 mg, 1 mmol) in THF was prepared and added dropwise to the above reaction mixture at a temperature of 0 °C. Instantaneous color change was observed. After 2 hours stirring at room

temperature, the solvent was removed under high vacuum. The dark residue was dissolved in CH_2Cl_2 and filtered through celite bed. The filtrate was collected and CH_2Cl_2 was removed under vacuum. The residue was triturated with hexane. Dark green colored solid was obtained in 72% yield. From the Mössbauer and EPR spectroscopic data it is clear that the complex **1** is a mixture of two species, namely **1a** and **1b**. We proposed the **1b** as an 'ate" complex, whose identity was confirmed from negative mode ESI mass spectrometry. For 1b: HRMS (ESI, m/z) calcd. for $C_{19}H_{12}ClFeN_4O_2$ $[M - H]^-$: 420.9977; found: 420.9970.

5.10.4. Solid State Magnetic Moment Analysis of Fe(III) formazanate (1)

The magnetic moment analysis was performed on Quantum Design PPMS. The applied magnetic field was set at 15000 Oe and data collection was performed at a temperature of 305 K. The magnetic moment for Fe(III) formazanate was found to be 0.00688 emu. The effective magnetic moment (μ_{eff}) was found to be 5.8 BM using mathematical equations as described below:

$$\chi = \frac{D \times \text{Molecular mass}}{\text{Weight taken}} \qquad \text{where } D = \frac{\text{Moment (in emu)}}{\text{Magnetic field (in Oe)}}$$

$$\mu_{eff} = 2.828 \times \sqrt{\chi \times \text{Temperature (in K)}}$$

5.10.5. Procedure for Synthesis of One-electron Oxidation of 1

In a Schlenk flask 1 (264 mg, 0.5 mmol) was dissolved in 5 mL of THF and solid silver triflate (129 mg, 0.5 mmol) was added to the solution. During the addition, the colour of the reaction mixture turned to brown from greenish blue over the course of 1 h. The reaction mixture was further stirred for 5 h at room temperature. At the completion of the reaction, the reaction mixture was filtered and filtrate was removed under high vacuum. The oxidized product 2 was isolated in 83% yield (281 mg) as a brown solid. ^{19}F NMR spectroscopic data was collected on the sample to find the resonance at -19 ppm (with respect to $BF_3.OEt_2$). The crude sample was subjected to HRMS for further studies. From mass spectrum, the signature of 2a, where a triflate ligand is bound to Fe(III) was observed. Similarly, the oxidized version of 1b was further diagnosed via mass spectrometry to retain the chloride ion (2b).

For **2a**: HRMS (ESI, m/z) calcd. for $C_{20}H_{14}F_3FeN_4O_5S$ $[M + H]^+$: 534.9987; found: 534.9941.

For **2b**: HRMS (ESI, m/z) calcd. for $C_{19}H_{12}ClFeN_4O_2$ $[M - H]^-$: 420.9977; found: 420.9981.

5.10.6. EPR Simulation

We claim the X-band EPR data collected at 4.2 K features the presence of organic radical, that is centered primarily on the formazanate ligand backbone along with the signatures of S = 5/2 Fe(III) species. To prove this conjecture further, we have theoretically simulated the part of the spectrum, where the ligand-based oxidation is centralized. The portion of the EPR spectrum was interpreted using a spin Hamiltonian, H, containing the electron Zeeman interaction with the applied magnetic field B_o and the hyperfine coupling (hfc) term:

$$H = \beta_e S.g.B_0 + h\ S.A.I$$

Where S, A, I, *g*, β_e , and h represent electron spin operator, hyperfine constant tensor in frequency units, nuclear spin of ^{57}Fe, electronic *g*- tensor, bohr magneton and Planck's constant respectively. The best fit spectrum to the experimental data was obtained considering high spin Fe^{3+} (S = 5/2) and radical spin (S = ½). Spectral simulations were performed using the EasySpin package (v 5.2.35) and based on Matlab R2020b. Easyspin employs calculation of EPR resonance fields from the energies of the spin states obtained by direct diagonalization of the spin Hamiltonian. The fitting of the spectra was obtained from Monte Carlo type iteration to minimize the root-mean-square deviation between experimental and simulated spectra.

parameter	Simulated values
gx	2.47
gy	2.01
gz	1.86
Ax (MHz) (57Fe)	45.8
Ay (MHz) (57Fe)	46.2
Az (MHz) (57Fe)	41.3
Ax (MHz) (14N)	22.5
Ay (MHz) (14N)	19.3
Az (MHz) (14N)	2.2
lwpp (mT) [a]	1.1 0.2
Temperature	4.2 K
[a]First and second values correspond to Gaussian and Lorentzian line widths, respectively.	

The iteration was performed until the optimum values for the following parameters: principal components of the *g*-tensor, hfc tensor A and peak-to-peak line widths.

The fitting of the spectra clearly indicates hyperfine interactions between the unpaired electron and two nitrogen atoms. While higher value of *g*-tensor implies contribution from the spin system of the high spin Fe^{3+} ($S = 5/2$). The fitting parameters are also given below in the table.

5.10.7. Computational Details

All DFT calculations have been carried out using the ORCA 4.2.1 program.[61] Optimized geometries were computed using the B3LYP functional.[62-65] Atom-pairwise dispersion correction with the Becke−Johnson damping scheme (D3BJ),[66-67] the scalar relativistic zero-order regular approximation (ZORA),[68] has been used. A combination of the CP(PPP)[69,70] for the iron atom and def2-TZVP for all other atom were used.[71,72]

5.10.8. General Procedure for the Reaction

An oven-dried pressure tube was charged with benzofuran **3** (0.25 mmol) and ethyl α-bromoisobutyrate **4** (0.2 mmol). A base NEt_3 (0.3 mmol) was added to the reaction mixture under nitrogen atmosphere. The above reaction mixture was loaded with catalyst **1** (1 mol%), followed by 1 mL degassed MeCN. The reaction mixture was stirred at a temperature of 100 $^{\circ}C$ for 12 hours. Solvent was removed under rotary evaporator. The desired product was isolated by column chromatography using hexane/ethylacetate mixture as the eluent. The pure product was further analysed by NMR spectroscopy.

5.10.9. Procedure for Diversity of Oxindole Products

5.10.9.1. Procedure for Synthesis of 3, 3-dimethylindolin-2-on via Demethylation of oxindole[73]

A solution of oxindole **5a** (1 mmol, 175 mg) and benzoyl peroxide (BPO, 2.0 equiv.) in dry DCM (2 mL) was packed in a sealed tube and was heated slowly to 80 °C. After stirring for 18 h, the reaction mixture was cooled to room temperature and the solvent was evaporated. The residue was dissolved further in MeOH (4 mL), NaOH (3.65 mmol, 146 mg) was added and the reaction mixture was stirred at room temperature for 18 h. Then the slurry was poured into saturated aqueous NH_4Cl (10 mL) and extracted with DCM (3×6 mL). The combined organic layers were dried by anhydrous Na_2SO_4 and concentrated. The residue was dissolved in a methanolic NH_3 solution (5 mL, 7M) and stirred for 19 h at room temperature. After that, the

mixture was extracted by EtOAc (3×10 mL) and dried by anhydrous Na_2SO_4 and concentrated, purified by silica gel flash chromatography using Hexane/EtOAc (10:3) to afford the desired product 3, 3-dimethylindolin-2-on (**13aa**) as a white solid in 73% yield. **^{1}H NMR** (400 MHz, $CDCl_3$) δ 8.63 (s, 1H), 7.20 (t, *J* = 7.2 Hz, 2H), 7.07 – 7.01 (m, 1H), 6.93 (d, *J* = 8.4 Hz, 1H), 1.41 (s, 6H). **^{13}C NMR** (101 MHz, $CDCl_3$) δ 184.17, 139.88, 136.41, 127.78, 122.77, 122.61, 109.98, 44.80, 24.46.

5.10.9.2. Procedure for Synthesis of the indoline-2-thione[74]

Oxindoles (**5a**, 1 mmol) and Lawesson's reagent (0.51 equiv.) were added into a test tube under N_2. Then dry toluene (2 mL) was added by syringe. It was sealed and refluxed for 2 h. After cooling down, the mixture was poured into water. The organic layer was separated and the aqueous layer was extracted with ether. The organic layers were combined, washed with brine, dried over Na_2SO_4, concentrated in vacuo and finally purified by silica gel chromatography eluting with EtOAc/PE (1:40) to afford the product **13ab** in 91% yield. **^{1}H NMR** (400 MHz, $CDCl_3$) δ 7.31 (d, *J* = 7.8 Hz, 2H), 7.21 – 7.16 (m, 1H), 7.05 (d, *J* = 7.6 Hz, 1H), 3.65 (s, 3H), 1.43 (s, 6H). **^{13}C NMR** (101 MHz, $CDCl_3$) δ 212.01, 143.94, 140.45, 127.88, 124.31, 122.77, 109.62, 54.98, 31.56, 28.11.

5.10.10. Procedure for Trapping of Intermediates

5.10.10.1. Procedure for Trapping of Alkyl Radical Using TEMPO

An oven-dried pressure tube was charged with **3** (30 μL, 0.25 mmol), **4** (15 μL, 0.2 mmol). NEt_3 (28 μL, 0.3 mmol) was added under nitrogen atmosphere. The above reaction mixture was loaded with catalyst **1** (1 mol%), followed by the addition of 1 mL degassed MeCN. Then TEMPO (1 equiv.) was added to the above reaction mixture. The reaction mixture was stirred at a temperature of 100 °C for 12 hours. The in situ- generated radical species was trapped by TEMPO. The TEMPO radical adducts **14a** and **14b** were analysed by high-resolution mass spectrometry (HRMS).

For **14a**: HRMS (ESI, m/z) calcd. for $C_{15}H_{30}NO_3$ $[M + H]^+$: 272.2226; found: 272.2228.

For **14b**: HRMS (ESI, m/z) calcd. for $C_{23}H_{36}NO_4$ $[M + H]^+$: 390.2644; found: 390.2676.

5.10.10.2. Procedure for Trapping of Alkyl Radical Using Butylated Hydroxy Toluene (BHT)

An oven-dried pressure tube was charged with **4** (0.4 mmol) and NEt_3 (0.6 mmol) was added to it under nitrogen atmosphere. The above reaction mixture was loaded with catalyst **1** (1 mol%), followed by 1 mL degassed MeCN. Then BHT (1 equiv.) was added to above reaction mixture. The reaction mixture was stirred at 100 °C for 12 hours. The generated radical species was trapped by BHT as **15** (82% yield). The BHT radical adduct **15** was analyzed by ^{1}H and ^{13}C NMR spectroscopies and High-Resolution Mass Spectrometry (HRMS). HRMS (ESI, m/z) calcd. for $C_{21}H_{35}O_3$ $[M + H]^+$: 335.2586; found: 335.2551.

5.10.10.3. Procedure for Trapping of 2-(1-ethoxy-2-methyl-1-oxopropan-2-yl)-2,3-dihydrobenzofuran-3-ylium (19) Using Diethylmalonate

An oven-dried pressure tube was charged with **3** (0.25 mmol), **4** (0.2 mmol), diethylmalonate (0.25 mmol), and NEt_3 (0.3 mmol) under nitrogen atmosphere. The above reaction mixture was loaded with catalyst **1** (1 mol%), followed by 1 mL degassed MeCN. The reaction mixture was stirred at 100 °C for 15 hours. The generated carbocation at C3 position of benzofuran **19** was trapped by diethylmalonate anion. The adduct **16** was analysed by High Resolution Mass Spectrometry (HRMS). HRMS (ESI, m/z) calcd. for $C_{21}H_{29}O_7$ $[M + H]^+$: 393.1913; found: 393.1917.

5.10.10.4. Procedure for Trapping of Br radical[75]

An oven-dried pressure tube was charged with oxidized **2** (6 mg, 0.01 mmol), tetrabutylammonium bromide (3 mg, 0.01 mmol) and benzaldehyde dimethyl acetal (1.5 mg, 0.01 mmol. In 1 mL of degassed MeCN to result clear solution. The above reaction mixture was stirred at a temperature of 100 °C. After 12 hours, the crude reaction mixture was analysed by High Resolution Mass Spectrometry (HRMS). Formation of methyl benzoate was not observed.

5.10.11. Analytical data of products

Ethyl 2-(benzofuran-2-yl)-2-methylpropanoate (5a)[76]

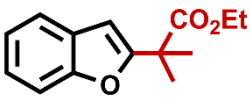

The general procedure described above was followed for the synthesis of **5a**. Column chromatographic separation (SiO_2, eluting with 99:1 hexane/ethyl acetate) afforded the desired product **5a** as a yellow oil (105 mg, yield 91%). **^{1}H NMR** (400 MHz, $CDCl_3$) δ 7.54 – 7.50 (*m*,

1H), 7.47 – 7.41 (*m*, 1H), 7.25 – 7.16 (*m*, 2H), 6.55 (*d*, *J* = 0.9 Hz, 1H), 4.16 (*q*, *J* = 7.1 Hz, 2H), 1.65 (*s*, 6H), 1.20 (*t*, *J* = 7.1 Hz, 3H). **^{13}C NMR** (101 MHz, $CDCl_3$) δ 174.49, 160.90, 154.85, 128.50, 123.88, 122.69, 120.86, 111.22, 101.83, 61.41, 44.05, 24.56, 14.20.

Ethyl 2-methyl-2-(3-methylbenzofuran-2-yl)propanoate (5b)[76]

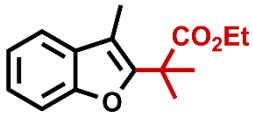

The general procedure described above was followed for the synthesis of **5b**. Column chromatographic separation (SiO_2, eluting with 99:1 hexane/ethyl acetate) afforded the desired product **5b** as a yellow oil (96 mg, yield 78%).**^{1}H NMR** (400 MHz, $CDCl_3$) δ 7.46 – 7.38 (*m*, 2H), 7.25 – 7.18 (*m*, 2H), 4.18 (*q*, *J* = 7.1 Hz, 2H), 2.18 (*s*, 3H), 1.67 (*s*, 6H), 1.22 (*t*, *J* = 7.1 Hz, 3H). **^{13}C NMR** (101 MHz, $CDCl_3$) δ 175.21, 154.21, 153.12, 131.08, 123.72, 122.21, 118.95, 110.91, 109.73, 61.35, 44.47, 25.05, 14.27, 8.37. HRMS (ESI, m/z) calcd. for $C_{15}H_{19}O_3$ $[M + H]^+$: 247.1334; found: 247.1303.

Ethyl 2-(5-bromobenzofuran-2-yl)-2-methylpropanoate (5c)[76]

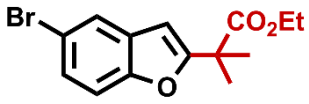

The general procedure described above was followed. Column chromatography (SiO_2, eluting with 99:1 hexane/ethyl acetate) afforded the desired product **5c** as a yellow oil (127 mg, yield 82%).**^{1}H NMR** (400 MHz, $CDCl_3$) δ 7.64 (*dd*, *J* = 1.9, 0.6 Hz, 1H), 7.35 – 7.28 (*m*, 2H), 6.49 (*d*, *J* = 0.8 Hz, 1H), 4.15 (*q*, *J* = 7.1 Hz, 2H), 1.64 (*s*, 6H), 1.20 (*t*, *J* = 7.1 Hz, 3H). **^{13}C NMR** (101 MHz, $CDCl_3$) δ 174.18, 162.33, 153.61, 130.52, 126.79, 123.51, 115.74, 112.66, 101.48, 61.51, 44.11, 24.47, 14.18. HRMS (ESI, m/z) calcd. for $C_{14}H_{16}BrO_3$ $[M + H]^+$: 313.0264; found: 313.0241.

Ethyl 2-(5-formylbenzofuran-2-yl)-2-methylpropanoate (5d)[77]

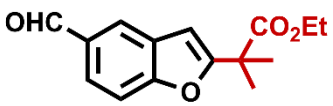

The general procedure was followed. Column chromatography (SiO_2, eluting with 20:1 hexane/ethyl acetate) afforded the desired product **5d** as a colourless oil (68 mg, yield 52%). **^{1}H NMR** (400 MHz, $CDCl_3$) δ 10.03 (*s*, 1H), 8.06 (*d*, *J* = 1.7 Hz, 1H), 7.81 (*dd*, *J* = 8.5, 1.7 Hz, 1H), 7.54 (*d*, *J* = 8.4 Hz, 1H), 6.65 (*s*, 1H), 4.16 (*q*, *J* = 7.1 Hz, 2H), 1.66 (*s*, 6H), 1.20 (*t*, *J* = 7.1 Hz, 3H). **^{13}C NMR** (101 MHz, $CDCl_3$) δ 191.94, 173.99, 163.04, 158.27, 132.23, 129.09, 125.74, 124.04, 111.91, 102.51, 61.56, 44.16, 24.43, 14.16. HRMS (ESI, m/z) calcd. for $C_{15}H_{17}O_4$ $[M + H]^+$: 261.1127; found: 261.1118.

Tert-butyl 2-(benzofuran-2-yl)-2-methylpropanoate (5e)[76]

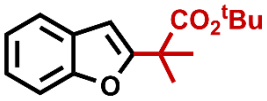

The general procedure was followed. Column chromatography (SiO_2, eluting with 99:1 hexane/ethyl acetate) afforded the desired product **5e** as a yellow solid (117 mg, yield 90%).**^{1}H NMR** (400 MHz, $CDCl_3$) δ 7.52 (*d*, *J* = 6.5 Hz, 1H), 7.45 (*d*, *J* = 8.4 Hz, 1H), 7.26 – 7.17 (*m*, 2H), 6.52 (*s*, 1H), 1.61 (*s*, 6H), 1.41 (*s*, 9H). **^{13}C NMR** (101 MHz, $CDCl_3$) δ 173.60, 161.51, 154.81, 128.61, 123.69, 122.58, 120.76, 111.12, 101.48, 81.16, 44.78, 27.95, 24.54.

Diethyl 2-(benzofuran-2-yl)-2-methylmalonate (5f)[76]

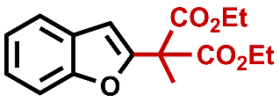

The general procedure was followed. Column chromatography (SiO_2, eluting with 99:1 hexane/ethyl acetate) afforded the desired product **5f** as a yellow oil (133 mg, yield 92%).**^{1}H NMR** (400 MHz, $CDCl_3$) δ 7.55 (*ddd*, *J* = 7.6, 1.5, 0.7 Hz, 1H), 7.47 (*dq*, *J* = 8.1, 0.9 Hz, 1H), 7.30 – 7.24 (*m*, 1H), 7.22 (*td*, *J* = 7.5, 1.2 Hz, 1H), 6.80 (*d*, *J* = 1.0 Hz, 1H), 4.28 (*qd*, *J* = 7.1, 2.5 Hz, 4H), 1.94 (*s*, 3H), 1.28 (*t*, *J* = 7.1 Hz, 6H). **^{13}C NMR** (101 MHz, $CDCl_3$) δ 169.31, 154.85, 153.94, 128.13, 124.39, 122.89, 121.21, 111.35, 104.89, 62.28, 55.83, 20.81, 14.08. HRMS (ESI, m/z) calcd. for $C_{16}H_{19}O_5$ $[M + H]^+$: 291.1233; found: 291.1215.

Ethyl 1-(benzofuran-2-yl)cyclobutane-1-carboxylate (5g)[76]

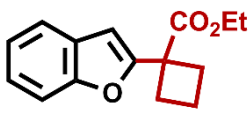

The general procedure was followed. Column chromatography (SiO_2, eluting with 98:2 hexane/ethyl acetate) afforded the desired product **5g** as a yellow oil (99 mg, yield 81%).**^{1}H NMR** (400 MHz, $CDCl_3$) δ 7.57 (*dd*, *J* = 7.4, 1.6 Hz, 1H), 7.49 (*d*, *J* = 7.6 Hz, 1H), 7.31 – 7.21 (*m*, 2H), 6.66 (*s*, 1H), 4.24 (*q*, *J* = 7.1 Hz, 2H), 2.85 (*ddd*, *J* = 12.3, 9.3, 7.4 Hz, 2H), 2.61 (*ddd*, *J* = 12.4, 8.6, 6.2 Hz, 2H), 2.09 (*ddt*, *J* = 15.2, 9.1, 6.7 Hz, 2H), 1.27 (*t*, *J* = 7.1 Hz, 3H). **^{13}C NMR** (101 MHz, $CDCl_3$) δ 173.60, 158.84, 155.07, 128.57, 123.95, 122.75, 120.85, 111.24, 102.74, 61.46, 61.46, 48.06, 30.80, 16.70, 14.24.

Methyl 1-(benzofuran-2-yl)cyclohexane-1-carboxylate (5h)[76]

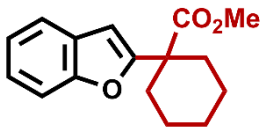

The general procedure was followed. Column chromatography (SiO_2, eluting with 98:2 hexane/ethyl acetate) afforded the desired product **5h** as a yellow oil (89 mg, yield 69%).**^{1}H NMR** (400 MHz, $CDCl_3$) δ 7.55 – 7.51 (*m*, 1H), 7.45 (*dd*, *J* = 8.0, 1.0 Hz, 1H), 7.27 – 7.18 (*m*, 2H), 6.57 (*d*, *J* = 0.8 Hz, 1H), 3.68 (*s*, 3H), 2.39 – 2.28 (*m*, 2H), 2.08 (*dq*, *J* = 9.6, 4.3 Hz, 2H), 1.65 – 1.48 (*m*, 6H). **^{13}C NMR** (101 MHz, $CDCl_3$) δ 174.05, 159.40, 154.66, 128.57, 123.86, 122.71, 120.81, 111.31, 103.06, 52.54, 48.72, 32.70, 25.58, 22.90. HRMS (ESI, m/z) calcd. for $C_{16}H_{19}O_3$ $[M + H]^+$: 259.1334; found: 259.1337.

4-methoxybenzyl 2-(benzofuran-2-yl)-2-methylpropanoate (5i)

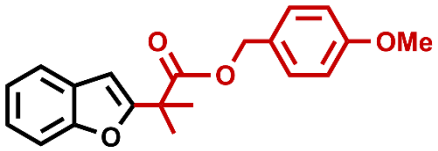

The general procedure was followed. Column chromatography (SiO_2, eluting with 20:1 hexane/ethyl acetate) afforded the desired product **5i** as a yellow solid (136 mg, yield 84%).**^{1}H NMR** (400 MHz, $CDCl_3$) δ 7.57 (*d*, *J* = 7.6 Hz, 1H), 7.49 (*d*, *J* = 8.1 Hz, 1H), 7.33 – 7.21 (*m*, 4H), 6.87 (*d*, *J* = 8.8 Hz, 2H), 6.59 (*s*, 1H), 5.15 (*s*, 2H), 3.82 (*s*, 3H), 1.72 (*s*, 6H). **^{13}C NMR** (101 MHz, $CDCl_3$) δ 174.21, 160.62, 159.49, 154.78, 129.54, 128.41, 128.11, 123.88, 122.66, 120.83, 113.85, 111.13, 101.93, 66.68, 55.26, 44.11, 24.41. HRMS (ESI, m/z) calcd. for $C_{20}H_{20}O_4$ $[M - H]^-$: 323.1283; found: 323.1266.

2-(benzofuran-2-yl)-N-benzyl-2-methylpropanamide (5j)

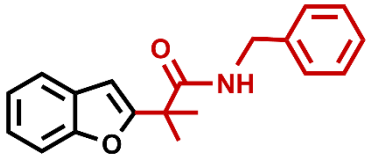

The general procedure was followed. Column chromatography (SiO_2, eluting with 9:1 hexane/ethyl acetate) afforded the desired product **5j** as a yellow solid (113 mg, yield 77%).**^{1}H NMR** (400 MHz, $CDCl_3$) δ 7.55 (*d*, *J* = 7.3 Hz, 1H), 7.48 (*d*, *J* = 8.3 Hz, 1H), 7.33 – 7.22 (*m*, 6H), 7.18 (*d*, *J* = 6.5 Hz, 2H), 6.66 (*s*, 1H), 5.98 (*s*, 1H), 4.43 (*d*, *J* = 5.9 Hz, 2H), 1.71 (*s*, 6H). **^{13}C NMR** (101 MHz, $CDCl_3$) δ 174.22, 161.08, 155.04, 138.43, 128.75, 128.24, 127.44, 127.33, 124.46, 123.12, 121.05, 111.32, 103.41, 44.50, 43.72, 24.96. HRMS (ESI, m/z) calcd. for $C_{19}H_{20}NO_2$ $[M + H]^+$: 294.1494; found: 294.1458.

2-(benzofuran-2-yl)-N-cyclohexyl-2-methylpropanamide (5k)[76]

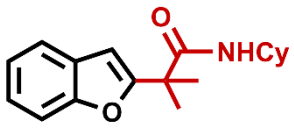

The general procedure was followed. Column chromatography (SiO_2, eluting with 9:1 hexane/ethyl acetate) afforded the desired product **5k** as a white solid (90 mg, yield 63%).**^{1}H NMR** (400 MHz, $CDCl_3$) δ 7.57 (*d*, *J* = 7.1 Hz, 1H), 7.48 (*d*, *J* = 8.0 Hz, 1H), 7.33 – 7.22 (*m*, 2H), 6.64 (*s*, 1H), 5.51 (*d*, *J* = 7.3 Hz, 1H), 3.82 – 3.66 (*m*, 1H), 1.99 – 1.77 (*m*, 3H), 1.64 (*s*, 6H), 1.61 – 1.52 (*m*, 2H), 1.38 – 1.27 (*m*, 2H), 1.16 – 0.96 (*m*, 3H). **^{13}C NMR** (101 MHz, $CDCl_3$) δ 173.17, 161.39, 154.97, 128.26, 124.28, 123.00, 120.96, 111.19, 103.12, 48.39, 44.37, 32.82, 25.54, 24.95, 24.72. HRMS (ESI, m/z) calcd. for $C_{18}H_{24}NO_2$ $[M + H]^+$: 286.1807; found: 286.1780.

Diethyl 2-(benzofuran-2-yl)-2-methylmalonate (5l)[77]

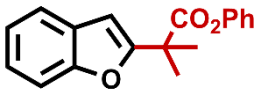

The general procedure was followed. Column chromatography (SiO_2, eluting with 99:1 hexane/ethyl acetate) afforded the desired product **5l** as a yellow solid (98 mg, yield 70%).**^{1}H NMR** (400 MHz, $CDCl_3$) δ 7.60 (*d*, *J* = 7.4 Hz, 1H), 7.53 (*d*, *J* = 8.1 Hz, 1H), 7.38 (*t*, *J* = 7.9 Hz, 2H), 7.34 – 7.21 (*m*, 3H), 7.07 (*d*, *J* = 7.3 Hz, 2H), 6.70 (*s*, 1H), 1.85 (*s*, 6H). **^{13}C NMR**

(101 MHz, $CDCl_3$) δ 173.11, 160.22, 154.98, 151.01, 129.47, 128.45, 125.98, 124.13, 122.84, 121.46, 121.00, 111.27, 102.23, 44.36, 24.54. HRMS (ESI, m/z) calcd. for $C_{18}H_{15}O_3$ $[M + H]^+$: 279.1021; found: 279.1094.

4-formylphenyl 2-(benzofuran-2-yl)-2-methylpropanoate (5m)

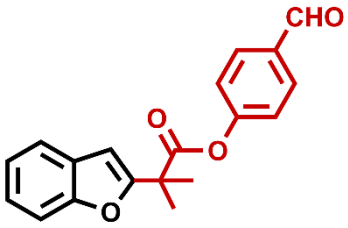

The general procedure was followed. Column chromatography (SiO_2, eluting with 20:1 hexane/ethyl acetate) afforded the desired product **5m** as a yellow solid (135 mg, yield 88%).**^{1}H NMR** (400 MHz, $CDCl_3$) δ 9.99 (*s*, 1H), 7.91 (*d*, *J* = 8.6 Hz, 2H), 7.60 (*d*, *J* = 7.5 Hz, 1H), 7.52 (*d*, *J* = 8.1 Hz, 1H), 7.34 – 7.26 (*m*, 2H), 7.24 (*d*, *J* = 8.6 Hz, 2H), 6.71 (*d*, *J* = 0.9 Hz, 1H), 1.85 (*s*, 6H). **^{13}C NMR** (101 MHz, $CDCl_3$) δ 191.02, 172.48, 159.66, 155.67, 154.97, 134.15, 131.26, 128.31, 124.31, 122.96, 122.32, 121.06, 111.27, 102.45, 44.44, 24.43. HRMS (ESI, m/z) calcd. for $C_{19}H_{17}O_4$ $[M + H]^+$: 309.1127; found: 309.1065.

4-nitrophenyl 2-(benzofuran-2-yl)-2-methylpropanoate (5n)

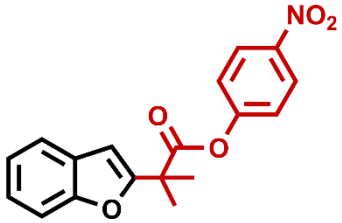

The general procedure was followed. Column chromatography (SiO_2, eluting with 20:3 hexane/ethyl acetate) afforded the desired product **5n** as a yellow solid (122 mg, yield 75%).**^{1}H NMR** (400 MHz, $CDCl_3$) δ 8.23 (*d*, *J* = 9.3 Hz, 2H), 7.53 (*dd*, *J* = 33.2, 8.0 Hz, 2H), 7.33 – 7.17 (*m*, 5H), 6.68 (*s*, 1H), 1.82 (*s*, 6H). **^{13}C NMR** (101 MHz, $CDCl_3$) δ 172.28, 159.42, 155.74, 155.01, 145.54, 128.28, 125.30, 124.44, 123.06, 122.47, 121.13, 111.31, 102.57, 44.50, 24.43. HRMS (ESI, m/z) calcd. for $C_{18}H_{16}NO_5$ $[M + H]^+$: 326.1028; found: 326.1042.

[1,1'-biphenyl]-4-yl 2-(benzofuran-2-yl)-2-methylpropanoate (5o)

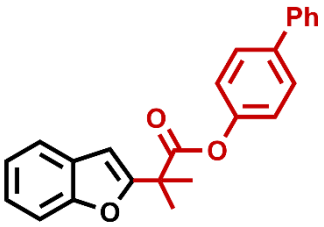

The general procedure was followed. Column chromatography (SiO_2, eluting with 95:5 hexane/ethyl acetate) afforded the desired product **5o** as a yellow solid (146 mg, yield 82%).**^{1}H NMR** (400 MHz, $CDCl_3$) δ 7.59 – 7.45 (*m*, 6H), 7.45 – 7.36 (*m*, 2H), 7.36 – 7.17 (*m*, 4H), 7.08 (*d*, *J* = 8.6 Hz, 1H), 6.65 (*s*, 1H), 1.80 (*s*, 6H). **^{13}C NMR** (101 MHz, $CDCl_3$) δ 173.17, 160.18, 154.99, 150.43, 140.45, 128.91, 128.44, 128.21, 127.48, 127.23, 124.17, 122.88, 121.75, 121.02, 111.29, 102.30, 44.40, 24.56. HRMS (ESI, m/z) calcd. for $C_{24}H_{21}O_3$ $[M + H]^+$: 357.1491; found: 357.1490.

Ethyl 2-(1H-indol-2-yl)-2-methylpropanoate (7a)

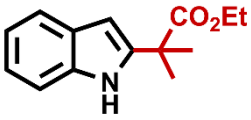

The general procedure was followed. Column chromatography (SiO_2, eluting with 90:10 hexane/ethyl acetate) afforded the desired product **7a** as a white solid (86 mg, yield 74%). **^{1}H NMR** (400 MHz, $CDCl_3$) δ 8.05 (*s*, 1H), 7.68 (*d*, *J* = 8.1 Hz, 1H), 7.35 – 7.30 (*m*, 1H), 7.21 – 7.15 (*m*, 1H), 7.10 (*ddd*, *J* = 8.1, 7.0, 1.1 Hz, 1H), 7.02 (*d*, *J* = 2.5 Hz, 1H), 4.13 (*q*, *J* = 7.1 Hz, 2H), 1.70 (*s*, 6H), 1.16 (*t*, *J* = 7.1 Hz, 3H). **^{13}C NMR** (101 MHz, $CDCl_3$) δ 177.29, 136.93, 125.76, 121.99, 120.95, 120.64, 120.50, 119.44, 111.40, 60.92, 42.16, 26.29, 14.27.

Ethyl 2-(5-cyano-1H-indol-2-yl)-2-methylpropanoate (7b)

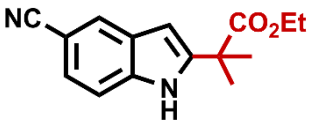

The general procedure was followed. Column chromatography (SiO_2, eluting with 85:15 hexane/ethyl acetate) afforded the desired product **7b** as a yellow solid (81 mg, yield 63%). **^{1}H NMR** (400 MHz, $CDCl_3$) δ 8.59 (*s*, 1H), 8.06 (*d*, *J* = 1.2 Hz, 1H), 7.39 (*s*, 2H), 7.16 (*s*, 1H), 4.14 (*q*, *J* = 7.1 Hz, 2H), 1.68 (*s*, 6H), 1.19 (*t*, *J* = 7.1 Hz, 3H). **^{13}C NMR** (101 MHz, $CDCl_3$) δ

176.58, 138.67, 126.38, 125.64, 124.95, 123.00, 121.87, 120.97, 112.37, 102.57, 61.28, 42.13, 26.28, 14.26. HRMS (ESI, m/z) calcd. for $C_{15}H_{17}N_2O_2$ $[M - H]^-$: 257.1290; found: 257.1291.

Ethyl 2-(5-methoxy-1H-indol-2-yl)-2-methylpropanoate (7c)

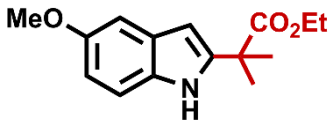

The general procedure was followed. Column chromatography (SiO_2, eluting with 80:20 hexane/ethyl acetate) afforded the desired product **7c** as a yellow solid (102 mg, yield 78%).**^{1}H NMR** (400 MHz, $CDCl_3$) δ 8.02 (*s*, 1H), 7.20 (*d*, *J* = 8.8 Hz, 1H), 7.13 (*d*, *J* = 2.4 Hz, 1H), 7.00 (*d*, *J* = 2.6 Hz, 1H), 6.85 (*dd*, *J* = 8.8, 2.4 Hz, 1H), 4.13 (*q*, *J* = 7.1 Hz, 2H), 3.84 (*s*, 3H), 1.68 (*s*, 6H), 1.17 (*t*, *J* = 7.1 Hz, 3H). **^{13}C NMR** (101 MHz, $CDCl_3$) δ 177.30, 153.76, 132.09, 126.04, 121.44, 120.51, 112.15, 112.08, 102.31, 60.93, 55.99, 42.06, 26.11, 14.32. HRMS (ESI, m/z) calcd. for $C_{15}H_{20}NO_3$ $[M + H]^+$: 262.1443; found: 262.1443.

Ethyl 2-(5-bromo-1H-indol-2-yl)-2-methylpropanoate (7d)

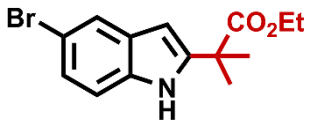

The general procedure was followed. Column chromatography (SiO_2, eluting with 85:15 hexane/ethyl acetate) afforded the desired product **7d** as a yellow solid (96 mg, yield 62%).**^{1}H NMR** (400 MHz, $CDCl_3$) δ 8.10 (*s*, 1H), 7.83 – 7.80 (*m*, 1H), 7.24 (*d*, *J* = 1.8 Hz, 1H), 7.21 (*dd*, *J* = 8.7, 0.6 Hz, 1H), 7.06 (*d*, *J* = 2.6 Hz, 1H), 4.14 (*q*, *J* = 7.1 Hz, 2H), 1.66 (*s*, 6H), 1.19 (*t*, *J* = 7.1 Hz, 3H). **^{13}C NMR** (101 MHz, $CDCl_3$) δ 176.81, 135.57, 127.52, 124.97, 123.21, 121.91, 120.78, 112.84, 112.79, 61.13, 42.11, 26.25, 14.27. HRMS (ESI, m/z) calcd. for $C_{14}H_{17}BrNO_2$ $[M + H]^+$: 310.0443; found: 310.0447.

Ethyl 2-methyl-2-(3-methyl-1H-indol-2-yl)propanoate (7e)

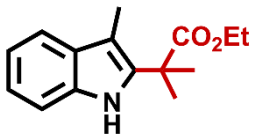

The general procedure was followed. Column chromatography (SiO_2, eluting with 98:2 hexane/ethyl acetate) afforded the desired product **7e** as a white solid (93 mg, yield 76%).**^{1}H NMR** (400 MHz, $CDCl_3$) δ 8.12 (*s*, 1H), 7.52 (*d*, *J* = 7.7 Hz, 1H), 7.32 (*d*, *J* = 8.1 Hz, 1H), 7.19 – 7.07 (*m*, 2H), 4.17 (*q*, *J* = 7.1 Hz, 2H), 2.28 (*s*, 3H), 1.70 (*s*, 6H), 1.22 (*t*, *J* = 7.1 Hz, 3H). **^{13}C NMR** (101 MHz, $CDCl_3$) δ 175.80, 135.64, 134.36, 130.05, 121.68, 119.30, 118.33, 110.62, 107.24, 61.40, 43.32, 25.71, 14.25, 9.43, 9.40.

Ethyl 2-(benzo[b]thiophen-2-yl)-2-methylpropanoate (9a)[76]

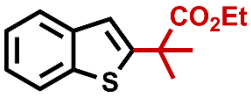

The general procedure was followed. Column chromatography (SiO_2, eluting with 99:1 hexane/ethyl acetate) afforded the desired product **9a** as a colourless oil (98 mg, yield 79%).**^{1}H NMR** (400 MHz, $CDCl_3$) δ 7.79 (*d*, *J* = 8.2 Hz, 1H), 7.72 (*d*, *J* = 6.7 Hz, 1H), 7.36 – 7.27 (*m*, 2H), 7.19 (*s*, 1H), 4.18 (*q*, *J* = 7.1 Hz, 2H), 1.74 (*s*, 6H), 1.25 (*t*, *J* = 7.1 Hz, 3H). **^{13}C NMR** (101 MHz, $CDCl_3$) δ 175.11, 150.15, 139.66, 139.41, 124.29, 124.11, 123.42, 122.19, 120.34, 61.48, 45.43, 27.45, 14.16. HRMS (ESI, m/z) calcd. for $C_{15}H_{19}O_2S$ $[M + H]^+$: 263.1106; found: 263.1195.

Ethyl 2-methyl-2-(5-methylthiophen-2-yl)propanoate (9b)

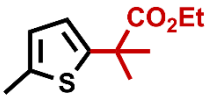

The general procedure was followed. Column chromatography (SiO_2, eluting with 98:2 hexane/ethyl acetate) afforded the desired product **9b** as a yellow oil (97 mg, yield 92%).**^{1}H NMR** (400 MHz, $CDCl_3$) δ 6.72 (*d*, *J* = 3.5 Hz, 1H), 6.58 (*d*, *J* = 2.3 Hz, 1H), 4.14 (*q*, *J* = 7.1 Hz, 2H), 2.44 (*s*, 3H), 1.62 (*s*, 6H), 1.23 (*t*, *J* = 7.1 Hz, 3H). **^{13}C NMR** (101 MHz, $CDCl_3$) δ 175.58, 146.92, 138.51, 124.62, 123.46, 61.20, 44.77, 27.55, 15.35, 14.13. HRMS (ESI, m/z) calcd. for $C_{11}H_{17}O_2S$ $[M + H]^+$: 213.0949; found: 213.0970.

Ethyl 2-(5-bromothiophen-2-yl)-2-methylpropanoate (9c)

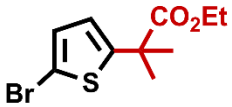

The general procedure was followed. Column chromatography (SiO_2, eluting with 98:2 hexane/ethyl acetate) afforded the desired product **9c** as a yellow oil (95 mg, yield 69%).**^{1}H NMR** (400 MHz, $CDCl_3$) δ 6.87 (*d*, *J* = 3.8 Hz, 1H), 6.70 (*d*, *J* = 3.8 Hz, 1H), 4.14 (*q*, *J* = 7.1 Hz, 2H), 1.60 (*s*, 6H), 1.23 (*t*, *J* = 7.1 Hz, 3H). **^{13}C NMR** (101 MHz, $CDCl_3$) δ 174.86, 150.78, 129.35, 124.16, 110.81, 61.50, 45.17, 27.38, 14.13. HRMS (ESI, m/z) calcd. for $C_{10}H_{14}BrO_2S$ $[M + H]^+$: 278.9877; found: 278.9868.

Ethyl (E)-4-(4-methoxyphenyl)-2,2-dimethylbut-3-enoate (11a)[76]

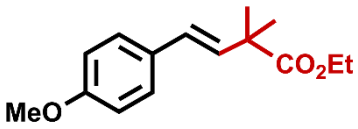

The general procedure was followed. Column chromatography (SiO_2, eluting with 98:2 hexane/ethyl acetate) afforded the desired product **11a** as a white solid (120 mg, yield 94%).**^{1}H NMR** (400 MHz, $CDCl_3$) δ 7.32 (*d*, *J* = 8.8 Hz, 2H), 6.85 (*d*, *J* = 8.8 Hz, 2H), 6.39 (*d*, *J* = 16.2 Hz, 1H), 6.27 (*d*, *J* = 16.3 Hz, 1H), 4.15 (*q*, *J* = 7.1 Hz, 2H), 3.80 (*s*, 3H), 1.40 (*s*, 6H), 1.26 (*t*, *J* = 7.1 Hz, 3H). **^{13}C NMR** (101 MHz, $CDCl_3$) δ 176.54, 159.15, 132.45, 130.01, 127.54, 127.39, 114.02, 60.83, 55.34, 44.37, 25.23, 14.27. HRMS (ESI, m/z) calcd. for $C_{15}H_{21}O_3$ $[M + H]^+$: 249.1491; found: 249.1485.

Tert-butyl (E)-4-(4-methoxyphenyl)-2,2-dimethylbut-3-enoate (11b)

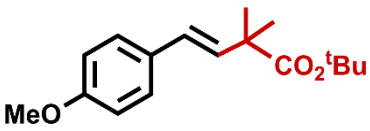

The general procedure was followed. Column chromatography (SiO_2, eluting with 98:2 hexane/ethyl acetate) afforded the desired product **11b** as a white solid (92 mg, yield 67%).**^{1}H NMR** (400 MHz, $CDCl_3$) δ 7.31 (*d*, *J* = 8.6 Hz, 2H), 6.85 (*d*, *J* = 8.4 Hz, 2H), 6.37 (*d*, *J* = 16.2 Hz, 1H), 6.25 (*d*, *J* = 16.2 Hz, 1H), 3.80 (*s*, 3H), 1.45 (*s*, 9H), 1.36 (*s*, 6H). **^{13}C NMR** (101 MHz, $CDCl_3$) δ 175.81, 159.08, 133.01, 130.28, 127.50, 127.07, 114.03, 55.39, 44.98, 28.07, 25.26. HRMS (ESI, m/z) calcd. for $C_{17}H_{24}O_3$ [M - H] : 275.1647; found: 275.1643. HRMS (ESI, m/z) calcd. for $C_{17}H_{23}O_3$ $[M - H]^-$: 275.1647; found: 275.1643.

Diethyl (E)-2-(4-methoxystyryl)-2-methylmalonate (11c)[76]

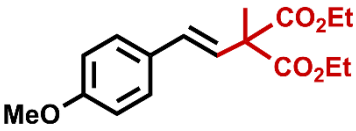

The general procedure was followed. Column chromatography (SiO_2, eluting with 98:2 hexane/ethyl acetate) afforded the desired product **11c** as a yellow oil (136 mg, yield 89%).**^{1}H NMR** (400 MHz, $CDCl_3$) δ 7.34 (*d*, *J* = 8.7 Hz, 2H), 6.84 (*d*, *J* = 8.7 Hz, 2H), 6.55 (*d*, *J* = 16.4 Hz, 1H), 6.44 (*d*, *J* = 16.4 Hz, 1H), 4.21 (*qd*, *J* = 7.1, 2.1 Hz, 4H), 3.78 (*s*, 3H), 1.65 (*s*, 3H), 1.26 (*t*, *J* = 7.1 Hz, 6H). **^{13}C NMR** (101 MHz, $CDCl_3$) δ 171.28, 159.45, 130.20, 129.32, 127.80, 125.39, 113.97, 61.62, 55.61, 55.28, 20.38, 14.05. HRMS (ESI, m/z) calcd. for $C_{17}H_{23}O_5$ [M + H]$^+$: 307.1545; found: 307.1521.

Phenyl (E)-4-(4-methoxyphenyl)-2,2-dimethylbut-3-enoate (11d)

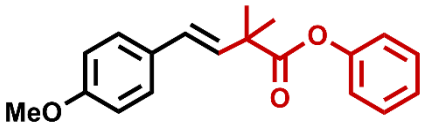

The general procedure was followed. Column chromatography (SiO_2, eluting with 98:2 hexane/ethyl acetate) afforded the desired product **11d** as a yellow solid (120 mg, yield 81%).**^{1}H NMR** (400 MHz, $CDCl_3$) δ 7.39 (*dt*, *J* = 8.1, 3.5 Hz, 4H), 7.24 (*t*, *J* = 7.4 Hz, 1H), 7.13 – 7.07 (*m*, 2H), 6.90 (*d*, *J* = 8.4 Hz, 2H), 6.56 (*d*, *J* = 16.2 Hz, 1H), 6.43 (*d*, *J* = 16.2 Hz, 1H), 3.83 (*s*, 3H), 1.59 (*s*, 6H). **^{13}C NMR** (101 MHz, $CDCl_3$) δ 175.05, 159.33, 151.17, 131.54, 129.79, 129.45, 128.34, 127.66, 125.79, 121.54, 114.10, 55.38, 44.69, 25.26. HRMS (ESI, m/z) calcd. for $C_{19}H_{21}O_3$ [M + H]$^+$: 297.1491; found: 297.1450.

4-formylphenyl (E)-4-(4-methoxyphenyl)-2,2-dimethylbut-3-enoate (11e)

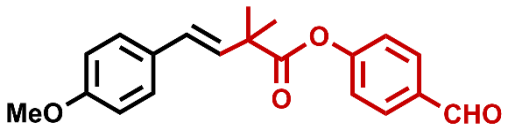

The general procedure was followed. Column chromatography (SiO_2, eluting with 95:5 hexane/ethyl acetate) afforded the desired product **11e** as a yellow solid (149 mg, yield 92%).**^{1}H NMR** (400 MHz, $CDCl_3$) δ 9.99 (*s*, 1H), 7.92 (*d*, *J* = 8.7 Hz, 2H), 7.39 (*d*, *J* = 8.6 Hz, 2H), 7.27 (*d*, *J* = 8.4 Hz, 2H), 6.90 (*d*, *J* = 8.6 Hz, 2H), 6.56 (*d*, *J* = 16.1 Hz, 1H), 6.39 (*d*, *J* = 16.1 Hz, 1H), 3.83 (*s*, 3H), 1.60 (*s*, 6H). **^{13}C NMR** (101 MHz, $CDCl_3$) δ 191.01, 174.37, 159.40,

155.89, 133.98, 131.21, 130.82, 129.51, 128.75, 127.66, 122.35, 114.10, 55.35, 44.77, 25.13. HRMS (ESI, m/z) calcd. for $C_{20}H_{19}O_4$ $[M - H]^-$: 323.1283; found: 232.1275.

(E)-N-cyclohexyl-4-(4-methoxyphenyl)-2,2-dimethylbut-3-enamide (11f)

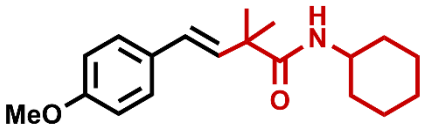

The general procedure was followed. Column chromatography (SiO_2, eluting with 90:10 hexane/ethyl acetate) afforded the desired product **11f** as a white solid (104 mg, yield 69%).**^{1}H NMR** (400 MHz, $CDCl_3$) δ 7.29 (*d*, *J* = 8.5 Hz, 2H), 6.83 (*d*, *J* = 8.8 Hz, 2H), 6.43 (*d*, *J* = 16.3 Hz, 1H), 6.16 (*d*, *J* = 16.2 Hz, 1H), 5.60 (*d*, *J* = 9.0 Hz, 1H), 3.76 (*s*, 3H), 3.73 – 3.62 (*m*, 1H), 1.81 (*dd*, *J* = 12.6, 4.0 Hz, 2H), 1.72 – 1.40 (*m*, 4H), 1.33 (*s*, 6H), 1.06 (*ddd*, *J* = 18.8, 10.5, 4.7 Hz, 5H). **^{13}C NMR** (101 MHz, $CDCl_3$) δ 175.31, 159.20, 132.48, 129.40, 128.59, 127.39, 113.97, 55.18, 48.07, 44.69, 32.87, 25.42, 25.32, 24.73. HRMS (ESI, m/z) calcd. for $C_{19}H_{28}NO_2$ $[M + H]^+$: 302.2120; found: 302.2093.

1,3,3-trimethylindolin-2-one (13a)[78]

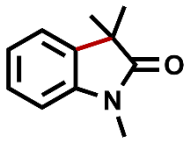

The general procedure was followed. Column chromatography (SiO_2, eluting with 95:5 hexane/ethyl acetate) afforded the desired product **13a** as a yellow oil (75 mg, yield 86%).**^{1}H NMR** (400 MHz, $CDCl_3$) δ 7.25 (*td*, *J* = 7.7, 1.3 Hz, 1H), 7.21 – 7.17 (*m*, 1H), 7.05 (*td*, *J* = 7.5, 1.0 Hz, 1H), 6.83 (*d*, *J* = 7.8 Hz, 1H), 3.20 (*s*, 3H), 1.36 (*s*, 6H). **^{13}C NMR** (101 MHz, $CDCl_3$) δ 181.42, 142.65, 135.84, 127.70, 122.53, 122.28, 108.06, 44.20, 26.23, 24.41.

5-chloro-1,3,3-trimethylindolin-2-one (13b)[78]

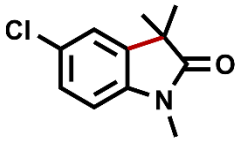

The general procedure was followed. Column chromatography (SiO_2, eluting with 95:5 hexane/ethyl acetate) afforded the desired product **13b** as a white solid (95 mg, yield 91%).**^{1}H**

NMR (400 MHz, $CDCl_3$) δ 7.22 (*dd*, *J* = 8.2, 2.1 Hz, 1H), 7.16 (*d*, *J* = 2.1 Hz, 1H), 6.75 (*d*, *J* = 8.3 Hz, 1H), 3.19 (*s*, 3H), 1.35 (*s*, 6H). **^{13}C NMR** (101 MHz, $CDCl_3$) δ 180.92, 141.29, 137.57, 127.96, 127.66, 123.03, 109.06, 44.56, 26.43, 24.36. HRMS (ESI, m/z) calcd. for $C_{11}H_{13}ClNO$ $[M + H]^+$: 210.0686; found: 210.0683.

1,3,3,5-tetramethylindolin-2-one (11c)[78]

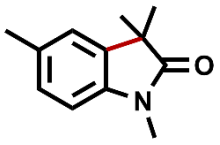

The general procedure was followed. Column chromatography (SiO_2, eluting with 95:5 hexane/ethyl acetate) afforded the desired product **11c** as a yellow oil (75 mg, yield 79%).**^{1}H NMR** (400 MHz, $CDCl_3$) δ 7.07 – 7.04 (*m*, 1H), 7.02 (*d*, *J* = 0.7 Hz, 1H), 6.73 (*d*, *J* = 7.8 Hz, 1H), 3.19 (*s*, 3H), 2.34 (*s*, 3H), 1.35 (*s*, 6H). **^{13}C NMR** (101 MHz, $CDCl_3$) δ 181.47, 140.34, 135.99, 132.10, 127.94, 123.27, 107.84, 44.33, 26.33, 24.51, 21.24.

5-methoxy-1,3,3-trimethylindolin-2-one (11d)[78]

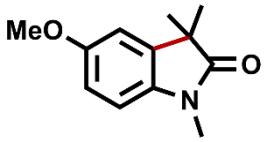

The general procedure was followed. Column chromatography (SiO_2, eluting with 95:5 hexane/ethyl acetate) afforded the desired product **11d** as a white solid (84 mg, yield 78%). **^{1}H NMR** (400 MHz, $CDCl_3$) δ 6.82 – 6.80 (*m*, 1H), 6.77 (*dd*, *J* = 8.4, 2.4 Hz, 1H), 6.73 (*d*, *J* = 7.8 Hz, 1H), 3.79 (*s*, 3H), 3.18 (*s*, 3H), 1.35 (*s*, 6H). **^{13}C NMR** (101 MHz, $CDCl_3$) δ 181.16, 156.16, 137.33, 136.23, 111.65, 110.15, 108.34, 55.92, 44.72, 26.38, 24.49.

5-fluoro-1,3,3-trimethylindolin-2-one (11e)[78]

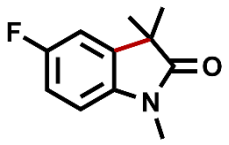

The general procedure was followed. Column chromatography (SiO_2, eluting with 95:5 hexane/ethyl acetate) afforded the desired product **11e** as a white solid (82 mg, yield 92%).**^{1}H**

NMR (400 MHz, $CDCl_3$) δ 6.96 – 6.88 (*m*, 2H), 6.73 (*dd*, *J* = 9.2, 4.2 Hz, 1H), 3.18 (*s*, 3H), 1.33 (*s*, 6H). **^{13}C NMR** (101 MHz, $CDCl_3$) δ 181.01, 158.25(d, $^1J_{C-F}$= 241 Hz), 138.57(d, $^4J_{C-F}$= 2 Hz), 137.48(d, $^3J_{C-F}$= 8 Hz), 113.67(d, $^2J_{C-F}$= 24 Hz), 110.45(d, $^2J_{C-F}$= 24 Hz), 108.45(d, $^3J_{C-F}$= 8 Hz), 44.72, 26.38, 24.32. **^{19}F** NMR (376 MHz, $CDCl_3$) δ -120.90.

1,3,3-trimethyl-5-(trifluoromethyl)indolin-2-one (11f)[78]

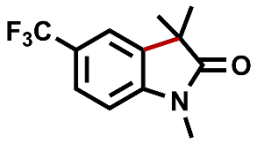

The general procedure was followed. Column chromatography (SiO_2, eluting with 95:5 hexane/ethyl acetate) afforded the desired product **11f** as a white solid (104 mg, yield 92%).**^{1}H NMR** (400 MHz, $CDCl_3$) δ 7.54 (*d*, *J* = 8.2 Hz, 1H), 7.42 (*s*, 1H), 6.90 (*d*, *J* = 8.1 Hz, 1H), 3.24 (*d*, *J* = 1.7 Hz, 3H), 1.38 (*d*, *J* = 1.8 Hz, 6H). **^{13}C NMR** (101 MHz, $CDCl_3$) δ 181.32, 145.75, 136.42, 125.62(q, $^3J_{C-F}$= 4 Hz), 124.69(q, $^2J_{C-F}$= 32 Hz), 123.25(q, $^1J_{C-F}$= 272 Hz), 119.43(q, $^3J_{C-F}$= 4 Hz), 107.86, 44.29, 26.50, 24.33. **^{19}F** NMR (376 MHz, $CDCl_3$) δ -61.36.

1,3,3-trimethyl-5-nitroindolin-2-one (11g)[78]

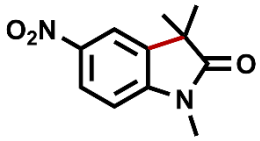

The general procedure was followed. Column chromatography (SiO_2, eluting with 95:5 hexane/ethyl acetate) afforded the desired product **11g** as a white solid (114 mg, yield 88%).**^{1}H NMR** (400 MHz, $CDCl_3$) δ 8.19 (*d*, *J* = 8.6 Hz, 1H), 8.05 (*d*, *J* = 1.9 Hz, 1H), 6.91 (*d*, *J* = 8.6 Hz, 1H), 3.25 (*s*, 3H), 1.38 (*d*, *J* = 1.2 Hz, 6H). **^{13}C NMR** (101 MHz, $CDCl_3$) δ 181.40, 148.50, 143.58, 136.58, 125.31, 118.44, 107.71, 44.34, 26.78, 24.28.

1-benzyl-3,3-dimethylindolin-2-one (11h)[78]

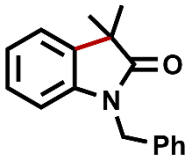

The general procedure was followed. Column chromatography (SiO_2, eluting with 95:5 hexane/ethyl acetate) afforded the desired product **11h** as a white solid (102 mg, yield 86%).**^{1}H NMR** (400 MHz, $CDCl_3$) δ 7.35 – 7.25 (*m*, 5H), 7.23 (*dd*, *J* = 7.4, 1.4 Hz, 1H), 7.14 (*td*, *J* = 7.7, 1.3 Hz, 1H), 7.06 – 7.00 (*m*, 1H), 6.74 (*d*, *J* = 7.8 Hz, 1H), 4.94 (*s*, 2H), 1.46 (*s*, 6H). **^{13}C NMR** (101 MHz, $CDCl_3$) δ 181.48, 141.69, 136.14, 135.81, 128.80, 127.62, 127.56, 127.19, 122.56, 122.37, 109.12, 44.21, 43.55, 24.59.

Ethyl 2-(3,5-di-tert-butyl-1-methyl-4-oxocyclohexa-2,5-dien-1-yl)-2-methylpropanoate (15)[76]

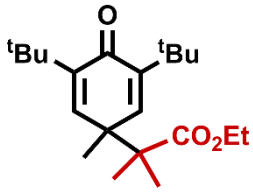

The general procedure was followed. Column chromatography (SiO_2, eluting with 98:2 hexane/ethyl acetate) afforded the desired product **15** as a yellow oil (137 mg, yield 82%).**^{1}H NMR** (400 MHz, $CDCl_3$) δ 6.53 (*s*, 2H), 4.10 (*q*, *J* = 7.1 Hz, 2H), 1.25 (*t*, *J* = 7.1 Hz, 3H), 1.20 (*s*, 18H), 1.18 (*s*, 3H), 1.11 (*s*, 6H). **^{13}C NMR** (101 MHz, $CDCl_3$) δ 186.25, 175.53, 147.11, 143.78, 60.82, 49.06, 42.99, 35.02, 29.57, 21.99, 21.70, 14.35. HRMS (ESI, m/z) calcd. for $C_{21}H_{35}O_3$ $[M + H]^+$: 335.2586; found: 335.2551.

5.11. References:

1. Lyaskovskyy, V.; de Bruin, B., Redox Non-Innocent Ligands: Versatile New Tools to Control Catalytic Reactions. *ACS Catal.* **2012,** *2*, 270-279.
2. Chirik, P. J.; Wieghardt, K., Radical Ligands Confer Nobility on Base-Metal Catalysts. *Science* **2010,** *327*, 794-795.
3. Singh, K.; Kundu, A.; Adhikari, D., Ligand-Based Redox: Catalytic Applications and Mechanistic Aspects. *ACS Catal.* **2022,** *12*, 13075-13107.
4. Bullock, R. M., *Catalysis Without Precious Metals*. Wiley-VCH: Weinheim, 2010.
5. Rittle, J.; Green, M. T., Cytochrome P450 Compound I: Capture, Characterization, and C-H Bond Activation Kinetics. *Science* **2010,** *330*, 933-937.
6. Borman, C. D.; Saysell, C. G.; Sokolowski, A.; Twitchett, M. B.; Wright, C.; Sykes, A. G., Reactivity of galactose oxidase. *Coord. Chem. Rev.* **1999,** *190-192*, 771-779.
7. Chirik, P. J., Iron- and Cobalt-Catalyzed Alkene Hydrogenation: Catalysis with Both Redox-Active and Strong Field Ligands. *Acc. Chem. Res.* **2015,** *48*, 1687-1695.
8. Singh, V.; Kundu, A.; Singh, K.; Adhikari, D., Redox noninnocence of the formazanate ligand applied to catalytic formation of α-ketoamides. *Chem. Commun.* **2022,** *58*, 6630-6633.
9. Sandl, S.; Maier, T. M.; van Leest, N. P.; Kröncke, S.; Chakraborty, U.; Demeshko, S.; Koszinowski, K.; de Bruin, B.; Meyer, F.; Bodensteiner, M.; Herrmann, C.; Wolf, R.; Jacobi von Wangelin, A., Cobalt-Catalyzed Hydrogenations via Olefin Cobaltate and Hydride Intermediates. *ACS Catal.* **2019,** *9*, 7596-7606.
10. Ren, Y.; Cheaib, K.; Jacquet, J.; Vezin, H.; Fensterbank, L.; Orio, M.; Blanchard, S.; Desage-El Murr, M., Copper-Catalyzed Aziridination with Redox-Active Ligands: Molecular Spin Catalysis. *Chem.-Eur. J.* **2018,** *24*, 5086-5090.
11. Derrick, J. S.; Loipersberger, M.; Chatterjee, R.; Iovan, D. A.; Smith, P. T.; Chakarawet, K.; Yano, J.; Long, J. R.; Head-Gordon, M.; Chang, C. J., Metal–Ligand Cooperativity via Exchange Coupling Promotes Iron- Catalyzed Electrochemical CO_2 Reduction at Low Overpotentials. *J. Am. Chem. Soc.* **2020,** *142*, 20489-20501.
12. Queyriaux, N., Redox-Active Ligands in Electroassisted Catalytic H^+ and CO_2 Reductions: Benefits and Risks. *ACS Catal.* **2021,** *11*, 4024-4035.
13. Wuttig, A.; Derrick, J. S.; Loipersberger, M.; Snider, A.; Head-Gordon, M.; Chang, C. J.; Toste, F. D., Controlled Single-Electron Transfer via Metal–Ligand Cooperativity Drives

Divergent Nickel-Electrocatalyzed Radical Pathways. *J. Am. Chem. Soc.* **2021,** *143*, 6990-7001.

14. van Leest, N. P.; Tepaske, M. A.; Oudsen, J.-P. H.; Venderbosch, B.; Rietdijk, N. R.; Siegler, M. A.; Tromp, M.; van der Vlugt, J. I.; de Bruin, B., Ligand Redox Noninnocence in $[CoIII(TAML)]^{0/-}$ Complexes Affects Nitrene Formation. *J. Am. Chem. Soc.* **2020,** *142*, 552-563.
15. Wang, D.; Bruner, C. O., Catalytic Water Oxidation by a Bio-inspired Nickel Complex with a Redox-Active Ligand. *Inorg. Chem.* **2017,** *56*, 13638-13641.
16. Bullock, R. M., Reaction: Earth-Abundant Metal Catalysts for Energy Conversions. *Chem* **2017,** *2*, 444-446.
17. Bullock, R. M.; Chen, J. G.; Gagliardi, L.; Chirik, P. J.; Farha, O. K.; Hendon, C. H.; Jones, C. W.; Keith, J. A.; Klosin, J.; Minteer, S. D.; Morris, R. H.; Radosevich, A. T.; Rauchfuss, T. B.; Strotman, N. A.; Vojvodic, A.; Ward, T. R.; Yang, J. Y.; Surendranath, Y., Using nature's blueprint to expand catalysis with Earth-abundant metals. *Science* **2020,** *369*, eabc3183.
18. White, M. C., Base-Metal Catalysis: Embrace the Wild Side. *Adv. Synth. Catal.* **2016,** *358*, 2364-2365.
19. Rana, S.; Biswas, J. P.; Paul, S.; Paik, A.; Maiti, D., Organic synthesis with the most abundant transition metal–iron: from rust to multitasking catalysts. *Chem. Soc. Rev.* **2021,** *50*, 243-472.
20. Plietker, B., *Iron Catalysis in Organic Chemistry*. Wiley-VCH: Weinheim, Germany, 2008.
21. Fürstner, A., Iron Catalysis in Organic Synthesis: A Critical Assessment of What It Takes To Make This Base Metal a Multitasking Champion. *ACS Central Science* **2016,** *2*, 778-789.
22. Doba, T.; Shang, R.; Nakamura, E., Iron-Catalyzed C–H Activation for Heterocoupling and Copolymerization of Thiophenes with Enamines. *J. Am. Chem. Soc.* **2022,** *144*, 21692-21701.
23. Linford-Wood, T. G.; Mahon, M. F.; Grayson, M. N.; Webster, R. L., Iron-Catalyzed H/D Exchange of Primary Silanes, Secondary Silanes, and Tertiary Siloxanes. *ACS Catal.* **2022,** *12*, 2979-2985.
24. Steinlandt, P. S.; Xie, X.; Ivlev, S.; Meggers, E., Stereogenic-at-Iron Catalysts with a Chiral Tripodal Pentadentate Ligand. *ACS Catal.* **2021,** *11*, 7467-7476.

25. Yamane, Y.; Yoshinaga, K.; Sumimoto, M.; Nishikata, T., Iron-Enhanced Reactivity of Radicals Enables C–H Tertiary Alkylations for Construction of Functionalized Quaternary Carbons. *ACS Catal.* **2019,** *9*, 1757-1762.
26. Myers, T. W.; Berben, L. A., A Sterically Demanding Iminopyridine Ligand Affords Redox-Active Complexes of Aluminum(III) and Gallium(III). *Inorg. Chem.* **2012,** *51*, 1480-1488.
27. Römelt, C.; Weyhermüller, T.; Wieghardt, K., Structural characteristics of redox-active pyridine-1,6-diimine complexes: Electronic structures and ligand oxidation levels. *Coord. Chem. Rev.* **2019,** *380*, 287-317.
28. Pierpont, C. G., Ligand Redox Activity and Mixed Valency in First-Row Transition-Metal Complexes Containing Tetrachlorocatecholate and Radical Tetrachlorosemiquinonate Ligands. *Inorg. Chem.* **2011,** *50*, 9766-9772.
29. Vlcek, A., Dithiolenes and non-innocent redox-active ligands. *Coord. Chem. Rev.* **2010,** *254*, 1357.
30. Webster, R. L., β-Diketiminate complexes of the first row transition metals: applications in catalysis. *Dalton Trans.* **2017,** *46*, 4483-4498.
31. Novoa, S.; Paquette, J. A.; Barbon, S. M.; Maar, R. R.; Gilroy, J. B., Side-chain boron difluoride formazanate polymers via ring-opening metathesis polymerization. *J. Mat. Chem. C* **2016,** *4*, 3987-3994.
32. Chang, M. C.; Otten, E., Synthesis and ligand-based reduction chemistry of boron difluoride complexes with redox-active formazanate ligands. *Chem. Commun.* **2014,** *50*, 7431-7433.
33. de Vries, F.; Otten, E., Reversible On/Off Switching of Lactide Cyclopolymerization with a Redox-Active Formazanate Ligand. *ACS Catal.* **2022,** *12*, 4125-4130.
34. Jin, D.; Sun, X.; Roesky, P. W., Heavy Alkaline–Earth Metal Formazanate Complexes and Their Catalytic Applications. *Organometallics* **2023,** *42*, 1725-1731.
35. Gilroy, J. B.; Patrick, B. O.; McDonald, R.; Hicks, R. G., Transition Metal Complexes of 3-Cyano- and 3-Nitroformazans. *Inorg. Chem.* **2008,** *47*, 1287-1294.
36. Speelman, A. L.; Skubi, K. L.; Mercado, B. Q.; Holland, P. L., Synthesis and Reactivity of Iron Complexes with a Biomimetic SCS Pincer Ligand. *Inorg. Chem.* **2021,** *60*, 1965-1974.
37. Morimoto, Y.; Hanada, S.; Kamada, R.; Fukatsu, A.; Sugimoto, H.; Itoh, S., Hydroxylation of Unactivated C(sp^3)–H Bonds with m-Chloroperbenzoic Acid Catalyzed by an Iron(III)

Complex Supported by a Trianionic Planar Tetradentate Ligand. *Inorg. Chem.* **2021,** *60*, 7641-7649.

38. Shankar, S.; Peters, M.; Steinborn, K.; Krahwinkel, B.; Sönnichsen, F. D.; Grote, D.; Sander, W.; Lohmiller, T.; Rüdiger, O.; Herges, R., Light-controlled switching of the spin state of iron(III). *Nat. Commun.* **2018,** *9*, 4750.
39. Geiger, D. K.; Scheidt, W. R., Control of spin state in (porphinato)iron(III) complexes. Effect of the porphyrin ligand. *Inorg. Chem.* **1984,** *23*, 1970-1972.
40. Rajput, A.; Sharma, A. K.; Barman, S. K.; Koley, D.; Steinert, M.; Mukherjee, R., Neutral, Cationic, and Anionic Low-Spin Iron(III) Complexes Stabilized by Amidophenolate and Iminobenzosemiquinonate Radical in N,N,O Ligands. *Inorg. Chem.* **2014,** *53*, 36-48.
41. Zeng, Y.; Caignan, G. A.; Bunce, R. A.; Rodríguez, J. C.; Wilks, A.; Rivera, M., Azide-Inhibited Bacterial Heme Oxygenases Exhibit an S = 3/2 $(dxz,dyz)^3(dxy)^1(dz^2)^1$ Spin State: Mechanistic Implications for Heme Oxidation. *J. Am. Chem. Soc.* **2005,** *127*, 9794-9807.
42. Nakamura, M., Electronic structures of highly deformed iron(III) porphyrin complexes. *Coord. Chem. Rev.* **2006,** *250*, 2271-2294.
43. Gordon, J. B.; McGale, J. P.; Prendergast, J. R.; Shirani-Sarmazeh, Z.; Siegler, M. A.; Jameson, G. N. L.; Goldberg, D. P., Structures, Spectroscopic Properties, and Dioxygen Reactivity of 5- and 6-Coordinate Nonheme Iron(II) Complexes: A Combined Enzyme/Model Study of Thiol Dioxygenases. *J. Am. Chem. Soc.* **2018,** *140*, 14807-14822.
44. Carney, M. J.; Papaefthymiou, G. C.; Spartalian, K.; Frankel, R. B.; Holm, R. H., Ground spin state variability in $[Fe_4S_4(SR)_4]^{3-}$. Synthetic analogs of the reduced clusters in ferredoxins and other iron-sulfur proteins: cases of extreme sensitivity of electronic state and structure to extrinsic factors. *J. Am. Chem. Soc.* **1988,** *110*, 6084-6095.
45. Broere, D. L. J.; Mercado, B. Q.; Lukens, J. T.; Vilbert, A. C.; Banerjee, G.; Lant, H. M. C.; Lee, S. H.; Bill, E.; Sproules, S.; Lancaster, K. M.; Holland, P. L., Reversible Ligand-Centered Reduction in Low-Coordinate Iron Formazanate Complexes. *Chem.-Eur. J.* **2018,** *24*, 9417-9425.
46. Maar, R. R.; Rabiee Kenaree, A.; Zhang, R.; Tao, Y.; Katzman, B. D.; Staroverov, V. N.; Ding, Z.; Gilroy, J. B., Aluminum Complexes of $N_2O_2^{3-}$ Formazanate Ligands Supported by Phosphine Oxide Donors. *Inorg. Chem.* **2017,** *56*, 12436-12447.
47. Gutlich, P.; Bill, E.; Trautwein, A., *Mossbauer Spectroscopyand Transition Metal Chemistry: Fundamentals and Applications*. Springer: Berlin, Heidelberg, 2011; p 1-568.

48. Metzinger, R.; Demeshko, S.; Limberg, C., A Novel Pentadentate Redox-Active Ligand and Its Iron(III) Complexes: Electronic Structures and O2 Reactivity. *Chem.-Eur. J.* **2014,** *20*, 4721-4735.
49. Jana, R. D.; Das, A.; Paine, T. K., Enhancing Chemo- and Stereoselectivity in C–H Bond Oxygenation with H_2O_2 by Nonheme High-Spin Iron Catalysts: The Role of Lewis Acid and Multimetal Centers. *Inorg. Chem.* **2021,** *60*, 5969-5979.
50. Hüppe, H. M.; Iffland-Mühlhaus, L.; Heck, J.; Eilers, M.; Gildenast, H.; Schönfeld, S.; Dürrmann, A.; Hoffmann, A.; Weber, B.; Apfel, U.-P.; Herres-Pawlis, S., Triflate vs Acetonitrile: Understanding the Iron(II)-Based Coordination Chemistry of Tri(quinolin-8-yl)amine. *Inorg. Chem.* **2023,** *62*, 4435-4455.
51. Weiss, R.; Gold, A.; Terner, J., Cytochromes c‘: Biological Models for the S = 3/2,5/2 Spin-State Admixture? *Chem. Rev.* **2006,** *106*, 2550-2579.
52. Que, L. Jr., *Physical Methods in Bioinorganic Chemistry: Spectroscopy and Magnetism*. University Science Books: Sausalito, CA, 2000.
53. Becke, A. D., Density-functional thermochemistry. III. The role of exact exchange. *J. Chem. Phys.* **1993,** *98*, 5648-5652.
54. Lee, C.; Yang, W.; Parr, R. G., Development of the Colle-Salvetti correlation-energy formula into a functional of the electron density. *Phys. Rev. B* **1988,** *37*, 785-789.
55. Noodleman, L.; Case, D. A.; Aizman, A., Broken symmetry analysis of spin coupling in iron-sulfur clusters. *J. Am. Chem. Soc.* **1988,** *110*, 1001-1005.
56. Dong, Z.; Ren, Z.; Thompson, S. J.; Xu, Y.; Dong, G., Transition-Metal-Catalyzed C–H Alkylation Using Alkenes. *Chem. Rev.* **2017,** *117*, 9333-9403.
57. Gensch, T.; Hopkinson, M. N.; Glorius, F.; Wencel-Delord, J., Mild metal-catalyzed C–H activation: examples and concepts. *Chem. Soc. Rev.* **2016,** *45*, 2900-2936.
58. Ding, K.; Lu, Y.; Nikolovska-Coleska, Z.; Wang, G.; Qiu, S.; Shangary, S.; Gao, W.; Qin, D.; Stuckey, J.; Krajewski, K.; Roller, P. P.; Wang, S., Structure-Based Design of Spiro-oxindoles as Potent, Specific Small-Molecule Inhibitors of the MDM2−p53 Interaction. *J. Med. Chem.* **2006,** *49*, 3432-3435.
59. Millemaggi, A.; Taylor, R. J. K., 3-Alkenyl-oxindoles: Natural Products, Pharmaceuticals, and Recent Synthetic Advances in Tandem/Telescoped Approaches. *Eur. J. Org. Chem.* **2010,** *2010*, 4527-4547.
60. Ozturk, T.; Ertas, E.; Mert, O., Use of Lawesson's Reagent in Organic Syntheses. *Chem. Rev.* **2007,** *107*, 5210-5278.

61. F. Neese, *Wiley Interdisciplinary Reviews: Computational Molecular Science*, **2018**, *8*, e1327.
62. Becke, A. D. Density-functional thermochemistry. III. The role of exact exchange. *J. Chem. Phys.* **1993**, *98*, 5648−5652.
63. Lee, C.; Yang, W.; Parr, R. G. Development of the Colle-Salvetti correlationenergy formula into a functional of the electron density. *Phys. Rev. B: Condens. Matter Mater. Phys.* **1988**, *37*, 785−789.
64. Vosko, S. H.; Wilk, L.; Nusair, M. Accurate spin-dependent electron liquid correlation energies for local spin density calculations: a critical analysis. *Can. J. Phys.* **1980**, *58*, 1200−1211.
65. Stephens, P. J.; Devlin, F. J.; Chabalowski, C. F.; Frisch, M. J. Ab Initio Calculation of Vibrational Absorption and Circular Dichroism Spectra Using Density Functional Force Fields. *J. Phys. Chem.* **1994**, *98*, 11623−11627.
66. Grimme, S.; Antony, J.; Ehrlich, S.; Krieg, H. A consistent and accurate ab initio parametrization of density functional dispersion correction (DFT-D) for the 94 elements H-Pu. *J. Chem. Phys.* **2010**, *132*, No. 154104.
67. Grimme, S.; Ehrlich, S.; Goerigk, L. Effect of the damping function in dispersion corrected density functional theory. *J. Comput. Chem.* **2011**, *32*, 1456−1465.
68. van Wüllen, C. Molecular density functional calculations in the regular relativistic approximation: Method, application to coinage metal diatomics, hydrides, fluorides and chlorides, and comparison with firstorder relativistic calculations. *J. Chem. Phys.* **1998**, *109*, 392−399.
69. Neese, F. Prediction and interpretation of the 57Fe isomer shift in Mössbauer spectra by density functional theory. *Inorg. Chim. Acta* **2002**, *337*, 181−192.
70. Sinnecker, S.; Slep, L. D.; Bill, E.; Neese, F. Performance of Nonrelativistic and Quasi-Relativistic Hybrid DFT for the Prediction of Electric and Magnetic Hyperfine Parameters in ^{57}Fe Mössbauer Spectra. *Inorg. Chem.* **2005**, *44*, 2245−2254.
71. Pantazis, D. A.; Chen, X.-Y.; Landis, C. R.; Neese, F. All-Electron Scalar Relativistic Basis Sets for Third-Row Transition Metal Atoms. *J. Chem. Theory Comput.* **2008**, *4*, 908−919.
72. Weigend, F.; Ahlrichs, R. Balanced basis sets of split valence, triple zeta valence and quadruple zeta valence quality for H to Rn: Design and assessment of accuracy. *Phys. Chem. Chem. Phys.* **2005**, *7*, 3297−3305.

73. Henegouwen, W. G.; Fieseler, R. M.; Rutjes, F. P. J. T.; Hiemstra, H. First total synthesis of ent-gelsedine via a novel iodide-promoted allene N-acyliminium ion cyclization. *J. Org. Chem.* **2000**, *65*, 8317– 8325.
74. Li, H.; Yan, X.; Zhang, J.; Guo, W.; Jiang, J.; Wang, J. Enantioselective Synthesis of C–N Axially Chiral N-Aryloxindoles by Asymmetric Rhodium-Catalyzed Dual C–H Activation. *Angew. Chem., Int. Ed.* **2019**, *58*, 6732– 6736.
75. Kariofillis, S. K.; Jiang, S.; Żurański, A. M.; Gandhi, S. S.; Martinez Alvarado, J. I.; Doyle, A. G. Using Data Science To Guide Aryl Bromide Substrate Scope Analysis in a Ni/Photoredox-Catalyzed Cross-Coupling with Acetals as Alcohol-Derived Radical Sources. *J. Am. Chem. Soc.* **2022**, *144*, 1045– 1055.
76. Yamane, Y.; Yoshinaga, K.; Sumimoto, M.; Nishikata, T. Iron-Enhanced Reactivity of Radicals Enables C-H Tertiary Alkylations for Construction of Functionalized Quaternary Carbons. *ACS Catal.* **2019**, *9*, 1757– 1762.
77. Theunissen, C.; Wang, J.; Evano, G. Copper-Catalyzed Direct Alkylation of Heteroarenes. *Chem. Sci.* **2017**, *8*, 3465−3470.
78. Singh, V.; Singh, R.; Hazari, A. S.; Adhikari, D. Unexplored Facet of Pincer Ligands: Super-Reductant Behavior Applied to Transition-Metal-Free Catalysis. *JACS Au*, **2023**, *3*, 1213−1220.